THESE DE DOCTORAT DE

ONIRIS
COMUE UNIVERSITE BRETAGNE LOIRE

ECOLE DOCTORALE N° 600
Ecole doctorale Ecologie, Géosciences, Agronomie et Alimentation
Spécialité : *Génie des procédés agroalimentaires*

Par
Veronica NESSI

Elaboration de nanocomposites à base d'amidon et potentiel d'application dans le domaine des biomatériaux

Thèse présentée et soutenue à Nantes, le 16 décembre 2019
Unité de recherche : INRA, UR 1268 BIA (Biopolymères, Interactions, Assemblages), Nantes, France

Rapporteurs avant soutenance :

Jean-Marie RAQUEZ	Professeur, Université de Mons, Belgique
Pedro FARDIM	Professeur, KU LEUVEN, Belgique

Composition du Jury :

Président du Jury :	Marie DE LAMBALLERIE	Professeure, ONIRIS, Nantes, France
Examinateur :	Graciela PAVON-DJAVID	Ingénieure de Recherche, Université Paris 13, France
Directeur de thèse :	Denis LOURDIN	Directeur de Recherche, INRA Nantes, France
Co-directeur de thèse :	Valérie GAUCHER	Professeure, Université de Lille, France
Co-encadrant de thèse :	Chloé CHEVIGNY	Chargée de Recherche, INRA Nantes, France

Invité(s)

	Nicolas DESCAMPS	Docteur, Roquette Frères, Lestrem, France

Development of starch-based nanocomposites and potentiality of application as biomaterials

---

Elaboration de nanocomposites à base d'amidon et potentiel d'application dans le domaine des biomatériaux

By:

VERONICA NESSI

Supervisors:

Dr. Denis LOURDIN

Pr. Valérie GAUCHER

Dr. Chloé CHEVIGNY

December 2019

Remerciements

A mes yeux une thèse n'est pas le simple fruit d'une recherche scientifique qui dure trois ans, et puis s'arrête. Une thèse, et plus en particulier cette thèse, est le fruit de deux histoires intrinsèquement liées : une purement professionnelle, et une plus personnelle, avec la science.

Une thèse classique vous direz….mais ça ne l'a pas été pour moi.

Cette histoire a démarré bien avant ma thèse, avec une bourse Erasmus pour mon stage de Master II à l'INRA de Nantes en 2016, ce qui me conduit à mes premiers remerciements : je voudrais remercier la Prof. Ambrogina Pagani et le Dr. Guy Della Valle pour m'avoir donné cette incroyable opportunité, et l'Union Européenne pour avoir favorisé et financé cet échange international. Un grand merci aussi à mes encadrants de ce stage de six mois, Agnès et Kamal, qui m'ont fait découvrir le monde de la recherche scientifique et qui m'ont transmis leur passion pour la science.

Un grand merci à mes amis de labo de cette époque-là : Alex, Gildas, Neeraj, Alice, Priscilla, Zahraa, Audrey, Ioana pour avoir fait disparaitre la peur et la solitude dès le premier jour. Je ne vous serai jamais assez reconnaissante pour tout ce que vous avez fait.

Merci Denis, pour m'avoir proposé cette thèse à la fin du 2016 même si, comme t'as rappelé pendant ma soutenance, une thèse ne s'inscrivait pas dans mes plans à cette époque-là.

Mais si j'ai bien appris une chose ces derniers trois ans c'est qu'on a beau faire des plans, mais ils ne teindront jamais la route.

Et aujourd'hui je peux affirmer, avec pleine certitude, qu'accepter cette thèse a été le meilleur choix non-planifié de ma vie. Donc merci pour cette opportunité.

Comme on dit toujours, la thèse est un peu comme des montagnes russes : parfois on se sent le roi du monde et parfois c'est tout le contraire. Et ma thèse n'a pas échappé à la règle. Mais j'ai eu l'incroyable chance de faire partie d'une équipe composée de collègues d'exception.

Par conséquence, merci à tous les membres de MC2, mais aussi de NANO, pour m'avoir aidée tout au long de ma thèse : en particulier merci Roselyne, Christine, Patrice, Anne-Laure et Magda pour votre aide technique et merci Laurent (le jeune docteur !), Kamal et Guy pour vos conseils. Merci Hubert, pour tes encouragements et pour avoir parfumé le bâtiment Loire avec tes créations ! Et merci Xavier pour les longues discussions de RMN : je te suis reconnaissante pour ta patience et ta précieuse formation.

Merci Karine et Jean-Eudes pour les journées passées à extruder des bandes, ou à les hydrolyser ou encore à les injecter en A4F. Je n'ai pas encore compté le nombre de kilomètres d'amidon extrudés mais je vous dirai un jour (peut-être).

Merci Isabelle et Bernard pour votre « nano » expertise si précieuse.

Merci Gregory et Clélia pour m'avoir formée à la culture cellulaire et aux tests de cytotoxicité : vous m'avez fait découvrir un monde fascinant et…très stérile (dans le bon sens!).

Un grand merci aux filles NANO et MC2 du labo : Mélissa, Mathilde, Dafne, Malika, Somia, Aicha, Maud, Zahraa, Imen et Yuzi, et aux collègues extérieures à l'INRA : Marion, Hanna, Marie et Coline pour votre soutien et compréhension tout au long de ma thèse.

Merci à tous pour les pauses et les repas en salle café et à la cantine, à parler de tout et de rien (mais surtout pas de boulot !) ; merci également pour m'avoir appris votre langue, si belle et complexe au même temps, mais aussi les jeux de mots et les anecdotes français.

Je tiens à remercier le Jury également, et plus en détail le Pr. Pedro Fardim, le Pr. Jean-Marie Raquez, la Pr. Marie De Lamballerie, la Dr. Graciela Pavon-Djavid et le Dr. Nicolas Descamps pour avoir accepté d'évaluer ma thèse et pour leurs commentaires bienveillants lors de la soutenance.

Mais surtout je tiens à remercier mes incroyables encadrants de thèse : merci Chloé, Denis et Valérie pour votre totale disponibilité et bienveillance, mais aussi pour m'avoir encouragée et pour m'avoir permis de partir en conférence en Belgique, Allemagne, Slovénie, Italie et Etats-Unis : pas beaucoup de doctorants ont une chance pareil !

Je tiens à remercier également le Pr. Jérémie Soulestin et le Dr. Eric Leroy qui ont participé à mes trois comités de suivi de thèse et qui m'ont conseillée tout au long de ma thèse.

Je sens de devoir remercier l’entreprise Roquette et l’Agence Nationale de la Recherche pour avoir accepté de financer ma thèse après la fermeture d’IFMAS. Sans vous cette thèse n’aurait pas été possible.

Enfin je tiens particulièrement à remercier ma famille et mes amies d’Italie, pour le soutien inconditionnel et pour avoir toujours cru en moi.

Merci Alexandre, car sans toi je n’aurais jamais entrepris ce chemin et je ne serais pas la personne que je suis aujourd’hui. Merci pour avoir écouté mes délires de jeune scientifique, pour avoir été présent pendant les moments difficiles mais aussi, et surtout, pour tout le reste.

Peut-être que, finalement, chaque thèse est une histoire personnelle plutôt que scientifique : au moins ça l’a été pour moi, une histoire très enrichissante et pleine de gratitude.

Merci.

Scientific publications and communications

Publications

Nessi V., Falourd X., Maigret J.E., Cahier K., D’Orlando A., Descamps N., Gaucher V., Chevigny C., Lourdin D. (2019). Cellulose nanocrystals-starch nanocomposites produced by extrusion: Structure and behavior in physiological conditions. *Carbohydrate Polymers*, 225, 115-123.

Nessi V., Rolland-Sabaté A., Lourdin D., Jamme F., Chevigny C., Kansou K. (2018). Multi-scale characterization of thermoplastic starch structure using Second Harmonic Generation imaging and NMR. *Carbohydrate Polymers*, 194, 80–88.

Oral communications

Nessi V., Falourd X., Descamps N., Gaucher V., Chevigny C., Lourdin D. *Bio-sourced starch-based nanocomposites for the elaboration of biomaterials.* **Journée Scientifique "Du phénome au Métabolome"**, Angers (France), October 2019.

Nessi V., Descamps N., Gaucher V., Chevigny C., Lourdin D. *Structure/properties relationship of bio-sourced nanocomposites.* **Journées Scientifiques de l’ED EGAAL**, Rennes (France), July 2019.

Nessi V., Descamps N., Gaucher V., Chevigny C., Lourdin D. *Starch-based nanocomposites for the elaboration of biomaterials.* **Journée Jeunes Chercheurs BIA**, Nantes (France), May 2019.

Nessi V., Rolland-Sabaté A., Lourdin D., Jamme F., Chevigny C., Kansou K. *Multi-scale characterization of thermoplastic starch structure using Second Harmonic Generation imaging and NMR.* **Starch Convention**, Detmold (Germany), April 2019.

Nessi V., Chevigny C., Descamps N., Gaucher V., Lourdin D. *Entirely bio-sourced nanocomposites for the elaboration of biomaterials.* **TERM summer school**, Trento (Italy), June 2018.

Nessi V., Chevigny C., Descamps N., Gaucher V., Lourdin D. *Entirely bio-sourced nanocomposites for the elaboration of biomaterials.* **EPNOE junior scientists meeting**, Maribor (Slovenia), May 2018.

Nessi V., Rolland-Sabaté A., Lourdin D., Jamme F., Chevigny C., Kansou K. *Biodegradation of potato starch: the role of microstructure*. **GDR Symbiose**, Montpellier (France), May 2017.

Posters

Nessi V., Chevigny C., Falourd X., Descamps N., Gaucher V., Lourdin D. *Structure-properties relationships of bio-sourced nanocomposites*. **Symbiose-Flower Conference**, Nantes (France), April 2019.

Nessi V., Chevigny C., Falourd X., Descamps N., Gaucher V., Lourdin D. *Structure-properties relationships of bio-sourced nanocomposites*. **American Chemical Society (ACS) Spring National Meeting**, Orlando (USA), March 2019.

Nessi V., Rolland-Sabaté A., Lourdin D., Jamme F., Chevigny C., Kansou K. *Microstructure and related properties. A case of study on extruded starch*. **Starch round table**, San Diego (USA), October 2017.

Nessi V., Chevigny C., Descamps N., Delaunay T., Gaucher V., Lourdin D. *Starch bio-composites for biomedical application*. **BIOPOL international conference on biodegradable and bio-based polymers.** Mons (Belgium), September 2017.

Table of contents

General introduction

In the last decades, the interest for degradable and sustainable materials manufactured from natural polymers grew up significantly. Among those, natural polymers are the ones occurring naturally, and they can be modified chemically or physically to obtain bio-based materials (as opposed to bio-based synthetic polymers where the monomer only is naturally occurring). These materials are usually produced by valorizing the co-products coming from the wood and the agro-food industry. The most important natural polymers include starch, cellulose and chitin: these are among the most available polymers in biomass and they are highly renewable and biodegradable. Besides their high degradability, they are also biocompatible with the human body (Reis et al. 2008). This allows employing these biopolymers for the most varied applications, from films for packaging to implants for medicine.

One advantage of starch compared to other biopolymers is its capacity to be processed easily by thermomechanical treatment such as extrusion, without the need of any solvent different from water, and allows the obtaining of a material called thermoplastic starch: this way 3D materials (as opposed to 2D thin films, obtained by solvent-casting for example) are obtained, whose production can be easily transferred to the industrial scale.

A potential and interesting application for thermoplastic starch is implants degradable on relatively short times of some weeks: for example starch-based stents and tubes for the treatment of salivary ducts under sialendoscopic surgery. These applications have been investigated starting from 2014 (Beilvert, Chaubet, et al. 2014; Beilvert, Faure, et al. 2014; Velasquez et al. 2015) at the INRA Institute of Nantes in the Biopolymers, Interactions and Assemblies (BIA) unit. These works proved that glycerol-plasticized potato starch processed by extrusion can be used as resorbable material for surgery with low invasiveness. This type of material showed low cytotoxicity, normal tissue integration with low inflammatory response and stable mechanical properties during implantation in rat and pig models. However, these materials show an excessively short lifespan (24h in a salivary buffer) to envisage longer-time (some weeks) applications, because of the fast degradation of thermoplastic starch in water and, during implantation, by amylases.

The addition of nano-sized fillers to polymers is a well-established method to modify the polymer properties in the desired direction while also using less product: for the same volume of fillers, if the dispersion is homogeneous, the effect on the macroscopic properties will be stronger for smaller (nano) particles, because of the increased polymer/filler interface (Cho et al. 2006). The key factor in getting significant change in the macroscopic properties upon addition of fillers is a homogeneous dispersion, this being mainly dependent on the nanocomposite preparation process and filler/polymeric matrix interactions.

Starting from this issue, cellulose and chitin nanocrystals are added to thermoplastic starch to create a nanocomposite. Because of their similar chemical structure, good interfacial adhesion is expected between starch and cellulose or chitin fillers: because of this interaction, the sensitivity of starch to water and enzyme could be reduced significantly, to obtain materials with controlled degradability.

The objective of this PhD is to understand the effect of the addition of nanofillers and their concentration on the structure-properties relationship in thermoplastic starch processed by extrusion, in order to develop entirely bio-sourced nanocomposites.

In order to achieve this goal, a multidisciplinary approach combining physical-chemistry of biopolymers, material science and process engineering has been developed.

This PhD, entitled “Development of starch-based nanocomposites and potentiality of application as biomaterials”, has been founded by ANR (French National Agency of Research), IFMAS and Roquette Frères companies. This project has been developed within the Materials, Creation and Behavior (MC2) team of the Biopolymers Interactions Assemblies (BIA) unit of INRA Institute, which have been studying agro-sourced materials, especially starch, for several decades. The Material and Transformation unit of the University of Lille contributed to the progression of this PhD as well.

Chapter 1 introduces the state of the art about the available knowledge on thermoplastic starch structure and properties, cellulose and chitin nanofillers and, eventually, starch-based nanocomposite systems. In addition, this chapter sheds light on the application of such materials in the biomedical domain. These insights have been necessary to the development of the experimental study and the comprehension of the phenomena.

Chapter 2 describes the raw materials employed in this work, details the processes used to form the starch-based nanocomposites and comprehensively describes the composition of each sample. It is meant as a reference chapter, where all the technical details about materials production necessary for understanding are gathered. To ease the reading, the experimental techniques used to characterize materials’ structure and properties are not listed in this chapter but they are rather presented gradually all along the manuscript.

The structure is the focus of Chapters 3 and 4, starting from the large-scale organization in the samples (microscopy, chains length) in Chapter 3 to very local structures in Chapter 4 (NMR and X-rays diffraction). Pure starch-based matrices are presented separately from nanocomposites to decorrelate the nanofillers effect on thermoplastic starch structure. Percolation and inter-particle distance theoretical models are reported in Chapter 3 as well to help in understanding the ongoing transformations.

Next, Chapter 5 reports the behavior of all produced materials in physiological conditions to test their potential application in the biomedical domain: the kinetic of glycerol release, swelling and enzymatic degradation are described in detail and related to the observed structures.

To assess their safety, materials have been investigated for their biological properties: cytotoxicity and cellular adhesion on materials surfaces. These are expounded in Chapter 6, together with the perspectives for more adapted experimental assays to improve the determination of materials safety (especially nanofillers).

At the end of the manuscript the conclusion highlights the structure-properties relationship characterized in this PhD, to identify new ways to optimize the properties in physiological conditions, for starch-based matrices alone and for nanocomposites.

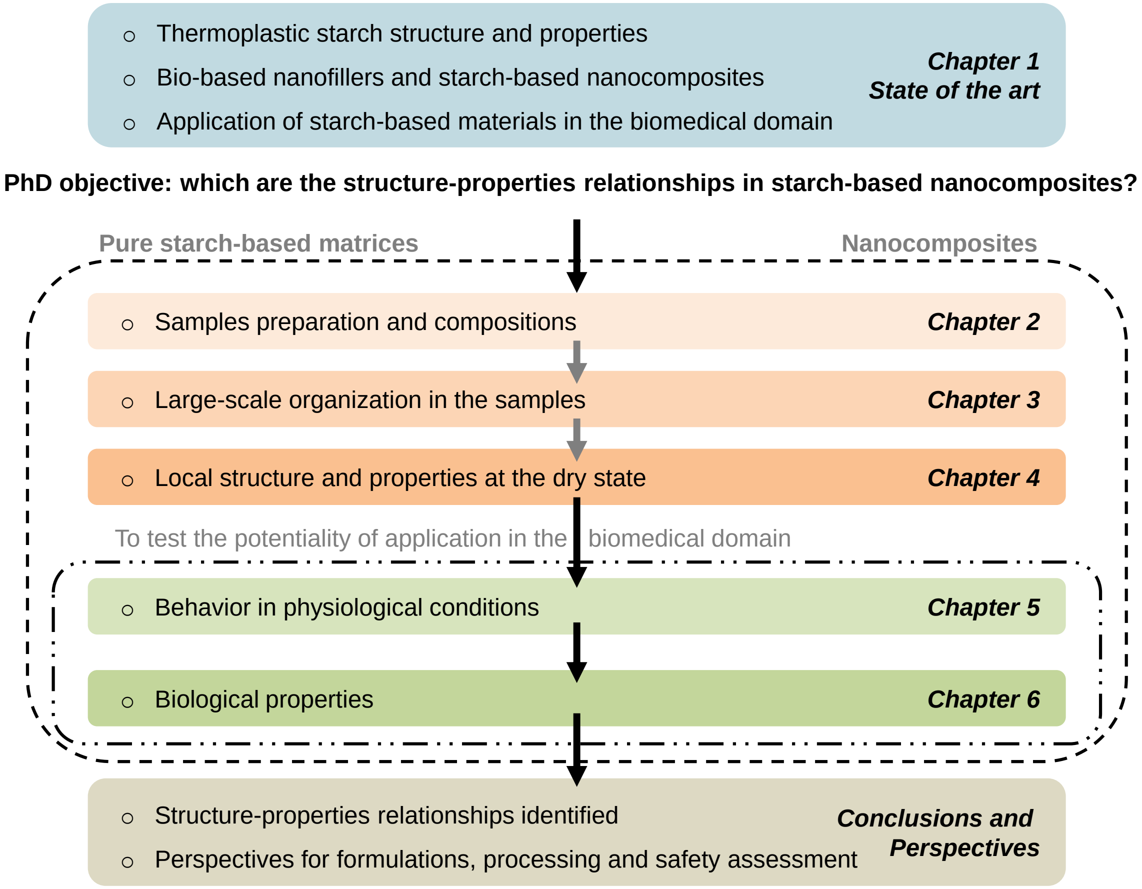

Figure 1: *Schematic representation of PhD plan.*

Chapter I

STATE OF THE ART

Table of contents

Section 1: Thermoplastic starch

1. Introduction

Starch is a biodegradable, renewable and natural polymer which belongs to the family of polysaccharides. Starch is a product of plant photosynthesis and it constitutes the second most abundant polymer in plants after cellulose. It represents one of the most important source of energy for human diet (Copeland et al. 2009) and for many other living beings. Starch is mainly found in plant roots, crop seeds, and staple crops such as rice, corn, wheat, cassava, or potato (Buléon et al. 1998) in the form of semi-crystalline granules in its native state. It is characterized by a high variability in structure and composition depending on botanical species and conditions of growth. This variability gives starch-based food or materials a wide range of properties (Copeland et al. 2009). Thanks to its natural and renewable features, and its low cost, starch has been used as a raw material for biodegradable materials, which are more and more used in industry (from films for packaging to implants for medicine) (Torres et al. 2011; Khan & Ahmad 2013). One advantage of starch is its ease of process: starting from a simple powder to obtain 3D polymeric matrices with satisfying mechanical properties. Plasticizers are commonly added to starch during processing to obtain a more plastic and flexible material.

2. From native to thermoplastic starch

Starch is found naturally in the form of semi-crystalline granules which have to be processed to obtain a polymeric matrix, referred to as thermoplastic starch (TPS). This part of the chapter describes native starch, together with the most common processes to obtain TPS. A brief overview of the structure and properties of TPS is provided as well.

2.1 Native starch

2.1.1 Starch constitutive molecules: amylose and amylopectin

Starch is a homoglucan composed up to 98-99% of α-glucans of D-glucose, linked together by α (1, 4) and α (1, 6) linkages to form two distinct molecules referred to as amylose and amylopectin. The remnant 1-2% of starch composition is made up of small amounts of lipids, minerals and phosphates (Copeland et al. 2009). The presence of α-type linkages in starch favors the pool of polar hydroxyl groups linked to carbons 1, 4 and 6, which is responsible for the hydrophilic behavior of this biopolymer.

Amylose is an essentially unbranched polymer in which glucose units are bounded by α (1, 4) linkages with few α (1, 6) linkages (**Figure I-1a**). Amylose shows properties typical of linear chains since only 0.5% of its glucoses are in α (1, 6) linkages. Amylose molar mass ranges between 10^5 - 10^6 g mol^{-1} and its degree of polymerization (DP) is on average 1000-10,000 glucose units (Copeland et al. 2009; Rolland-Sabaté et al. 2007). Because of their linearity, amylose chains organize in single or double helices (Avérous 2004) (**Figure I-1b**). Each helix is formed by 6 up to 8 glucose units and it is stabilized by intramolecular hydrogen linkages, which induce the formation of an inner hydrophobic cavity. This hydrophobic feature enables amylose to form complexes with non-polar molecules such as iodine, which is employed to quantify amylose fraction in starch.

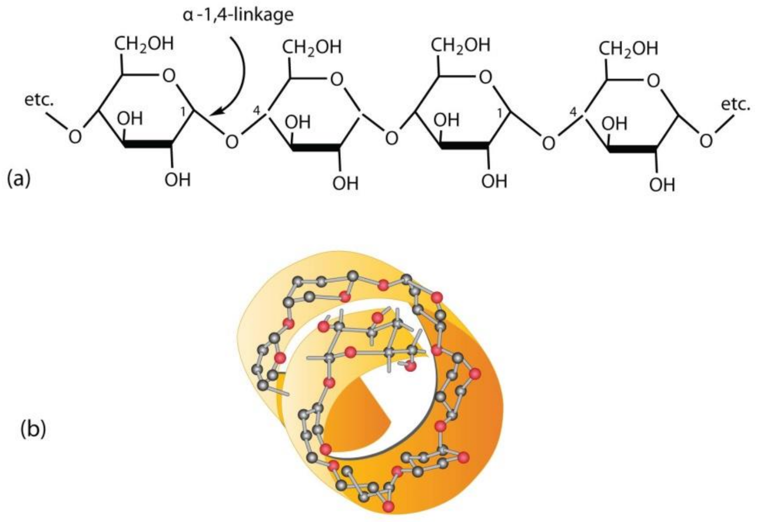

Figure I-1: *Chemical structure of amylose:* **a)** *α (1, 4) linkages between α-D-glucose units and* **b)** *single helix of amylose with 6 glucose units per turn (Bennett 2016).*

Amylopectin is a highly multiple-branched polymer in which glucose units are bounded by α (1, 4) linkages and around 5-6% of α (1, 6) linkages at branching points (**Figure I-2**). This macromolecule presents an extremely high molar mass, around 10^7 - 10^9 g mol^{-1} and a complex and arborescent branched structure with branching points each 22 - 70 glucose units (Rolland-Sabaté et al. 2007).

The exact branched structure of amylopectin and its conformation inside the native granule is unknown to date. Several models have been proposed, but the most supported is the cluster structure concept (**Figure I-3**). Amylopectin is composed of two types of chains, characterized by different length and DP. Short chains (S), with a mean DP ranging between 14 and 18, are connected by longer chains (L), of DP between 45 and 55, to form clusters. α

(1, 6) linkages are limited to L chains. Amylopectin chain length is usually expressed on a molar basis with a ratio (L/S), which strongly depends on the botanical origin of starch.

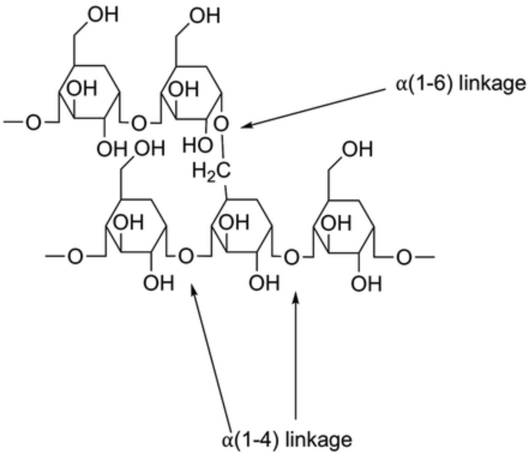

Figure I-2: *Chemical structure of amylopectin with linear α (1, 4) linkages and α (1, 6) linkages at branch points (Giri et al. 2018).*

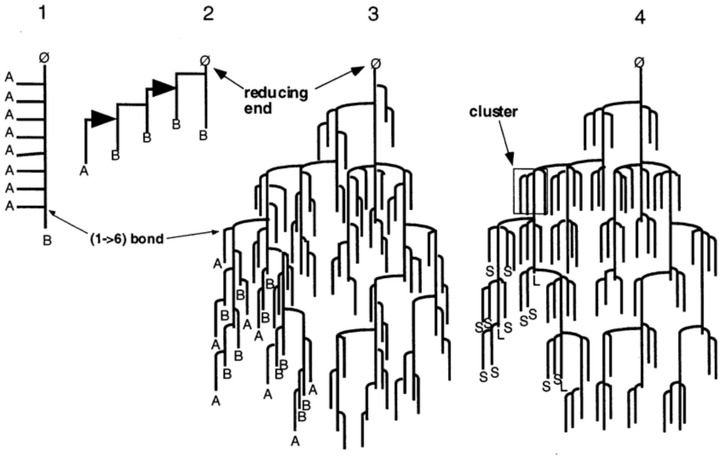

Figure I-3: *Diagrams of amylopectin molecular structure as proposed by (1) Hawort, (2) Staudinger, (3) Meyer and (4) Meyer redrawn as in the cluster-structure concept (Buléon et al. 1998).*

Similarly, the ratio between amylose and amylopectin in the starch granules is strictly related to the botanical source (**Table I-1**) and, to a latter extent, affected by environmental factors (soil, climate, etc.) (Tester et al. 2004). Classically, starch is composed of 20-25% amylose and 75-80% amylopectin, but starch can be genetically modified to change these ratios. For example, waxy starches are almost fully constituted of amylopectin (0-2% amylose) and high-amylose starches, on the contrary, have a very high rate of amylose (70%).

Table I-1: *Amylose mass fraction in major plant resources (Buléon et al. 1998).*

Source	Amylose (% total starch)
Wheat normal	25 - 29
Wheat waxy	1.2 - 2.0
Maize normal	25 - 28
Maize waxy	0.5
Maize high-amylose	60 - 73
Potato normal	18 - 21
Potato waxy	1

2.1.2 Granular organization

Wild type starch is organized on four length scales (Waigh et al. 2000):

- the molecular scale (~0.1 nm);
- the lamellar structure (~9 nm);
- the growth rings (~0.1 µm);
- the whole granule morphology (~ µm).

In nature, native starch is stored in plants in the form of granules, varying in size (2-100 µm) and shape depending on the botanical source. The size distribution of the granules can be monomodal (i.e. potato) or bimodal (i.e. wheat) and can also vary a lot even in the same species; for example, potato starch is stored in granules with an average diameter between 15 and 75 µm and with a general elliptical shape.

The observation of partially-hydrolyzed starch granules by Transmission Electron Microscopy (TEM) has highlighted the presence of two different layers in the granule, with different sensitivity to acid depending on their amorphous or semi-crystalline structure. Semi-crystalline and amorphous layers are concentrically positioned around a core, known as the hilum, characterized by a relatively disorganized structure. Semi-crystalline layers are formed by the alternation of amorphous and crystalline thin lamellae (**Figure I-4**).

In native starch, crystallinity is due to the amylopectin molecules: short amylopectin chains in the clusters are organized in double helices, packed together to form crystallites. The association of these clusters creates the crystalline lamella while the amorphous one contains amylopectin branching points and amylose molecules. The role of amylose is still unclear: a large portion is found in amorphous growth rings and only few units are associated with amylopectin within the crystalline lamella.

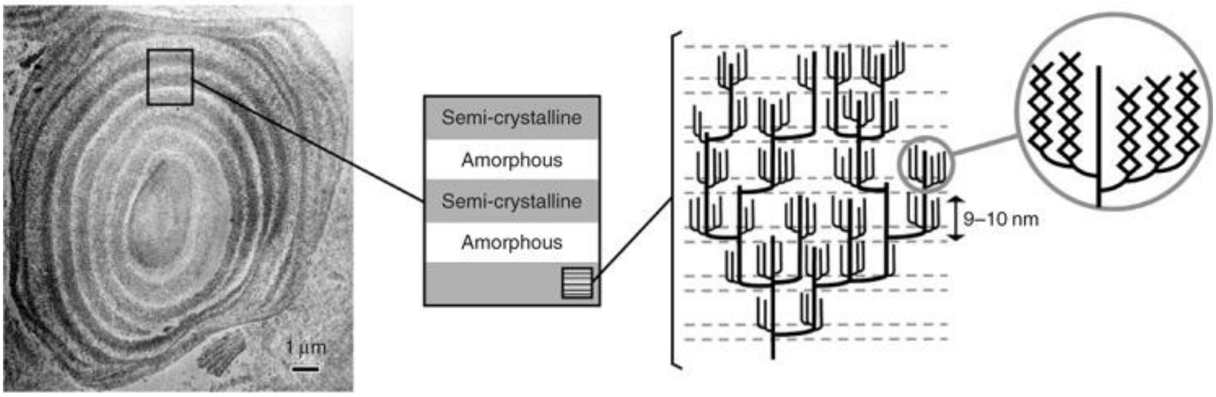

Figure I-4: *Section of waxy maize starch granule by Transmission Electron Microscopy (TEM) and schematic representation of starch granule ultrastructure (Buléon et al. 2007).*

Starch granules present a typical birefringence when observed under polarized light (**Figure I-5a**) due to the radial orientation of amylopectin double helices in crystalline lamellae. This birefringence is clearly visible in the form of a maltese cross centered in the hilum (Pérez & Bertoft 2010). A similar result is obtained using a less-conventional technique, named Second Harmonic Generation (SHG) imaging: the anisotropic nature of amylopectin is solicited using a laser input and a second harmonic wave is generated. This allows identifying the radial orientation of amylopectin molecules (**Figure I-5b**), both in native granules and in processed starch.

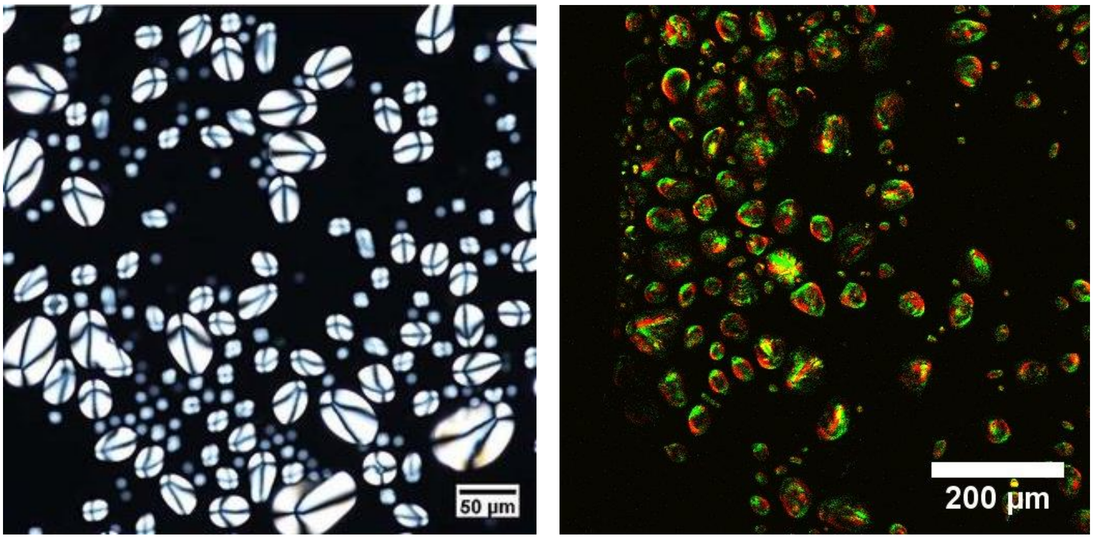

Figure I-5: *Potato starch native granules observed* **a)** *under polarized light (Zhao et al. 2018) and* **b)** *using SHG (Nessi et al. 2018).*

2.1.2.1 Semi-crystalline structure

The type of crystalline structure of starch varies with the botanical origin. Crystals, coming both from native granules and high-humidity stored processed starch, are able to diffract X-rays. Wide Angle X-ray Scattering (WAXS) typically goes from 3° to 35° and it allows identifying three different crystalline structures of starch, which depend on multiple parameters: the arrangement of glucose monomers in amylopectin double-helices, the number of water molecules trapped in the crystal structure, the branching degree of amylopectin and, if any, amylose interactions. Water plays a key role and it represents an integral part of starch polymorphs.

- The A-type is typical of cereal starches and it consists in starch double helices arranged in a compact monoclinic array (**Figure I-6**), with eight water molecules per unit. L/S ratio has an average value of 8-10 for this crystalline type. The typical X-ray diffraction angles, determined by CuKα1 radiation, for this polymorph are: 10.1°, 11.3°, 14.9°, 17°, 18.1°, 23°, 23.9° and 26°.
- The B-type occurs in tubers, amylose-rich starches and in retrograded starch. It is characterized by a hexagonal packing of double helices with an open structure capable to hold 36 water molecules (**Figure I-6**). L/S ratio is around 5 for B-crystalline type amylopectin. Typical peaks, determined by CuKα1 radiation, are found at: 5.6°, 10.1°, 11.3°, 14.9°, 17°, 19.5°, 22°, 23.9° and 26°.
- C-type is the result of the coexistence of A and B type in the same starch granule, with B-type positioned in the center and A-type at the periphery. It is mainly found in pulse starch and pea.

A fourth polymorph, named V-type, occurs when amylose complexes with non-polar molecules such as lipids, iodine or alcohols. These molecules insert in the hydrophobic cavity of amylose chains arranged in a simple helical structure.

Crystallinity quantification for starch is quite a challenging issue, as crystalline structures are highly sensitive to water and because crystalline standards for starch are not readily available. One of the most common methods to quantify crystallinity by X-ray diffraction is the Wakelin method (Wakelin et al. 1959). It consists in comparing the sample diffractogram with two standards, one amorphous and one crystalline, at the same hydration conditions. For starch, the amorphous standard is represented by amorphous starch while spherulitic crystals are the crystalline standard. Once the amorphous contribution discarded, the diffraction intensities coming both from the sample and the crystalline standard are linearly correlated, and the crystallinity rate of the sample is obtained. An alternative method consists in fitting the diffractogram of the sample with the peaks of the crystalline reference, using technical software such as PeakFit® or Origin®.

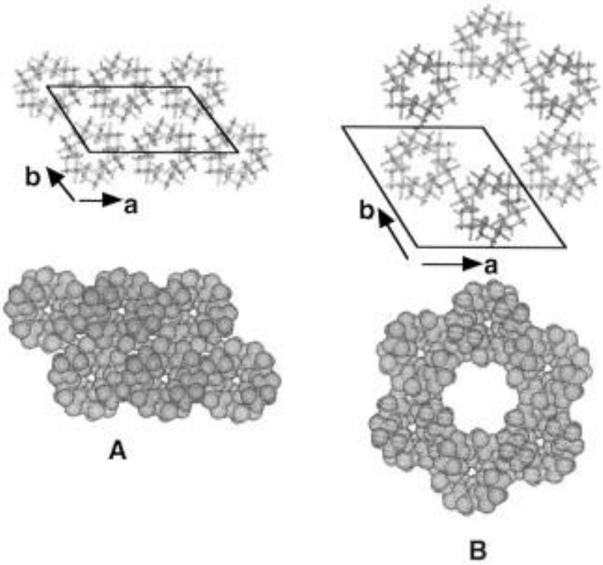

Figure I-6: *A and B type crystallinity in starch (Buléon et al. 1998).*

2.2 Processing of native starch

To obtain thermoplastic materials, native starch granules must be transformed. Thermomechanical starch processing requires the introduction of energy, usually in form of heat and/or mechanical stress, and water. Water has a key role in starch transformation because, unlike other polymers, starch cannot undergo thermic transitions in absence of water. Indeed, thermic transitions of anhydrous starch occur at temperatures higher than its degradation temperature (200-220°C).

2.2.1 Hydrothermal transition of starch

Starch already contains water in its native form. Native starches are commercialized with a water content ranging from 12-13wt% for cereals to 18-19wt% for potato. Starch is a highly hydrophilic polymer and it easily absorbs water. Indeed, the immersion of native starch granules in water or their storage in high relative humidity environments induces the diffusion of water molecules in their structure. However, depending on the temperature of the system, starch undergoes different phase transitions and transformations.

At 20°C starch absorbs water from the environment. The amount of water absorbed directly depends on the relative humidity of the environment, and follows precise sorption isotherms.

At increasing water activity (a_w), water penetrates the amorphous regions of starch, following a reversible phenomenon named sorption (**Figure I-7**). At 20°C and at maximum water activity ($a_w = 1$) starch absorbs water up to 40-50%.

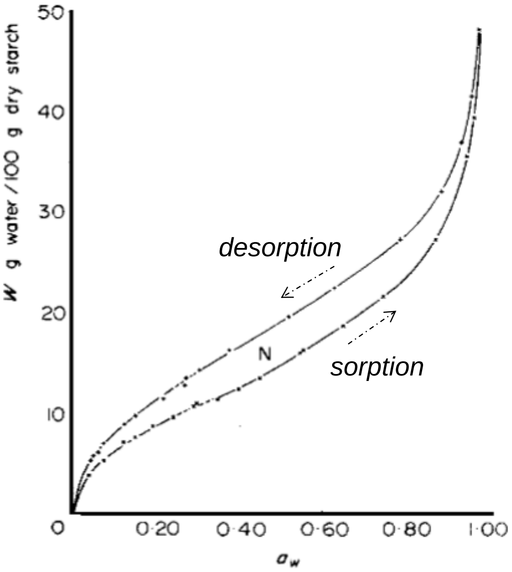

Figure I-7: *Water sorption and desorption of potato native starch as a function of water activity (a_w) at 20°C (Van Den Berg et al. 2007).*

Conversely, when water activity decreases, the water absorbed by native starch granules decreases gradually, following a kinetic of desorption (**Figure I-7**). A strong hysteresis is visible on almost all the water activity range (up to ~0.95) and ~30% of the water sorption capacity (**Figure I-7**); hysteresis reaches its maximum (4-5% water on a dry starch basis) at $a_w = 0.5$ (Van Den Berg et al. 2007).

In water excess, at intermediate temperatures (60-70°C) starch granules strongly swell and starch chains, mainly amylose, start migrating in the aqueous phase. This endothermic phenomenon, named gelatinization, is irreversible (**Figure I-8**). To obtain a complete solubilization of starch, it is necessary to reach temperatures around 130°C, under light stirring. In these conditions the crystalline regions and the granular organization are irreversibly disrupted and amylopectin double-helices uncoil. The result is a hot, viscous solution of starch.

Gelation and retrogradation occur upon cooling below the gelatinization temperature of starch (**Figure I-8**) as gelatinized starch starts re-organizing in a more ordered state. More in detail, amylose forms a coarse network in which gelatinized amylopectin gets stuck, acting as a filler (van Soest 1996). This is effectively a way to produce a crystalline and water-insoluble novel form of starch.

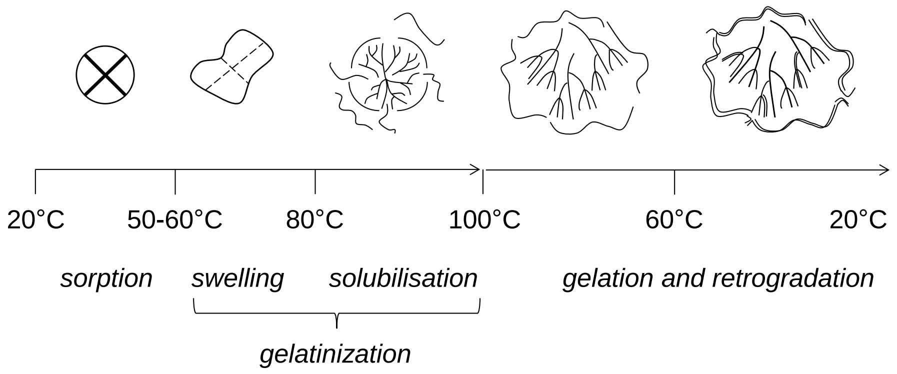

Figure I-8: *Effect of temperature on starch native granule in excess of water.*

Gelatinization can be observed starting from 40% water content in the sample. For high water contents an intense endothermic peak is identified around 60-70°C by Differential Scanning Calorimetry (DSC). For lower water content, the intensity of this gelatinization peak decreases and a second peak appears at higher temperatures due to granules melting (**Figure I-9**).

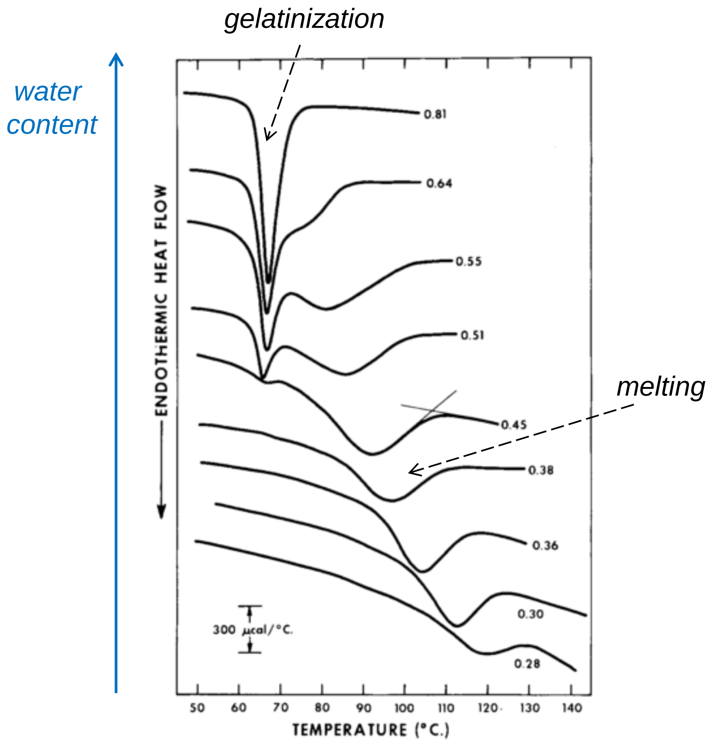

Figure I-9: *Gelatinization and melting of potato starch as a function of water content (Donovan 1979).*

In addition to water content, the melting of granular starch is influenced by the addition of various plasticizers (glycerol, sorbitol, lactic acid sodium, urea, ethylene, diethylene glycol…): once inside the granule, the plasticizers can form hydrogen bond with starch molecules which stabilizes the structure and brings about a rise of the temperature and enthalpy of fusion of the crystallites at 50% water content (J.J.G. van Soest, Bezemer, et al. 1996; Liu et al. 2011) (**Figure I-10**). The shift of the melting endotherm to higher temperatures performed by glycerol moves the helix-coil transition associated with the loss of granular birefringence to even higher temperatures (Liu et al. 2011; Li et al. 2014).

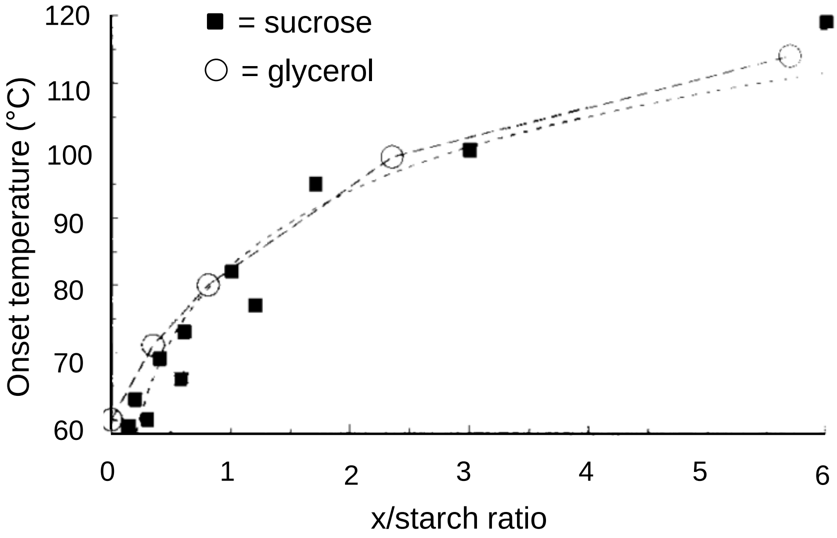

Figure I-10: *Onset temperature of potato starch melting as a function of sucrose and glycerol content: starch/water ratio is 1:1 (J.J.G. van Soest, Bezemer, et al. 1996).*

Depending on the water content, starch can be processed by solvent-casting or extrusion. In the solvent-casting method, starch granules are gelatinized in an excess of hot water under mild stirring, followed by an evaporation step to produce thin films. Evaporation must be developed at a temperature higher than the gelatinization temperature to obtain an amorphous material and avoid gelation/recrystallization. To do this, the gelatinized solution of starch is deposited on a heated anti-adherent surface.

Conversely, extrusion is a continuous process generally used to obtain amorphous materials at relatively low water content (~30%). During extrusion starch granules do not gelatinize but rather melt under the combined effects of heat and shear. The addition of water is necessary to transform native starch in a thermoplastic material. Counter to solvent-casting, the extrusion is a continuous process providing thick 3D polymeric materials, which justifies the interest industrially shown for this process.

2.2.2 Extrusion process

An extruder is typically composed of a feed hopper, a thermo-regulated sheath, one or two screws and a die (**Figure I-11a**).

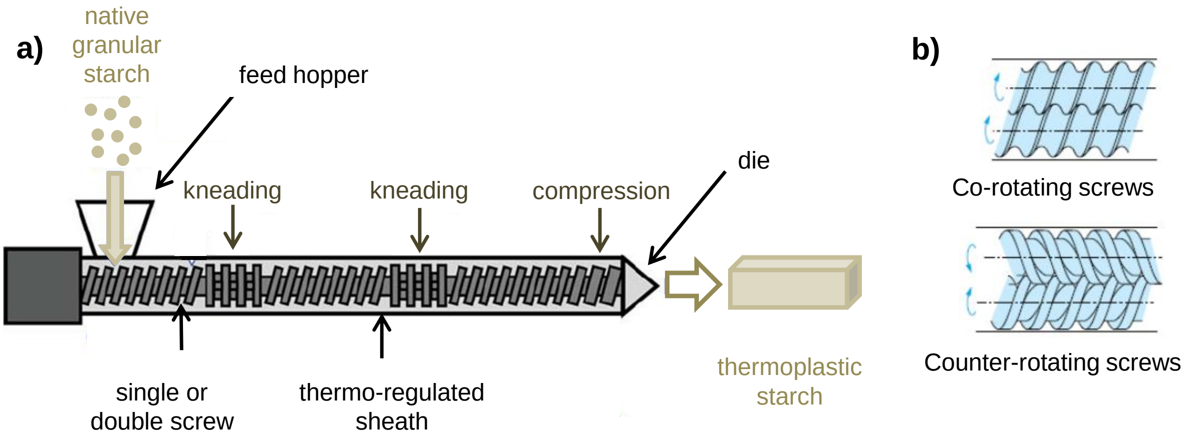

Figure I-11*: **a)** Schematic representation of starch processing by extrusion, adapted from (Xie et al. 2012) and **b)** two types of screws conformation in a twin-screw extruder (Vergnes & Chapet 2001).*

The feed hopper is where the raw material enters the extrusion system; the thermo-regulated sheath is the cylinder in which high heat and pressure are applied on the raw material; the screws apply the shear stress and push the melted material in the direction of the die, which gives the final shape. The screw profile can be modified with kneading elements, which favor mixing and destruction of the native structure.

Twin-screw extrusion is generally preferred to single-screw one for multiple reasons. First, the use of two screws (co-rotating or counter-rotating, **Figure I-11b**) instead of one potentially favors the homogeneous dispersion of all raw materials, and the variety of the screw constitutive elements makes it possible to control the shear applied on native starch, which is fundamental to destructurize starch as desired. Moreover, the independence of extrusion parameters (for example between feeding rate and screws speed) enables the fine control of shear-time-temperature parameters. Finally, twin-screw extrusion is the most industrially common process because it is economically viable, as it handles large quantities of material.

In order to obtain homogeneous thermoplastic starch at the exit of the extruder, the temperature settled at the thermo-regulated sheath must be higher than the melting temperature (Tm) of the hydrated starch formulation and the mechanical stress must be strong enough. The intensity of the thermomechanical treatment on starch is expressed as the Specific Mechanical Energy (SME) and it corresponds to the ratio between the applied motive force and the material flow:

$$SME = \frac{2\pi \cdot C \cdot N}{Q} \qquad \textbf{[I-1]}$$

Where C is the Couple (N m), N is the screw rotation speed (turn min^{-1}) and Q is the material flow (g min^{-1}). In the case of potato starch, a SME > 100 J g^{-1} is necessary to obtain a complete destructurization of starch native structure (Barron et al. 2001).

The application of mechanical energy alone causes the granules to fragmentate (**Figure I-12a**), but is not sufficient to completely destroy the crystalline structure. Conversely, the application of thermal treatment alone causes the starch granular structure to disorganize gradually, because of the melting of native crystalline structures. At temperature higher than the melting temperature of starch, a heterogeneous material containing a melted phase and remaining crystallites is obtained (**Figure I-12b**). A homogeneous melted phase, possibly accompanied by a partial depolymerization of starch chains, occurs when both high SME and temperatures are applied (**Figure I-12c**).

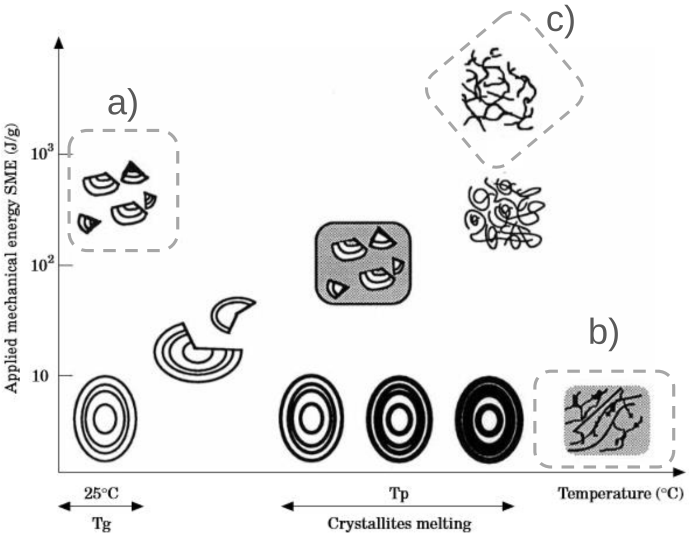

Figure I-12: *Schematic representation of starch deconstruction under shear and temperature (Barron et al. 2001).*

Generally, amylopectin chains depolymerize more easily during extrusion, because of their branched nature and inflexible structure, compared to amylose.

All these structural changes generated by the application of mechanical and thermal stress strongly modify the physicochemical properties of processed starch compared to native starch, as it will be shown in the following paragraphs.

3. Thermoplastic starch structure and properties

Thermoplastic starch (TPS) is defined as substantially amorphous starch which is obtained by thermomechanical treatment (for example by extrusion) of native starch.

The thermomechanical treatment of starch granules in the presence of water induces the disruption of their supramolecular structure and crystals melting.

The organization of amylose and amylopectin macromolecules in amorphous starch is unclear up to now. They are usually described as interpenetrating random coils stabilized by weak hydrogen interactions and entanglements (conformational constraints). Semi-crystalline structures, such as stand-alone double helices, double helices embryos or small (nano-sized) bundles of crystallinity may persist in TPS depending on the parameters applied during processing (**Figure I-13**).

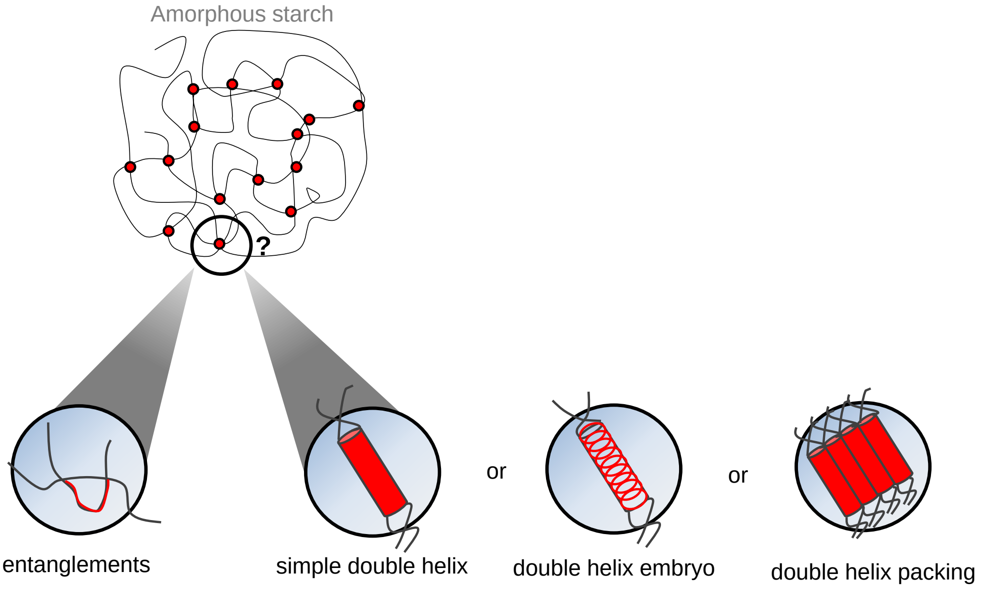

Figure I-13: *Schematic representation of thermoplastic starch system stabilized by "reticulation points" (Chevigny et al. 2016).*

3.1 Glass transition temperature (Tg)

The glass transition is a reversible phenomenon which affects the amorphous regions of a material. This transition is characterized by a temperature value (Tg), specific for each polymer, at which the material passes from the glassy to the rubbery state. Indeed, the Tg is determined by Differential Scanning Calorimetry (DSC) as the midpoint of the transition between the glassy and the rubbery behavior of the material.

At temperatures lower than the Tg, the mobility of material’s constitutive macromolecules is weak, while at higher temperature the mobility increases and the material becomes more ductile.

Thermoplastic starch amorphous regions are affected by glass transition as well. However when the water content is low, this transition occurs at really high temperatures: indeed, the glass transition temperature of anhydrous starch cannot be measured because it is higher than its degradation temperature (315°C).

Like all thermal transitions of starch, the glass transition is strongly affected by the water content; indeed, it has been measured that a change of 1% of water content can cause changes in Tg up to 10°C in amorphous starches, when the water content ranges between 8 and 18%. Non-aqueous plasticizers are added to thermoplastic starch to modify its glass transition temperature as well.

The presence of water and other plasticizers promotes molecular mobility and decreases weak macromolecular interactions, such as hydrogen bonds. The increase in starch chains mobility generated by the addition of polyols is explained by their high compatibility with starch and by the small size of their molecules, which can penetrate starch structure and induce a softening (Mikus et al. 2014).

The evolution of Tg depends on water and/or plasticizer contents and can be modelled using the Couchman-Karasz relation (1978):

$$Tg = \frac{\sum_i W_i \, \Delta Cp_i \, Tg_i}{\sum_i W_i \, \Delta Cp_i} \qquad \textbf{[I-2]}$$

Where W_i is the molar fraction of component i, ΔCp_i (J g^{-1}) is the variation of the heat capacity at the glass transition temperature Tg (K) of the pure component i.

On the whole, Tg of hydrated starch is higher than room temperature when water content is inferior to 20% (**Figure I-14**). A significant decrease in the glass transition temperature takes place as water and/or plasticizers concentrations increase. As an example, the case of glycerol, the most common starch plasticizer after water (J.J.G. van Soest, Benes, et al. 1996), is presented in **Figure I-14**.

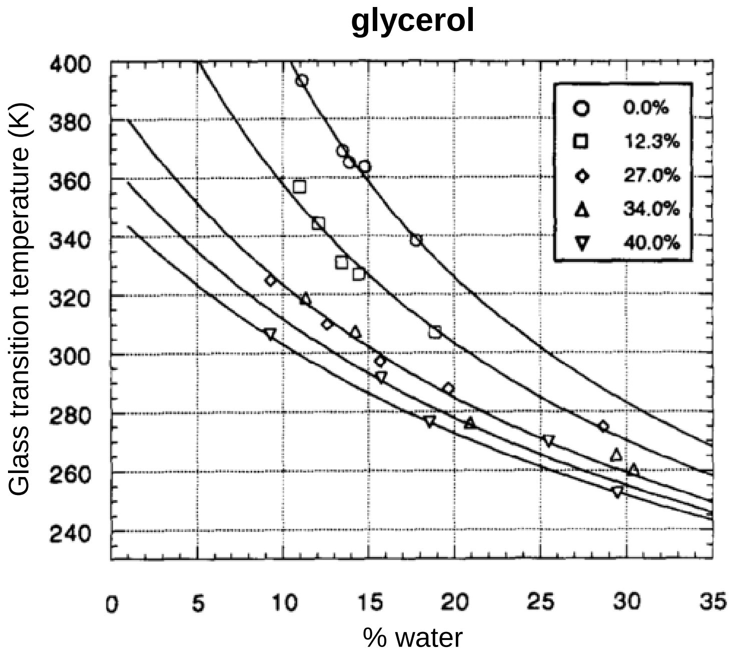

Figure I-14: *Variation in glass transition temperature depending on total water and glycerol content (Lourdin et al. 1997).*

To a lesser extent, differences in Tg can be observed on starches of different botanical origin as a function of their amylose/amylopectin ratio: amylopectin is known to have a Tg about 20°C lower than amylose, due to its branched nature inducing a less compact structure. Free volume generation due to branching is a well-known Tg depressor and named “internal plasticization” (Slade et al. 1991).

3.2 Thermomechanical behavior

The Tg is of great importance for the mechanical properties of the material. The mechanical behavior of TPS is dependent on its Tg and it can be studied by Dynamic Mechanical Thermal Analysis (DMTA).

During a DMTA mechanical test, a sinusoidal strain is applied to the sample and the force necessary to deform the material is measured, allowing the determination of the storage (E') or loss (E") modulus and the damping factor (Tanδ, the ratio between the loss and the storage modulus). The storage modulus (near to Young’s modulus E) varies as a function of temperature as the mechanical response of starch chains changes over heating: below Tg the material is glassy, with a modulus in the GPa range (**Figure I-15**). In the glassy state TPS chains present low mobility and the material is generally brittle. Above Tg, TPS behaves as a viscoelastic material and its modulus significantly decreases to values in the MPa range (**Figure I-15**). A slightly higher modulus compared to completely amorphous TPS can be observed for semi-crystalline polymers due to the presence of crystals (G'Sell et al. 1994) or in nanocomposites due to the presence of nanofillers in the amorphous matrix (V. Favier et al. 1995), as will be shown in Section 2 of this Chapter.

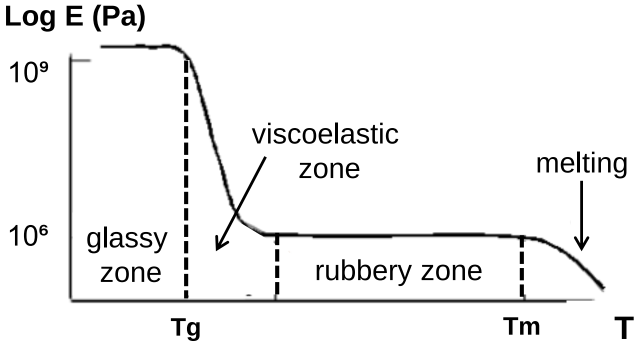

Figure I-15: *Evolution of storage modulus E' as a function of increasing temperature.*

In DMTA, the transition between glassy and rubbery state is identified by a major peak in the damping factor (Tanδ) signal, associated with α-relaxation. The α-relaxation corresponds to the main mechanical relaxation in the material generated by the simultaneous relaxation of multiple starch chains. The peak in the Tanδ signal corresponds to the α-relaxation and is associated to a specific temperature: Tα.

Non-aqueous plasticizers play an important role in modifying the thermomechanical properties of thermoplastic starch as they affect the mobility of starch chains. As a result, the α-relaxation occurs at much lower temperatures in glycerol-plasticized TPS compared to non-plasticized TPS for the same water content: an example of α-relaxation evolution at increasing glycerol concentration is reported in **Figure I-16** on wheat starch processed by twin-screw extrusion. Specifically, two major relaxations are visible in **Figure I-16**, due to the separation of the mixture into glycerol-rich and starch-rich phases. The first (below 0°C) is generated by the glycerol-rich phase while the second (above 0°C) is due to the starch-rich phase. Due to this greater molecular mobility, starch chains in polyol-plasticized TPS go through post-extrusion reorganization, forming semi-crystalline structures (D Lourdin et al. 1997).

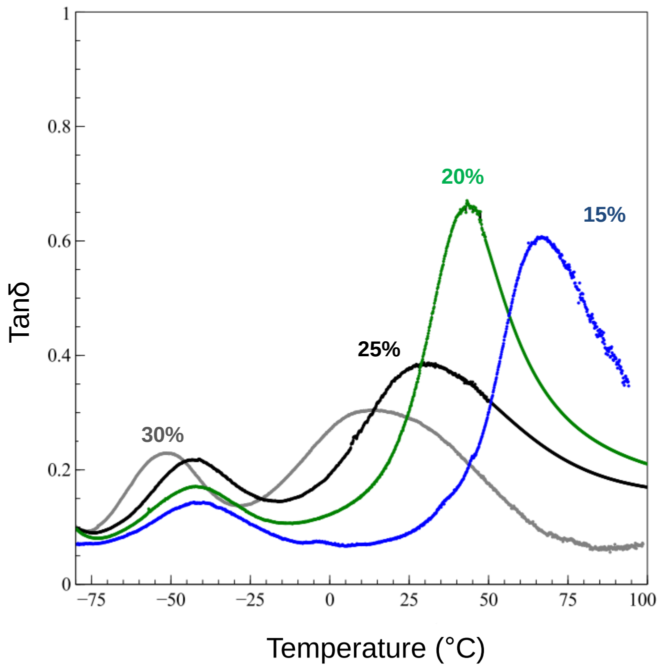

Figure I-16: *Tanδ curves obtained by DMTA measurements with different amount of glycerol (Mikus et al. 2014).*

To conclude, Tg and Tα give complementary information about chains motion (Lu et al. 2005): Tg (determined by DSC) refers to the temperature at which the phase transition of starch chains driven by heat occurs, whereas Tα (determined by DMTA) points out the main mechanical relaxation of starch chains during heating. For this reason, TPS shows different Tg and Tα values.

3.3 TPS swelling and enzymatic degradation

The main enzymes involved in starch hydrolysis are α-amylase, β-amylase, glucoamylase and pullulanase. Pancreatic α-amylase is responsible for the highest degradation rate of starch polymeric blends, and is therefore a key enzyme when studying the enzymatic degradation of starch-based materials (Azevedo et al. 2003).

Amylases may occur in body fluids other than saliva or gastric juices. Kipps and Whitehead measured amylases concentration in multiple body fluids, such as sweat, urine and serum (Kipps & Whitehead 1975). The spread values measured for each type of fluid (84 - 300 IU/L for serum, 130 - 3500 IU/L for urine, 72 - 1300 × 10^3 IU/L for saliva) are mostly dependent on the interpersonal variation in amylase production (Kipps & Whitehead 1975).

α-amylase hydrolyzes the α (1, 4) glucosidic bonds of amylose and amylopectin but is not able to hydrolyze α (1, 6) linkages. Hence, the final hydrolysis products from amylase digestion are mainly maltose, maltotriose, maltotetraose and not glucose. The hydrolysis process starts with the enzyme diffusion with water on the solid-liquid interface, and is followed by enzyme absorption and the formation of substrate-enzyme complexes.

Most starches contain a fraction that the enzyme digests rapidly (rapidly digestible starch – RDS), slowly (slowly digestible starch – SDS) and a fraction that is resistant to digestion (resistant starch – RS). This classification of starch is based on the kinetics of *in vitro* digestion and has been developed by Englyst at the beginning of the ‘90s (Englyst et al. 1992). It constitutes one of the most widely spread methods to classify starches. Based on this method, RDS corresponds to the amount of glucose released in the first 20 min, SDS is the amount of glucose released between 20 and 120 min, while RS is the amount of starch remaining after 120 min of *in vitro* digestion.

The RS fraction is composed of native starch granules and retrograded starch which cannot be completely degraded by the enzyme: in the case of granules, their high compactness/low chains mobility and their semi-crystalline structure are responsible for the very slow and incomplete enzymatic degradation (Colonna et al. 1992; Chanvrier et al. 2007).

Because of the shearing and kneading applied to starch during extrusion, TPS is characterized by a mainly amorphous structure, highly sensitive to the coupled effect of water (Xie et al. 2013) and enzyme (Beilvert, Faure, et al. 2014).

Two main structural factors, coming from the extrusion process, are responsible for the complete enzymatic degradation of amorphous TPS and its high sensitivity to water:

- The disruption of the crystalline structure, which induces the exposure of hydroxyl groups of amylose and amylopectin to water; water molecules form hydrogen bonds with the exposed groups of starch and cause an increase in starch swelling and solubility (Singh et al. 2010). As a consequence, water penetration in starch structure is facilitated and, with it, the ingress of the enzyme.
- The deconstruction of the granular structure and the partial degradation of starch chains into smaller components (Vikman et al. 1995) compared to raw samples (native starch), which broaden the surface exposed to water and enzyme, increasing swelling and digestibility (Anguita et al. 2006).

The addition of plasticizers is known to reduce the swelling of TPS and induce resistance to enzymatic hydrolysis (Beilvert, Faure, et al. 2014; Velasquez et al. 2015; Nessi et al. 2018) (see **Figure I-17**). Indeed glycerol helps in preserving starch native granular structure during extrusion: glycerol acts as a lubricant during extrusion, reducing the shear applied by the screw on native starch. In addition glycerol is known to produce crosslinking (between the hydroxyl groups of starch molecules) mainly within amorphous starch regions inside the granules (Smits et al. 2003). This stabilizes starch granular structure and makes the granules less susceptible to disruption during processing (J.J.G. van Soest, Bezemer, et al. 1996).

Eventually, the partial recrystallization of starch chains after extrusion, indirectly induced by glycerol through the lowering of materials' Tg, contributes to increase the RS fraction as well.

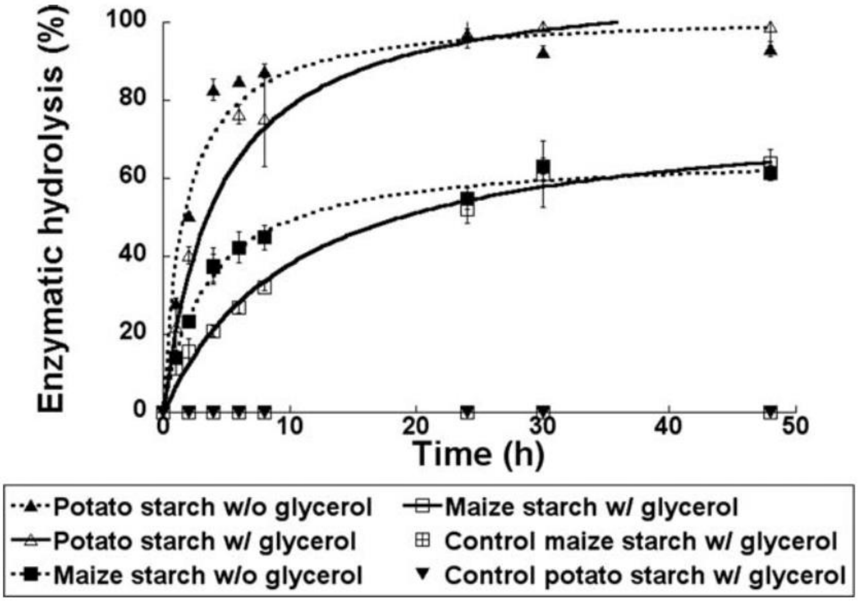

Figure I-17: *Thermoplastic starch-based materials enzymatic degradation under static conditions in the presence or in absence of α-amylase (control) (Beilvert, Faure, et al. 2014).*

Section 2: Starch-based nanocomposites: sustainable smart materials

This second section aims to present the potential advantages of thermoplastic starch (TPS) reinforced with bio-based nanomaterials: more specifically, polysaccharide-based nanofillers are described in detail as they have been used in this work for interacting with starch. A brief summary of the most common processing methods for nanocomposite production is presented as well.

1. What is a nanocomposite?

A composite is defined as a multiphase solid material resulting from the combination of two or more constitutive materials, one being the continuous phase (polymer, metal, ceramic) and one being a dispersed phase (fiberglass, carbon fibers, clays). In nanocomposites, the dispersed phase is formed by particles which present at least one dimension smaller than 100 nm (Nel 2007) (**Figure I-18**).

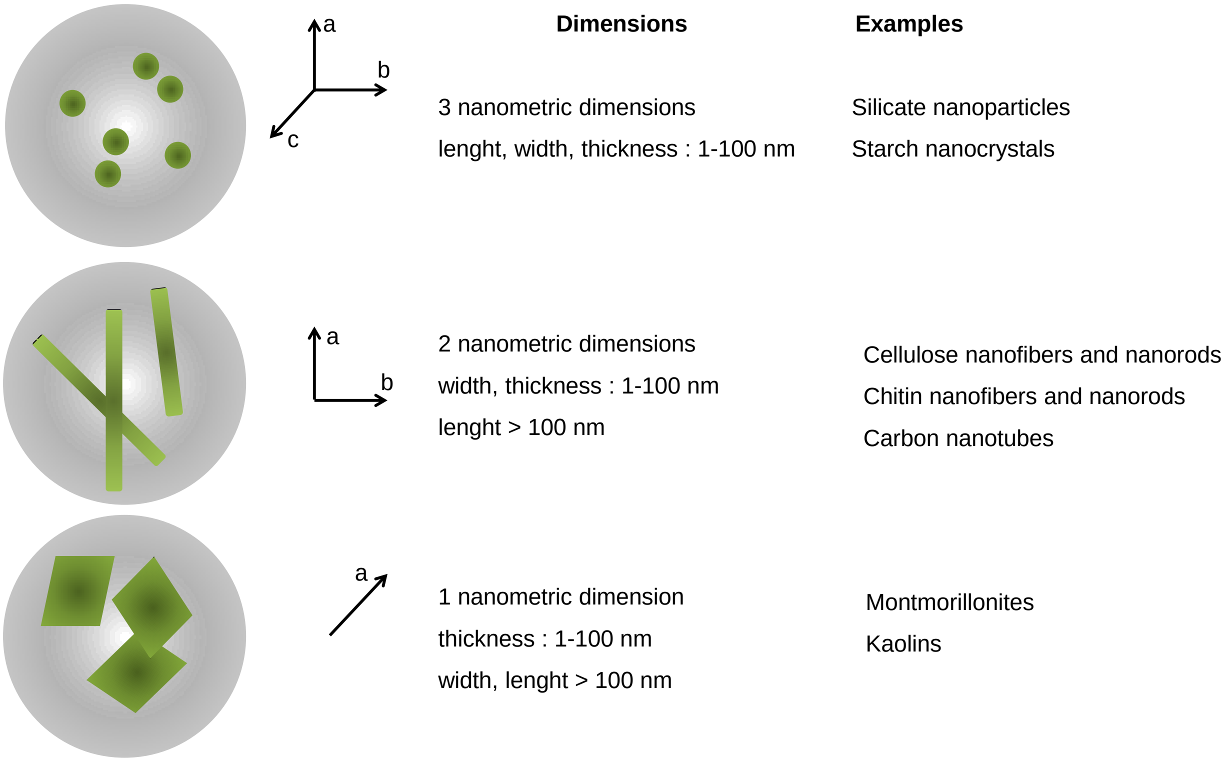

Dimensions	Examples
3 nanometric dimensions lenght, width, thickness : 1-100 nm	Silicate nanoparticles Starch nanocrystals
2 nanometric dimensions width, thickness : 1-100 nm lenght > 100 nm	Cellulose nanofibers and nanorods Chitin nanofibers and nanorods Carbon nanotubes
1 nanometric dimension thickness : 1-100 nm width, lenght > 100 nm	Montmorillonites Kaolins

Figure I-18*: Different types of nanofillers adapted from (Coativy 2013).*

The interest of nanometric fillers compared to larger particles is the “nano-size effect”: for the same amount of fillers, the contact surface (the interface) with the matrix (the continuous phase) increases with the decreasing size of the fillers, provided of course that the fillers dispersion is homogeneous.

Among nanofillers, the interface depends on the morphology of the particle: for example, for the same volume, crystals (nanorods) expose higher surface compared to fibers. Indeed chitin and cellulose nanocrystals show specific surfaces ranging between 250 and 350 m^2 g^{-1} while nanofibers show lower values, of about 100 - 150 m^2 g^{-1} (Goodrich & Winter 2007).

Another important parameter is the shape factor (or aspect ratio) of the filler, which is the ratio between its length and its thickness (L/d). As a consequence, this parameter depends on the shape of the object. For example, because of their elongated shape, nanofibers have higher aspect ratios (> 100) than nanocrystals (1-100).

Percolation occurs when the fillers are added in a sufficient amount to connect and form a network: the chance that fillers touch and form a network is higher for particles with higher aspect ratio. When nanofiller percolation occurs, the properties of the matrix change significantly and functional composite materials with novel properties are obtained.

For example, inorganic compounds, such as layered silicates, are well-known for conferring polymers with improved mechanical and barrier properties but also with other attributes such as flame retardancy of polymer matrix (Porter et al. 2000).

2. Nanofillers from natural polymers

Starting with the works of Favier (V. Favier et al. 1995), polysaccharides have gained much attention as a source of reinforcing nanofillers in polymer nanocomposites. In natural-based composites, percolation have been accounted to improve above all mechanical properties (Morin & Dufresne 2002; Salaberria et al. 2014).

However, nanofillers proved not to modify mechanical properties exclusively: the formation of a rigid nanofiller network has revealed to be useful to modify the water sorption abilities of natural polymers as well (Rodrigues et al. 2017; Gopalan Nair & Dufresne 2003).

Renewable and widely available polysaccharides such as cellulose, chitin and starch are naturally composed of both amorphous and crystalline regions. Amorphous domains can be removed under certain conditions, like acid hydrolysis, isolating the crystalline domains. The highly crystalline nanomaterials obtained this way are of great interest for multiple applications because, like the raw materials from which they are extracted, they are biodegradable, renewable and non-toxic. Besides, they can be applied to an even wider range of domains as their numerous surface hydroxyl groups can be easily modified (Missoum et al. 2013; Mincea et al. 2012).

Because of their similar chemical structure, good compatibility is expected between starch and cellulose or chitin nanofillers. Intermolecular hydrogen bonds are expected to form between the OH groups of starch backbone and the OH groups of nanocellulose and chitin. For chitin, residual NH_2 groups may participate to the interaction too.

Because of the long hydrolysis time (5 days) needed for their production and the low yield (~15.7wt%) (Dufresne & Castaño 2017), starch nanocrystals ruled out for fillers in our nanocomposites. Hence, in the next paragraphs only cellulose and chitin nanofillers are described, together with the advantages of bio-based nanocomposites compared to thermoplastic starch alone.

2.1 Cellulose and chitin nanofillers

Nanofillers are defined as bio-based when they are wholly or partly derived from the biomass, such as plants, trees or animals. The biomass can have undergone physical, chemical or biological treatment. Hence, nanofillers derived from cellulose and chitin can be referred to as bio-based but not as natural, even if produced from natural polymers, because they cannot be found in nature in this form.

The method for producing cellulose and chitin nanofillers is similar and involves mechanical shearing action and/or acid hydrolysis steps. A mechanical/chemical pre-treatment is necessary to extract cellulose and chitin from the biomass. Depending on the intensity and the type of the applied treatments, different types of nanofillers are obtained, and they are described in the following paragraphs.

2.1.1 Cellulose

Cellulose is the most abundant natural polymer produced in the biosphere, with an annual estimated production over 7.5×10^{10} tons. Cellulose is widely distributed in superior plants, in several marine animals (tunicates for example) and, to a lesser extent, in algae, fungi and bacteria (Habibi et al. 2010).

In nature, cellulose occurs as a fibrous material whose main function is to mechanically sustain cell walls. The fibrillary structure of cellulose makes it a viable alternative to fossil-based reinforcing fibers for developing all-natural composite materials (Avérous et al. 2001).

The molecular structure of cellulose consists in a linear repetition of β (1, 4) linked anhydrous-D-glucose units associated in dimers, named cellobiose (**Figure I-19a**). Glucose units are associated to form elementary fibrils of about 36 units, whose structure is stabilized by an intramolecular hydrogen bond network (**Figure I-19b**) (Malcom Brown Jr et al. 1996).

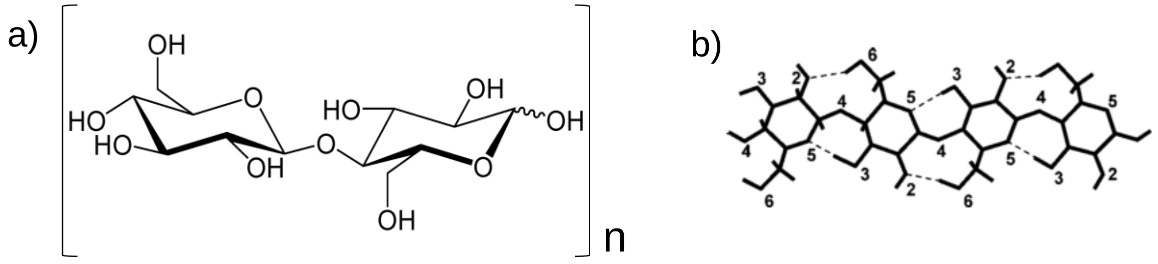

Figure I-19: **a)** *Cellubiose dimer repetition in cellulose structure and* **b)** *hydrogen intramolecular bonds in cellulose structure (Habibi et al. 2010).*

Elementary fibrils pack together to form microfibrils which are in turn associated in cellulose fibers (**Figure I-20**). Cellulose monomers may pack differently depending on their source and biosynthesis: hence microfibrils have wide cross-section variability, from 2 to 20 nm.

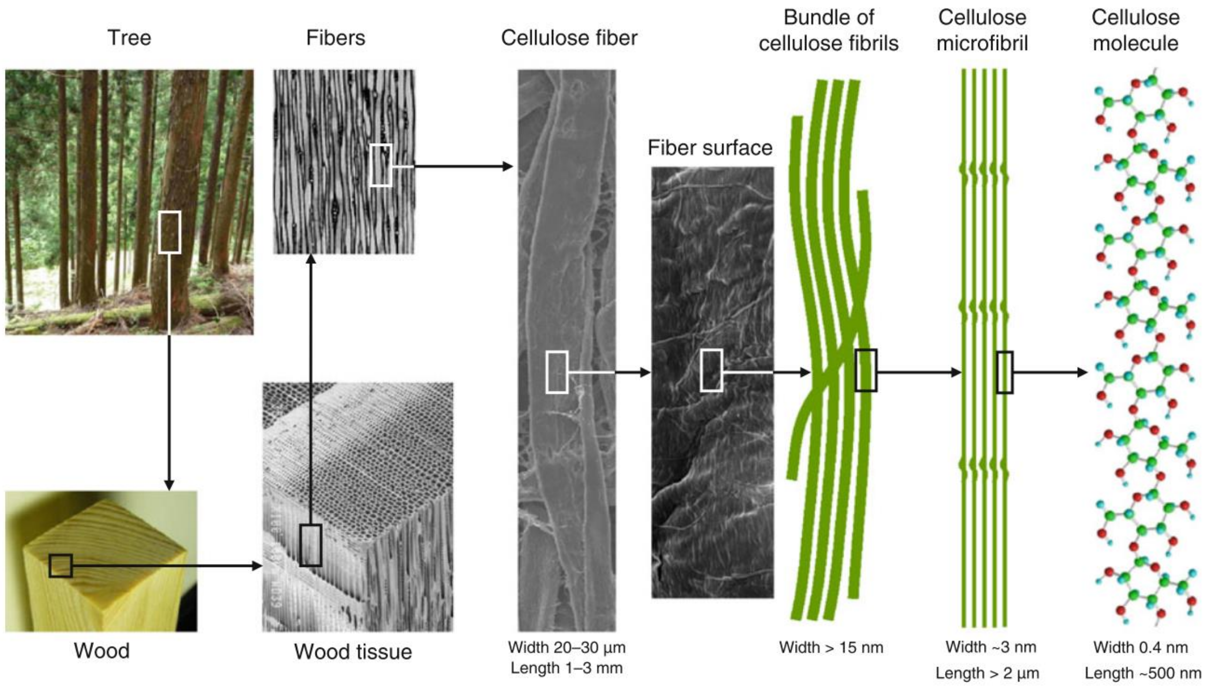

Figure I-20: *Hierarchical structure of wood cellulose, from molecular to fibril structure (Isogai 2013).*

The packing of cellulose chains is mostly driven by van der Waals forces and intra- and inter-molecular hydrogen bonds. The high density of hydrogen bonds among cellulose chains gives the cellulosic-ordered regions a highly crystalline structure. Only a limited number of amorphous regions can be generated in the elementary fiber structure depending on the biosynthesis mechanisms.

The network of hydrogen bonds in cellulose can vary widely, depending on the source and the treatments applied during extraction and/or processing. Six polymorphs of cellulose have been identified up to now, named I, II, III_I, III_{II}, IV_I and IV_{II}. Cellulose I and II are the most extensively studied allomorphs: the first is typical of native cellulose, while the second is generated by chemically dissolving and precipitating the cellulose I in water or by swelling cellulose I in concentrated NaOH solutions. These two allomorphs can be clearly distinguished by solid-state CP-MAS NMR, as it will be shown in Chapter IV.

Generally, nano-sized cellulose exists in three different forms: bacterial cellulose, nanofibers and nanocrystals:

- **Bacterial cellulose** (BC) is secreted by *Gluconacetobacter xylinus* in the form of a fine fiber network (**Figure I-21a**). BC has gained much attention in the last decades thanks to its biocompatibility with the human body (Schmitt et al. 1991), and its high tensile strength and water holding capacity (Svensson et al. 2005). All these qualities make BC an excellent ingredient for developing biomedical tools which mimic the mechanical properties of real tissues. However, its high water holding capacity does not make it a good candidate for reducing the water sensitivity of TPS.

- **Cellulose nanofibers** (CNFs) are obtained by mechanical fibrillation to the nano level of wood-derived fibers (pulp). Depending on the cellulosic starting materials, pre-treatments and intensity of mechanical fibrillations, CNFs show highly variable width and length distribution. Generally, CNFs are considered to have only a nanometric width and thickness, while their length is usually micrometric (**Figure I-21b**).
  CNFs are well-known for the role they play in enhancing the mechanical properties of starch-based nanocomposites (Babaee et al. 2015), because of their high aspect ratio compared to nanocrystals which enables a critical length for stress transfer from the matrix to the filler (Khalil et al. 2012). Besides, the remaining presence of amorphous regions in their structure makes CNFs highly hydrophilic (Siró & Plackett 2010).

- **Cellulose nanocrystals** (CNCs) are produced by the hydrolysis of native cellulose microfibrils in a strong acid aqueous solution. This acid treatment cleaves down the amorphous regions of the fibrils, leaving only highly crystalline fractions of nanometric size: rod-shaped nanofillers (**Figure I-21c**). Those are referred to as “whiskers”. Sulfuric acid is generally used as the hydrolyzing agent: during the reaction, it grafts anionic sulfate ester groups on the surface of the nanocrystals. These negatively charged groups form a negative layer at the surface of the crystals, which favors their stable dispersion in water through electrostatic repulsion (Dufresne & Castaño 2017). However, the acid treatment compromises the CNCs thermal stability (Roman & Winter 2004), which, hydrolyzed, degrade at lower temperatures and over a broader temperature range (175 - 350 °C) than non-hydrolyzed cellulose (250-350°C).

CNCs show nanometric width and thickness while their length ranges between 50 and a few hundred nanometers. The length of CNCs is much lower than CNFs, which makes CNCs not so well adapted for mechanical reinforcement in nanocomposites. In this study however, mechanical reinforcement is not a requirement, as the main objective is to increase the resistance to water and enzymes. The highly crystalline structure of CNCs actually makes them a good candidate for this type of application.

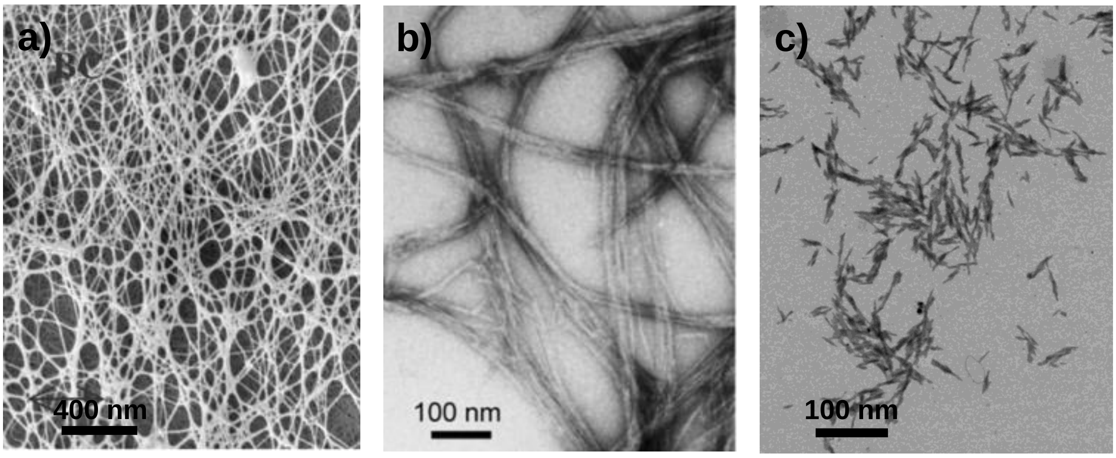

Figure I-21: a) *Scanning electron micrograph of bacterial cellulose (Svensson et al. 2005),* **b)** *transmission electron image of cellulose nanofibers from kraft pulp (Isogai 2013) and* **c)** *scanning transmission electron image of cellulose nanocrystals from wood.*

2.1.2 Chitin

Chitin is the second most abundant naturally occurring semi-crystalline polymer after cellulose. It is synthetized by numerous living organisms such as crabs, shrimps, tortoises and insects. In nature, chitin is a fibrous material whose main function is to protect the living organisms synthesizing it (Rinaudo 2006): it is an important component of shells, which are usually considered as a byproduct by the seafood industry (Chang, Jian, Yu, et al. 2010).

Chitin is a high molecular weight linear polymer of β (1, 4) linked acetyl-D-glucosamine chains with acetamide groups positioned at the C2 of the D-glucopyranose unit (**Figure I-**

22a). These lateral groups are partially responsible for the hydrophobic nature of chitin (Rinaudo 2006) and for its antimicrobial properties (Salaberria et al. 2015).

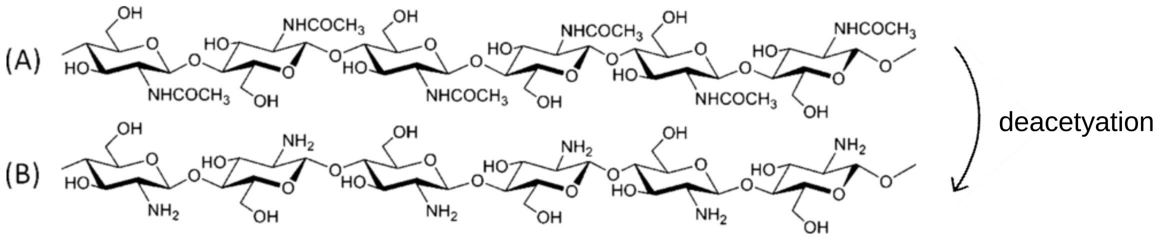

Figure I-22: *Chemical structure of* **a)** *chitin and* **b)** *chitosan.*

Chitin is often converted to its partially deacetylated derivative chitosan, which is a more easily soluble polymer (**Figure I-22b**). The presence of free amino groups in the chitosan structure also facilitates its chemical modification to obtain functional derivatives.

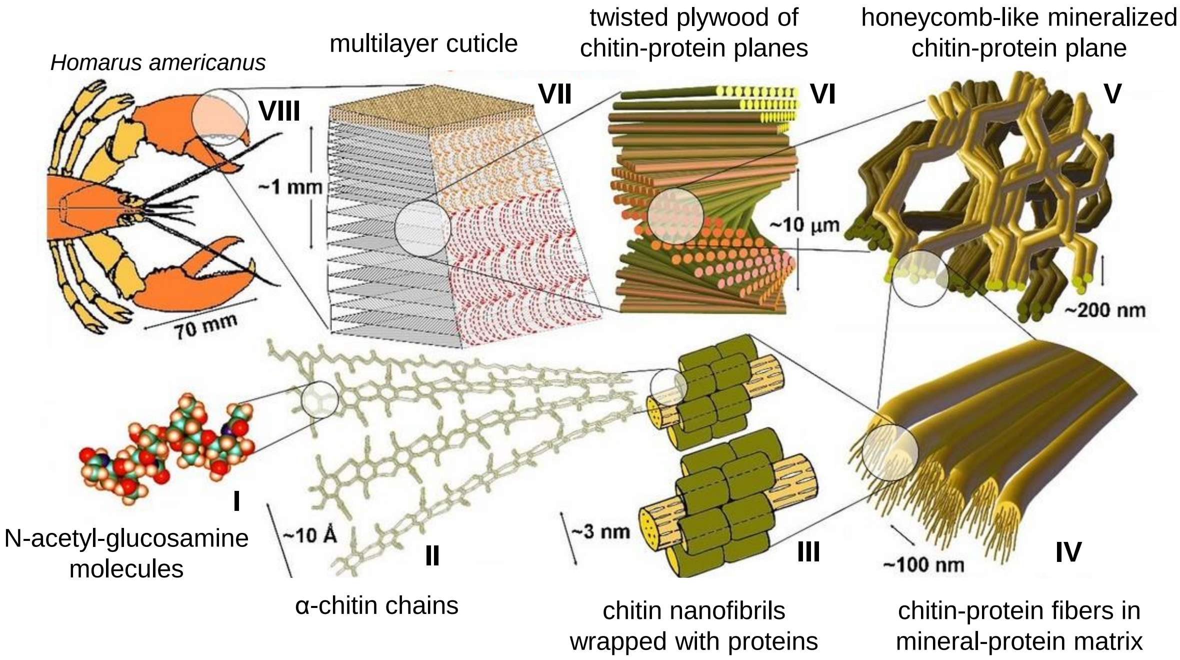

Figure I-23: *Hierarchical structure of chitin in Homarus americanus, from molecular to skeletal element (Raabe et al. 2007).*

In chitin, N-acetyl-glucosamine chains organize in the form of semi-crystalline nanofibrils embedded in a protein matrix. These fibrils, with diameters ranging from 2.5 to 25 nm depending on the origin, associate to form mineralized chitin-protein fibers in a honeycomb-like plane configuration. Multiple chitin-protein planes are then superposed in a twisted plywood structure and assemble to form the multilayer cuticle of shells (**Figure I-23**).

Chitin is found in nature under three different crystalline forms: α, β and γ chitin, depending on the resources. The γ form is only occasionally observed and is thought to be a variant of the α form (Zeng et al. 2012). α-chitin is by far the most common crystalline form and it is found in many living organisms, from yeast cell walls to crustaceous shells, except for squid pens and tubeworms which are composed of β-chitin. In both α and β crystalline forms, chitin chains are organized in sheets and tightly linked by strong intra-sheet hydrogen bonds (Rinaudo 2006; Mincea et al. 2012). While no inter-sheet bonds occur for β-chitin (**Figure I-24b**), some inter-sheet bonds are present in the structure of α-chitin (**Figure I-24a**). This gives α- and β-chitin different swelling behaviors: in α-chitin, polar molecules such as water and alcohols cannot penetrate its compact semi-crystalline structure, while they easily enter β-chitin.

Some authors have shown that after dissolving β-chitin in strong acids, a successive recrystallization will generate α-chitin structures. For this reason it was concluded that α-chitin is more thermodynamically stable than β-chitin.

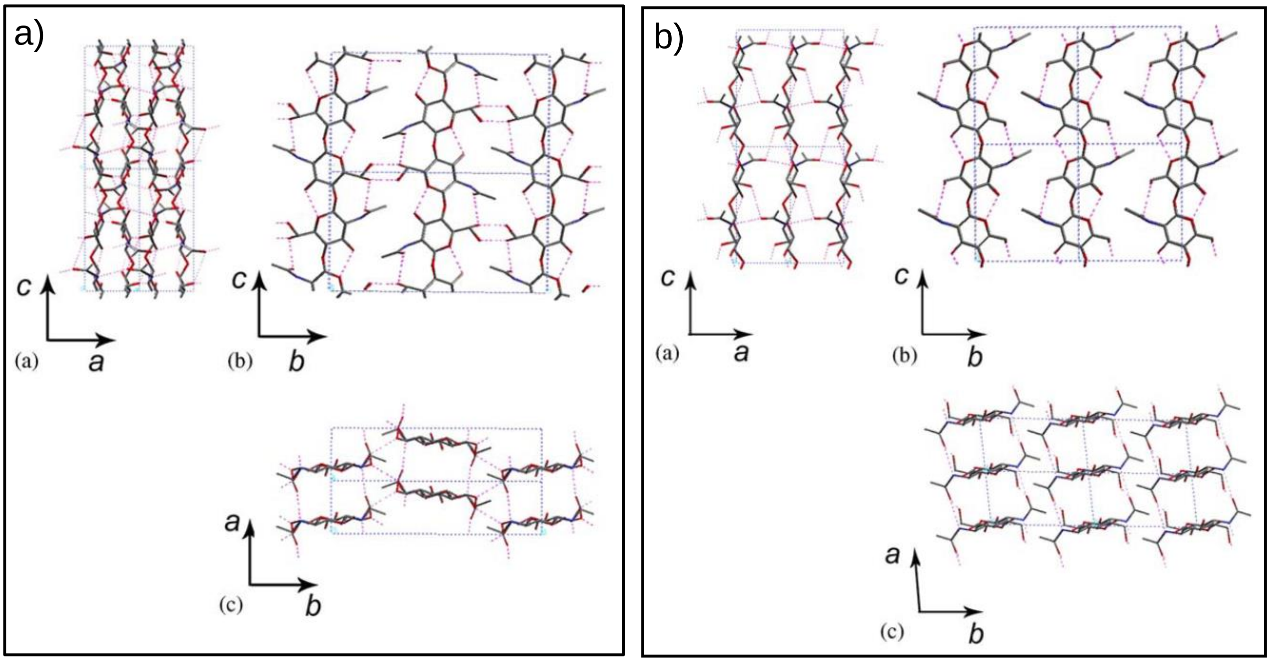

Figure I-24: *Structure of* **a)** *α-chitin and* **b)** *β-chitin (Zeng et al. 2012).*

To obtain the pure polymer, chitin must be separated from proteins, lipids, pigments and minerals of the biomass following a precise extraction process: acid treatment, alkaline extraction and decolorization are the principal steps. Different grades of purity and color will be obtained depending on the parameters adopted (Percot et al. 2003).

Starting from purified chitin, nano-sized chitins can be prepared in two different forms, nanofibers and nanocrystals:

- **Chitin nanofibers** (ChNFs) are produced by a mechanical shearing action on native chitin, with techniques such as high-pressure homogenization and sonication. ChNFs show highly variable width and length distribution, depending on the origin and the mechanical treatment intensity. However, as for all other nanofibers, ChNFs are generally a few hundred nanometers long, while width and thickness are inferior to 100 nm (**Figure I-25a**). Similarly to cellulose nanofibers (CNF), ChNFs can be used as mechanical reinforcements in nanocomposites because of their high (> 100) aspect ratio. ChNFs present amorphous regions which can be dissolved by acid hydrolysis to obtain water-insoluble, highly crystalline chitin nanocrystals (Paillet & Dufresne 2001).

- Unlike their CNC counterparts, **chitin nanocrystals** (ChNC) are generally produced by hydrochloric acid hydrolysis of purified chitin at high temperature. The hydrochloric acid treatment disrupts the less ordered chitin domains and protonates (NH_4^+) its amino groups. Like anionic groups in CNCs, positively charged ammonium groups help obtaining stably dispersed suspensions through electrostatic repulsion. By the end of the hydrolysis process, highly crystalline chitin rod-like whiskers are produced (**Figure I-25b**).

  ChNCs length ranges between 50 and a few hundred nanometers while width and thickness are of a few nanometers. As a result, ChNCs have a low aspect ratio (~15).

The important difference between cellulose and chitin nanofillers is the antimicrobial and antifungal properties of the chitin ones, which are very interesting for the development of biomaterials. However, one of the limitations of chitin nanofillers compared to cellulose is their relatively higher cost of making. This process requires a high quantity of reagents (mostly HCl and NaOH) and generates lots of wastewater which have to be cleaned thereafter. This anti-polluting treatment further increases the cost of chitin.

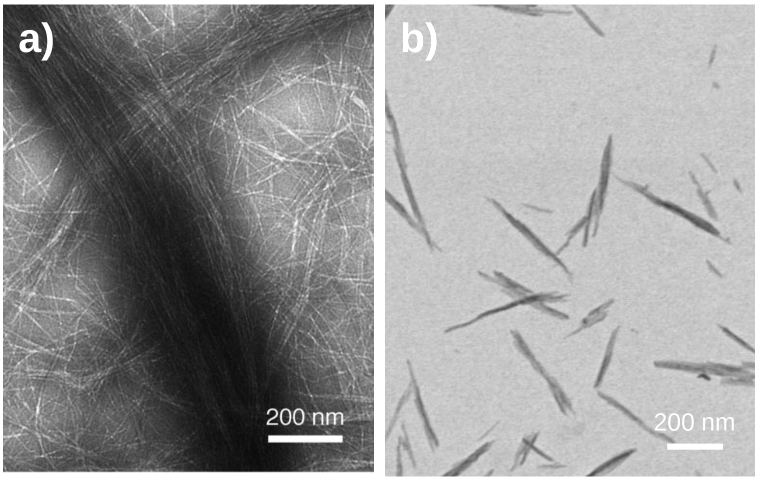

Figure I-25: a) *Transmission electron image of chitin nanofibers from lobster shell (Mushi et al. 2019) and* **b)** *scanning transmission electron image of chitin nanocrystals from shrimp.*

3. Physical properties of nanocomposites containing cellulose and chitin nanofillers

Hydrogen bonds form between nanocelluloses/nanochitins and the continuous phase when water-soluble polymers, such as starch, are used as matrices, due to the polar nature of both constituents. When the nanofillers are homogeneously well-dispersed in the matrix, novel materials with original properties are generated.

There are several factors which affect the effect of cellulose and chitin nanofillers on polymer matrices: first the glass-transition temperature of the matrix, but also some strictly-dependent nanofillers properties such as their aspect ratio, specific surface, concentration and, most importantly, their dispersion.

We will now present a rapid overview of the main functionalities of polymer matrices added with cellulose and chitin nanofillers as they have been reported in the literature, with a focus on starch-based nanocomposites.

3.1 Mechanical reinforcement

At the beginning of nanocomposite development, nanofillers were mainly used to obtain mechanical reinforcement in polymeric matrices. Indeed, polymer-based nanocomposites are known to show increased Young’s modulus and tensile strength while elongation at break is generally reduced compared to the matrix alone. The mechanical reinforcement is generally easier to obtain in polymers with a low glass transition temperature (Tg) (Zeng et al. 2012), such as glycerol-plasticized thermoplastic starch and natural rubber, because of their more flexible nature.

The achievement of improved mechanical performance is mainly dependent on three parameters (Salaberria et al. 2014):

1. Formation of a rigid nanofillers network, due to the formation of inter and intra molecular hydrogen bonds among nanofillers;
2. Entanglement between the nanofillers network and the continuous phase (the matrix);
3. Stress transfer from the matrix to nanofillers network.

Besides, the mechanical reinforcement is facilitated when nanofibers, rather than nanocrystals, are added to the matrix, because of their higher aspect ratio (L/d > 100): for example, Young’s modulus increased from 85 MPa (for TPS alone) to 220 and 390 MPa with 5 and 20wt% chitin nanocrystals and to 330 and 520 MPa for the same amount of nanofibers in starch-based nanocomposites produced by melt-mixing (Salaberria et al. 2014). Likewise, the tensile strength increased from 4.5 MPa (matrix) to 7 and 11 MPa at 5 and 20wt% chitin nanocrystals and to 10 and 15 MPa for the same amount of nanofibers, while elongation at break decreased importantly, from ~85% to 40% (at 5wt%) and 15% (at 20wt%) for crystals and to 25% (at 5wt%) and 10% (at 20wt%) for fibers (Salaberria et al. 2014).

Similar behaviors (increase in Young’s modulus and tensile strength, decrease in elongation at break) were observed for other composite systems, produced by solvent-casting evaporation methods:

- In glycerol plasticized starch/chitin nanocrystals nanocomposites, the addition of 1 to 5wt% chitin nanocrystals, induced a gradual increase in tensile strength, from 3 to 8 MPa, while elongation at break decreased from 60 to 20% at the highest nanocrystals concentration (Chang, Jian, Yu, et al. 2010);
- In waterborne polyurethane/chitin nanocrystals nanocomposites, the Young’s modulus increased from 3 to 9 MPa at 5wt% nanocrystals content, elongation at break decreased from 85 to 50%, and tensile strength increased from 11 to 21 MPa at 3wt%. It then decreased again to 14 MPa at 5wt% nanocrystals content, maybe because of nanocrystals’ self-aggregation at higher concentrations;
- In glycerol-plasticized starch mixed with flax cellulose nanocrystals, tensile strength and Young’s modulus increased from 4 to 12 MPa (30wt% nanocrystals) and from 30 to 500 MPa respectively, while the elongation at break decreased by one order of magnitude, from 70 to 7% (Cao, Chen, Chang, Muir, et al. 2008).

Many other examples of the nanofillers mechanical reinforcing ability can be found in the literature (Lu et al. 2006; Cao, Chen, Chang, Stumborg, et al. 2008; Lu et al. 2005; Zeng et al. 2012).

The reinforcing effect of cellulose and chitin nanofillers has been studied on nanocomposite systems produced by melt processes as well, even if to a lesser extent. Melt processes are less common than solvent-casting processes to produce reinforced composites because obtaining good nanofiller dispersion is more difficult with a melt process. Nair and Dufresne studied the effect of nanocomposite processing on the mechanical properties of rubber nanocomposites added with chitin nanocrystals, and showed that the reinforcing effect was higher in nanocomposites produced by casting/evaporation method than in the ones produced by freeze-drying and hot-pressing, because of the uneven nanofiller dispersion in the latter materials: at 20wt% nanocrystals content, Young’s modulus was equal to 230 MPa for evaporated systems and only 10 MPa for freeze-dried/hot-pressed systems (Gopalan Nair & Dufresne 2003).

Hietala and colleagues (Hietala et al. 2013) however, observed, for sorbitol-plasticized thermoplastic starch reinforced with cellulose nanofibers and produced by twin-screw extrusion, an important increase in tensile strength and Young’s modulus, as well as a lower elongation at break: tensile strength and Young’s modulus increased from 9 to 18 MPa and from 455 to 1320 MPa respectively, while the elongation at break decreased from 23 to 2% when 20wt% nanofibers were introduced in the system.

3.2 Thermomechanical and thermal properties

The mechanical reinforcement can be quantified by Dynamic Mechanical Thermal Analysis (DMTA) as well, by an increase in storage and loss moduli (E' and E") in the rubbery state. This effect has been observed for multiple nanocomposite systems, independently from the type of processing. For example, the formation of chitin nanocrystals/polycaprolactone nanocomposites by solvent-casting gave materials with a higher storage modulus in the rubbery state, from 350 MPa for the matrix to 590 MPa for the 2.5wt% filled nanocomposite (Morin & Dufresne 2002). When the materials are formed by hot-pressing, this storage modulus increases from 320 to 930 MPa with 2.5wt% nanocrystals (Morin & Dufresne 2002). Lu and colleagues proved that increasing the cellulose nanocrystals concentration in glycerol-plasticized TPS gradually increases the storage modulus in the rubbery region (at 100°C in their study), from 20 MPa for the matrix to 120 MPa with 30wt% nanocrystals (Lu et al. 2005).

Similar observations were done concerning the mechanical relaxation measured by DMTA: the α-relaxation temperature (Tα) gradually increases with the nanofiller concentration. In glycerol-plasticized starch/chitin nanocrystals systems produced by solvent casting, Tα increased from 20°C (in the matrix) to 25°C at 2wt% nanocrystals content, and at 5wt% it splits into a double peak, possibly because of the formation of a starch-rich (32°C) and a nanofiller-rich (46°C) phase (Chang, Jian, Yu, et al. 2010).

In another study, on glycerol-plasticized starch/cellulose nanocrystals systems, the Tanδ relaxation peaks due to glycerol-rich and starch-rich phases shifted to higher temperatures as well (from – 62°C to – 41°C and from 24°C to 52°C). Besides, the Tanδ peak related to the starch-rich phase became flatter, indicating restricted molecular motions of the starch chains, due to the strong interaction between starch and nanocelluloses (Lu et al. 2005). The flatter shape of the Tanδ curve is coming from the storage modulus E': in the rubbery domain of nanocomposites, it is generally higher than in matrices (Zeng et al. 2012; Dufresne & Vignon 1998; Paillet & Dufresne 2001).

The nanofiller morphology does not seem to play a significant effect on the intensity of storage modulus or on the shift of Tα to higher temperatures, as shown in the case of chitin nanofillers: at 20wt% nanofiller content, the Tα shift of the starch-rich phase (69°C) obtained with fibers (75°C) and crystals (76°C) is the same (Salaberria et al. 2014).

The mobility loss of the macromolecules due to their interaction with stiff nanofillers (Zeng et al. 2012) can be detected as a general increase of the hosting polymer Tg in nanocomposites as well. This increase of Tg has been observed by DSC in multiple nanocomposite systems produced by solvent-casting: in glycerol-plasticized starch added with cellulose nanocrystals, Tg goes from 22°C in the matrix to 48°C in 30wt% nanocrystals-loaded nanocomposites (Lu et al. 2005). Similarly, in hemp cellulose nanocrystals/glycerol-plasticized starch nanocomposites, the Tg of the starch-rich phase increases from 43 to 49°C at 25wt% nanocrystals content, while the Tg of the glycerol-rich phase (-58°C) seems unchanged by the nanofillers presence (Cao, Chen, Chang, Stumborg, et al. 2008).

Thermal stability is another important property to take into account for nanocomposite processing. However this is a quite controversial subject.

Some authors affirm that the addition of nanofillers to polymeric matrices induces a decrease in the thermal stability of the composite, because the preparation of the nanofillers involves sulfuric acid hydrolysis, which grafts OSO_3^- groups at the surface of the nanofiller, reducing its thermo-stability (Chen et al. 2009). The reduction in thermal stability would be stronger as longer hydrolysis times and/or larger acid concentrations are employed for nanofillers production, as these processes graft a higher number of sulfate groups on the surface (Roman & Winter 2004). For example, for glycerol-plasticized starch/cellulose nanocrystals films, the temperature at which the maximum rate of mass loss (as measured by Thermo-Gravimetric Analysis, TGA) occurs decreases from 310 to 299°C between nanocrystals produced by 4 and 24h of acid hydrolysis (Chen et al. 2009).

Conversely, other authors pointed out the slightly higher thermal stability of nanocomposites because of the interaction between the polymer and the nanofiller. In the case of poly(vinyl alcohol) (PVA) based composites, chitin nanocrystals seem to increase PVA thermal stability, as proven by (Sriupayo et al. 2005a) (from 290°C for the matrix to 310°C at 30wt%) and by (Wu et al. 2007) (from 260°C for pure PVA to ~310°C at 30wt%). In other studies (Salaberria et al. 2015; Salaberria et al. 2014), the thermal stability of glycerol-plasticized starch-based nanocomposites increased when chitin nanofibers were used as nanofillers (from 285°C for the matrix to 289°C at 20wt%) while it was reduced to 270°C with 20wt% chitin nanocrystals, maybe because of the lower thermal stability of nanocrystals compared to nanofibers.

3.3 Behavior in humid environment

Previous works showed that well-dispersed nanocelluloses and nanochitins in hydrophilic polymer matrices form a 3D inter-molecular hydrogen network between the dispersed (filler) and the continuous (polymer matrix) phases (Lu et al. 2005). Because of this physical bonding with the matrix, the number of available sites for water to bind and enzyme to cut is reduced at increasing nanofiller content and the sensitivity of the hydrophilic polymer to water and enzyme decreases (Popescu 2017).

3.3.1 Water sorption and diffusion

Improved resistance to water sorption and reduction of water diffusion (as measured gravimetrically) in hydrophilic polymers are reported for multiple nanocomposite systems produced by the solvent-casting method and enriched with chitin nanocrystals.

The water uptake at equilibrium and the diffusion of water decrease when increasing concentrations of chitin nanocrystals are introduced in a soy protein matrix: the water uptake decreases from 40% (in the pure matrix) to 20% at 30wt% nanocrystals content, and the water diffusion coefficient decreases from 2.56×10^{-14} m^2 s^{-1} to 1.23×10^{-14} m^2 s^{-1} (Lu et al. 2004). The same amount of chitin nanocrystals (30wt%) have been proved to reduce the swelling of chitosan films by about 44% (Sriupayo et al. 2005a) and of PVA matrices by about 35% (Sriupayo et al. 2005b).

Similar results were obtained for glycerol-plasticized starch reinforced with cellulose nanofillers and produced either by solvent-casting or by twin-screw extrusion.
By solvent casting:

- The water uptake at equilibrium and water diffusion coefficient of glycerol-plasticized starch reinforced with ramie cellulose nanocrystals decrease non-lineally with increasing nanofiller content, from 63% (in the pure starch film) to 45% (with 40wt% nanocrystals) and from 2.8×10^{-14} m^2 s^{-1} to 2.2×10^{-14} m^2 s^{-1}, respectively (Lu et al. 2006). Very similar results were found by the same author with nanocrystals from cottonseed linters (Lu et al. 2005);
- The water uptake of glycerol-plasticized starch films with hemp nanocrystals decreased from 70% (in the pure matrix) to 50% (with 30wt%) after 3 days of conditioning at 98%RH (Cao, Chen, Chang, Stumborg, et al. 2008) and very similar results were obtained using nanocrystals from flax fibers (Cao, Chen, Chang, Muir, et al. 2008).

By extrusion the results are less straightforward:

- Thermoplastic starch mixed with cellulose nanofibers showed the same water content at equilibrium than a TPS matrix alone, but the water diffusion coefficient decreased from 1.66×10^{-13} m^2 s^{-1} in the matrix to 1.27×10^{-13} m^2 s^{-1} with 20% nanofibers (at 98%RH) (Hietala et al. 2013);
- No differences in water uptake between a matrix of glycerol-plasticized TPS and the corresponding nanocomposite system reinforced with wood nanofibers, were found: this was attributed to the lower crystallinity of fibers compared to crystals, or to the aggregation of the fibrils in the matrix (Ferreira & Carvalho 2014).
- In glycerol-plasticized TPS added with chitin nanocrystals, the water uptake increased (88% at 120 min with 20% nanocrystals) compared to the reference matrix (75% at 120 min); when nanocrystals were replaced by nanofibers, the water uptake increased at 5 and 10wt% (up to 82%) before decreasing at 15 and 20wt% (up to 76% with 20wt% nanofibers) (Salaberria et al. 2014).

These results suggest that it is more difficult to obtain homogeneous nanofiller dispersion in nanocomposites systems produced by extrusion and, hence, to effectively change the properties of the polymeric matrix.

3.3.2 Enzymatic degradation

The number of studies about the enzymatic degradation of nanocomposites systems by α-amylase is very limited compared to the number of studies about biodegradation (degradation by microorganisms in nature), and is almost exclusively focused on the effects of nanoclays.

A study about the enzymatic degradation of a starch/PVA blend mixed with sodium montmorillonite clay nanoparticles (MMT-Na) showed that the gradual increase in MMT-Na concentration in the nanocomposite, from 0 to 5wt%, was responsible for the lower rate of glucose released (from 29 µg/mL h to 19.5 µg/mL h) by the cleaving action of the enzyme from the PVA/starch matrix (Taghizadeh et al. 2012). A similar result (from 85.5 µg/mL h for the pure blend to 61.7 µg/mL h of glucose release with 5wt% MMT-Na) was obtained when carboxymethyl cellulose was added to the starch/PVA blend and hydrolyzed by α-amylase and cellulase. This was attributed to the stabilizing effect against enzymatic attack played by MTT-Na.

No study focused on the effect of cellulose and chitin nanoparticles on the enzymatic degradation of starch-based blends is reported in the literature. However, it is possible that these bio-based nanofillers play a similar role as the nanoclays, as they are accounted to interact with hydrophilic polymers and limit water sorption.

Due to the absence, in the literature, of information about the enzymatic degradation of starch-based nanocomposites, the studies about the enzymatic degradation of thermoplastic starch alone (see paragraph 3.3 of section 1, *TPS swelling and enzymatic degradation*) constitute the basis of the experimental analysis developed in this thesis.

4. How to obtain functional nanocomposites?

A key step in the development of functional nanocomposites is the control of the manufacturing process, as it strongly affects the dispersion and the distribution of nanofillers in the matrix. As mentioned above, homogeneous dispersion of the nanofillers is a key issue because it determines the polymeric matrix/nanofillers interface and, hence, the magnitude of the interaction between the two.

The most common techniques for developing nanocomposites with well-dispersed nanofillers are casting/evaporation, followed by melt-processing, while other techniques such as freeze-drying and electrospinning are gradually gaining attraction to produce porous structures. Here we will focus only on the first two techniques, the most common.

Casting/evaporation is the oldest technique used for nanocomposites development (V. Favier et al. 1995; V Favier et al. 1995). It is also the most widespread, because it ensures a relatively easy and homogeneous dispersion of the nanofillers within the starch matrix, only necessitates basic laboratory materials, and only requires small amounts of polymer/fillers. The homogeneous dispersion will depend especially on the speed of water evaporation during drying.

Continuous melt processes however, can handle much larger quantities of material, and are used at the industrial scale. Nevertheless, the low water content of this type of process (~30wt%) promotes the aggregation of the fillers (Dufresne & Castaño 2017).

Good results have been obtained using water-assisted production of thermoplastic nanocomposites (Karger-Kocsis et al. 2015). With this technique nanomaterials are pumped continuously in the extruder as a liquid and the “blow-up” phenomena which occurs by pressurized liquid evaporation from the melt improves the dispersion of nanofillers in the system. However to use this technique nanofillers must satisfy precise requirements, such as pumpability and low viscosity).

The nanoparticles surface can also be functionalized (i.e. TEMPO oxidation), to promote repulsion and thus a good dispersion. However, these modifications are often not environmentally-friendly, and are not adapted for all applications, as they are sometimes toxic.

As it can be noticed from the literature, a significantly lower number of publications about nanocomposites produced by melt-processing have been published compared to solvent-casting method. For this reason, this work is rather focused on the investigation of nanocomposites processed by extrusion: the objective is to propose industrially-valid alternatives for nanocomposites production compared to solvent/casting.

Section 3: Biomaterials

1. Introduction: what are biomaterials?

The word *biomaterial* is often employed in many different fields of study but improperly. For example, it is sometimes employed to refer to materials of biological origin, such as wood and tissues. However, the correct appellation of this kind of materials is *biological materials*. *Biomaterials* have been defined in 1974 during the 6th Annual International Biomaterial Symposium (Clemson, UK) as a "*systemically, pharmacologically inert substance designed for implantation within or incorporation with a living system*". A more recent definition describes a biomaterial as a material that can be used alone, or as a part of a system, to drive therapeutic or diagnostic procedures for human beings or animals (Williams 2009). This means that biomaterials are, in practice, implants with the function of replacing and restoring living tissues and their functions. Artificial limbs and hearing aids are not considered as implants (Park 2012).

To be functional, a biomaterial must be safe, reliable, economically sustainable and physiologically acceptable (Park & Lakes 2007) as it comes in contact, continuously or intermittently, with biological fluids and tissues. Biomaterials can be inert or bioactive, biodegradable or permanent, they can be used to deliver active pharmaceutical ingredients (API), or to host and grow cells, depending on the desired application. In any case biomaterials must be biocompatible, which means that "*the biomaterial must be able to develop an appropriate response in the host for a specific application*" (Williams 2009).

The biocompatibility of a material can be evaluated *in vitro* and *in vivo*. One of the most commonly used biocompatibility test methods *in vitro* is the evaluation of the cytotoxic response of cells to the contact with the material or its extracts. The *in vivo* biocompatibility is determined by studying the perturbation of homeostatic mechanisms during implantation and the tissue response to the foreign body during reparation (Williams 2008; Ratner et al. 2004).
There are specific requirements to assess the biocompatibility of a material and, before approval for implantation, the material has to go through a series of tests, which include: acute system toxicity, cytotoxicity, hemolysis, intravenous toxicity, mutagenicity, oral toxicity, pyrogenicity and sensitization.

2. Types of biomaterials

Four main groups of biomaterials used for implantation are reported in **Table I-2**: polymers, metals, ceramics and composites.

Table I-2: *Classes of materials used in the body (Park & Lakes 2007).*

Materials	Advantages	Disadvantages	Examples
Polymers (nylon, silicone, rubber, polyester, polytetrafluoroethylene, etc.)	Resilient, easy to fabricate, low density	Low mechanical strength, time-dependent degradation	Sutures; blood vessels; maxillofacials: nose, ear, mandible, teeth, maxilla; cement, artificial tendon
Metals (Ti and its alloys, Co-Cr alloys, Au, Ag stainless steels, etc.)	High tensile strength, wear resistant, ductile	Corrosion in physiological environment, low biocompatibility, high density	Joint replacements; dental root implants; pacer and suture wires; bone plates and screws
Ceramics (alumina zirconia, calcium phosphates including hydroxyapatite, carbon)	Good biocompatibility, corrosion resistance, inert, high compression resistance	Brittle, not resilient, weak in tension	Dental and orthopedic implants
Composites (carbon-carbon, wire- or fiber-reinforced bone cement)	Strong Tailor-made	Lack of consistency of material fabrication	Bone cement, dental resin, joint implants, heart valve

Table I-3: *Synthetic polymers and their application in the biomedical domain (Ratner et al. 2004; von Recum 1998).*

Polymer	Application in the biomedical domain
High-density polyethylene (PE)	Hip, knee and shoulder joints
Polypropylene (PP)	Sutures, reinforced meshes, catheters
Polyvinyl chloride (PVC)	Catheters, tubing, shunts, blood containers
Polytetrafluoroethylene (PTFE)	Vascular graft, membranes
Polyacrylic acid (PAA)	Cement for dental restoration
Polymethyl methacrylate (PMMA)	Bone cement, intraocular lens, artificial teeth, hard contact lens
Polyhydroxyethyl methacrylate (PHEMA)	Contact lens, membranes, coatings, controlled release systems of active principle
Polymethyl 2-cyanoacrylate	Surgical adhesive
Polyethylene terephthalate (PET)	Sutures, vascular grafts, meshes, sewing rings
Polyurethane–urea (PUU)	Vascular grafts, intra-aortic balloon, tubings, left ventricular assist device
Polysiloxane	Finger joints, maxillofacial implants, heart valve, tubings, membranes, adhesives

Among polymers, synthetic ones were traditionally preferred to natural ones for the most varied applications (**Table I-3**) because of their inertness and stability (no time-dependent degradation).

However, synthetic polymers rarely mimic the structure and the function of the tissue they replace because they lack in chemical flexibility, biodegradability, thermal targeting and release mechanisms (Gagner et al. 2014).

In order to develop matrices and scaffolding systems that mimic native tissues, many researchers have explored the use of natural polymers due to their biochemical, mechanical and structural properties similar to those of soft human tissues. In particular, protein-based polymers have gained attention as potential good candidates, because of their 3D structure which supports cellular proliferation and tissue formation. Indeed, these materials, among which are found collagen, keratin, elastin, fibrin and silk fibroin, can function as a synthetic extracellular matrix, which favors the interaction with cells (Rouse & Van Dyke 2010).

Table I-4: *Properties of natural polysaccharides for biomedical application (Anitha et al. 2014; Jayakumar et al. 2010; Jorfi & Foster 2015; Miyamoto et al. 1989; Lin & Dufresne 2014; Marques et al. 2002; Beilvert, Chaubet, et al. 2014; Kunal et al. 2006; Reis et al. 2008; Szekalska et al. 2016; Kogan et al. 2007; Burdick & Prestwich 2011).*

Material	Source	Biomedical application
Chitin/Chitosan	Marine animals, insects, fungi	Drug delivery, gene therapy, tissue engineering and wound healing, regenerative medicine, sensor, antibacterial coatings
Cellulose	Superior plants, marine animals, algae, fungi, bacteria	Vascularization, 3D porous scaffolds, hydrogels and membranes for tissue engineering, wound healing, drug delivery, enzyme immobilization, antimicrobial materials
Starch	Plant roots, crop seeds,staple crops	3D porous scaffolds and stents, microparticles, bone cement, drug delivery, cross-linked hydrogels
Alginate	Brown algae, bacterial biosynthesis	Cartilage regeneration, release of active principles, wound coatings, cell immobilization, gels/porous scaffolds/membranes/fibers for tissue engineering
Hyaluronic acid	Rooster comb, umbilical cord	Release fo active principles, tissue repair, diagnostic marker, scaffolds and hydrogels for tissue engineering

Besides proteins, the field of polysaccharides-based biomaterials has gained much attention in the last decades because of their highly availability in nature and their low manufacturing cost. Furthermore, they represent an interesting alternative to synthetic polymers as they are

highly biodegradable and biocompatible (Khan & Ahmad 2013). Among polysaccharides, starch, cellulose, chitin/chitosan, alginate and hyaluronic acid and their derivatives are the most used to produce implants and scaffolds. Their high variability in degree of substitution (DS, number of substituent groups attached per monomeric unit) and molecular weight (M_w) gives these materials a range of different physical and chemical properties, which makes them useful for the most varied applications, as reported in **Table I-4**.
The properties listed in **Table I-4** are usually obtained by chemical modification of the native polymer or by blending with other synthetic and/or natural polymers.

In the following paragraph we will focus on the application of starch blends and derivatives in the biomedical domain, with a particular focus on starch-based nanocomposites.

3. Starch in the biomedical domain

As mentioned in the first section of this chapter, in nature, starch is found in granules in vegetal tissues. In order to use it for biomedical applications, it has to be transformed by mechanical/chemical processing or blended with other polymers.

3.1. Starch blends

Starch can be blended with different synthetic polymers to satisfy a broad range of market requirements. To do this, two main types of synthetic polymers are used:

- Synthetic polymers containing hydrophilic and hydrophobic units (i.e. ethylene-vinyl alcohol (EVOH));
- Cellulose derivatives (i.e. cellulose acetate (AC)) and aliphatic polyesters (i.e. poly-Ɛ-caprolactone (PCL), polylactic acid (PLA), polybutylene succinate adipate (PBSA), polyhydroxyalkanoates (PHAs)).

The first type of synthetic polymers forms an “interpenetrated” structure with amylose, making starch almost insoluble (Bastioli 1998), while aliphatic polyesters are more strongly affected by the blending with starch, which has an important effect on the degradation and the mechanical properties of the blend (Bastioli et al. 1995).

By changing the synthetic polymer and the processing route, the resulting melt can be tailored for different properties. The mechanical behavior especially, can range from rubbery (when PCL is used) to stiff (when EVOH, AC or PLA are employed).

These blends can be processed with conventional melt-based processing classically used for thermoplastic starch alone, such as extrusion, melt spinning, compression molding and injection molding to produce the most varied materials: scaffolds, fibers, meshes, tablets and hydrogels. Processing is often accompanied by the use of a blowing agent (based on citric acid for example) to obtain highly porous structures, in which the native structure of starch is completely lost. These materials possess an important biomedical potential, as they have been proven biocompatible in several *in vitro* and *in vivo* studies (Reis et al. 2008).

For example, a starch-AC blend has been extruded to produce scaffolds for bone tissue engineering: the obtained material showed good mechanical properties (compressive modulus = 125 MPa, compressive strength = 8 MPa), good cellular viability and colonization (Salgado et al. 2002). In another study, starch has been blended with PCL to produce a fiber mesh scaffold for cartilage tissue engineering. Here as well, chondrocytes exhibited high cell coverage of the scaffold with extracellular matrix deposition, indicating the good biocompatibility of the material (Oliveira et al. 2007).

Other porous structures can be obtained using 3D printing to process starch-synthetic polymer blends (**Figure I-26**). This processing consist in extruding and simultaneously deposing the extruded material layer by layer to form precise architectures, prepared in advance by computer assisted design. In this type of structures the mechanical properties of the scaffold can be modulated by playing on its porosity but also on the orientation pattern of the fibers, their length and the number of contact points between the fibers (Reis et al. 2008).

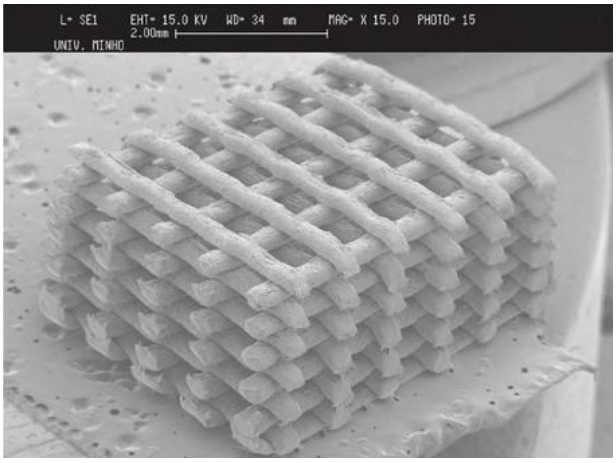

Figure I-26: *Starch-PCL scaffold produced by 3D printing (Reis et al. 2008).*

Beside synthetic polymers, starch is often blended with hydroxyapatite in order to produce materials with mechanical properties matching those of the human bone. The materials usually show no cytotoxicity and good adhesion and proliferation of osteoblastic-like cells (Gomes et al. 2001; Mendes et al. 2001).

3.2 Thermoplastic starch

Fewer studies are focused on the biomedical application of entirely starch-based materials, probably because of their unsatisfactory properties in a humid environment (high swelling and fast degradation). Nowadays, pure starch-based materials have been used only for fractional drug release devices (Bialleck & Rein 2012) and sialendoscopy implants. This second study was developed in our team and it proved the potential of purely starch-based materials for biomedical purpose.

Beilvert and colleagues developed shape-memory resorbable materials for less-invasive surgery by extruding potato starch with only 20% of glycerol. During implantation in a rat model, the material showed normal tissue integration with low inflammatory response and stable mechanical properties (tensile modulus = 2.4 MPa in physiological conditions for 21 days) (Beilvert, Chaubet, et al. 2014). The application of these materials for the treatment of salivary ducts pathologies demonstrated that stents based on TPS could be easily inserted in dilated salivary ducts without harming the epithelium, thanks to their flexible nature. However the starch-based stents were rapidly hydrolyzed in simulated saliva because of the high concentration in α-amylases (Beilvert, Faure, et al. 2014).

Then, Velasquez et al. showed that materials based on glycerol-plasticized potato and amylomaize starch presented a good cellular viability on fibroblastic (BALB/c 3T3) cells after direct contact with their extracts (viability > 70%). In addition, potato starch materials showed good tissue integration and no significant inflammation or foreign body response after implantation in a rat model. Conversely amylomaize starch-based materials induced a pathological foreign-body reaction, attributed to the presence of proteins and lipids in amylomaize (unlike in potato starch) (Velasquez et al. 2015).

This work proved that the botanical origin of starch has a significant effect on the biomaterial biocompatibility. Potato starch, which is the most free from proteins and lipids, appears as the most adapted for obtaining low inflammatory responses.

In addition, these previous works also proved that the addition of glycerol to potato starch-based materials did not have any effect on the immune response during implantation even if, by *in vitro* testing, glycerol proved to decrease the cellular viability by about 27%. Besides, their resorption times were comparable to those observed with materials obtained by blending starch with synthetic polymers (Marques et al. 2013).

4. Nanofillers in the biomedical domain

As mentioned in Section 2, chitin and cellulose nanofillers can be incorporated to TPS in order to modify the matrix and make it more adapted to the contact with physiological fluids (reduced water sorption and enzymatic degradation). However, no literature is available on biomedical applications of starch-based nanocomposites reinforced with this type of nanofillers: they are usually designed for packaging applications.

4.1 Nanofillers potential toxicity

Nanofillers can be introduced in the human body by multiple means (inhalation, ingestion, skin contact, etc.) but, in our case, they are associated with starch to form nanocomposites. Once implanted, the starch-based composite material degrades and nanofillers are released. Nanofillers will then come in contact with cells of different tissues and may play a cytotoxic effect: for example, they could be internalized by the cells because recognized as a nutrient, or rather as a foreign body to eliminate.

The intake process is dependent on both nanoparticles and cells properties.

For nanofillers, the most important features to consider are:

- Size and shape: the higher the specific surface exposed by the filler, the higher the possibility to interact with cells (Nel 2007); besides, spherical and needle-shaped nanoparticles require different binding energies (lower for spheres) for internalization (Li et al. 2015);
- Surface functionalization by ligands: the addition of molecules on nanoparticles surface allows the interaction with specific biological materials (Ling et al. 2014), and possibly increases the particles dispersion and the surface available for interaction, increasing the possibilities for the fillers to access to the cellular membrane (Ahamed et al. 2008);
- Surface charge: electrostatic attraction between cell membrane (negatively charged) and positively charged nanoparticles favors their adhesion onto the cell surface, favoring the uptake (Albanese et al. 2012; Gratton et al. 2008; Yue et al. 2011).

For cells, the expression of membrane receptors compatible with the geometry and the ligand density of the nanoparticles determines the intake process (Albanese et al. 2012): for example, specialized phagocytic cells are known to favor nanofillers intracellular uptake (Dos Santos et al. 2011). **Figure I-27** reports a schematic representation of the main factors involved in nanoparticles internalization by the cells as discussed above.

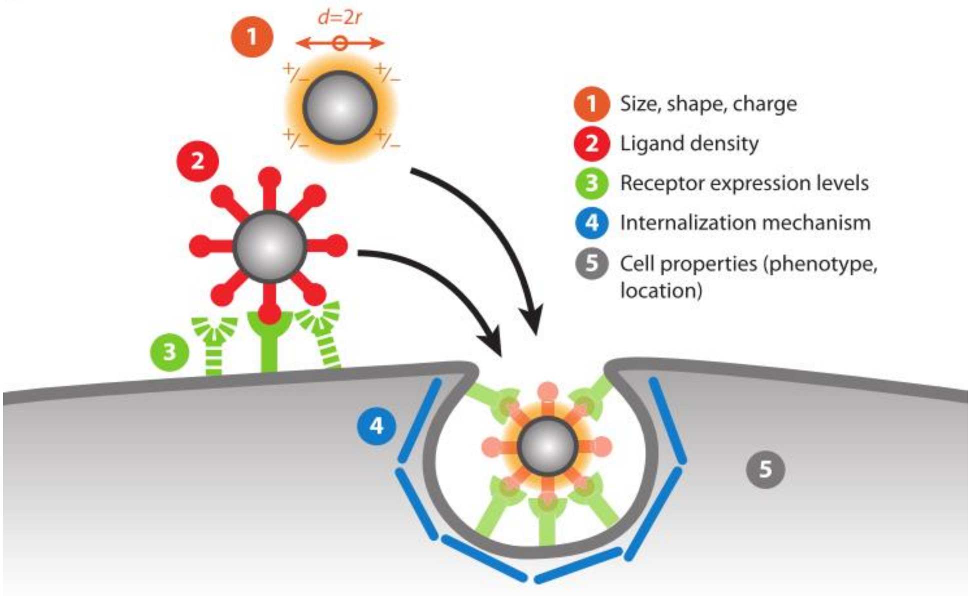

Figure I-27: *Main factors determining the nanofiller-cell interaction in the biological system (Albanese et al. 2012).*

When a nanoparticle enters the cell, it can interact with subcellular structures, affect cell behavior and cause local toxicity (Zhang et al. 2017). For example, nanoparticles can alter the mitochondrial function and activate oxidative stress in the cell (AshaRani et al. 2009) or they can damage DNA and, as a consequence, prevent protein synthesis (Albanese et al. 2012).

Nanofiller internalization may be dangerous because it can lead to mechanisms of accumulation with drawbacks on the behavior of the cell. For cellulose and chitin nanofillers, accumulation is highly possible, because they cannot be degraded in the human body due to their high crystalline and compact structure and lack of specific enzymes.

4.1.1 Cellulose and chitin nanofillers

Generally, cellulose/chitin nanofillers are known for their low cytotoxicity.

During *in vitro* experiments pure cellulose nanocrystals proved non-cytotoxic on fibroblastic and adenocarcinoma cells up to concentrations of 250 μg mL^{-1}, independently from their size (Hanif et al. 2014); only at higher concentrations of 500 and 1000 μg mL^{-1} the cellular viability decreased significantly, probably because nanofillers are internalized by the cells and hinder the functionality of cellular organelles, inducing a structural and chemical damage.

In a recent review on the use of nanocellulose in biomedicine (Lin & Dufresne 2014), the authors report that there is no evidence, up to now, of serious damages induced by nanocelluloses on both the cellular and the genetic level during *in vivo* organ and animal-model experiments: the cytotoxicity of cellulose nanocrystals against nine cell lines showed that no cytotoxic effect were measured up to concentrations of 0 - 50 µg mL^{-1}, for an exposure time of 48h (Dong et al. 2012).

Pure cellulose nanofibers were proven to have low toxicity as well: at low concentrations (0.02 - 100 µg mL^{-1}), cellulose nanofibers do not have any cytotoxic effect and do not affect gene expression of fibroblastic cells *in vitro*; however, exposure to higher concentrations (2000 - 5000 µg mL^{-1}) decreased the cells viability by about 15%, and affected the expression of stress/apoptosis genes (Pereira et al. 2013). In addition to concentration, the chemical modification of the surface can affect the cytotoxicity of cellulose nanofibers: modified nanofibers (crosslinked with cetyl trimethylammonium bromide) caused a significant reduction in cellular viability *in vitro* (by about 60%) compared to non-modified cellulose nanofibers (Alexandrescu et al. 2013), while cationic-modified nanofibers (with glycidyltrimethylammonium chloride) proved non-cytotoxic on human dermal fibroblasts, just like unmodified cellulose nanofibers (Hua et al. 2014).

Similarly, chitin nanofillers have been described as non-cytotoxic: the cell viability of fibroblastic cells in contact with cyclodextrin-based hydrogels containing up to 2.5wt% chitin nanocrystals was close to 100% for a contact time of 48h (Zhang et al. 2010). Another study about pure carboxymethyl nanochitins proved the complete absence of cytotoxic effects *in vitro* at a concentration of 300 µg mL^{-1} on fibroblastic cells for contact times of 24 and 48h (Dev et al. 2010).

Besides, unlike cellulose, chitin presents antimicrobial activity due to its chemical structure (Salaberria et al. 2015), which encourages its use in biomaterials.

Even if generally reported as non-cytotoxic, the available literature proves that the toxicology study of cellulose/chitin nanofillers and their nanocomposites is, for now, limited to the very preliminary steps, mainly based on *in vitro* cytotoxicity evaluations. Nanocellulose and nanochitin biocompatibility varies importantly depending on the manufacturing process, the type of cell they are tested on, their functionalization and their concentration. In the light of this important variability, nanofillers must be investigated for their interactions with biological systems, with respect to their size, shape, and surface chemistry. The investigation path is long and needs both *in vitro* and *in vivo* evaluations steps.

Chapter II

SAMPLES PREPARATION AND COMPOSITIONS

Table of contents

This chapter provides a detailed presentation of the raw materials used throughout this work: starch, cellulose and chitin nanocrystals and the plasticizer, glycerol. It then describes the fabrication of the samples, from formulation to extrusion and storage/drying. Finally, the nomenclature that will be used for the rest of the manuscript is presented along with a basic check-up on composition (water and plasticizer content determination).

Starting from this chapter, the experimental sets up used in this work are highlighted with black frames filled in light color to ease the reading. A specific table of contents has been established to easily find all the experimental sets up along the manuscript (see List of Experimental Sets-Up, page XXXI).

1. Raw materials

1.1 Native potato starch

Starch-based materials were produced starting from only one botanical source: potato. **Native potato starch** was provided by Roquette (lot VNN44, Lestrem, France) with an amylose content of 23% (information provided by the furnisher). The potato starch native granules used in this work show a flattened and ellipsoid shape, with a very smooth surface (**Figure II-1a**).

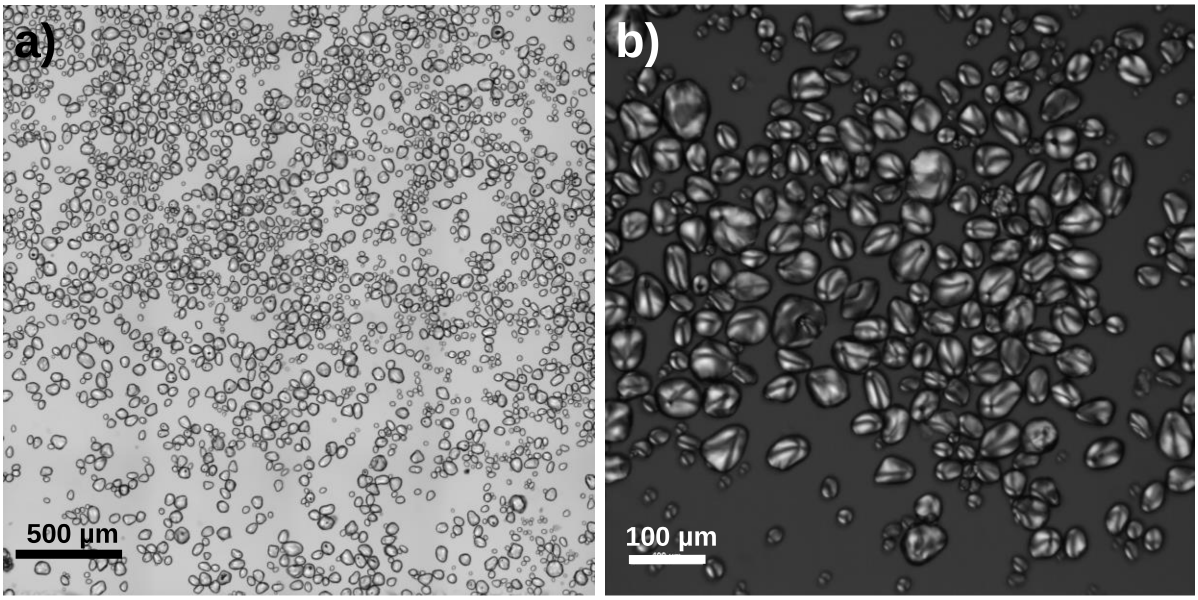

Figure II-1: *Native potato starch observed* **a)** *by optical microscopy and* **b)** *under polarized light.*

Potato granule size ranges between 15 and 75 µm, following a monomodal size distribution and with an average median particle size of 44µm (information provided by the furnisher). When observed under polarized light native potato starch granules show a typical birefringence, visible in the form of a “maltese cross”, due to the radial orientation of amylopectin double helices in crystalline lamellae (**Figure II-1b**). Indeed in their native form potato starch granules are highly crystalline entities, whose macromolecules show average molar mass (M_w) and radius of gyration (R_G) of about $11.4 \cdot 10^7$ g mol^{-1} and 161 nm respectively (Rolland-Sabaté et al. 2011).

As mentioned in Chapter I, potato has been chosen as the sole botanical source for starch because of the almost total absence of lipids and proteins.

1.2 Glycerol

Glycerol used in this work is 100% pure and it was purchased by VWR chemicals (lot 16C140014, GPR Rectapur). It presents a molar mass of 92.09 g mol^{-1} and a density of 1.26 g mL^{-1}. Glycerol constitutes the sole polyol used in this work for starch plasticization.

1.3 Cellulose and chitin nanocrystals

Wood cellulose nanocrystals (**CNCs**) were used as received from the University of Maine (Orono, Maine, US) in the form of aqueous gels.

The producing institute does not provide the exact procedure used for CNCs production. However the main steps needed for CNCs development are well known: these nanocrystals are produced by applying an acid treatment with sulfuric acid to cellulose wood pulp; the objective is to hydrolyze the less ordered regions of cellulose and collect exclusively highly crystalline fractions, in the form of nano-rods. The use of sulfuric acid for hydrolysis grafts anionic groups (OSO_3^-) at the surface of the nanoparticle, which favors electrostatic repulsion between the CNCs.

After hydrolysis, the protocol consists in an alternation of washings, precipitation with sodium chloride and a final session of dialysis to purify the nanocrystals from the acid. The step of precipitation is used to easily recover the nanocrystals and leaves protonic groups (Na^+) at the surface of the CNCs (**Figure II-2a**).

The procedure used by the University of Maine to produce CNCs generates two allomorphs of cellulose: cellulose I (CI) and cellulose II (CII). CII is probably generated during the precipitation step of CI with sodium chloride in water. Hence, both allomorphs are present in the CNCs used in this work.

Chitin nanocrystals (**ChNCs**) were produced by hydrochloric acid hydrolysis at high temperature of chitin powder from shrimp shells (lot SLBS6470, Sigma Aldrich, practical grade), following the protocol proposed by Perrin (Perrin et al. 2014) on the example of Revol (Revol et al. 1993). As for CNCs, the acid hydrolysis in strong acid media is needed to induce the disruption of the less ordered chitin domains and obtain chitin nano-rods. The use of hydrochloric acid causes the protonation (NH_4^+) of chitin amino groups (**Figure II-2b**).

After hydrolysis, multiple washings and centrifugations are alternated to recover the ChNCs. A final long step of dialysis is applied to purify the ChNCs from the acid before being sonicated and filtrated to remove the residual detritus. The ChNCs are recovered in the form of a highly diluted aqueous suspension.

The detailed procedure, with solvent and raw material specific dosing, is reported in the Annexes.

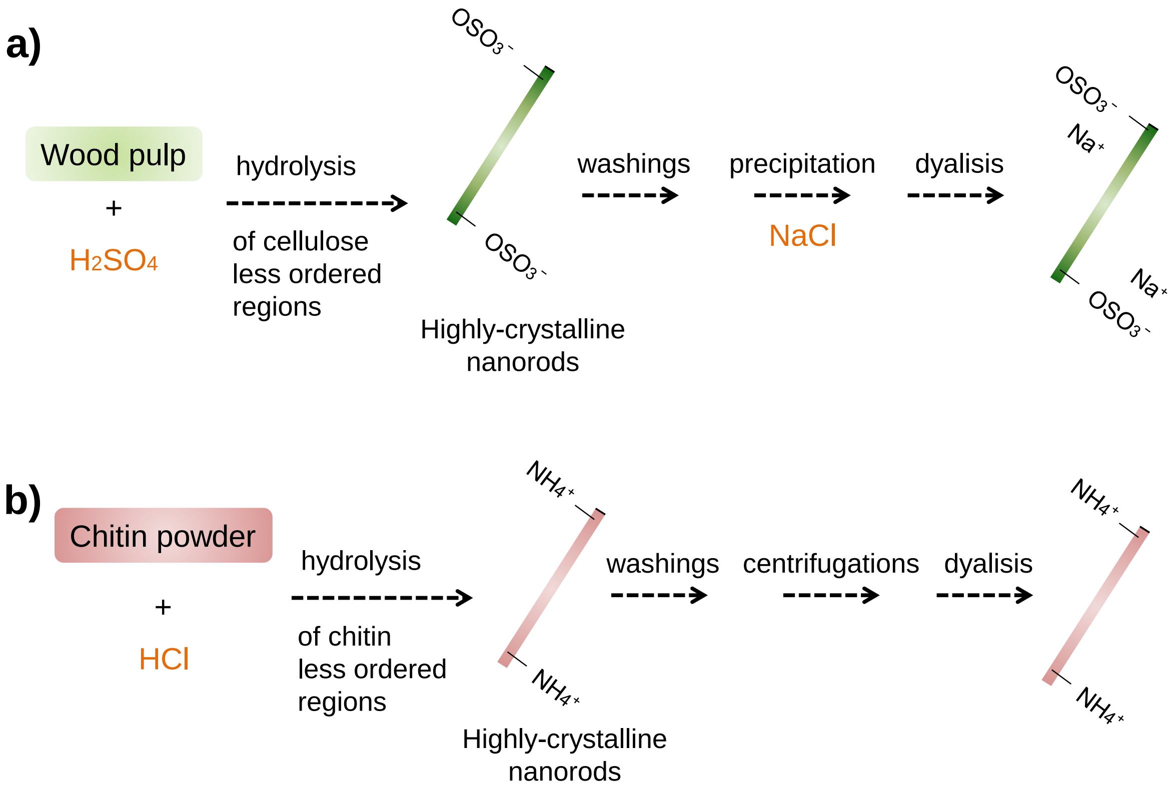

Figure II-2: *Protocol steps for the production of* **a)** *CNCs and* **b)** *ChNCs by acid hydrolysis.*

CNCs and ChNCs size have been determined by different means: a) Scanning Transmission Electron Microscopy (STEM) and b) Small Angle Neutron Scattering (SANS).

a) Scanning Transmission Electron Microscopy (STEM)

Images of nanofillers were obtained using a STEM (Quattro S, Thermo Scientific, US) operating at an accelerating voltage of 15 kV at 10^{-3} *Pa.*

Drops of nanofiller suspensions at ~0.8 g L^{-1} *and at ~0.025 g* L^{-1} *for cellulose and chitin nanocrystals respectively were deposited on glow-discharged carbon-coated grids and let dry overnight. Then specimens were sputter-coated with a 0.5 nm thick Pt/Pd layer and rapidly introduced in the STEM chamber for observation.*

Dimensions of the nanocrystals were determined manually from the analysis of 100 nanocrystals using ImageJ® software. The measured sizes do not refer to only one nanocrystal but rather to small 2-3 nanocrystal packings, because of CNCs and ChNCs tend to slightly aggregate already in aqueous suspension.

b) Small Angle Neutron Scattering (SANS)

Colleagues succeeded in determining average dimensions of cellulose and chitin nanocrystals from the SANS curve fit using a parallelepiped form factor. Nanofillers were dispersed in 2mL NaCl solutions and analyzed at a concentration of 2 g L^{-1}*.*

In **Table II-1** are reported the features for each type of nanofiller.

Table II-1: *Nanofiller size, concentration, pH and surface charge in accordance with (Jiménez Saelices & Capron 2018).*

	Size (nm)		**Concentration**	**pH**	**Surface charge**
	STEM	**SANS**	**(%wt)**		**(e nm^{-2})**
CNCs	width = 5-20 length = 50-250 thickness = N/A	average width = 21 average length = 175 average thickness = 6.5	12.2	5	0.25 (OSO_3^-)
ChNCs	width = 5-20 length = 50-350 thickness = N/A	average width = 48 average length = 250 average thickness = 5	0.8	5.5	1.08 (NH_4^+)

SANS and STEM measurements of CNCs and ChNCs slightly differ because of the different approach used for their determination. However both measurements give similar results and confirm that nanocrystals present nanometric width and thickness, while they are some hundreds nanometers long.

2. Formulation

Two categories of samples were developed for this study: starch-based matrices and starch-based nanocomposites.

Two formulations were prepared for starch-based matrices: the first is composed of only native potato starch and water (G0) while the second is added with glycerol as further plasticizer (G20).

Two variants of nanocomposites were developed starting from the glycerol-plasticized formulation: the first is added with cellulose nanocrystals (CNCs) while the second with chitin nanocrystals (ChNCs).

Prior to extrusion, the water content of starch flours was adjusted to 37wt% of starch dry mass and, for the glycerol-plasticized formulations, glycerol content was set to 22.5wt% of starch dry mass (**Table II-3**). As shown in **Figure II-3a** glycerol was pre-mixed with water before to be added to starch.

For the nanocomposites, CNCs and ChNCs aqueous suspensions were pre-mixed with glycerol and water and then added at different concentration to the native starch powder (**Figure II-3b**): this gave formulations at 1.5, 2.5, 4, 5 and 10wt% CNC content and formulations at 2, 4, 8wt% ChNCs content on the final total mass of the composition. All the formulations were mixed using a blender (Major Titanium, Kenwood, UK), in order to obtain a homogeneous mix, especially in the case of nanofillers.

The higher CNCs-concentrated compositions (5 and 10wt% CNCs) and all compositions with ChNCs were obtained by alternating the addition of nanofiller suspension with drying steps in oven at 40°C (**Figure II-3c**), because of the low concentration of nanofiller suspensions (especially for ChNCs, see **Table II-1**). This allows obtaining a composition hydrated on 37wt% of starch dry mass at the desired nanofiller content before extrusion.

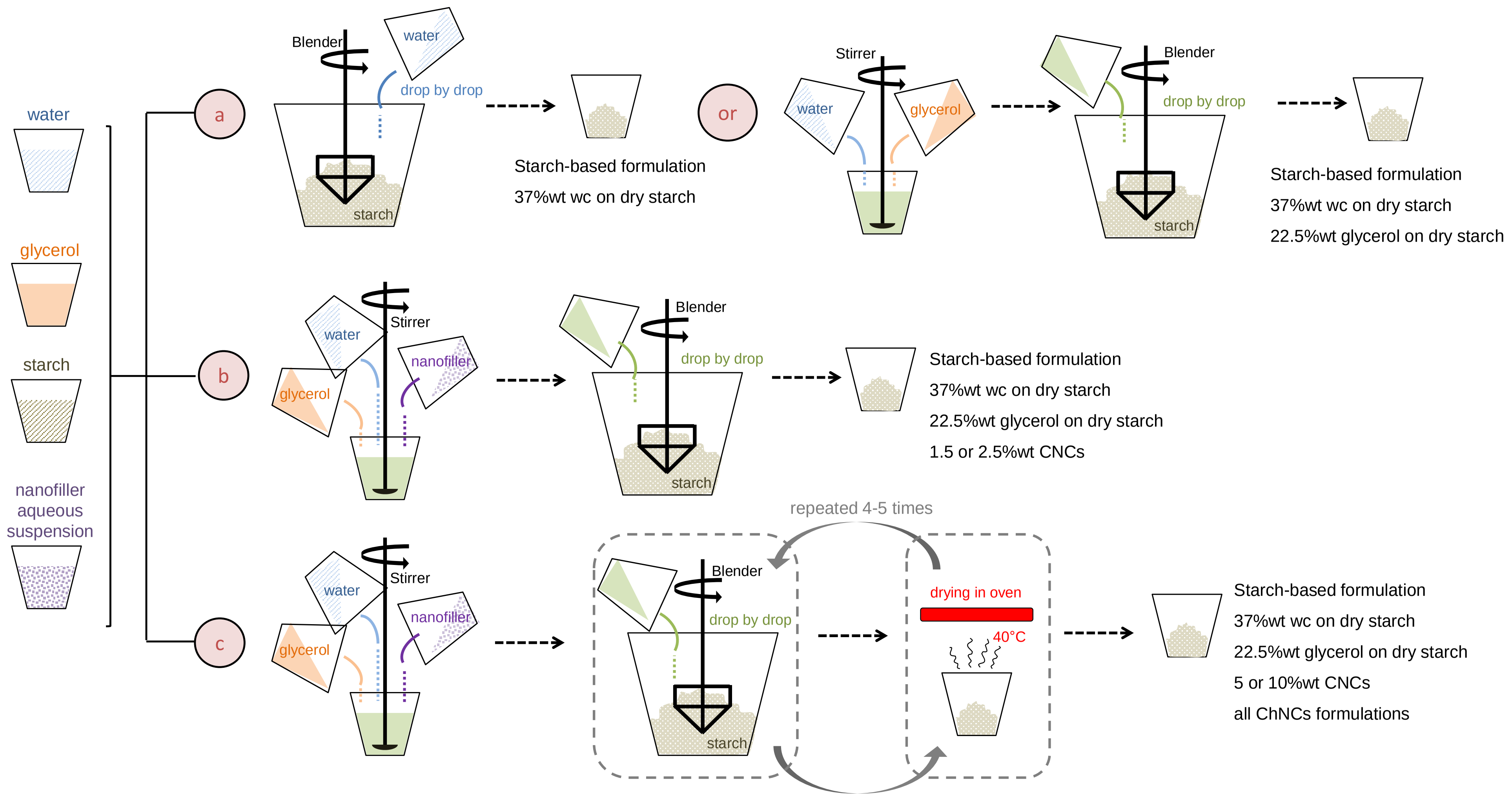

Figure II-3: *Preparation of* **a)** *starch-based matrices,* **b)** *compositions at 1.5 and 2.5wt% CNCs and* **c)** *compositions at 5 and 10wt% CNC and all ChNC-based compositions before extrusion.*

2.1 Preliminary study of ready-to-extrude formulations melting features

A preliminary study of starch-based formulations melting features was necessary before to proceed with the extrusion processing. This initial analysis is fundamental to determine the optimal thermal conditions to apply during native starch processing to obtain the desired thermoplastic materials. To obtain such information all formulations have been analyzed by Differential Scanning Calorimetry (DSC) to observe their melting endotherms.

Melting properties determination by DSC

The melting endotherm of starch-based formulations was determined using a Q100 DSC (T.A. Instruments, New Castle, DE, US). About 25mg of each formulation were accurately weighted and sealed in hermetic inox pans. Sample pans were heated using one cycle from 20°C to 200°C at 3°C min^{-1}*. An inox empty sealed pan was used as reference.*

The transition temperatures T_o, T_p *and* T_c *are, respectively, the onset, peak and conclusion temperatures of the melting endotherm. The melting enthalpies (ΔH) were determined by integration using TA (Thermal Advantage) Universal Analysis software and were adjusted on dry starch content in the formulation.*

Each sample was analyzed in triplicate.

Thermal characteristics obtained from melting endotherms of starch-based formulations are reported in **Table II-2**.

To ease the interpretation of the results, the exact composition of each sample before extrusion is reported in **Table II-3**.

The temperature values T_o, T_p and T_c determined for starch without glycerol (G0) are very close to the ones reported by van Soest (J.J.G. van Soest, Bezemer, et al. 1996) and Coativy (Coativy 2013) in works related to the melting of potato starch. G0 melting endotherm onset and conclusion are clear and well-definite: melting starts at about 77°C and ends around 115°C, with a peak at 99.5°C (**Table II-2**).

Conversely, T_o and T_c values are more difficult to determine for G20 formulation, because the addition of glycerol broadens the melting endotherm of starch (T_c - T_o = 61°C, **Table II-2**). This broadening is due to the strong interaction which forms between glycerol and starch and to the lower amount of water available to starch for melting, because of the high hydrophilicity of glycerol. As a consequence, the energy ($\Delta H = 8 \pm 1.7$ J g^{-1}) and temperature (T_p = 105.9°C, **Table II-2**) needed for the starch crystallites melting rise in G20 formulation.

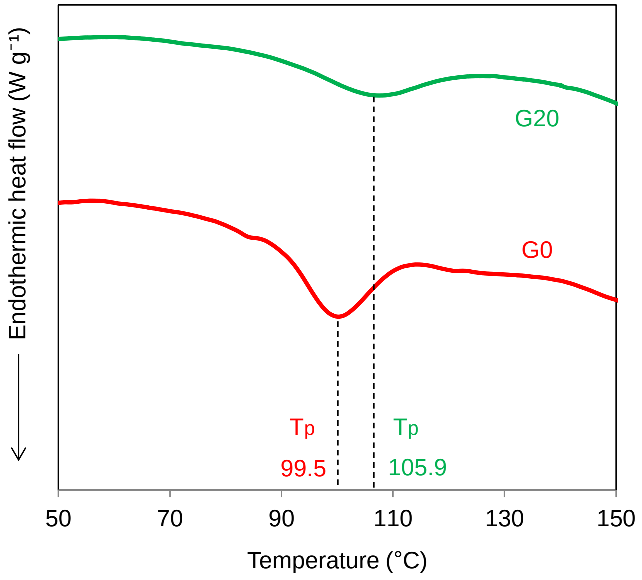

Figure II-4: *Melting endotherms of G0 and G20 starch-based formulations analyzed by DSC. Peak temperature (T_P) for each formulation is highlighted by dotted lines.*

No differences can be identified among the thermal characteristics of starch-CNCs and starch-ChNCs nanocomposite formulations. No trend explained by the increasing nanofiller amount in the formulation is observed for melting enthalpies and temperatures. This means that nanocrystals do not influence the melting of native potato starch in these conditions (37wt% water and 22.5wt% glycerol on potato starch dry mass).

Table II-2: *Thermal characteristics of starch-based formulations: onset (T_o), peak (T_p) and conclusion (T_c) temperatures, temperature ranges (T_c-T_o) and enthalpies (ΔH) (standard deviations in parentheses).*

Formulation	T_o (°C)	T_p (°C)	T_c (°C)	T_c -T_o (°C)	ΔH (J g⁻¹)
G0	77.7 (3.1)	99.5 (0.6)	115.1 (0.9)	37.4 (3.2)	6.6 (0.4)
G20	69.0 (1.4)	105.9 (0.5)	130.0 (1.4)	61.0 (2.8)	8.0 (1.7)
CNC_1.5	71.7 (5.0)	104.8 (1.1)	124.3 (1.5)	52.7 (4.9)	7.5 (0.8)
CNC_2.5	70.0 (3.2)	103.1 (0.8)	124.3 (1.0)	54.3 (3.9)	8.6 (0.7)
CNC_5	71.4 (2.2)	107.1 (0.3)	125.0 (1.2)	53.6 (2.7)	6.9 (0.4)
CNC_10	70.6 (6.1)	104.8 (0.7)	126.2 (1.1)	55.6 (6.6)	7.5 (0.6)
CNC_4	68.6 (7.0)	104.8 (0.8)	128.0 (2.0)	59.4 (7.8)	8.3 (1.3)
ChNC_2	63.3 (5.2)	101.5 (0.3)	128.5 (2.4)	65.3 (6.6)	10.7 (1.0)
ChNC_4	67.5 (3.5)	101.6 (0.4)	127.5 (0.7)	60.5 (2.1)	9.5 (1.0)
ChNC_8	64.7 (3.2)	105.4 (0.4)	126.7 (0.6)	62.0 (3.5)	7.5 (0.5)

3. Twin-screw extrusion

Samples were extruded in a twin-screw extruder (Process 11, Thermo Scientific, US) equipped with co-rotating screws and a plate die (1 × 30 mm) in the form of band-shaped materials (**Figure II-6a**). This extruder presents a barrel length of 40 L/D (640 mm), divided over eight independent temperature zones, and a diameter of 11mm (**Figure II-5**).

To produce reproducible samples, it was necessary to reach a steady state during extrusion: the material was collected when temperature, couple and the other parameters were stable. Material flow was checked by withdrawing the material every ten minutes maximum, for avoiding excessive heterogeneity in the samples. The data recorded during sample collecting were then used to compute the Specific Mechanical Energy (SME) applied on each formulation.

In order to stabilize their water content, band-shaped samples were stored at constant relative humidity at 20°C (0.59 a_w with NaBr solution) for two weeks after extrusion.

3.1 Starch-based matrices

Two different screw profiles have been used to extrude starch with glycerol (G20) and without glycerol (G0). The objective was to obtain two completely opposite degrees of native starch structure destructurization using the two screw profiles. To do this the SME (Specific Mechanical Energy) applied on starch with the first and the second profile was importantly different (**Table II-3**).

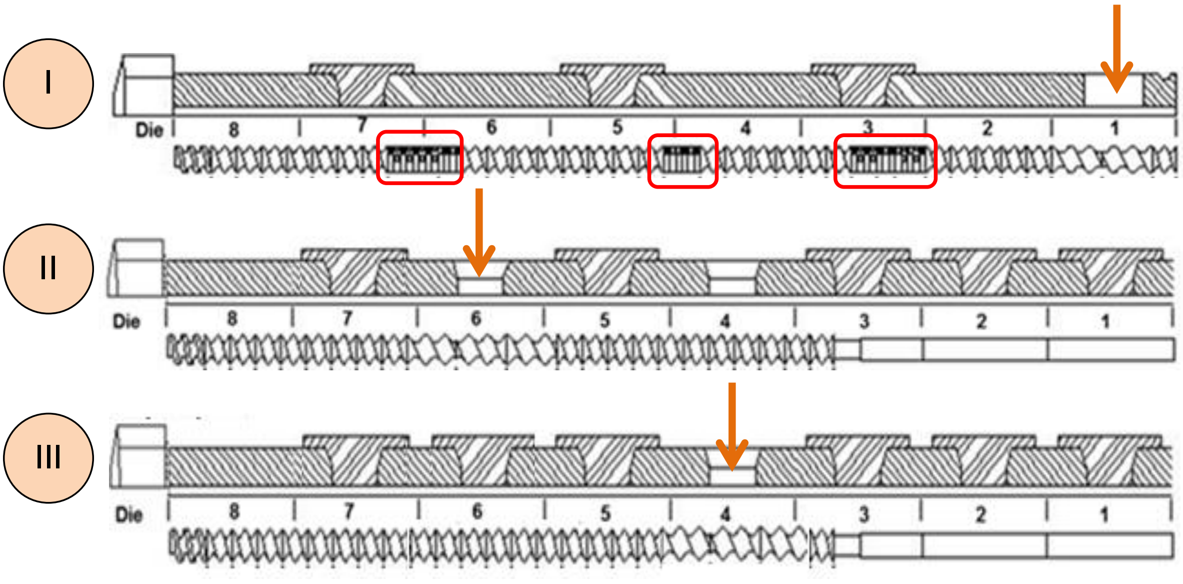

Figure II-5: *Screw profiles used to extrude starch-based matrices and nanocomposites. Arrows indicate raw material feeding. Mixing zones are highlighted by red frames.*

Screw profile I was added with three mixing zones (highlighted by red frames, **Figure II-5**) with the aim of applying high shear stress to native starch; high temperatures were applied and raw material feeding was positioned in zone 1 in order to use all the screw length (40 L/D) to completely destructurize and melt native starch structure (G0_HIGH and G20_HIGH, **Table II-3**). The resulting SME applied with this profile was equal to 1900 J g^{-1}.

Screw profile II (**Figure II-5**) was simple with the only aim of conveying native starch in the heated barrel and preserve starch native structure; the raw material feeding was located in zone 6 so that the screw length was importantly reduced (15.5 L/D). In addition, lower temperatures were used for starch melting (G0_LOW and G20_LOW, **Table II-3**) with this second screw profile. SME was equal to 100 J g^{-1} during the extrusion of these samples.

Some tunings of the extrusion parameters were necessary depending on the raw material formulation in order to obtain a dense material and a regular flow at the outlet of the die.

Samples' thickness precisely measured using a micrometer varied between 1.2 and 2.5 cm. More specifically, samples extruded at higher temperatures (G0_HIGH and G20_HIGH) showed the highest thickness.

For sample G0_LOW, it was not possible to extrude at 37wt% water content on starch dry mass because of the high viscosity of the formulation during processing. To extrude this formulation, hydration was raised up to 54wt% on dry starch (**Table II-3**) and extruded using a cylindrical die (**Figure II-6b**).

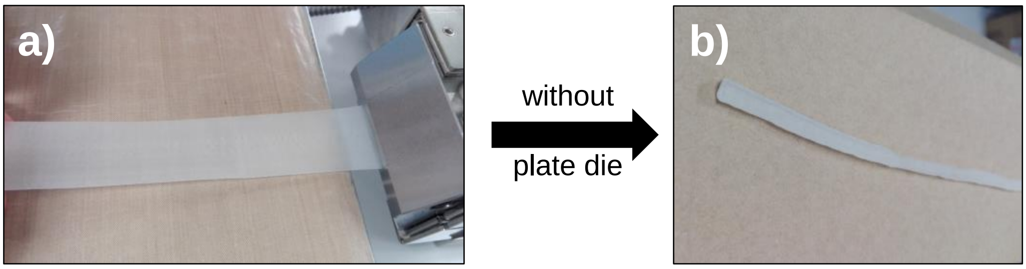

Figure II-6: a) *Band-shape extruded samples and* **b)** *cylindrical shape of G0_LOW.*

3.2 Nanocomposites

3.2.1 Cellulose nanocrystal-starch nanocomposites

Screw profile III was used for the extrusion of starch-CNCs (see **Figure 5**): it is a very simple and conveying screw profile, to avoid CNCs degradation due to shear stress. Temperature ranged from 50°C (at the feed hopper) to 110°C (at the die) along the barrel (**Table II-3**) and the rotation speed of the screw with this extruder gave a SME that ranged between 90 and 130 J g^{-1} (**Table II-3**) for these nanocomposites.

As done for the starch-based matrices, the extrusion parameters were adjusted depending on the composition in order to obtain visually homogeneous materials, without any un-melted fractions at the exit of the extruder (**Table II-3**). For example, the temperature of extrusion of compositions at 5 and 10wt% CNCs was slightly risen because of the lower amount of water in the system (**Table II-3**). In addition to compositions at 5 and 10wt% CNCs, nanocomposites at lower CNCs content (1.5 and 2.5wt %) were prepared as well.

A starch based matrix of reference extruded with similar extrusion parameters and by using the same screw profile as CNCs-starch nanocomposites was made to isolate the effect of CNCs on starch structure from the other parameters (REF_CNC, **Table II-3**).

All samples obtained with screw profile III are ~1.2 mm thick.

3.2.2 Chitin nanocrystal-starch nanocomposites

Profile II (**Figure II-5**) was used to extrude ChNCs-starch nanocomposites; once again the use of a simple and conveying screw profile has the aim to avoid ChNCs degradation. Temperature ranged between 50 and 105°C along the barrel, and SME varied from 80 to 115 J g^{-1} depending on the ChNC concentration in the sample (2, 4 and 8wt%).

Slightly higher temperatures were used for formulations at 4 and 8wt% ChNCs content because of the lower total water content in the samples.

Starch-ChNCs extruded nanocomposites are ~1.2 mm thick here too.

The starch-based matrix of reference for ChNCs-starch nanocomposites is G20_LOW (**Table II-3**).

A last nanocomposite (CNC_4, **Table II-3**) containing 4wt% CNCs was extruded by using screw profile II, as for ChNCs-starch nanocomposites (**Figure II-5**). The aim of this sample is to help in understanding the effect of nanofiller type (CNC or ChNC) on nanocomposite structure and properties, independently from the extrusion parameters used for its production.

Table II-3: Samples nomenclature, extrusion conditions and composition.

Nomenclature	Description	Screw length (L/D)	SME (J g^{-1})	Flow rate (g min^{-1})	Screw rotation (rpm)	Temperature profile	Theoretical ratio (%wt) starch:water:glycerol:NPs		Screw profile
							at extrusion	after conditioning	
G0_LOW	potato starch	15.5	100	1.7	10	[90; 90; 90; 90; 50]	65:35:00:0	86:14:00:0	II
G20_LOW	potato starch + glycerol	15.5	100	0.9	20	[90; 90; 90; 90; 50]	63:23:14:0	72:12:16:0	II
G0_HIGH	potato starch	40	1900	1.1	50	[90; 100; 115; 100; 100; 80; 80; 50; 50; 20]	73:27:00:0	85:15:00:0	I
G20_HIGH	potato starch + glycerol	40	1900	1.5	60	[95; 100; 115; 115; 110; 90; 80; 50; 50; 20]	63:23:14:0	71:13:16:0	I
REF_CNC	potato starch + glycerol	26.5	80	1	20	[105; 105; 100; 90; 80; 70; 50]	63:23:14:0	71:13:16:0	III
CNC_1.5	potato starch + glycerol + CNCs	26.5	130	0.9	20	[105; 105; 100; 90; 80; 70; 50]	62:23:14:1	70.5:12:16:1.5	III
CNC_2.5	potato starch + glycerol + CNCs	26.5	110	1.2	20	[105; 105; 100; 90; 80; 70; 50]	61:23:14:2	70:12:15.5:2.5	III
CNC_5	potato starch + glycerol + CNCs	26.5	90	1.4	20	[105; 105; 105; 95; 85; 70; 50]	60:22:13.5:4.5	68:11.5:15.5:5	III
CNC_10	potato starch + glycerol + CNCs	26.5	90	1.4	20	[110; 110; 105; 95; 85; 70; 50]	57:21:13:9	63.5:12:14.5:10	III
CNC_4	potato starch + glycerol + CNCs	15.5	90	1.5	20	[105; 105; 105; 90; 50]	60.5:22.5:13.5:3.5	69:11.5:15.5:4	II
ChNC_2	potato starch + glycerol + ChNCs	15.5	115	1.6	20	[90; 90; 90; 90; 50]	61.5:23:14:1.5	70:12.5:15.5:2	II
ChNC_4	potato starch + glycerol + ChNCs	15.5	60	1.6	20	[105; 105; 105; 90; 50]	60.5:22.5:13.5:3.5	68:12.5:15.5:4	II
ChNC_8	potato starch + glycerol + ChNCs	15.5	80	2.4	20	[105; 105; 105; 90; 50]	58:21.5:13:7.5	66:11:15:8	II

4. Glycerol and water content in the samples after conditioning

The water content in the samples was assessed in order to compute the weight theoretical ratio starch:water:glycerol:nanoparticles (NPs) in the samples after conditioning, reported in **Table II-3**. To do this, a classical weight technique, described below, has been employed.

The percentage of the other components was computed from this value and the compositional weight ratio before extrusion.

Drying in oven

For water content 50 mg of extruded sample were collected after stabilization at constant relative humidity at 20°C (0.59 a_w *with NaBr solution) for two weeks and put in oven at 130°C until stable weight was reached. The time of drying in oven is dependent on sample geometry, especially thickness. The sample was weighted before and after drying using a high precision balance (33g/0.01mg, Sartorius). The water content results from the difference of sample weight before and after drying, as shown in* **Equation II-1***:*

$$\%\mathrm{wc} = \frac{\mathrm{m_t} - \mathrm{m_d}}{\mathrm{m_t}} \cdot 100 \quad \textbf{[II-1]}$$

Where $\%\mathrm{w_c}$ *is the water content percentage on the weight basis,* $\mathrm{m_t}$ *and* $\mathrm{m_d}$ *are the sample mass (mg) before and after drying respectively. Each sample was analyzed in triplicate.*

The water content ranges between 11 and 15wt% on the total mass of the sample, which are normal values for starch-based materials stabilized at this relative humidity.

For nanocomposites, water content appears as generally lower on the total mass of the sample because of the increasing nanofiller content (**Table II-3**). However, the ratio dry starch/water does not significantly vary between the samples.

To better ensure the reliability of these ratios, glycerol content in the conditioned samples after extrusion was measured using ^{1}H Nuclear Magnetic Resonance (NMR).

^{1}H NMR in DMSO-d6

To assess if any loss of glycerol occurred during the pre-extrusion mixing step or during extrusion, 125 mg of one starch-based matrix, one CNCs-starch and one ChNCs-starch nanocomposites were solubilized in 5 mL each of deuterated dimethyl sulfoxide (DMSO-d6, Eurisotop, FR) at 20°C and their glycerol content was analyzed using a Bruker AvanceIII-400 MHz spectrometer for ^{1}H detection operating at a frequency of 400.16 MHz.

G20_LOW, CNC_5 and ChNC_4 were used as representative of G20 starch-based matrices, CNCs-starch and ChNCs-starch nanocomposites respectively.

Calibration solutions at 11, 22, 43, 54 and 108mM of glycerol in DMSO-d6 were prepared as well. Calibration solutions and sample solubilizing were developed in a glove box to avoid solvent (DMSO-d6) denaturation.

The spectra obtained for the calibration solutions are typical of glycerol in DMSO-d6. No contaminant is observed in the ^{1}H spectra (**Figure II-7a**). The residual signals of HDO (~3.3 ppm) and DMSO-d6 (~2.5 ppm) show the same order of magnitude of glycerol signal (~4.3 and 4.45 ppm), thus no water-signal pre-saturation is needed for the calibration solutions. With regard to the highest calibration point (G5, 108mM), which is considered as exact, the glycerol concentration of the other calibration points is normalized and a calibration curve is obtained (**Figure II-7b**).

The resulting calibration curve appears linear in the analyzed interval. The glycerol content in the solubilized samples G20_LOW, CNC_5 and ChNC_4 is determined from the calibration curve. Results are reported in **Table II-4**.

The experimental concentration of glycerol in the samples (from 14.8 to 16.2wt%) is very close to the theoretical one (from 15.5 to 16wt%) and no significant differences are detected among the samples. This confirms the theoretical compositional values reported in **Table II-3** for the extruded starch-based matrices and nanocomposites.

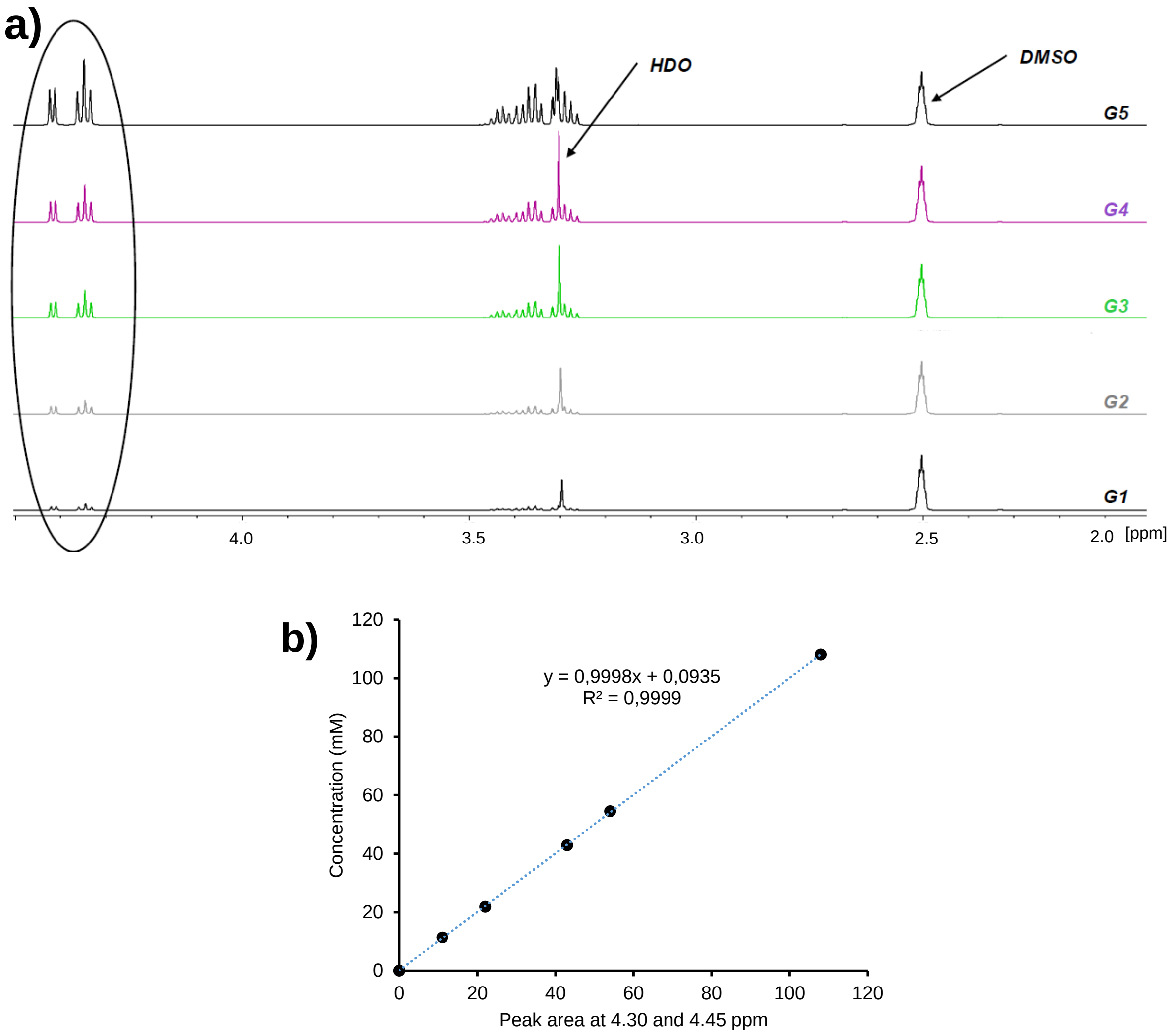

Figure II-7: a) *Focus from 2.0 to 4.5 ppm of ^{1}H spectra of glycerol calibration solutions in DMSO-d6. G1 (11mM), G2 (22mM), G3 (43mM), G4 (54mM) and G5 (108mM).Glycerol peaks are highlighted by a black circle.* **b)** *Calibration curve of glycerol concentration.*

Table II-4: *Comparison between theoretical and experimental glycerol concentration in the analyzed samples.*

Sample	**[Experimental glycerol]**		**[Theoretical glycerol]**	
	(mM)	**(%)**	**(mM)**	**(%)**
G20_LOW	44	16	41	16.2
CNC_5	41	15.5	42	14.8
ChNC_4	43	15.5	42	15.7

Chapter III

LARGE-SCALE ORGANIZATION IN THE SAMPLES

Table of contents

In this chapter we provide a description of starch-based matrices and nanocomposites organization after extrusion. To do this, a Differential Scanning Calorimetry (DSC) gelatinization test is used in addition to Scanning Electron Microscopy to get information at the macroscopic scale. At the macromolecular scale, Asymmetrical Flow Field Flow Fractionation (AF4) is used to check on the starch macromolecules degradation during extrusion. As nanocrystals cannot be visualized, a simple theoretical model is used to predict nanofillers distribution and percolation thresholds in the extruded nanocomposites, and its results discussed with the experimental measurements.

1. Surface state and gelatinization features of starch-based matrices

Characterizing the dispersion state of cellulose and chitin nanocrystals in the starch matrix after extrusion is a big challenge. Multiple techniques are available nowadays, but each has a few drawbacks as well: Small-Angle X-ray (SAXS) and Neutron (SANS) Scattering, and Transmission Electron Microscopy (TEM).

Cellulose and chitin are chemically similar to starch, making contrast almost non-existent when using classical techniques such as SAXS and TEM. The similar chemical structure of starch, cellulose and chitin prevents from using staining techniques as well, while the low resolution of optical microscopy prevents from using other contrast techniques, such as Second Harmonic Generation imaging (SHG), which is based on the detection of highly crystalline and ordered structures, such as in cellulose and in chitin nanocrystals.

As for SANS, a contrast could be created by using deuterated fillers; however, the extremely large quantities of deuterated nanocrystals which would need to be synthetized, not to mention the unknown effect of the extrusion on the stability of deuteration, weighted against the use of this technique.

To get around this issue, Scanning Electron Microscopy (SEM) is used here to investigate the morphology of samples surface after fracture (Slavutsky & Bertuzzi 2014; Montero et al. 2017) at a very large scale. SEM is used to determine the surface state of the material; in particular it gives information about the macroscopic organization of starch after extrusion.

Scanning Electron Microscopy

Fracture surface of the samples were analyzed by secondary electron imaging using a Scanning Electron Microscope (Quattro S, Thermo Scientific, US). Samples were frozen in liquid nitrogen during a few seconds, broken to obtain the fracture surfaces, and then quickly introduced in the microscope chamber for observation.

Images were obtained in low-vacuum conditions (130 Pa) at room temperature. An accelerating voltage of 5-10 kV was used without any sputter-coating of the specimens.

Samples were analyzed in triplicate.

SEM micrographs of the fracture surface of thermoplastic starch-based matrices are reported in **Figure III-1**. Many granule-shaped residuals are visible in SEM micrographs of G0_LOW and G20_LOW matrices (**Figure III-1**). For both samples, the size of these granule-shaped residuals ranges between 10 and 85 µm, which is in accordance with the median granulometry of the native granules (~44 µm).

This observation means that the use of light extrusion parameters (SME = 100 J g^{-1}), low temperatures and a short/conveying screw profile (L/D = 15.5, **Table II-3**) induced the preservation of some of the starch native structure.

By contrast, REF-CNC (matrix of reference for starch-CNCs nanocomposites) presents a homogeneous and smooth surface (**Figure III-1**), without any visible residual granule. The use of a longer screw (L/D = 26.5, **Table II-3**) and the longer residence time of starch in the heated barrel compared to G20_LOW sample seem to have induced the total melting of the native starch structure. This result points out the very narrow range of extrusion parameters which allows preserving native starch structure in the sample during extrusion.

The REF-CNC surface is much more similar to the one of starch extruded by applying a more severe thermomechanical treatment (G20_HIGH, **Figure III-1**), as presented in the following paragraph.

G0_HIGH and G20_HIGH matrices extruded at high SME (1900 J g^{-1}) and temperature (see **Table II-3**) present a homogeneous and smooth surface (**Figure III-1**). The shear applied, with a SME superior to 100 J g^{-1}, causes the complete destructurization of native granules during the extrusion. This observation is in accordance with the total absence of granular organization observed by (Logié et al. 2018) in thermoplastic starch extruded at SME superior to 200 J g^{-1}.

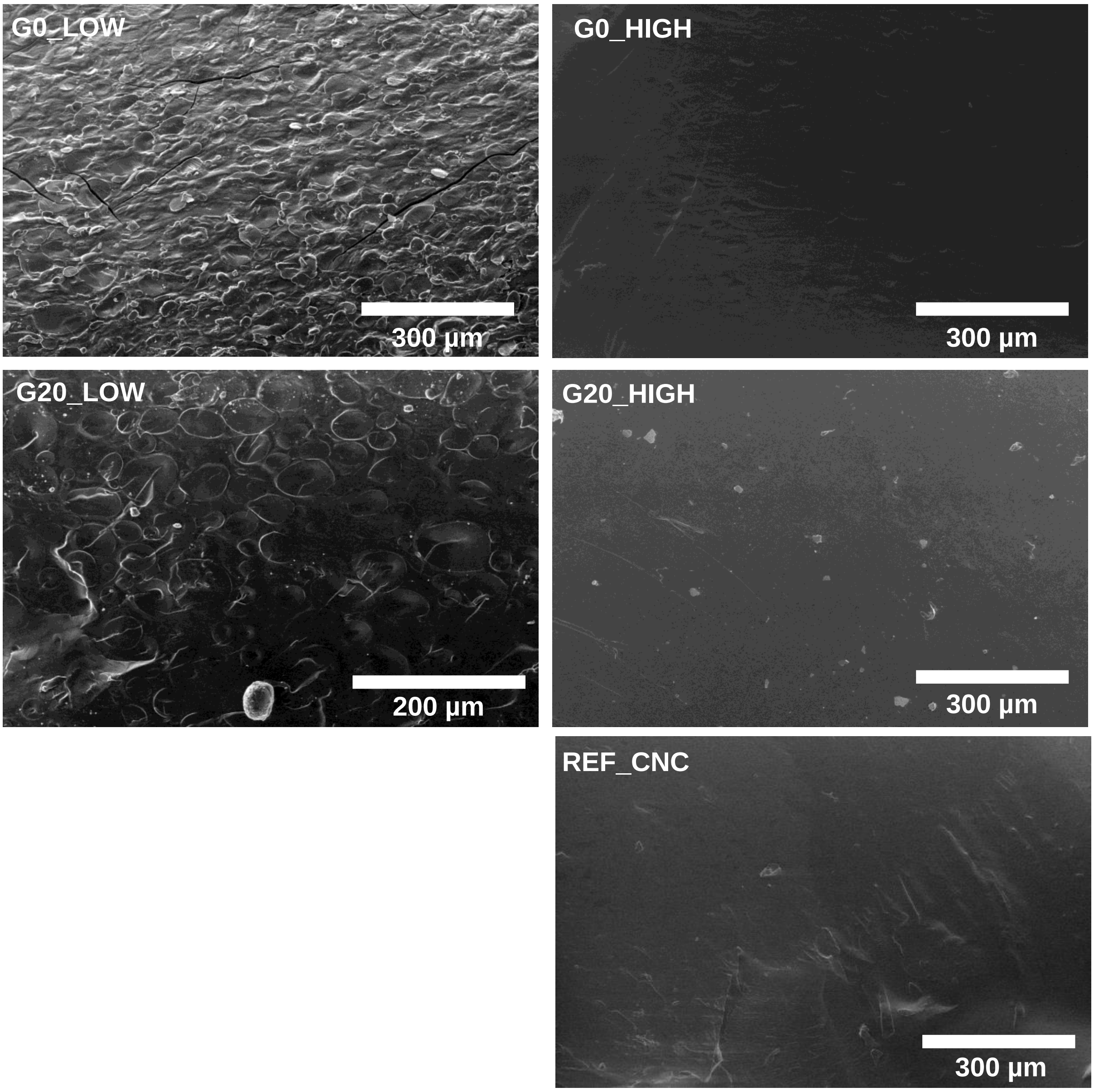

Figure III-1: *SEM micrographs of fracture surface of starch-based matrices.*

In order to confirm these first results, Differential Scanning Calorimetry (DSC) was used to quantify the amount of residual native granules in the extruded matrices and precisely determine the effect of the extrusion parameters and formulation (plasticization with glycerol) on the preservation of native granules in the extruded samples.

Differential Scanning Calorimetry for residual granules detection

The residual gelatinization features of starch-based samples were determined using a Q100 DSC (T.A. Instruments, New Castle, DE, US). Cryoground samples of 10-15 mg mass were heated from 20°C to 120°C at 3°C min^{-1} in excess of water (mass ratio starch:water = 20:80).

Hermetic inox pans were used to avoid water disturbance. Gelatinization enthalpy ΔH_g of the extruded sample was determined by integrating the produced endotherm.

In comparison with gelatinization enthalpy of native starch, percentage of residual enthalpy was defined to describe the amount of starch residual granules in the extrudate, on the example of (Jenkins & Donald 1998; Logié et al. 2018).

$$Residual\ granules\ (\%) = \frac{\Delta H_{sample}}{\Delta H_{native}} \times 100 \quad \textbf{[III-1]}$$

Each sample was analyzed in triplicate.

The absence of granular structures in the matrices G20_HIGH, G0_HIGH and REF-CNC is confirmed by DSC results, in which no gelatinization endotherm is detectable for these samples.

A small endotherm (**Figure III-2**), corresponding to a few residual granules (16 and 25% for G0_LOW and G20_LOW respectively, **Table III-1**), is detected in the two matrices extruded at the lowest SME. Gelatinization enthalpy is higher for the glycerol-plasticized sample G20_LOW, probably because of the lubricant action of glycerol, which helps in preserving starch granular structure during extrusion (Nessi et al. 2018).

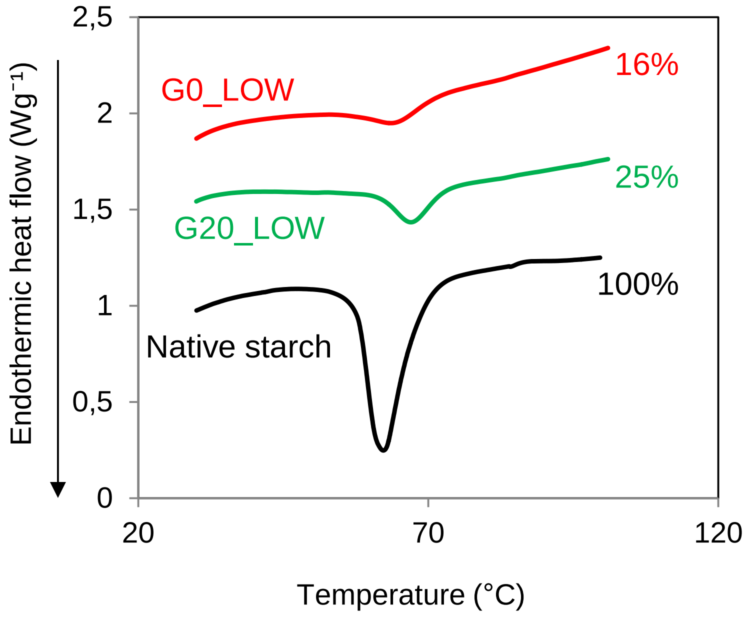

Figure III-2: *DSC thermograms of starch-based matrices compared to native potato starch. Only samples with detectable gelatinization enthalpies are reported.*

Table III-1: *Gelatinization enthalpy and temperature of native and extruded starch-based samples by differential scanning calorimetry in excess of water.*

Sample	Gelatinization enthalpy (J g^{-1})	Residual granules (%)	Gelatinization temperature (°C)
Native starch	14.5 ± 0.5	100	62.5
G0_LOW	2.3 ± 0.3	16	64
G20_LOW	3.6 ± 0.3	25	67

The endothermic peak corresponding to the gelatinization temperature is shifted to slightly higher temperatures for the granules in the extruded matrices (64 and 67°C for G0_LOW and G20_LOW respectively, **Table III-1**) when compared to native starch (62.5°C), in particular for the glycerol-plasticized sample G20_LOW (**Figure III-2**). This shift to higher gelatinization temperatures is probably due to structural changes (crystals alignment and larger size) generated by the heat-moisture treatment that granules undergo during extrusion (Gunaratne & Hoover 2002). In addition, glycerol is known to increase the gelatinization temperature of starch native granules, as suggested by (Nashed et al. 2003), because of its tendency to bind to water more rapidly than starch and reduce the effective amount of water available for starch gelatinization.

2. Macromolecular characterization of starch chains in starch-based matrices

In the previous paragraph we have seen that extrusion affects the native granular organization of starch, inducing a more important destructurization when severe parameters are applied.
On a smaller scale too, this process affects starch macromolecules.
To determine the degrading effect of extrusion, the characteristics of starch macromolecules were studied by Asymmetrical Flow Field-Flow Fractionation coupled with multi-angle laser light scattering and differential refractometric detection (AF4-MALLS-DRI).

AF4-MALLS-DRI

Asymmetrical flow field-flow fractionation (AF4) is employed since the late 80's as an effective alternative to size exclusion chromatography to separate colloids, proteins, hydrophilic polymers and particles on a large range of size (from 1 nm to 50 µm).
Separation is driven by the difference in diffusion coefficients of particle center of mass, which is directly related to particle size.

The principle of AF4 is reported in **Figure III-3**. *Samples are injected in an asymmetrical channel of separation containing a carrier and composed of a rigid wall and an ultrafiltration membrane. Here the particles are confined in a thin layer using a crossflow and they redistribute depending on their size: bigger particles gather near to the ultrafiltration membrane, at the bottom on the channel, while smaller particles move toward the center of the channel. When the cross-flow is stopped, the small particles are eluted more rapidly than the big ones, thanks to the laminar flow which forms in the channel.*

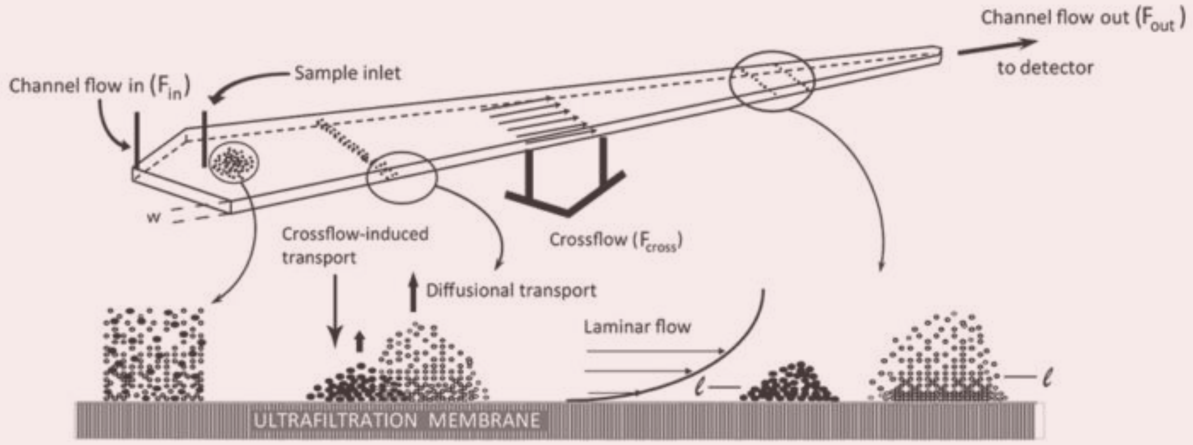

Figure III-3: Separation of particles of different size in AF4 system (Nilsson 2013). Large particles (filled symbol) are separated from small particles (open symbol) during elution in the channel. *w*=channel thickness. *l*=average particle populations distance from the ultrafiltration membrane.

Samples were prepared as previously described (Rolland-Sabaté et al. 2007). Native and extruded starches were solubilized at room temperature in DMSO (95%, Merck, US) under mild stirring during 5 days and precipitated in ethanol (96%, Carlo Erba, Spain). Then samples were solubilized in water by microwave heating under pressure and the solutions were filtrated on 5 µm DuraporeTM filters to avoid the injection of aggregates in the channel.

Molar mass and molecular size of starch molecules were determined using an AF4 instrument constituted by a trapezoidal channel 275 mm-long, a polyester spacer 350 µm-thick and a regenerated cellulose membrane with a nominal cut-off of 10 kDa (Millipore, Bedford, US).

The flows in the channel and the sample injection were controlled with an Eclipse system (Wyatt Technology Corporation, US), a pump and an auto-sampler from Thermo Scientific (Waltham, US).

Samples were eluted following the method previously described by (Rolland-Sabaté et al. 2011). The carrier (Millipore water with 0.02% NaN_3) was initially eluted at 0.84 mL min^{-1} for channel conditioning.

After 2 minutes, a cross-flow of 0.84 mL min^{-1} *was set for sample injection and for the focus/relaxation of the sample. 100 µL of sample at a concentration of 0.5 g L*$^{-1}$ *were injected for 5 min and a ramp of crossflow from 0.4 to 0.05 mL min*$^{-1}$ *was used for elution for 8 min and then maintained at 0.05 mL min*$^{-1}$ *for 10 min. The channel was finally freed of all sample residues using a crossflow at 0 mL min*$^{-1}$ *for 5 min.*

The AF4 instrument was coupled to two online detectors: a MALLS instrument (DAWN Heleos II) associated with a K5 flow cell and a GaAs laser (λ=663 nm), and a refractometric detector operating at the same wavelength (Optilab T-rEX) (Wyatt Technology Corporation, US).

Data were acquired using Wyatt ASTRA® software (v. 6.1.4.25) as previously described (Rolland-Sabaté et al. 2011) and treated to determine the average weight and number molar masses ($\bar{M}_w$ *and* $\bar{M}_n$*), the polydispersity (* $\bar{M}_w/\ \bar{M}_n$*) and the z-average radius of gyration (*$\bar{R}_{Gz}$*) of the injected samples.*

Elution recovery was computed using the concentration of the eluted sample (determined by the differential refractive index signal) and the carbohydrate concentrations before and after filtration determined by the sulfuric acid-orcinol method (Planchot et al. 1997). Molar masses ($\bar{M}_w$ *and* $\bar{M}_n$*) and the macromolecular size distribution (*$\bar{R}_{Gz}$*) were established by applying the Berry model to the elution time results.*

Determination of total sugar concentration by the orcinol-sulfuric method

The total sugar concentration of samples injected in AF4 system is determined by the orcinol-sulfuric colorimetric technique.

Dosing is carried out in a continuous flow system using a Skalar autoanalyzer (**Figure III-4a**)*.*

The polysaccharides contained in the sampling solutions are hydrolyzed to glucose units, and then to furfural units, by the combined action of temperature (98°C) and acid.

Furfural units interact with orcinol and generate a complex absorbing at 420nm (**Figure III-4b**)*.*

Sulfuric orcinol is the solvent in which the total sugar is dosed. It is obtained by gradually adding sulfuric acid (98%, 1400mL) to cold water (650mL). Once the water-acid mixing done, 50mL of an aqueous solution containing 2 g of 3,5-dihydroxytoluene are added to the solution. This final solution can be stored up to 15 days protected from light.

A glucose range from 25 to 100 mg L^{-1} *must be developed to determine sample glucose concentration. Before injection in the Skalar autoanalyzer, samples must be diluted so as to be positioned in the glucose range.*

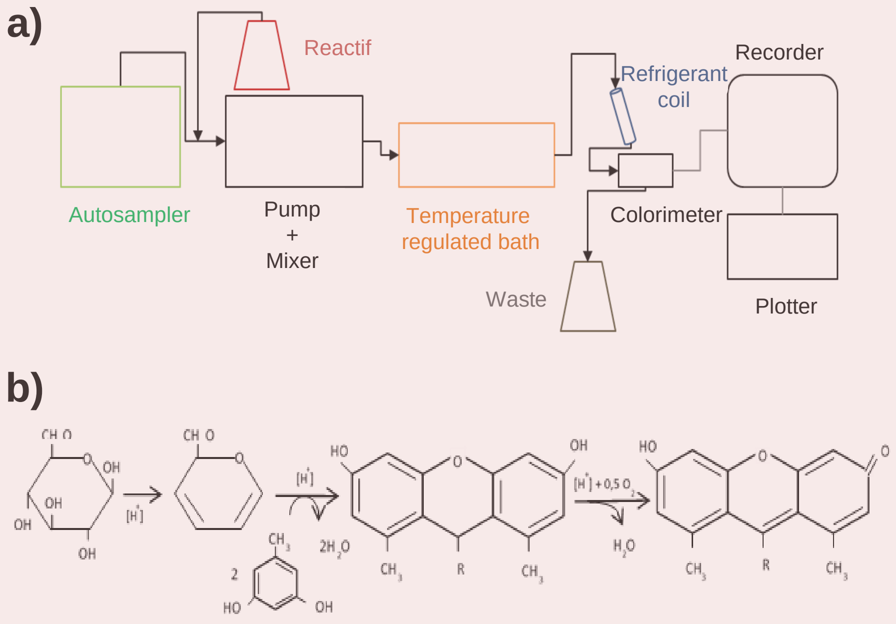

Figure III-4: a) Schematic representation of continuous flow system for colorimetric dosing and **b)** furfural units-orcinol interaction to form a complex absorbing at 420nm.

The absorbance of the colored furfural complex is proportional to its concentration, as proposed by Beer-Lambert equation:

$$A = \varepsilon \cdot l \cdot C \quad \textbf{[III-2]}$$

Where A *is the absorbance at 420nm,* ε *is the molar extinction coefficient,* l *is the length of the cell and* C *is the concentration of the sample.* A *is drawn as a function of* C *to determine the calibration curve* (**Figure III-5**)*. A calibration curve is developed before each analysis and it is regularly verified all over the experience. Samples are analyzed in triplicate.*

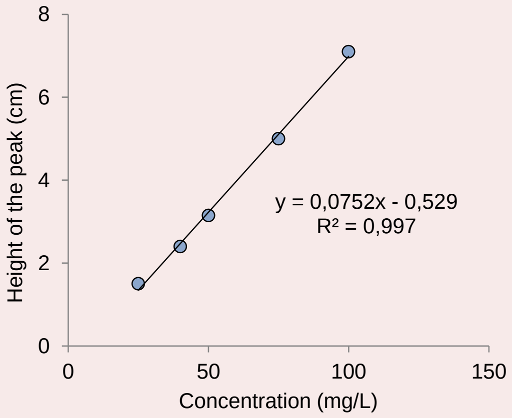

Figure III-5: Calibration curve of glucose range in PBS.

No significant loss of material occurred during elution through the AF4 channel and global starch elution recovery was superior to 90% (**Table III-2**). The values were calculated as follows:

$$Elution\ recovery\ (\%) = \frac{C_G \cdot C_{bf}}{C_{af}} \quad \textbf{[III-3]}$$

Where C_G is the concentration of the eluted glucans, determined by integrating the differential refractive index (DRI) signals, and C_{bf} and C_{af} are the carbohydrate concentrations before and after filtration respectively, computed using the orcinol sulfuric method (Planchot et al. 1997) (see III-2, *Determination of total sugar concentration by the orcinol-sulfuric method*). By reason of the high elution recovery rate, fractionation responses are considered as quantitative for all the samples.

The size distribution of native potato starch is characterized by a typical large peak, due to the presence of large molecules of amylopectin, and a smaller shoulder at smaller size due to amylose macromolecules (**Figure III-6**).

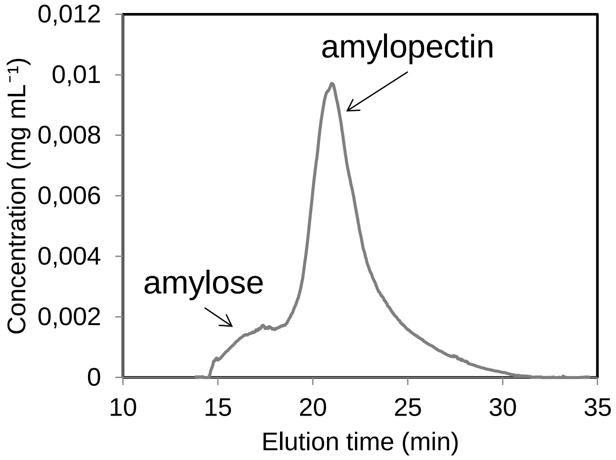

Figure III-6: *Concentration evolution over elution time for native potato starch.*

At low SME, G0_LOW and G20_LOW give a molar mass evolution over time similar to the one of native starch (**Figure III-7b**) with two separate populations of amylose and amylopectin. The typical two-peak distribution of native starch is visible as well in **Figure III-7a**, meaning that amylopectin structure is still well-preserved in G0_LOW and G20_LOW samples.

This hypothesis is confirmed by $\bar{M}_w$, $\bar{M}_n$ and $\bar{R}_{Gz}$ values observed for these samples, which are very similar to native starch values (**Table III-2**). The application of slower screw rotation (10 rpm, **Table II-3**) and the use of only the cylindrical die (**Figure II-6**) justify the slightly higher $\bar{M}_w$, $\bar{M}_n$ and $\bar{R}_{Gz}$ values observed for G0_LOW compared to G20_LOW.

The glycerol-plasticized matrix REF-CNC has been extruded using weak SME, like G20_LOW, but it has a reduced molar mass and molecular size compared to this matrix (**Table III-2**).

The more important degradation observed for REF-CNC is not generated by the difference in mechanical energy applied during extrusion (SME = 80 J g^{-1} and 100 J g^{-1} for REF-CNC and G20_LOW respectively), as reported in the literature (Li et al. 2014; Logié et al. 2018), but rather because of the higher temperature and residence time of starch in the barrel during REF-CNC extrusion (see **Table II-3**).

Table III-2: *Weight and number average molar masses ($\bar{M}_w$, $\bar{M}_n$), polydispersity ($\bar{M}_w/\bar{M}_n$), z-average radius of gyration ($\bar{R}_{G_z}$) of native starch and starch-based matrices.*

Sample	Mw^a (x 10^7 g mol^{-1})	Mn^a (x 10^7 g mol^{-1})	Mw/Mn^b	$R_{Gz}{}^c$ (nm)
NATIVE	13.5	5.3	2.5	198
G0_LOW	13.3	9.5	1.4	202
G20_LOW	11.3	7.74	1.5	188
G0_HIGH	0.8	0.4	1.7	60
G20_HIGH	1.6	0.8	2.1	76
REF-CNC	9.2	3.2	2.8	179

Computed standard deviations:
a ≤ 10%
b < 15%
c < 5%
Elution recovery > 90%

The extrusion thermomechanical treatment is not only responsible for granules melting and destructurization; indeed, mechanical energy plays a dominant role in reducing starch molecular mass and size (Li et al. 2014).

At high SME, as for G0_HIGH and G20_HIGH, the typical two-peaks distribution of native starch is lost, and a wide single peak is obtained (**Figure III-7a**), in good agreement with previous results reported in the literature (J.J.G. van Soest, Benes, et al. 1996). The loss of the double-peak distribution is mainly due to amylopectin degradation, which is more sensitive than amylose to shear, because of its larger size and its branched and less flexible structure (Logié et al. 2018; Li et al. 2014).

Amylopectin chain-splitting in these samples is confirmed by the low $\bar{M}_w$, $\bar{M}_n$ and $\bar{R}_{Gz}$ values (**Table III-2**) and by the homogeneous molar mass distribution (**Figure III-7b**). Similar size reduction due to amylopectin degradation has been observed as well by (Logié et al. 2018) in TPS extruded at 800-900 J g^{-1}.

While no differences arising from plasticization can be detected between the samples extruded at low SME, significant differences are visible between G0_HIGH and G20_HIGH. The amorphous sample G0_HIGH shows a higher reduction of $\overline{M}_w$, $\overline{M}_n$ and $\overline{R}_{Gz}$ values compared to the glycerol-plasticized G20_HIGH. The plasticization induced by glycerol renders the structure of amylopectin more flexible and less prone to split, even at this high SME. Polydispersity values ($\overline{M}_w/\ \overline{M}_n$, **Table III-2**) are low for all the extruded samples compared to native potato starch, except for REF-CNC. The high polydispersity value observed for this sample is generated by the significant difference between its $\overline{M}_n$ and $\overline{M}_w$ values. The application of higher temperatures without any additional shear may induce the melting of some of the largest macromolecules and affect $\overline{M}_n$ more importantly than $\overline{M}_w$.

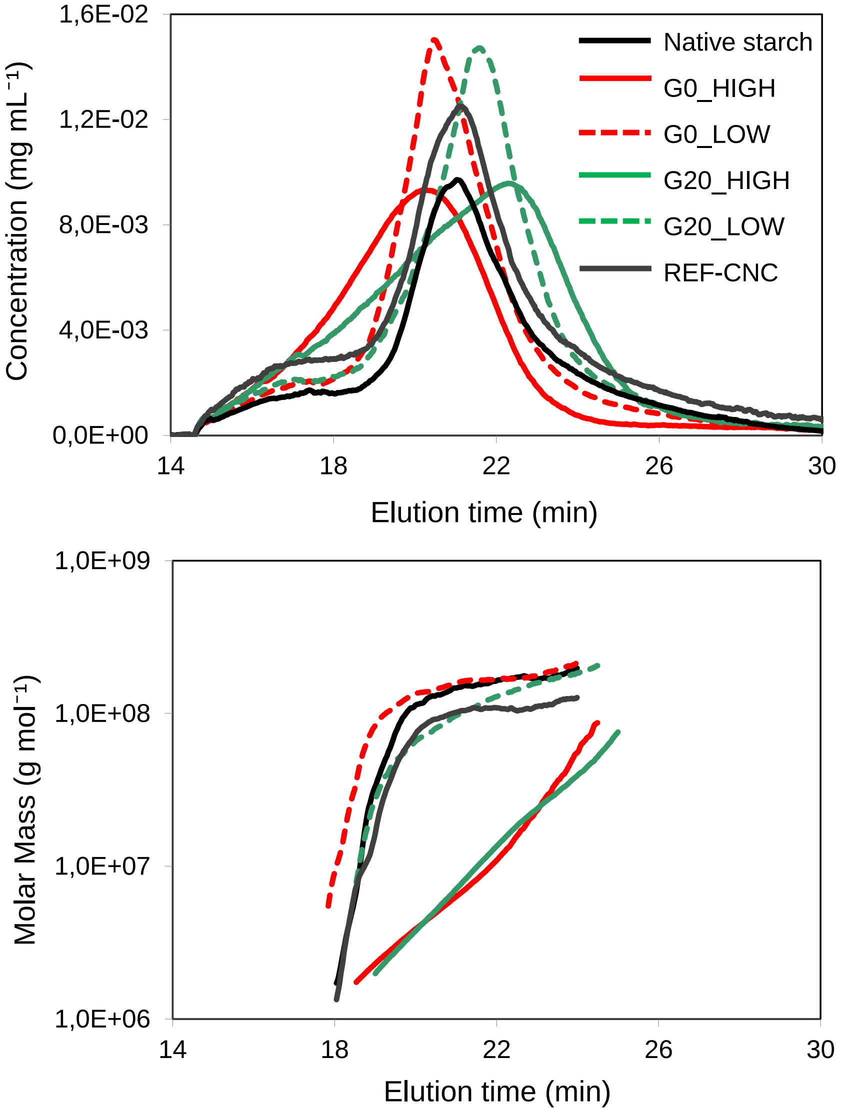

Figure III-7: a) *Concentration and* **b)** *molar mass evolution over elution time for native potato starch and extruded starch-based matrices. Differences in peaks height are due to differences in size distribution and/or in the mass injected for each sample.*

3. Effect of nanofiller addition on TPS surface state and gelatinization features

To understand the effect of CNCs addition on TPS surface state, SEM micrographs of the fracture surface of thermoplastic starch-based matrix of reference (REF-CNC, **Figure III-1**) should be compared to the ones of CNCs-starch nanocomposites (**Figure III-8**).

While CNC_1.5 and CNC_2.5 show a smooth and regular surface as in the matrix, in CNC_5 and, even more, in CNC_10 nanocomposites the surfaces are not uniform anymore (**Figure III-8**). Small voids and discontinuities are visible in the nanocomposite surfaces, coming from the increased CNC concentration. This roughness must come from the increasing proportion of cellulose nanoparticles in the sample: nanocrystals make the sample prone to roughness upon fracture. The aggregation of the nanocrystals would also worsen this roughness.

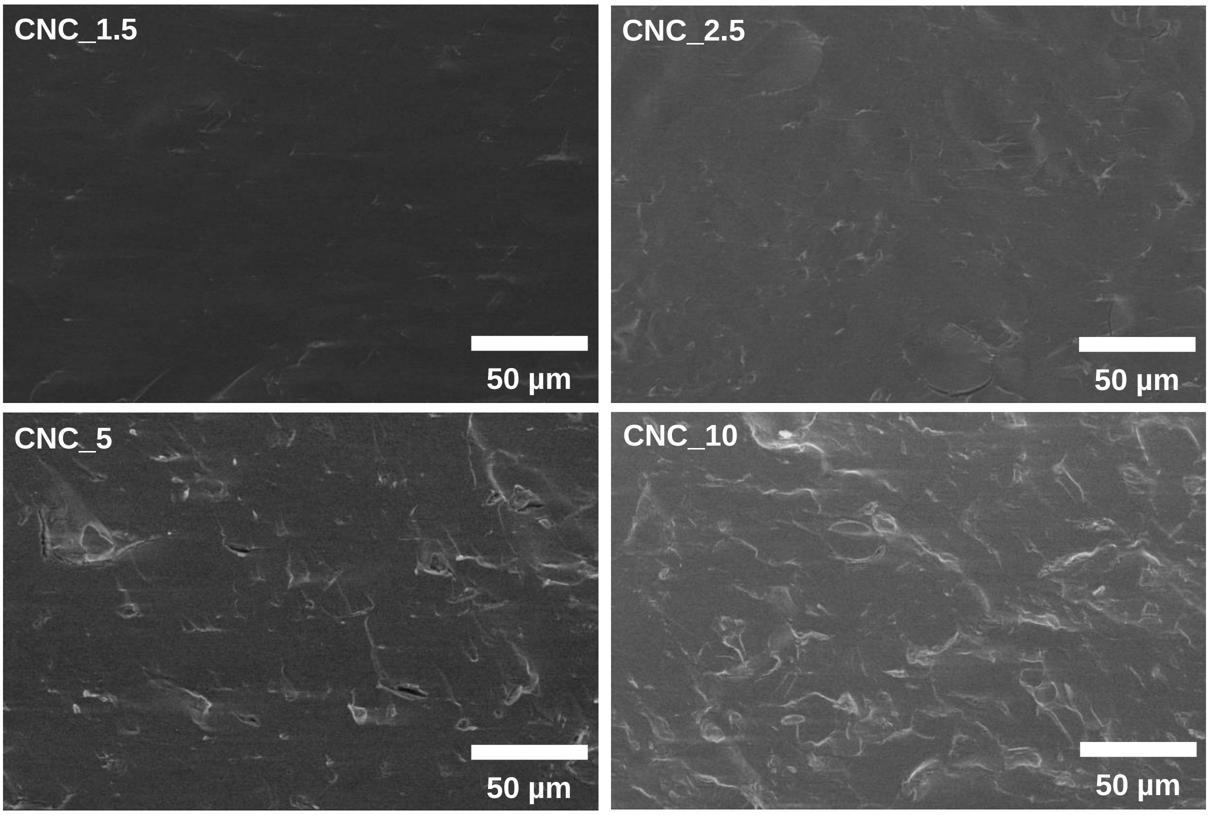

Figure III-8: *SEM micrographs of fracture surface of CNC-starch nanocomposites.*

Similarly to their matrix, no residual granules were found in CNCs-starch nanocomposites by DSC.

The fracture surfaces of starch-ChNCs nanocomposites (**Figure III-9**) are not as smooth as the low-concentrated starch-CNCs nanocomposites. Indeed, starch-ChNCs nanocomposites have been extruded using a shorter screw profile (L/D = 15.5, **Table II-3**), same as

G20_LOW, in order to partially preserve native starch structure; for this reason G20_LOW, whose micrograph is reported in **Figure III-1**, constitutes the matrix of reference for starch-ChNCs samples.

As observed for G20_LOW, the use of a shorter screw profile favored the preservation of numerous granule-shaped residuals, which render ChNC_2 nanocomposite surface uneven and irregular (**Figure III-9**).

At higher ChNCs content the surface of the materials appears even less smooth because of ChNCs increasing concentration in the samples, as shown above for starch-CNCs nanocomposites. Furthermore only few granule ghosts can be identified in the micrographs of ChNC_4 and ChNC_8 samples (**Figure III-9**), probably because of the higher temperatures used for the extrusion of these nanocomposites compared to G20_LOW and ChNC_2.

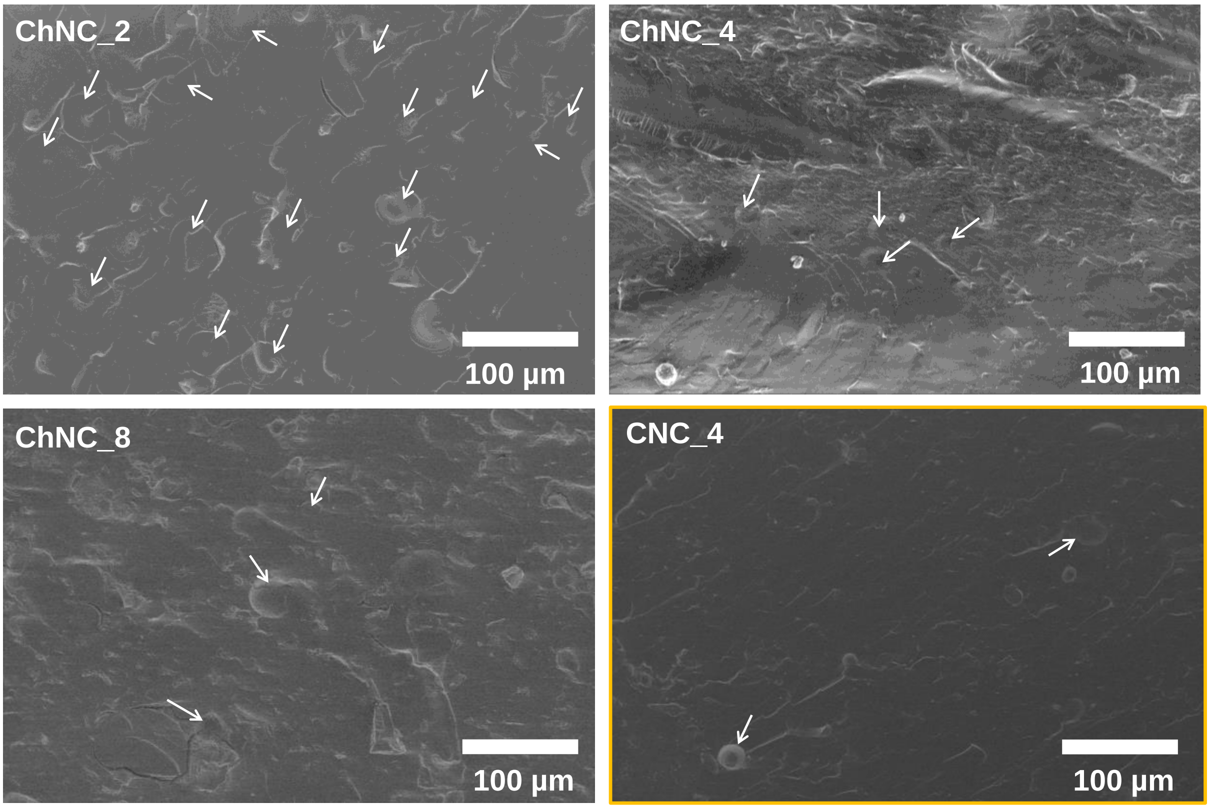

Figure III-9: *SEM micrographs of fracture surface of ChNC-starch nanocomposites. CNC_4 micrograph is reported as well (yellow outline). Granule-shaped residuals are pointed out with white arrows.*

Indeed no endothermic signal corresponding to the presence of residual granules is detected for ChNC_4 and ChNC_8 samples by DSC. It is less likely that ChNCs increasing concentration in the samples may have played a role in native granules deconstruction.

Conversely, it was possible to quantify the amount of residual granules in ChNC_2. DSC gelatinization test pointed out the presence of about 18% of residual potato starch granules in this sample (**Table III-3**). As visible in **Figure III-10**, the gelatinization temperature for this sample is higher compared to the gelatinization temperature of native starch due to the plasticization with glycerol.

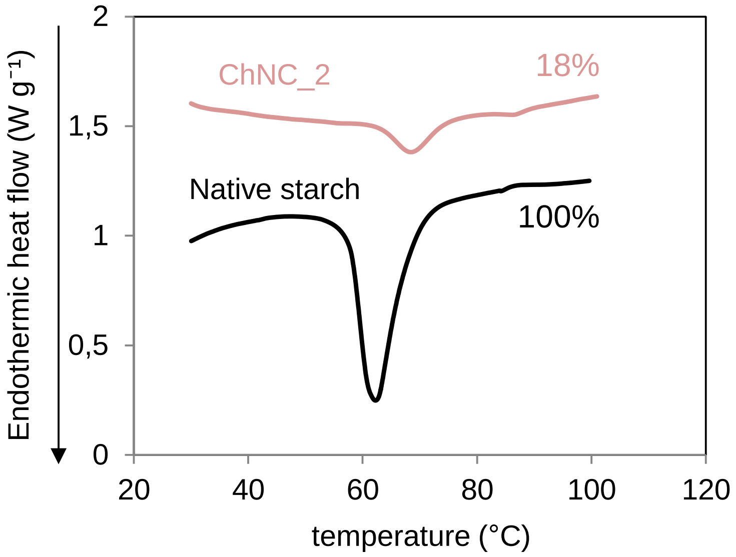

Figure III-10 *DSC thermogram of ChNC_2 compared to native potato starch.*

Table III-3: *Gelatinization enthalpy and temperature of native and ChNC_2 nanocomposite by differential scanning calorimetry in water excess.*

Sample	Gelatinization enthalpy (J g^{-1})	Residual granules (%)	Gelatinization temperature (°C)
Native starch	14.5 ± 0.5	100	62.5
ChNC_2	2.6 ± 0.1	18	68.5

As starch-CNCs and starch-ChNCs nanocomposites were extruded using different parameters, an intermediate sample, named CNC_4, was produced using starch-ChNCs extrusion parameters and by replacing ChNCs by CNCs (**Table II-3**). The aim is to decorrelate the effect of the nanofiller type (CNCs and ChNCs) from the one of the extrusion parameters.

CNCs do not seem to play a different effect on TPS fracture surface compared to ChNCs: like ChNC_4, the CNC_4 surface is not completely smooth (**Figure III-9**), and it presents some granule ghosts, but not enough to be detected by DSC.

4. Effect of CNCs on starch macromolecules during extrusion

Characteristics of starch macromolecules in nanocomposites were measured to determine if, at this small size, nanofillers play any degrading effect on starch chains during extrusion. Starch-CNCs nanocomposites fractionation responses are considered as quantitative for all the samples as the global elution recovery was superior to 90% (**Table III-4**).

Table III-4: *Weight and number average molar masses ($\overline{M}_w$, $\overline{M}_n$), polydispersity ($\overline{M}_w/\overline{M}_n$), z-average radius of gyration ($\overline{R}_{G_z}$) of starch-CNCs nanocomposites and CNCs. Values of native starch and starch-based matrix (REF-CNC) are reported for comparison.*

Sample	***Mw*** ^{a} **(x 10^7 g mol^{-1})**	***Mn*** ^{a} **(x 10^7 g mol^{-1})**	***Mw/Mn*** ^{b}	***RGz*** ^{c} **(nm)**
NATIVE	13.5	5.3	2.5	198
REF-CNC	9.2	3.2	2.8	179
CNC_1.5	7.3	5.8	1.3	142
CNC_2.5	7.7	5.5	1.4	135
CNC_5	7.9	5.1	1.6	163
CNC_10	8.3	4.8	1.7	168
CNC_4	9.3	3.4	2.9	189
CNCs	1.3	1.1	1.2	47

Computed standard deviations:
a = 15%
b < 10%
c < 5%
Elution recovery > 90%

Starch-CNCs nanocomposites show values of $\overline{M}_w$ and $\overline{R}_{G_z}$ lower than their matrix of reference REF-CNC. This could be due to the slight differences in specific mechanical energy between REF-CNC and starch-CNCs nanocomposites during extrusion (SME values, **Table II-3**), or to increased shear induced by CNCs on starch chains during extrusion. This is confirmed by the decreasing average number molar mass ($\overline{M}_n$, **Table III-4**) and increasing polydispersity values ($\overline{M}_w/\ \overline{M}_n$, **Table III-4**) observed for the nanocomposites.

$\overline{M}_w$ appears to slightly increase with the amount of CNCs present in the nanocomposite. This is probably an artefact which comes from the retention of a small quantity of CNCs in the solubilized samples, which get stuck in starch molecules during the treatment before injection and increase their apparent size.

The size distribution and the molar mass evolution over time of all starch-CNCs nanocomposites point out the preservation of two separate populations of amylose and amylopectin (**Figure III-11**), as previously observed for REF-CNC, meaning that the amylopectin structure is still well-preserved in these samples.

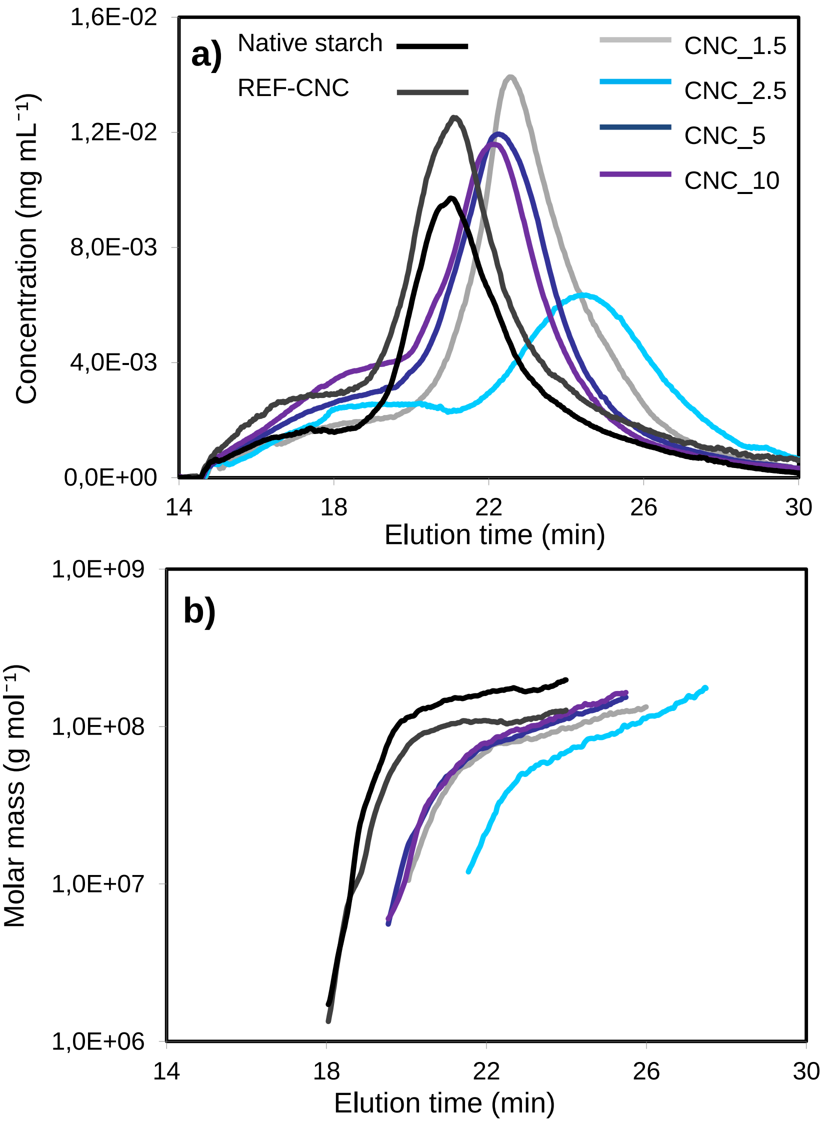

Figure III-11: a) *Concentration and* **b)** *molar mass evolution over elution time for starch-CNCs nanocomposites. Native starch and starch-based matrix REF-CNC signals are reported for comparison. Differences in peaks height are due to differences in size distribution and/or in the mass injected for each sample.*

CNC_4 macromolecules characteristics were determined to get an idea of the effect of nanocrystals on the macromolecules during extrusion with a shorter screw profile.

The concentration and molar mass evolution of this sample over time are reported in **Figure III-12**.

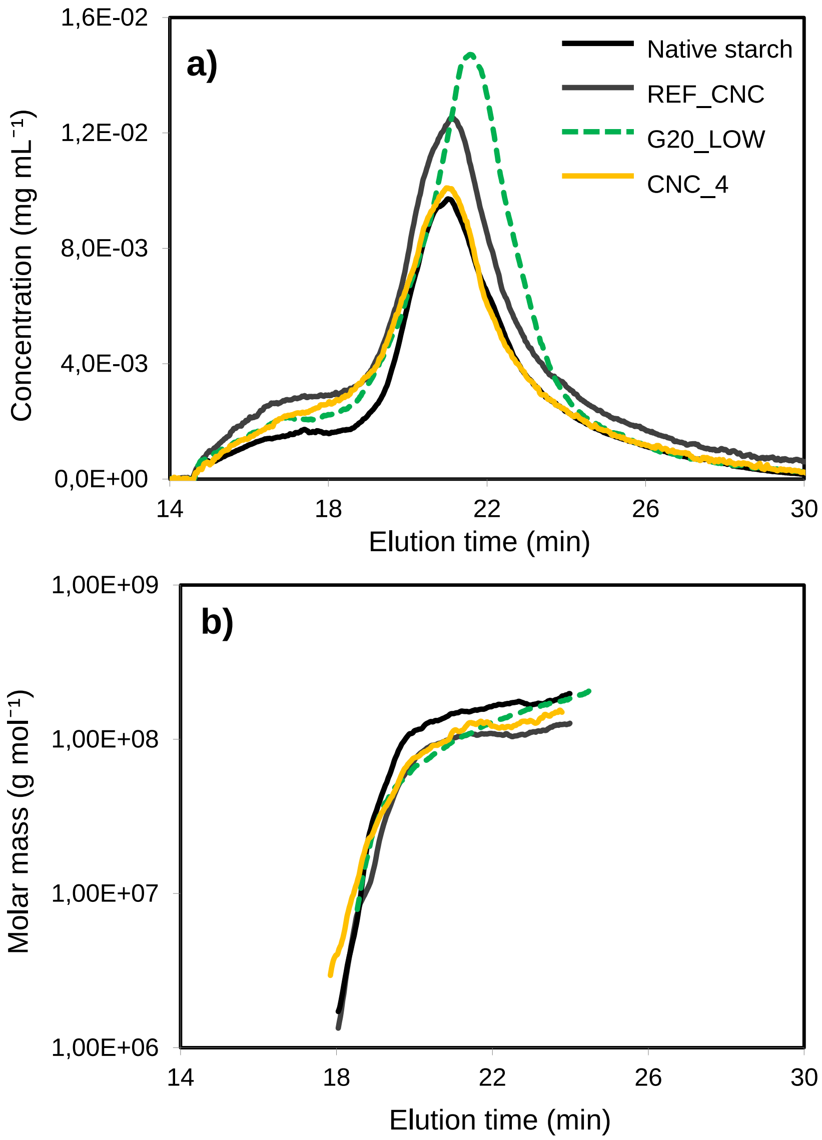

Figure III-12: a) *Concentration and* **b)** *molar mass evolution over elution time for nanocomposite CNC_4. Native starch, starch-based matrix REF-CNC and G20_LOW signals are reported for comparison. Differences in peaks height are due to differences in size distribution and/or in the mass injected for each sample.*

Because of the shorter residence time in the barrel, CNC_4 presents $\bar{M}_w$, $\bar{R}_{G_z}$, $\bar{M}_n$ and $\bar{M}_w/\ \bar{M}_n$ values intermediate between REF-CNC and G20_LOW (**Table III-4** and **Table III-2** respectively). When compared to its reference sample G20_LOW (**Table III-2**), CNC_4 presents the same radius of gyration ($\bar{R}_{Gz}$ = 188-189 nm), but lower $\bar{M}_w$ and $\bar{M}_n$ values. This

could be due, as suggested for the other starch-CNCs nanocomposites, to the higher temperatures used for its extrusion or to the shear applied by CNCs on starch chains during extrusion, rather than to differences in mechanical stress (SME = 90 J g^{-1} and 100 J g^{-1} for CNC_4 and G20_LOW respectively, **Table II-3**).
The high polydispersity value observed for CNC_4 may be generated by the application of higher temperatures without any additional shear compared to G20_LOW, as previously suggested for REF-CNC.

The characteristics of starch macromolecules in ChNCs-starch nanocomposites were trickier to determine and the obtained values were not repeatable for this type of nanocomposite. ChNCs interact differently from CNCs with the solvents used for sample preparing to injection. As a consequence, ChNCs cannot be separated from starch and they perturb its size distribution in the channel. A protocol for ChNCs-starch nanocomposites preparing for analysis by AF4 is not available nowadays, and we were not able to develop it.

5. Theoretical dispersion of nanofillers in the starch matrix

SEM and DSC provided information about the general morphology of extruded starch while AF4 was used to characterize starch macromolecules after extrusion. The results of these analyses, together with the use of theoretical models, can help us in predicting the distribution and the theoretical percolation values at different nanofiller concentration in the starch matrix.

5.1 Theoretical percolation values

Percolation values were computed for both cellulose and chitin nanocrystals. On the example of (Favier et al. 1997; Capadona et al. 2008) and the more recent work of (Moberg et al. 2017; Lourdin et al. 2016), the onset of percolation of a polymeric system containing cylindrical nanofillers is computed as follows:

$$\%\, vol\, percolation = \frac{0.7}{A} \cdot 100 \quad \textbf{[III-4]}$$

Where A is the shape factor of the nanofiller, obtained from the ratio between the average length and the width of the nanofiller. The gravimetric percolation onset is then obtained by multiplying the volumetric percolation onset by the density of the nanofiller.

CNCs and ChNCs have a variable shape factor depending on their dispersion/aggregation state. Assuming a length comprised between 50 and 250 nm, a width between 5 and 20 nm (STEM measurements, **Table II-1**) and a density of 1.6 g cm^{-3}, the CNCs studied here have a percolation ratio of 9.8 ± 1.2wt%. Similarly, assuming a length of 50-350 nm, a width of 5-20 nm (STEM measurements, **Table II-1**) and a density of 1.462 g cm^{-3}, the ChNCs analyzed in this study have percolation ratio of 7.5 ± 2.4wt%.

Given these percolation onset values, CNCs-starch and ChNCs-starch nanocomposites could start presenting a percolating behavior from 10wt% CNC content (CNC_10 sample) and 8wt% ChNCs content (ChNC_8 sample) respectively. It is important to remind that percolation would only occur at these values if the nanofillers are separately and homogeneously dispersed in the starch matrix; any aggregation would drastically reduce the contact surface with the matrix and either shift the percolation threshold to higher concentrations (in the case of small, homogeneously dispersed aggregates), or prevent any percolation from happening at all (in the case of larger aggregates and/or inhomogeneous dispersion).

5.2 Theoretical inter-particle distance

Aggregation is a key issue in nanocomposites, as it can significantly impact important properties. One key parameter to consider for predicting nanofillers aggregation is the average inter-particle distance. This distance is usually assessed experimentally by small-angle scattering or microscopy techniques. In our case, it cannot be directly measured because there is no contrast between starch matrix, CNCs and ChNCs (see III-1).

To get around this issue, we have chosen to use a theoretical model based on the stereological principle from (Luo & Koo 2008) and later adapted by (Coativy 2013). This model has been developed in a study of nanoclays dispersion by Transmission Electron Microscopy (TEM). The authors proposed a model which predicts the inter-particle distance as a function of nanoclay concentration in the matrix.

The stereological model assumes that the volume fraction of nanofillers is equivalent to their lineic fraction (d/d_0) in the matrix. The hypothesis of this model is that the nanoclays inter-particle distance (d) is higher than the nanoclay sheet thickness (d_0) and also that the sheet thickness is significantly lower than the length of the nanoclay.

The theoretical inter-particle distance is computed from the material volume fraction as follows **[III-5]**:

$$d = d_0 \cdot \frac{\frac{w_{clay}}{\rho_{clay}} + \frac{w_{matrix}}{\rho_{matrix}}}{\frac{w_{clay}}{\rho_{clay}}} \qquad \textbf{[III-5]}$$

Where w_{clay}, w_{matrix}, ρ_{clay} and ρ_{matrix} are the weight fractions and the densities of the nanoclay sheets and the polymeric matrix respectively.

Even if this model has been developed for nanoclays, which are subjected to exfoliation, it can easily be adapted also to our case of study. We propose to modify this model to consider also the water and glycerol content **[III-6]**:

$$d = d_0 \cdot \frac{\frac{w_{NFs}}{\rho_{NFs}} + \frac{w_{matrix}}{\rho_{matrix}} + \frac{w_{water}}{\rho_{water}} + \frac{w_{glycerol}}{\rho_{glycerol}}}{\frac{w_{NFs}}{\rho_{NFs}}} \qquad \textbf{[III-6]}$$

Where d_0 is the nanofiller width, w_{NFs}, w_{matrix}, w_{water}, $w_{glycerol}$, ρ_{NFs}, ρ_{matrix}, ρ_{water} and $\rho_{glycerol}$ are the weight fractions and the densities of the nanofillers, starch matrix, water and glycerol respectively.

The average theoretical inter-particle distance is drawn as a function of nanofiller content in the matrix, as reported in **Figure III-13**. Three different widths are used in the model for each type of nanofiller: 5, 12.5 and 20 nm. These are the minimum, average and maximum width values which were measured for the nanofillers (STEM measurements, **Table II-1**), the highest values being generated by the packing of multiple nanocrystals. The use of different widths allows estimating different theoretical inter-particle distances between the nanofillers depending on their packing.

To compare the inter-particle distance to the size of the macromolecules, the distance corresponding to $2 \times \overline{R}_{Gz}$ (radius of gyration of the starch macromolecules) has been reported on the same graph. The $\overline{R}_{Gz}$ values measured by AF4 on extruded starch solubilized in water were used. In this condition, water is a θ solvent of starch. In the amorphous polymer, the radius of gyration is approximated as equivalent to the radius of gyration of macromolecules in θ solution (De Gennes 1979).

Two $\overline{R}_{Gz}$ values are reported in the graph for starch-CNCs nanocomposites: the one of the matrix of reference REF-CNC and the one of CNC_2.5. They constitute the highest and the lowest $\overline{R}_{Gz}$ values measured for this type of nanocomposite respectively (**Figure III-13a**).

No $\overline{R}_{Gz}$ typical of starch-ChNCs nanocomposites could be measured by AF4 (see III-4). Therefore the $\overline{R}_{Gz}$ value of G20_LOW (starch-based matrix of reference for starch-ChNCs nanocomposites, see **Table II-3**) was used (**Figure III-13b**).

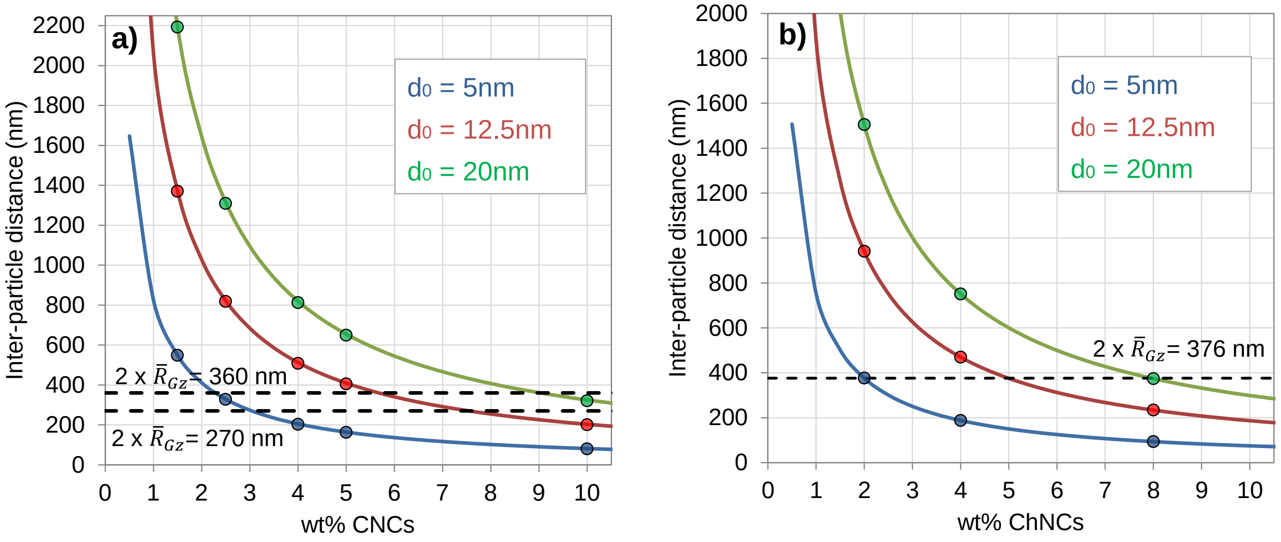

Figure III-13: *Average inter-particle distance as a function of* **a)** *CNCs and* **b)** *ChNCs content. Inter-particle distance is drawn as well as a function of nanofiller variable width.* $2 \times \overline{R}_{Gz}$ *values of REF_CNC and CNC_2.5 are reported in the first graph, while* $2 \times \overline{R}_{Gz}$ *value of G20_LOW is reported in the second.*

Figure III-13 points out that theoretically inter-particle distance can be higher or lower of starch macromolecules size ($2 \times \overline{R}_{Gz}$) depending on nanofiller concentration and width (d_0).

For each CNCs and ChNCs theoretical width, we can identify a concentration threshold, at which the average inter-particle distance is equal to starch macromolecules size. Nanofillers aggregation may occur when the theoretical inter-particle distance is lower than the starch macromolecules estimated size, because it is possible that nanofillers come in contact and interact between them rather than with starch.

- ☐ In the case of starch-CNCs nanocomposites:
  - For individual CNCs (d_0 = 5nm) (**Figure III-13a**, blue line): starting from 2.5wt% of CNCs in the starch matrix and above, the theoretical inter-particle distance is lower than the starch macromolecules average size. CNCs may aggregate in these conditions because of the reduced inter-particle distance.
  - For average-size CNCs (d_0 = 12.5nm) (**Figure III-13a**, red line): the inter-particle theoretical distance is lower than the starch macromolecules average size starting from CNCs content > 5wt%. At lower concentrations, CNCs could be well-dispersed in the starch matrix.
  - For packed CNCs (d_0 = 20nm) (**Figure III-13a**, green line): the presence of small CNCs packings induces, at equal concentration rates, an increase in the theoretical inter-particle distance. In these conditions aggregation may occur only for the most concentrated nanocomposites (CNC = 10wt%).

The same model can be applied to starch-ChNCs nanocomposites. As visible in **Figure III-13b**, average theoretical inter-particle distances are lower for starch-ChNCs nanocomposites when compared to starch-CNCs ones. For the same mass of nanofiller, ChNCs occupy a higher volume because their density (~1.462 g cm^{-3}) is slightly lower when compared to the one of CNCs (~1.6 g cm^{-3}), and this reduces the theoretical inter-particle distance between ChNCs.

- ☐ In the case of starch-ChNCs nanocomposites:
  - For individual ChNCs (d_0 = 5nm) (**Figure III-13b**, blue line): the theoretical inter-particle distance is equal to starch macromolecules size already at 2wt% ChNCs content in the nanocomposite. This means that aggregation would occur already at the lowest loadings in the case ChNCs were not associated in small packing of 2-3 nanocrystals each.

- For average-size ChNCs (d_0 = 12.5nm) (**Figure III-13b**, red line): the inter-particle distance gets near to starch macromolecules size around 5wt% ChNCs content in the nanocomposite.
- For packed ChNCs (d_0 = 20nm) (**Figure III-13b**, green line): the inter-particle distance is equal to starch macromolecules size up to 8wt% ChNCs in the nanocomposite, meaning that ChNCs may aggregate at this concentration in the nanocomposite.

Nanofillers seem to have the tendency to form small aggregates when added to starch and processed by extrusion, because of the low water content (~30wt%) in the formulation (Hietala et al. 2013), as in our case of study. These small aggregates can be homogeneously dispersed in the matrix, depending on their concentration and the parameters applied for their production.

Theoretically, it is thus more probable that, in our nanocomposites systems, nanofillers would aggregate only in the highest loaded nanocomposites, because of the larger inter-particle distance which separate the small nanofillers packings. Conversely, it is less probable that nanofillers are dispersed as single particles in the starch matrix, with lower inter-particle distance to separate them. Of course, there are a lot of other parameters which will influence the dispersion state: the processing conditions, drying, pH, temperature…and this calculation does not account for any of those.

To conclude, we have proved that the extrusion conditions importantly affect the general structure of starch-based matrices, both in presence and in absence of glycerol. Similarly, the addition of cellulose and chitin nanofillers seems to induce some structural changes as well, in particular on the surface morphology and starch chains degradation. We adapted the theoretical models on nanoparticle percolation and inter-particle distance to our case of study. This will help us in understanding the nanocomposites physical behavior.

In the next chapter the structural study will be completed with the characterization of the more local structure of the materials, and we will fully discuss the structural findings of both chapters.

Chapter IV

LOCAL STRUCTURE AND PROPERTIES AT THE DRY STATE

Table of contents

As shown in the previous chapter, extrusion parameters, glycerol addition and introduction of nanofillers have an influence on residual granules, starch chain length and samples surface roughness; it is now important to check if this influence extends to the local structure in the samples. To do this, in this chapter we provide a description of the crystalline structure of the extruded materials by X-Ray Diffraction (XRD), coupled with an in-depth analysis of starch local orders by solid state Nuclear Magnetic Resonance (NMR).

Then, to make the link between structure and properties, the thermomechanical behavior of the samples "at the dry state" (after stabilization at $a_w = 0.59$ for two weeks) is described by means of Dynamic Mechanical Thermal Analysis (DMTA) and by uniaxial deformation. These effects are then linked to the local structure, and the chapter finishes with a discussion on the complete structural characterization (Chapters III and IV) and a tentative schematic representation of their structure.

1. Crystalline and local structure of starch-based matrices

Wide Angle X-ray Scattering

The principle consists in putting a sample through a focused X-ray beam and studying the diffracted beam (**Figure IV-1**). *In a crystal, the macromolecular polymeric chains are periodically stored to form reticular (parallele) plans separated by a reticular distance* (d, **Figure IV-1**). *When a X-ray beam meets these plans, a diffraction signal is generated. This signal is characterized by a typical θ angle, which is defined as the angle between the incident and the diffracted beam* (**Figure IV-1**).

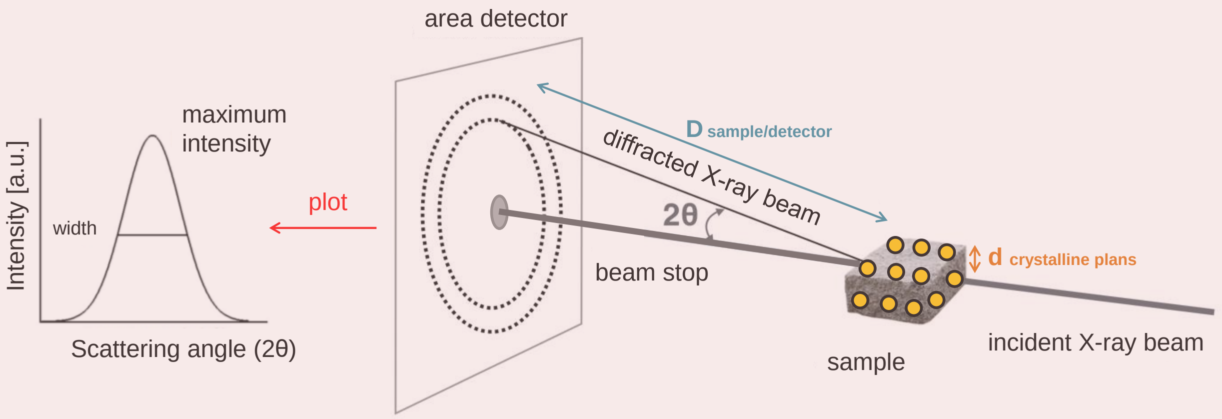

Figure IV-1: X ray diffraction setup from (Yan et al. 2018) and principle of diffraction of crystalline plans.

Using the Bragg's law **[IV-1]** *the distance between crystalline/diffracting plans can be determined from the intensity of the beam as a function of the angle θ:*

$$2\mathrm{d}\,\sin\theta = \mathrm{n}\,\lambda \quad \textbf{[IV-1]}$$

Where d *is the distance between two diffracting plans,* 2θ *the diffracted angle,* λ *the wavelenght of the incident X-ray beam and* n *(integer number) the diffraction order.*

Larger distances between two diffracted plans are detected at smaller angles, while smaller distances are observed at wider angles. For this work we used only a 2θ-range of 3 to 30° and a sample-to detector distance of 8.7 cm, corresponding to observable distances from 0.2 nm to 3 nm. A diffractogramm is obtained by plotting the scattering intensities as a function of angle 2θ originating from the material (**Figure IV-1**).

The width of diffraction peaks have been determined using Scherrer's law **[IV-2]***:*

$$L = \frac{K\,\lambda}{\Delta 2\theta\,\cos(\theta_0)} \quad \textbf{[IV-2]}$$

Where K *is a constant equal to 0.89,* λ *the wavelenght of the incident X-ray beam,* Δ2θ *the full width at half maximum and* θ_0 *the angle at peak maximum.*

A typical amorphous halo with no distinguishable peaks is obtained for desorganized materials, while crystalline samples generate diffractogramms with intensities at angles characteristic of their crystalline type (A, B, V type…).

Scattering experiments were performed with a Bruker D8 X–ray diffractometer (Karlsruhe, Germany) equipped with Vantec 500 detector operating at 40kV and 40mA. The CuKα1 radiation (λ = 0.15406 nm) was oriented using two crossed Göbel mirrors to obtain a beam of 300 or 500 µm in diameter.

Samples were stabilized for one week by vapor phase isopiestic equilibration over saturated salt solutions. Partial water vapor pressure was set to 0.75 using NaCl saturated solution at 20°C. This allows a better resolution of the diffractograms, and adjusted water content in all samples prior to analysis. Starch B-type crystalline structures are particularly sensitive to hydration content (Buléon et al. 1987); hence it is fundamental to have homogeneous hydration among the samples for the results to be comparable. Conversely, CNC and ChNC aqueous suspensions were completely dried in oven at 40°C before analysis to obtain thin films.

The recorded diffractograms I = f (2θ) were normalized to remove the influence of absorption coefficient and thickness variation among the samples and then drawn in function of the angle 2θ to obtain diffracting curves.

Cristallinity rates for all samples are obtained by simply calculating the ratio of crystalline areas over the total diffractogram area. A purely amorphous potato starch diffractogram is used as reference for the amorphous halo shape. The calculation is done on the PeakFit® software (Systat Software, Inc., US).

Starch-based matrices were analyzed by Wide Angle X-ray Scattering (WAXS) and their diffractograms are presented in **Figure IV-2**. B-type crystallinity profile is easily identified by the peaks at $2\theta = 5.6°$, 17°, 19.3° and 22.1° typical of potato starch (Sarko & Wu 1978).

The starch-based matrices present various degrees of B-type crystallinity, always at lower rates than native potato starch, and in one case no crystallinity at all (G0_HIGH).

The diffractogram of G0_HIGH is composed of an amorphous halo only (**Figure IV-2**), without any sharp peak pointing out the presence of crystalline structures. Indeed no residual granules were detected by DSC gelatinization test in this sample (see III-1). Besides, the absence of any crystallinity signifies that no recrystallization occurs during cooling, drying and storage in this sample.

Conversely, G20_HIGH presents 7 ± 3% crystallinity and typical B-type peaks are easier to detect for this sample (**Figure IV-2**), despite the SME being equal to 1900 J g^{-1}. In chapter III, we showed that glycerol induces the plasticization of starch granules during extrusion and helps in preserving some part of the native crystallinity while, simultaneously, favoring starch recrystallization during storage (Nessi et al. 2018). The crystallinity detected for G20_HIGH comes exclusively from glycerol-induced recrystallization during storage ($a_w = 0.59$, two weeks) as no residual granules were found in this sample after extrusion by DSC (see III-1). In glycerol-plasticized samples starch chains are more mobile and can reorganize easily in semicrystalline structures.

G0_LOW and G20_LOW diffractograms point out the higher crystallinity rate of these samples, because of the low SME applied during extrusion. Their crystallinity rates vary between 8 ± 3% and 17 ± 3% for G0_LOW and G20_LOW respectively. The higher crystallinity measured for G20_LOW comes from the higher quantity of native granules preserved in this sample (25% for G20_LOW and 16% for G0_LOW) and from post-process glycerol-induced starch chains recrystallization.

REF-CNC matrix is 10% less crystalline than G20_LOW (7 and 17 ± 3% B-type crystallinity respectively, **Figure IV-2**), even if SME values were slightly lower for REF-CNC (80 J g^{-1})

than for G20_LOW (100 J g^{-1}). Nevertheless, the use of a longer screw profile and higher temperatures during extrusion (see **Table II-3**) has been able to induce the partial melting of starch crystallites, and the complete loss of native starch granules in the sample (DSC results, III-1) simultaneously.

This produces a more amorphous structure, much more similar to the one of G20_HIGH (**Figure IV-2**).

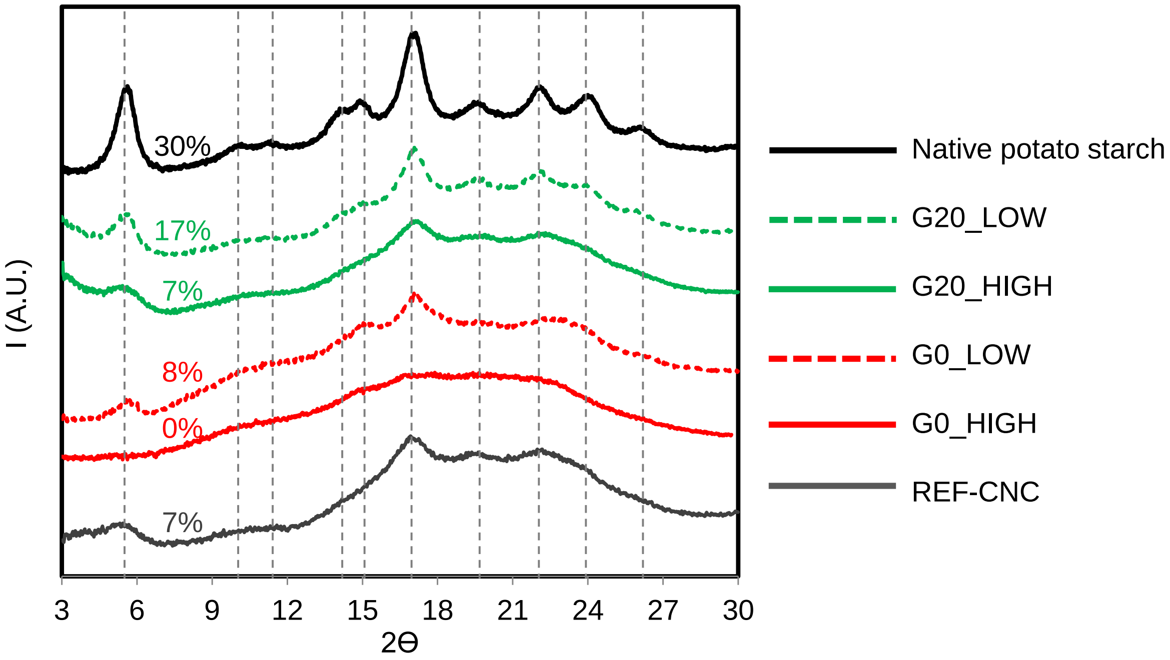

Figure IV-2: *X-ray diffractograms of non-plasticized (G0), glycerol-plasticized (G20) and REF-CNC matrices after stabilization at* a_w*=0.75. Native potato starch diffractogram after stabilization at* a_w*=0.75 is reported as reference. The differences between the spectra are highlighted with dotted grey lines.*

However, extrusion settings and glycerol do not only influence the crystalline structure, they affect local starch structures as well. Nuclear Magnetic Resonance (NMR) can be employed to characterize starch chains conformations at the smallest scale (10^{-1} nm). More in detail, NMR of ^{13}C is mainly used for studying polysaccharides, as carbon is the constitutive element of macromolecules skeleton. The use of such a precise technique allows obtaining information on processing/formulation impact on starch local structure.

^{13}C Cross-Polarization Magic-Angle-Spinning (CP-MAS) Nuclear Magnetic Resonance (NMR)

The NMR experiments were carried out on a Bruker AvanceIII-400 MHz spectrometer operating at 100.61 MHz for ^{13}*C, equipped with a double-resonance H/X CP-MAS 4-mm probe for CP-MAS solid state experiments. Cross polarization is used to enhance the signal from weakly coupled nuclei such as* ^{13}*C nuclei while high resolution conditions in solids are obtained by spinning the sample very rapidly at the magic angle (54.74° with respect to the direction of the magnetic field).*

100 mg of extruded sample were cut in small pieces and their water content was stabilized as done for WAXS experiments (see IV-1, Wide Angle X-ray Scattering). The samples were spun at 9000 Hz at room temperature; CP-MAS spectra were acquired with a contact time of 1.5ms and over accumulation of 5120 scans. The carbonyl carbon was set to 176.03 ppm through external glycin calibration. NMR spectra deconvolution was performed using the PeakFit® software (Systat Software, Inc., US). Peak chemical shift and relative contribution were assigned according to the method described by Paris et al. (Paris et al. 1999; Tang et al. 2000) on processed potato starch.

Figure IV-3 *reports the region of interest of the* ^{13}*C CP-MAS spectra for an amorphous extruded starch, from 50 to 110 ppm. As labelled in* **Figure IV-3**, *the attributions are 92-108 ppm for C1 resonances, 58-65 ppm for C6, 83 ppm for C4 and the 69-78 ppm range for C2, C3 and C5 overlapping signals (Paris et al. 2001).*

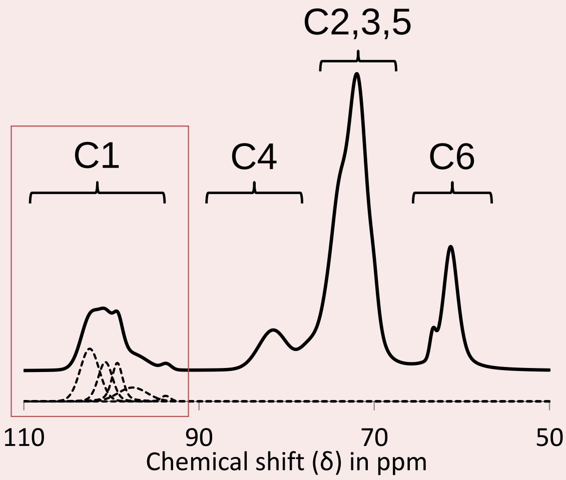

Figure IV-3: ^{13}C CP-MAS NMR full spectra of amorphous extruded potato starch adapted from (Chevigny et al. 2016) with the corresponding deconvolutions of C1 regions.

C1 region is particularly interesting for starch-based samples because it gives information about starch chains local conformations. For this reason C1 deconvolution is explained separately.

Chemical shifts in C1 region of ^{13}C CP-MAS NMR spectra

As visible in **Figure IV-4***, the amplitude of conformational angles ϕ and ψ at the α-1,4 linkage determines the conformation of the glucose chain. The C1 is the most affected by the amplitude of these angles, which determine the major chemical shifts assigned to the C1 region. Hence, the different isotropic chemical shifts of C1 can be attributed to different conformations of glucose molecules at the α-1,4 linkage.*

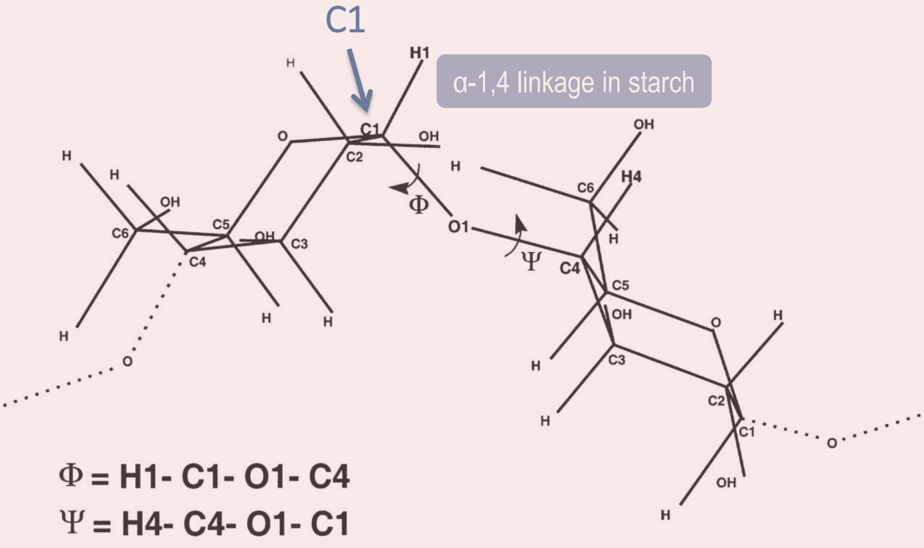

Figure IV-4: α-1,4 linkage in starch with atomic labelling and (ϕ, ψ) dihedral angles definition (Paris et al. 2001).

In starchy substrates, four to five α-1,4 linkage conformations of starch chains can be identified. These are distributed around a most probable value of (ϕ, ψ) and are represented in gaussian lineshapes. **Figure IV-5** *shows an example of spectral decomposition for extruded potato starch; each peak is characterized by a chemical shift value corresponding to an average well-defined angular starch chain conformation. Angular conformations identified by decreasing chemical shifts point out the presence of more constrained structures, such as in energically less-favored conformations* (**Figure IV-5**).

The works of Gidley and Bociek (Gidley & Bociek 1988) and the more recent work of Paris (Paris 2000) laid the foundations for a deep understanding of chemical shifts conformational attributions (labelled alphabetically from low to high field) in native and processed starch. More in detail, A *peak (whose chemical shift is in the range 102.1–102.7 ppm) is attributed to energically-favored/relaxed conformations, similar to single helices in Va-type structures of amorphous starch. Typically,* A *peak has the most intense relative intensity of about 40%.*

B *(100.0-100.9 ppm) and* C *(98.9-99.3 ppm) peaks appear in the range of double-helical conformations and have been associated to crystalline structures or paracrystalline bundles in amorphous samples. A doublet (highlighted with a red dotted line in* **Figure IV-5***) typical of B-type crystallinity (Yu et al. 2013), forms at high* B *and* C *relative abundance around 100 ppm, indicating the presence of crystalline structures. However, even in the presence of a doublet, paracrystalline and crystalline contributions cannot be quantified separately with this technique. Even in amorphous samples,* B *and* C *peaks constitute a non-negligible part of starch chains conformations (*B *and* C *coupled relative intensities = 25-35%).*

Finally, D *(96.7-97.7 ppm) and* E *(93.7-93.8 ppm) peaks are more difficult to associate with one given conformation.* D *has been observed as an exotic case of twisted glycosidic linkage in crystalline α-cyclodextrins; it was also suggested that* D *attributions are typical of conformations in the proximity of branching points, as at the α-1,6 linkage, which are responsible for their less-relaxed assignation (Paris et al. 2001).*

E *is the peak with the weakest intensity and it is related to an energically less favorable conformation (Furó et al. 1987), such as constrained linkages, favored by drastic methods of preparation (such as freeze-drying) which give less time to starch chains to relax.* E *contributions are found in native starch as well, in this case being formed during starch granule biosynthesis. In the case of processed samples, constrained/unfavorable conformations (*D *and* E *peaks) are generated by the extrusion process.*

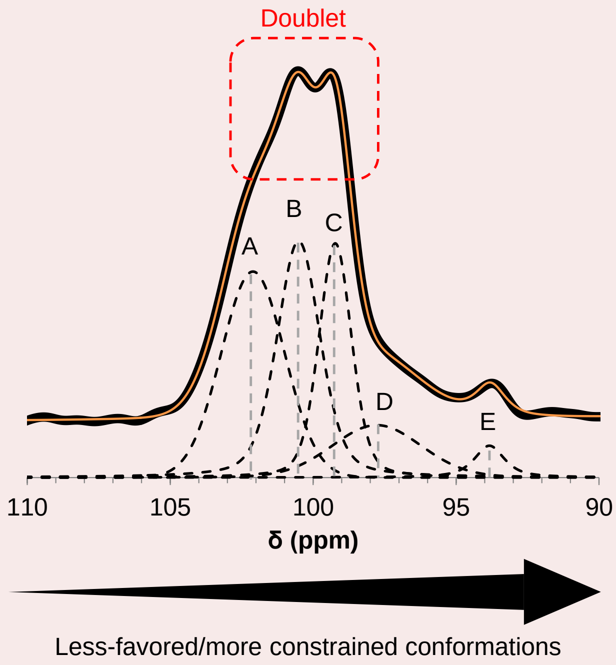

Figure IV-5: Example of C1 region deconvolution in extruded potato starch. Measurements are in black, peak deconvolution (with peak assignment) in dotted black lines, and simulated curves in color.

To make clearer the interpretation of the results reported in this chapter, **Table IV-1** *reports numerical values for peaks decomposition and the conformations attributed to each peak.*

Table IV-1: C1-region peaks obtained after deconvolution; chemical shift (δ) and conformations attributed to each peak are reported.

Peak	δ (ppm)	Attribution
A	102.1-102.7	V-type single helices in amorphous starch
B	100-100.9	Double helical conformations Paracrystalline bundles
C	98.9-99.3	
D	96.7-97.7	Twisted linkages in unfavorable conformations
E	93.7-93.8	Constrained/unfavorable conformations

Differences in the local organization of extruded starches can be detected through the study of the C1 region of their NMR spectra (**Figure IV-6**).

Before analyzing the spectral decompositions (**Table IV-2**), we can notice from **Figure IV-6** that G0 samples appear amorphous, as expected from the WAXS results. In G0 samples (G0_LOW and G0_HIGH), the A peak, typically associated to more amorphous conformations (see **Table IV-1**), represents the most abundant component (from 38.9 to 49.3%, **Table IV-2**).

Conversely, crystalline and paracrystalline conformations, represented by B and C peaks, represent the most abundant component in G20 samples (G20_LOW and G20_HIGH, from 45.8 to 49.6%, **Table IV-2**).

When the sample is partially crystalline (B-type), a doublet can be seen around 101-99 ppm (for details see the experimental set up above, **Figure IV-5**). This doublet is clearly visible in G20_LOW spectrum (**Figure IV-6**), confirming the higher crystallinity of this sample, as already pointed out by WAXS results.

For all types of matrices, the use of lower SME (100 J g^{-1}) and temperature (max 90°C) during extrusion, induce a higher amount of “ordered” conformations (B and C). This comes from the preservation of native double helical structures of amylopectin in G0_LOW and G20_LOW samples (see DSC results, III-1).

Energically less favorable (D peak) and even more constrained (E peak) conformations are higher for G0 samples (from 22.4 to 25.0%, **Table IV-2**) than for G20 ones (from 16.9 to 19.9%, **Table IV-2**) because glycerol increases the mobility of starch chains during extrusion, favoring their relaxation. This result is in agreement with a previous study which proved that constrained conformations are almost non-existents in glycerol-plasticized starch processed by extrusion (Nessi et al. 2018).

The fundamental role of glycerol in starch chains reorganization after extrusion can be highlighted by comparing G20_HIGH and G0_LOW spectral deconvolutions (**Table IV-2**): even if G0_LOW is as crystalline as G20_HIGH (see WAXS results, **Figure IV-2**) and it has been extruded at significantly lower SME (see **Table II-3**), G20_HIGH presents a local structure with higher paracrystalline conformations.

It is interesting to notice that G20_HIGH presents a slightly higher paracrystalline conformations proportion, even when compared to REF-CNC (**Table IV-2**), although REF-CNC was extruded at lower SME and with the same amount of glycerol (see **Table II-3**). This might be explained by the smaller size of starch macromolecules in G20_HIGH matrix (see AF4 results, III-2), which would reorganize easier in the sample during storage. The hypothesis of starch chains higher mobility in G20_HIGH compared to REF-CNC is confirmed by the lower amount of constrained conformation (D peak contribution = 17.5% in REF-CNC and 12.4% in G20_HIGH) observed for this sample.

Table IV-2: *Results of ^{13}C CP-MAS NMR deconvolution fits of the C1 region for starch-based matrices. Chemical shift (δ) and peak normalized contribution are reported for each sample. Differences above 3% in peak normalized area are considered as significant.*

	Peak assignment					
	A	B	C	D	E	
G0_LOW	102.7	100.9	99.1	96.7	93.8	**δ (ppm)**
G20_LOW	102.3	100.6	99.3	97.7	93.7	
G0_HIGH	102.7	100.6	98.9	96.8	93.8	
G20_HIGH	102.4	100.6	99.2	97.6	93.9	
REF-CNC	102.3	100.6	99.3	97.6	93.8	
G0_LOW	38.9	21.3	17.5	18.9	3.5	**Normalized area (%)**
G20_LOW	33.5	25.6	24.0	14.4	2.5	
G0_HIGH	49.3	16.9	8.9	19.2	5.8	
G20_HIGH	39.2	24.6	21.2	12.4	2.6	
REF-CNC	44.2	17.4	18.5	17.5	2.4	

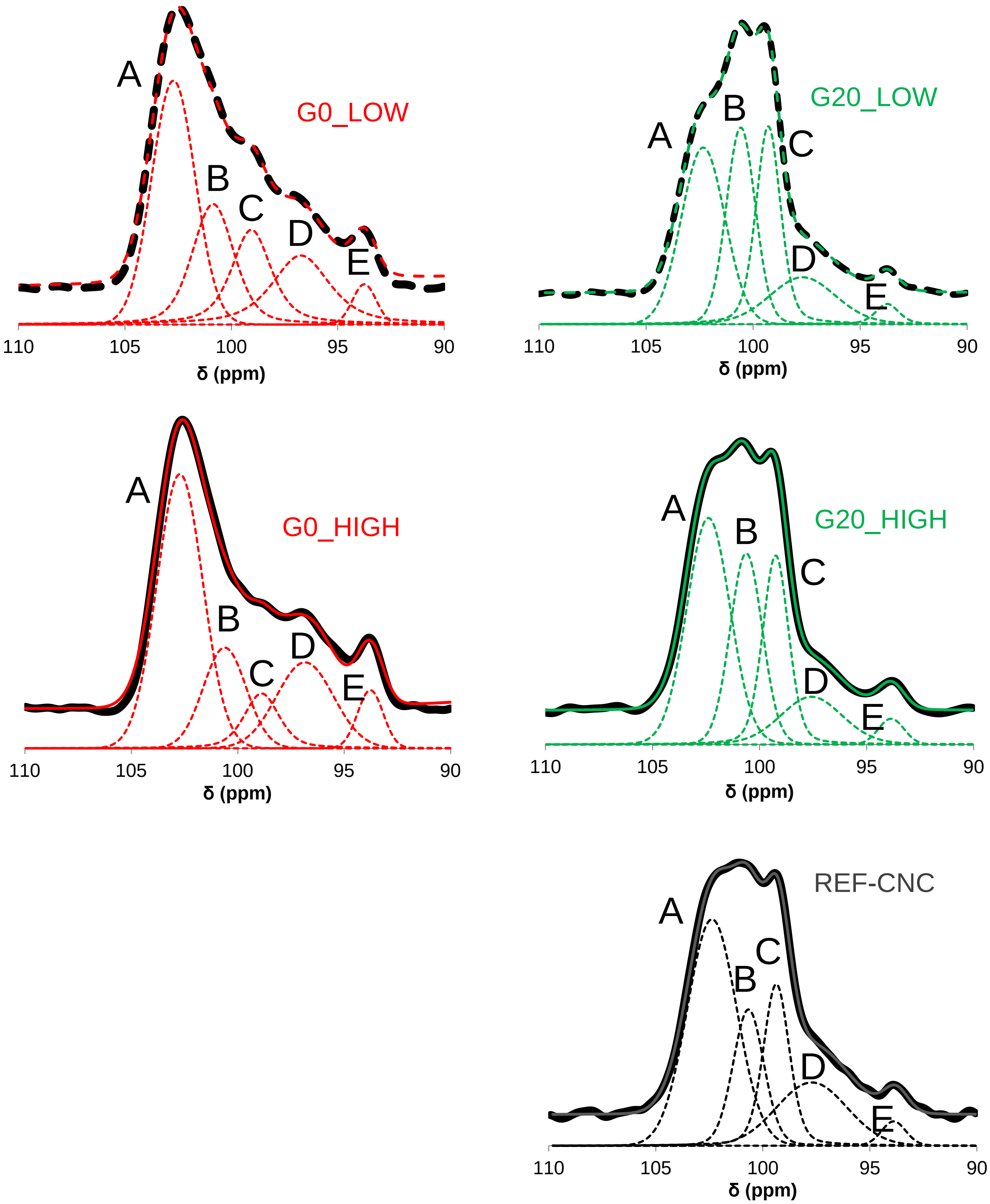

Figure IV-6: *Focus on C1 region of* ^{13}*C CP-MAS NMR spectra for extruded starch-based matrices. Each spectrum reports measured values (black line), computed values (color line) and peaks deconvolutions (dotted color line).*

2. Crystalline and local structure in the nanocomposites

XRD and NMR characterization were performed on nanocomposites to determine the effect of CNCs and ChNCs on the crystalline and local structure of thermoplastic starch.

2.1 Cellulose nanocrystals-starch nanocomposites

In starch-CNCs nanocomposites, crystallinity comes from both starch and CNCs contributions.

Between $3° < 2\theta < 30°$, CNCs present the most intense diffracting peaks at $2\theta = 20.5°$, 22.5° and 28.5° (**Figure IV-7b**). CNCs peaks at $2\theta = 20.5°$, 22.5° comes from both cellulose I and II (see II-1.3) and are very close to the starch ones (**Figure IV-7a**), making it impossible to precisely differentiate starch and CNCs crystallinity in the nanocomposites. Two major drawbacks made it impossible: first, the resolution was too low and baselines were too wildly different from one sample to another to make any quantification significant; and second, the pure cellulose peak around 29° is fairly low already in pure cellulose and invisible even in the highest-loaded starch-CNCs nanocomposite, and without it, it was not really possible to determine the diffraction pattern generated by starch independently from cellulose. For these reasons no separate deconvolutions were developed in order to avoid misleading results.

As it can be seen in **Figure IV-7a**, all nanocomposites diffractograms are similar to the one of their matrix of reference REF-CNC and present the characteristic peaks of B-type crystallinity. Similarly to REF-CNC, this stems from storage-induced recrystallization, as no residual granules were detected in the nanocomposites (see DSC results, III-3). Besides, XRD patterns vary depending on the amount of CNCs in the sample. As expected, peaks at 20° and 22° are higher in nanocomposites with high CNC content due to the overlapping of starch and cellulose peaks. This result is particularly striking for CNC_10 sample (**Figure IV-7a**). Indeed, the crystallinity rates measured for the nanocomposites gradually increase with CNCs concentration, from 10 ± 3% in CNC_1.5 to 13 ± 3% in CNC_10, because of the crystalline contribution of CNCs.

To confirm this hypothesis, the theoretical extra crystallinity added by the sole CNCs presence have been computed by multiplying the volume content of nanofillers in the sample by the crystallinity rate of pure CNCs (35%, **Figure IV-7b**): this was equal to 0.2% for CNC_1.5, 0.3% for CNC_2.5, 0.9% and 1.3% for CNC_5 and CNC_10 respectively.

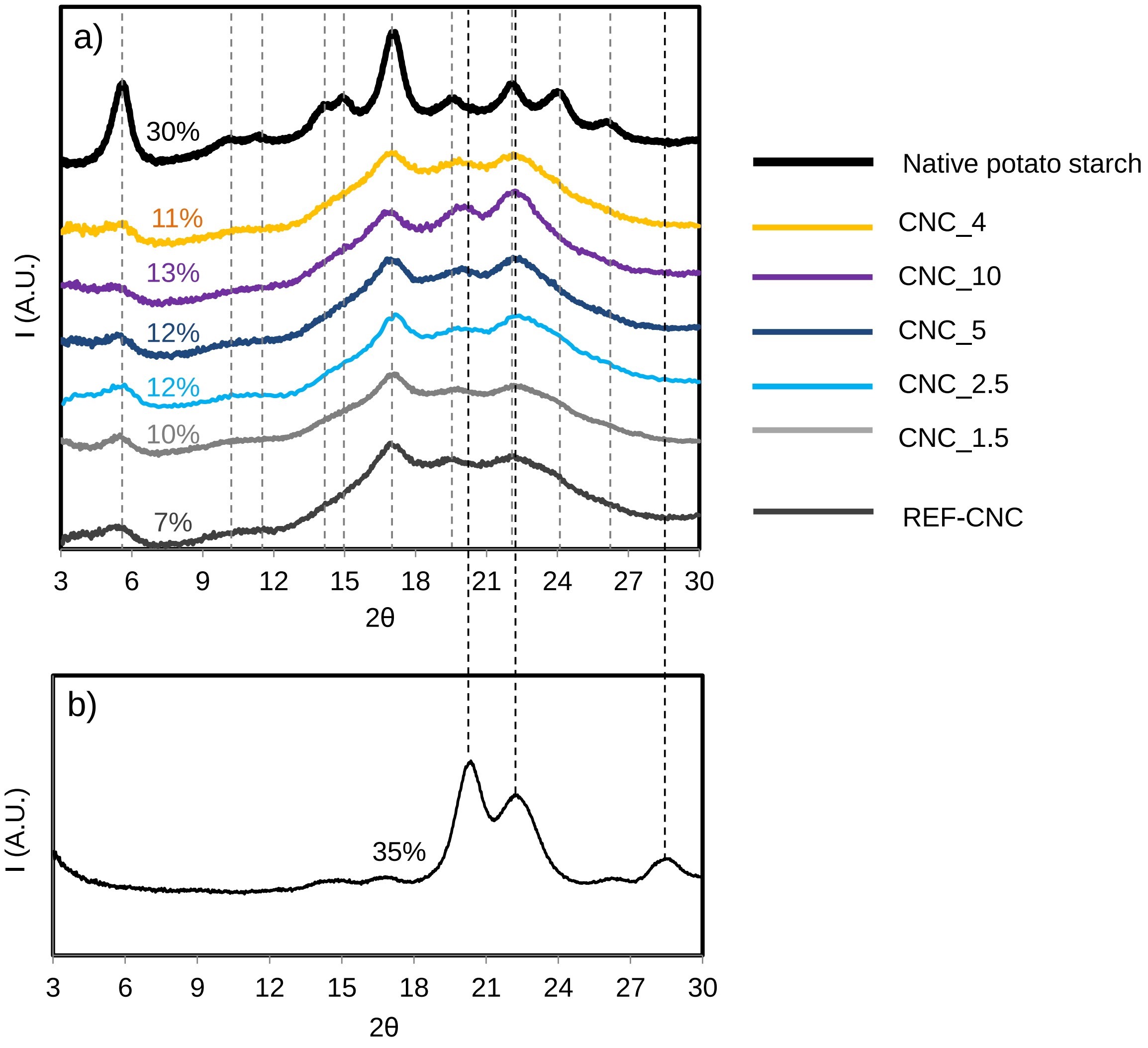

Figure IV-7: *X-ray diffractograms of* **a)** *starch-CNC nanocomposites after stabilization at* a_w*=0.75 and* **b)** *of CNC after drying in oven at 40°C. Native potato starch and REF-CNC diffractograms after stabilization at* a_w*=0.75 are reported for comparison. Differences between native starch and nanocomposites diffractograms are highlighted with dotted grey lines while differences arising from CNC content in the sample are highlighted by black dotted lines.*

Even if WAXS could not elucidate the effect of CNCs on the crystalline structure of starch, NMR analysis revealed useful to obtain multiple information about the effect of CNCs on starch local orders (10^{-1} nm).

The regions of interest (50-110 ppm) of the ^{13}C CP-MAS spectra for the reference sample REF-CNC and CNC_10 nanocomposite are reported in **Figure IV-8a** while ^{13}C CP-MAS spectra for CNCs is reported in **Figure IV-8b**.

CNCs present high-intensity peaks between 60 and 68 ppm (C6), 70 and 78 ppm (C2, C3 and C5), 82 and 90 ppm (C4) and between 103 and 107 ppm (C1). CNCs spectrum presents multiple peaks due to the presence of both cellulose I (CI) and cellulose II (CII) in the nanocrystals (see II-1.3).

The differences visible in **Figure IV-8a** between REF-CNC and CNC_10 spectra (highlighted by the dotted lines) are generated by cellulose nanocrystals in the nanocomposite. In CNC_10, new peaks appear at 65 ppm (C6), 87-89 ppm (C4) and at 105-107 ppm (C1).

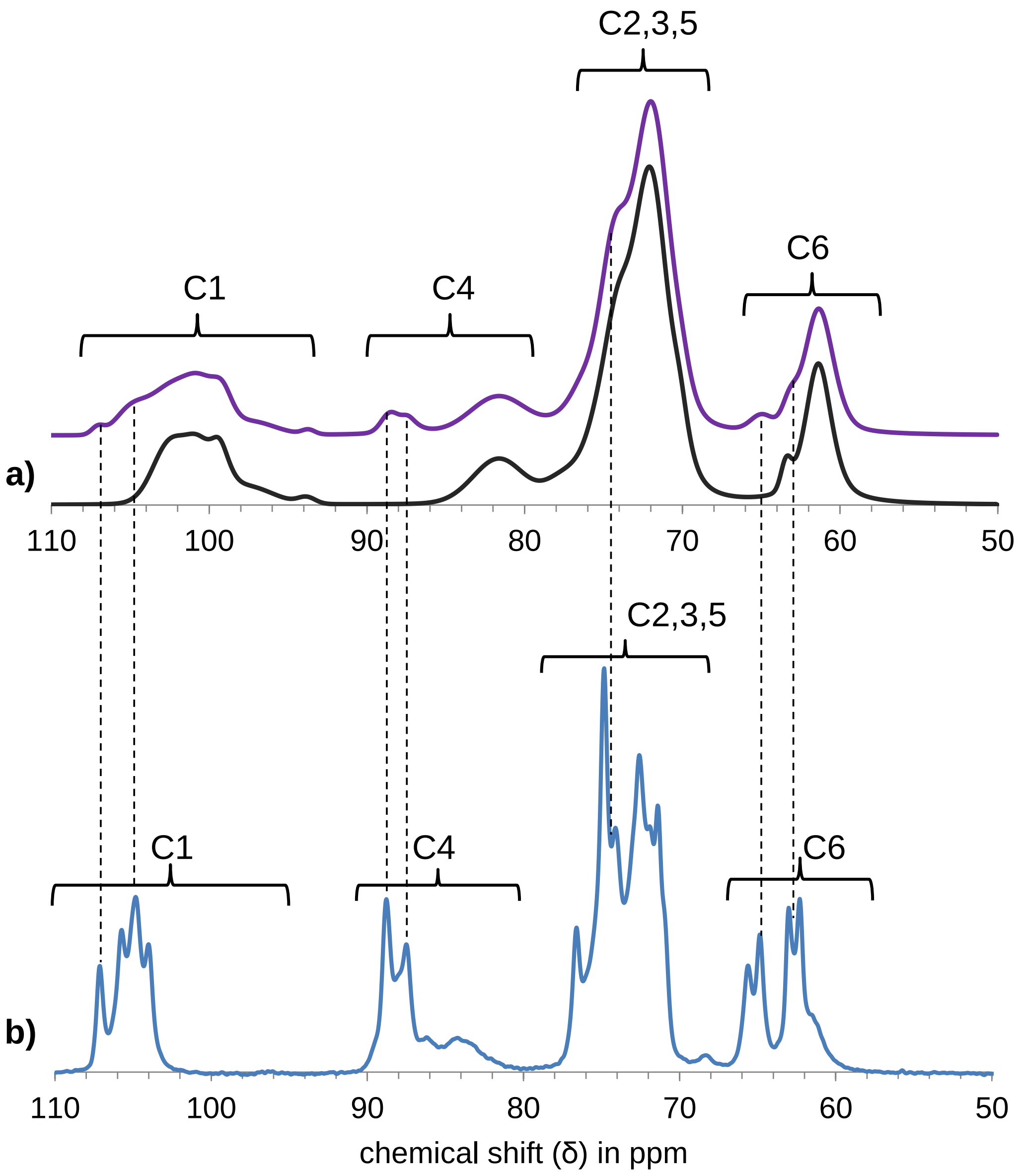

Figure IV-8: *^{13}C CP-MAS NMR spectra of* **a)** *starch-based matrix REF-CNC (black) and CNC_10 (purple). Differences in spectra are highlighted by dotted lines.* **b)** *^{13}C CP-MAS NMR spectra of CNCs.*

The two peaks identified at 105 and 107 ppm in the C1 region of CNC_10 are generated by the two forms of cellulose (CI and CII) in the CNCs, as reported by Kono and Numata (Kono & Numata 2004) (**Figure IV-8b**).

As shown in **Figure IV-9**, this cellulose doublet is detected in the C1 region of the nanocomposites already from 1.5wt% CNC content in the sample, and its surface increases with nanocrystals concentration.

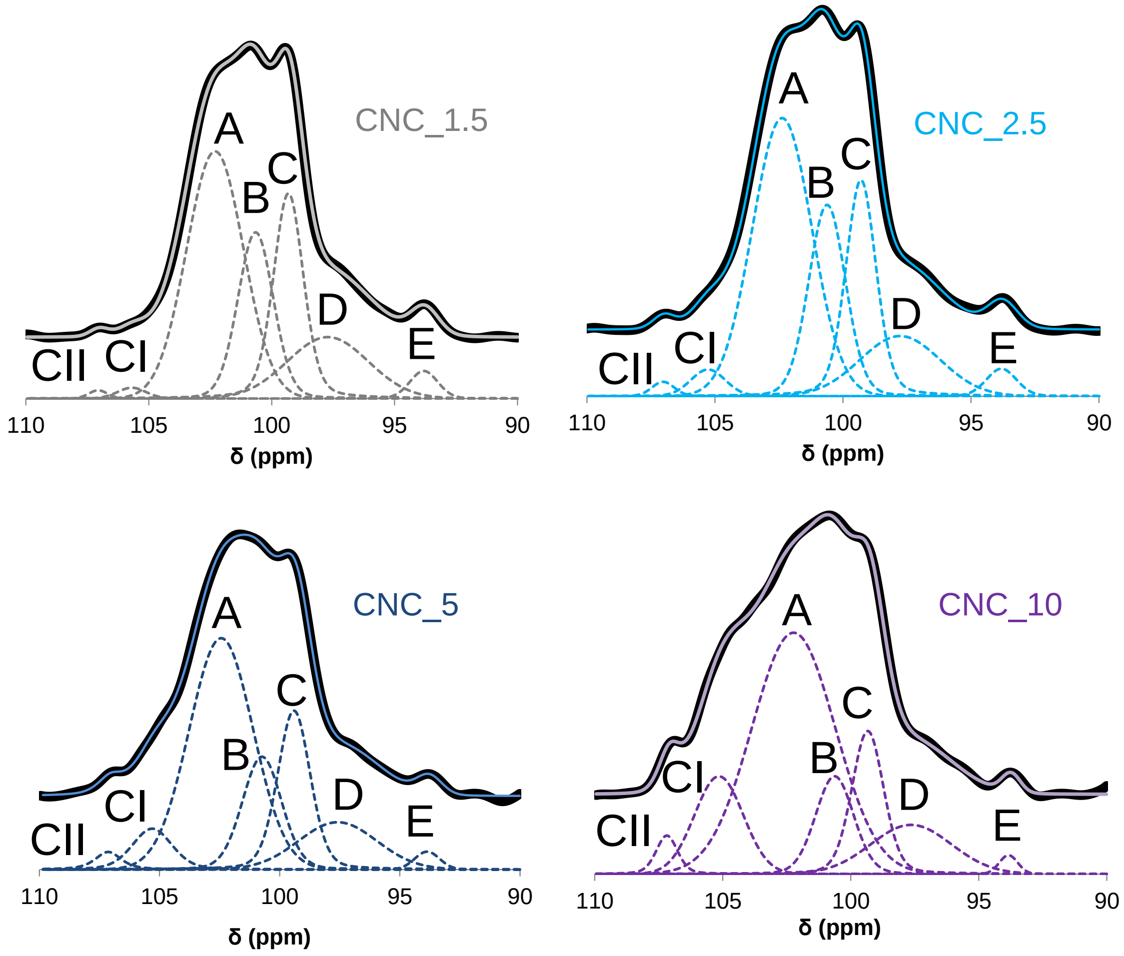

Figure IV-9: *Focus on C1 region of starch-CNCs nanocomposites. Each spectrum reports measured values (black line), computed values (color line) and peaks deconvolutions (dotted color line).*

In order to understand the role of CNCs in the nanocomposites local organization, we focused on the analysis of C1 region (**Figure IV-9**). In addition to cellulose residues at 105-107 ppm, five different conformations (from A to E) can be identified for starch (see **Table IV-1** for details).

The area percent of each peak was computed to allow a better interpretation of conformational changes (**Table IV-3**).

As visible from the contributions normalized on starch (computed by removing normalized area contributions of CI and CII from the total surface of the spectrum, **Table IV-3**), the two forms of cellulose constitute a non-negligible part of CNC_5 and CNC_10 samples and they affect starch chains local order. It appears that CNC concentration at 5wt% and above favors simple-helices/amorphous conformations (A peak from 43-45% in CNC_1.5 and CNC_2.5 to 51-60% in CNC_5 and CNC_10, **Table IV-3**) while reducing double-helical/paracrystalline structures (B and C peaks contribution from 40% to 35-27%, **Table IV-3**).

Below this concentration, no effect is visible at this scale, and samples at 1.5 and 2.5wt% CNC concentration show the doublet (B and C peaks) of B-type crystallinity (**Figure IV-9**).

D and E peaks seem not to be influenced by the addition of CNCs in the starch matrix whatever the amount.

Table IV-3: *Results of ^{13}C CP-MAS NMR deconvolution fits of the C1 region for starch-CNCs nanocomposites. REF-CNC deconvolution fits are reported for comparison. Chemical shift (δ) and peak normalized contribution are reported for each sample. Cellulose estimated amount (CI and CII) and starch chains contributions based only on starch spectra are added for nanocomposites. Differences above 3% in peak normalized area are considered as significant.*

	Peak assignment							
	CII	**CI**	**A**	**B**	**C**	**D**	**E**	
REF_CNC			102.3	100.6	99.3	97.6	93.8	**δ (ppm)**
CNC_1.5	107.0	105.6	102.3	100.6	99.3	97.7	93.8	
CNC_2.5	107.0	105.2	102.3	100.6	99.3	97.7	93.8	
CNC_4	106.9	105.2	102.5	100.6	99.3	97.7	93.8	
CNC_5	107.0	105.2	102.3	100.6	99.3	97.5	93.8	
CNC_10	107.1	105.1	102.1	100.5	99.2	97.5	93.7	
REF_CNC			44.2	17.4	18.5	17.5	2.4	**Normalized area (%)**
CNC_1.5	0.5	1.0	42.1	18.5	20.6	14.9	2.4	
CNC_2.5	0.9	2.5	43.3	19.3	19.0	12.7	2.3	
CNC_4	1.4	5.1	47.7	16.4	15.6	12.2	1.6	
CNC_5	1.8	5.7	46.7	14.8	17.9	11.7	1.4	
CNC_10	2.4	12.2	51.7	9.9	12.7	10.1	0.9	
CNC_1.5			43	19	21	15	2	**Normalized area on starch (%)**
CNC_2.5			45	20	20	13	2	
CNC_4			51	17	17	13	2	
CNC_5			51	16	19	13	1	
CNC_10			60	12	15	12	1	

To get an estimation of CNC amount in the samples, NMR spectra were fitted with the peaks of starch and the unfitted remaining surface at 105-107 ppm was filled out with the peaks associated to the two allomorphs of cellulose (CI and CII respectively).

As visible in **Table IV-3**, deconvolution fits gave an estimated CNCs amount (CI + CII normalized area) in the nanocomposites close to the theoretical one. This validates the method used for deconvolution.

2.2 Chitin nanocrystals-starch nanocomposites

As for starch-CNCs nanocomposites, in starch-ChNCs nanocomposites crystallinity comes from both starch and ChNCs contributions.

On pure ChNCs, the most intense crystalline diffraction peaks are observed for $3° < 2θ < 30°$. More precisely peaks are identified at $2θ$ = 9.4°, 12.8°, 17.8°, 19.4°, 22.5° and 26.6° (Goodrich & Winter 2007) (**Figure IV-10b**).

The theoretical crystallinity coming from the sole ChNCs presence has been computed as done before for CNCs: this was equal to 0.3% for ChNC_2, 0.7% for ChNC_4 and 1.4% for ChNC_8.

ChNCs crystalline contribution is really light and not visible in ChNC_2. In this sample, the diffractogram is very resolute (**Figure IV-10a**) and it shows a crystallinity rate very similar to the one of the matrix of reference G20_LOW (18 ± 3% and 17 ± 3% respectively). Indeed, native granules were found in both the matrix and the nanocomposite at a rate of 25% and 18% respectively (see DSC results, III-1 and III-3), confirming the presence of native crystallinity in this nanocomposite.

At higher ChNC concentration, diffracting peaks associated with B-type crystallinity lose resolution (ChNC_4, **Figure IV-10a**) and crystallinity decreases from 17 ± 3% to 11 ± 3%. This loss in crystallinity is not attributed to the degrading effect of ChNCs, but rather to the higher temperatures employed for its extrusion (**Table II-3**), which may have induced the melting of the native crystallites. Indeed, no native granules were detected by DSC in ChNC_4, meaning that the crystallinity of this sample comes from storage-induced recrystallization favored by glycerol only.

While chitin peaks are not visible at lower nanofiller content, in ChNC_8 peaks clearly appear in the diffractogram, because of the superposition of starch and ChNCs crystalline contributions. This almost complete superposition of ChNCs and starch peaks makes it tricky to precisely differentiate starch and ChNCs crystallinity in the nanocomposite. ChNC_8 shows high resolute peaks at $2θ$ = 9.4°, 17.8°, 19.4° and 26.6° and a slightly less resolute peak at $2θ$ = 12.8°, coming from ChNCs crystalline structure. As a result the crystalline rate of this sample is of 15 ± 3%.

As done in chapter III, the nanocomposite CNC_4 (**Figure IV-7a**) was employed here to assess if any effect coming from nanofiller type on the crystalline structure of the sample occurred. CNC_4 (11 ± 3% B-type crystallinity, **Figure IV-7a**) is as crystalline as ChNC_4 (**Figure IV-10a**), meaning that nanofiller type does not have any effect on the crystalline structure of starch.

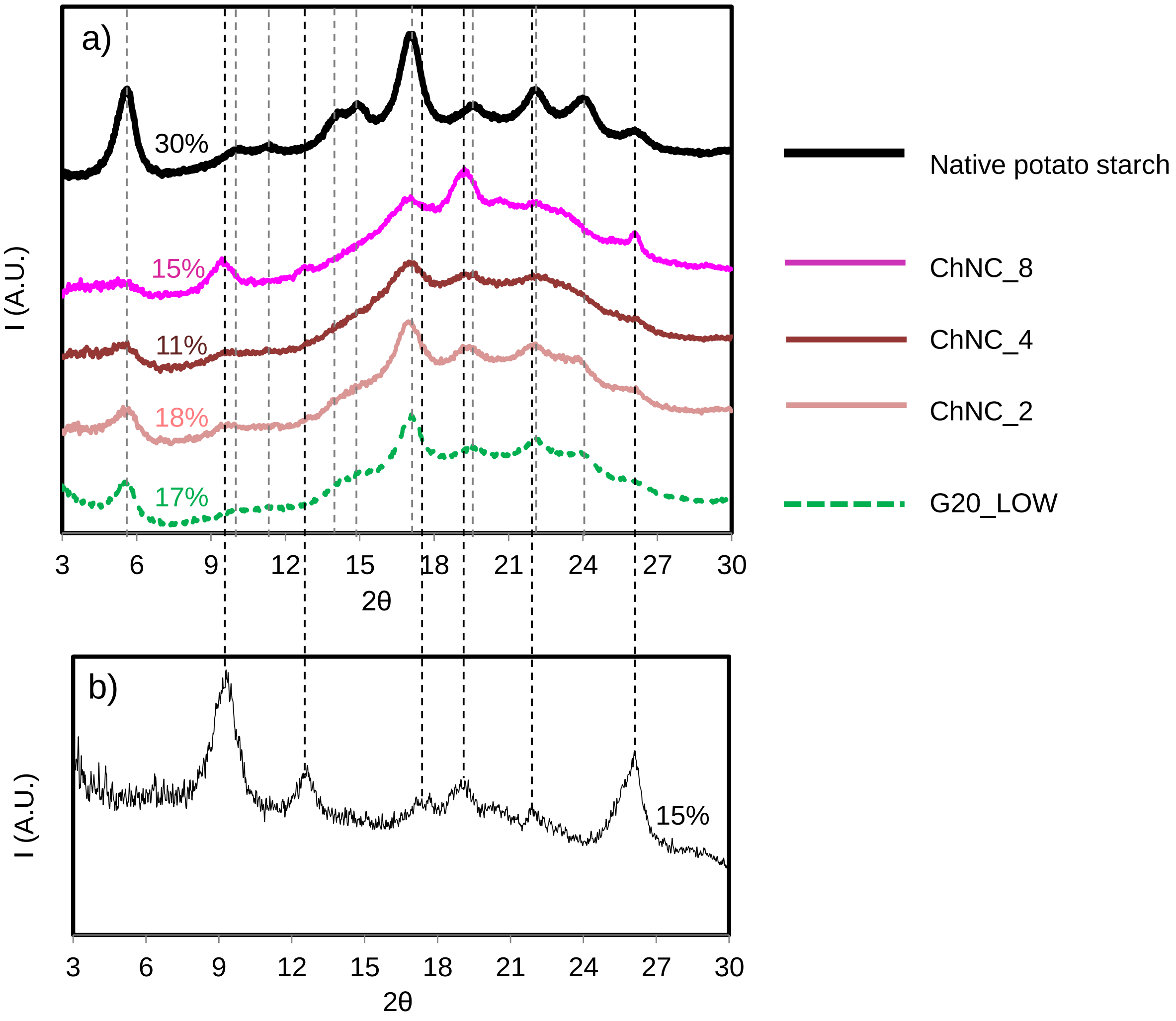

Figure IV-10: *X-ray diffractograms of* **a)** *starch-ChNC nanocomposites after stabilization at* a_w*=0.75 and* **b)** *of ChNCs after drying in oven at 40°C. Native potato starch and G20_LOW diffractograms after stabilization at* a_w*=0.75 are reported for comparison. Differences between native starch and nanocomposites diffractograms are highlighted with dotted grey lines while differences arising from ChNC content in the sample are highlighted by black dotted lines.*

For the study of starch-ChNCs nanocomposites local structure, larger regions of interest (20-110 ppm) of the ^{13}C CP-MAS spectra were considered.

Spectra for the reference sample G20_LOW and ChNC_8 nanocomposite are reported in **Figure IV-11a**, while ^{13}C CP-MAS spectrum for chitin is reported in **Figure IV-11b**.

Chitin peaks are identified at 55 ppm (C2), 61 ppm (C6), 82 ppm (C4) and 103.5 ppm (C1). Two nearby peaks are assigned to C3 (72 ppm) and C5 (76 ppm) regions. In addition, chitin presents a high-intensity peak at 22 ppm, generated by its methyl groups (CH_3).

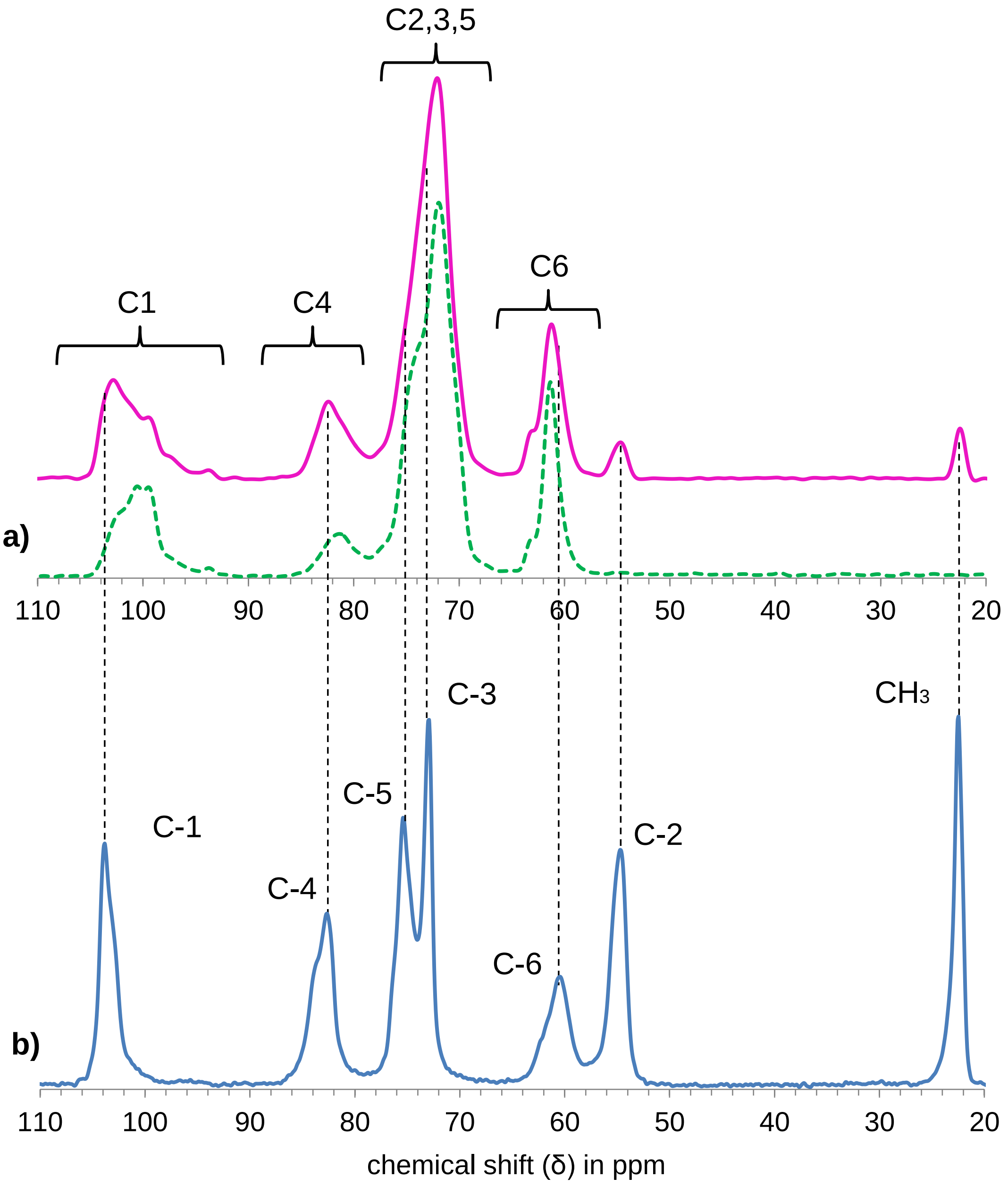

Figure IV-11: *^{13}C CP-MAS NMR spectra of* **a)** *starch-based matrix G20_LOW (green dotted line) and ChNC_8 (fuchsia). Differences in spectra are highlighted by grey dotted lines.* **b)** *^{13}C CP-MAS NMR spectra of chitin.*

The effect of chitin nanocrystals addition on extruded starch spectrum is highlighted by the dotted lines in **Figure IV-11a**: ChNC_8 shows new peaks at 22 ppm (CH_3), 55 ppm (C2), 82 ppm (C4) and at 103.5 ppm (C1). The other peaks of chitin are not visible because of their overlay with starch ones.

Similarly to CNCs, ChNCs are detected already at the lowest concentration (2wt%) in the sample. The peak around 103.5 ppm increases as higher ChNCs concentrations are introduced into the starch matrix (**Figure IV-12**).

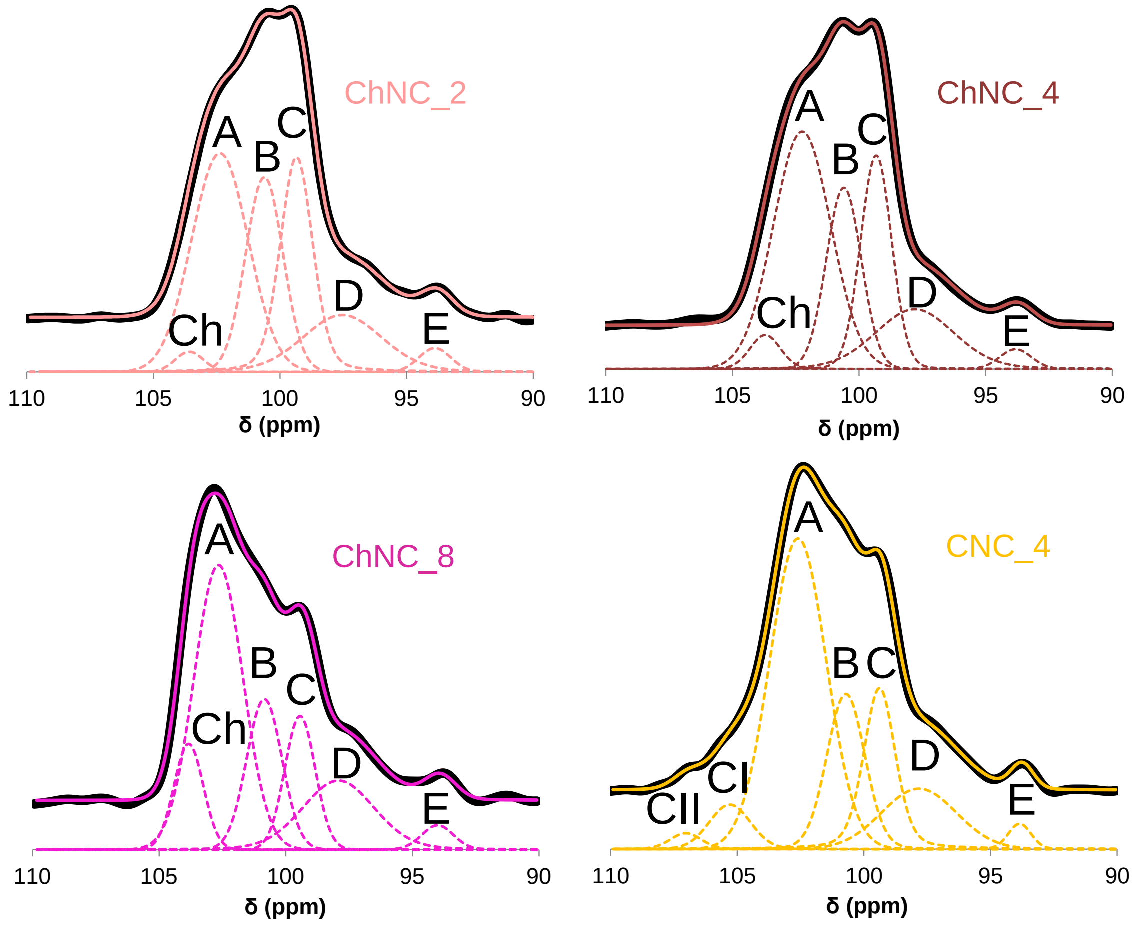

Figure IV-12: *Focus on C1 region of ChNC-starch nanocomposites and CNC_4. Each spectrum reports measured values (black line), computed values (color line) and peaks deconvolutions (dotted color line).*

The doublet of B-type crystallinity is clearly visible in ChNC_2 and ChNC_4, confirming the existence of B-type crystalline structures (WAXS results, **Figure IV-10a**) in these samples. However, ChNC_2 shows slightly higher A and lower B and C peaks (**Table IV-4**) than the matrix of reference G20_LOW, meaning that ChNCs reduce double-helical structures in favor of simple-helices/amorphous conformations already at this rate in the sample.

Indeed, the increase of ChNCs concentration in ChNC_4 and ChNC_8 is accompanied by an even more significant increase in amorphous conformations and reduction of double-helical/paracrystalline structures (**Table IV-4**), similarly to high-concentrated starch-CNCs nancomposites (CNC_5 and CNC_10). Unfavorable conformations (D peak) slightly increase from ChNC_4 to ChNC_8 as well, while constrained conformations (E peak) do not show any tendency.

ChNCs concentrations in the nanocomposites were computed as explained above for CNCs, and deconvolution fits gave an estimated ChNCs amount in the nanocomposites close to the theoretical one (**Table IV-4**), proving once again the validity of the method used for deconvolution.

The transformation of double-helical/paracrystalline structures to amorphous ones played by the nanocrystals is less important for chitin than for cellulose. Even if they have been extruded with the same parameters, ChNC_4 shows a significantly lower amount of amorphous conformations (A peak = 42%, **Table IV-4**) than CNC_4 (A peak = 51%, **Table IV-3**), suggesting that ChNCs affect starch local structure to a lesser extent than CNCs.

Table IV-4: *Results of ^{13}C CP-MAS NMR deconvolution fits of the C1 region for starch-ChNCs nanocomposites. G20_LOW deconvolution fits are reported for comparison. Chemical shift (δ) and peak normalized contribution are reported for each sample. Chitin estimated amount (Ch) and starch chains contributions based only on starch spectra are reported as well.*

	Peak assignment						
	Ch	**A**	**B**	**C**	**D**	**E**	
G20_LOW		102.3	100.6	99.3	97.7	93.7	**δ (ppm)**
ChNC_2	103.5	102.3	100.5	99.3	97.4	93.8	
ChNC_4	103.6	102.2	100.5	99.2	97.7	93.7	
ChNC_8	103.7	102.6	100.8	99.3	97.8	93.9	
G20_LOW		33.5	25.6	24.0	14.4	2.5	**Normalized area (%)**
ChNC_2	1.7	36.9	21.9	22.9	14.3	2.3	
ChNC_4	3.2	40.9	18.9	20.2	14.9	1.9	
ChNC_8	9.5	42.8	16.4	12.5	16.3	2.4	
G20_LOW		34	26	24	14	2	**Normalized area on starch (%)**
ChNC_2		38	22	23	15	2	
ChNC_4		42	20	21	15	2	
ChNC_8		47	18	14	18	3	

3. Physical properties at the dry state

The crystalline structure and the local orders in starch-based matrices and nanocomposites now well characterized, we can complete our knowledge on the structure of the samples by studying the mobility of starch chains by Dynamic Mechanical Thermal Analysis (DMTA). This technique, coupled with the characterization of the materials uniaxial deformation, gives a complete overview of the structure and the mechanical behavior of the materials “at the dry state” (samples stabilized at $a_w = 0.59$ for two weeks).

3.1 Thermomechanical properties and uniaxial deformation in starch-based matrices

Dynamic Mechanical Thermal Analysis

Dynamic Mechanical Thermal Analysis (DMTA) is used to study the thermomechanical behavior of a material under a small sinusoidal deformation. The strain applied to the material must be weak enough to investigate the behavior of the material in its linear viscoelastic domain. For DMTA measurement, the sample is placed in a temperature controlled environment with a thermocouple placed in close proximity.

Dual cantilever bending mode is one of the most common mode for materials which can be formed into bars. A sinusoidal strain is applied and the resulting specimen response may be expressed in terms of a dynamic storage modulus, a dynamic loss modulus and a mechanical damping term. Storage modulus (E') describes the ability of the material to store energy and release it upon deformation. Loss modulus (E'') is proportional to the energy dissipated inside the material in form of heat upon deformation. And finally mechanical dumping term (δ) is the phase angle which forms between the strain applied and the stress of a viscoelastic material, due to the time necessary to molecular motion and relaxation to occur. The phase angle is expressed as:

$$Tan\delta = E''/E' \quad \textbf{[IV-3]}$$

The storage modulus (E') is related to the elastic response of thermo-plastic materials and it is usually considered as an index of the stiffness of the material. Conversely the loss modulus (E'') is associated with the viscous portion of the material. During DMTA measurement at a constant oscillatory frequency over a sufficiently wide range of temperature, the main mechanical relaxation associated to calorimetric glass transition of the material can be clearly observed. The main relaxation (called α relaxation for DMTA) is detected as a major variation in the elastic modulus and an attendant peak in the Tan δ curve.

In this work a DMTA (DMTA MKIV, Rheometric Scientific, US) was used to investigate the dynamic thermo-mechanical behavior of the extruded starch-based samples. Rectangular specimens of 35 mm in length and 4 mm in width were cut from the extruded band-shaped samples and thickness was precisely measured with a micrometer.

The samples were analyzed in the dual cantilever mode at the frequency of 1 Hz with bending strain amplitude of 0.1% (**Figure IV-13**). *A scanning rate of 3°C min*$^{-1}$ *from 20°C to 180°C for G0 samples and from 0°C to 180°C for glycerol-plasticized samples (G20 and nanocomposites) was chosen. The samples were covered with silicon grease in order to avoid dehydration during heating. Each sample was analyzed in triplicate.*

It was not possible to cut rectangular specimens from G0_LOW as this sample has been extruded in cane-shape due to its high viscosity (see II-3.1). However, the surface of this slightly flattened cane has been approximated to be equivalent to those of the other rectangular samples, and the sample has been analyzed in cane-shape.

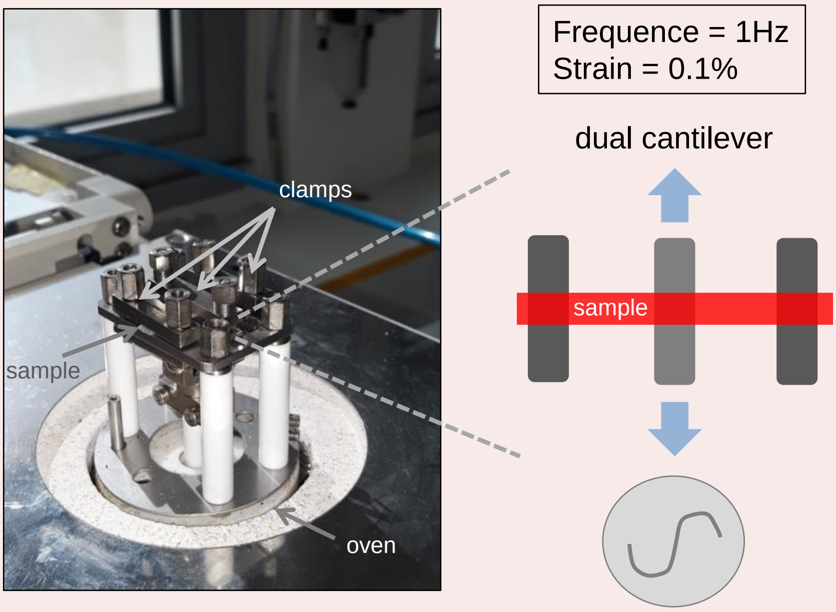

Figure IV-13: *Dynamic Mechanical Thermal Analyzer and focus on the dual cantilever principle used in this study.*

A quite important gap between the temperature registered by the thermocouple during the experience and the real temperature inside the sample was observed. This deviation has been corrected, as explained in the Annexes (Correction of temperature deviation in DMTA experiences), and the temperature values reported below are the correct ones.

A spread and not very well defined glass transition temperature (Tg) is detected by DSC but this is not precise enough to differentiate the samples. For this reason DMTA is used to obtain more detailed information about the thermo-mechanical behavior of the samples.

By DSC, Tg occurs at about 70°C and 35°C for G0 and G20 matrices respectively (see the Annexes, *Glass transition temperature in the extruded samples,* for details). This confirms the higher chain mobility in the glycerol-plasticized samples.

As mentioned in the State of the art chapter (see I-3.2), the maximum of damping factor (Tanδ) peak determined by DMTA (Tα) is often different from the Tg determined by DSC because of the different nature between the two measure techniques (mechanical and thermal respectively).

The thermomechanical behavior of the extruded samples was characterized by DMTA, using a dual cantilever bending test. The storage modulus (E'), the loss modulus (E'') and the damping factor (Tan δ) obtained for the starch-based matrices are reported in **Figure IV-14**.

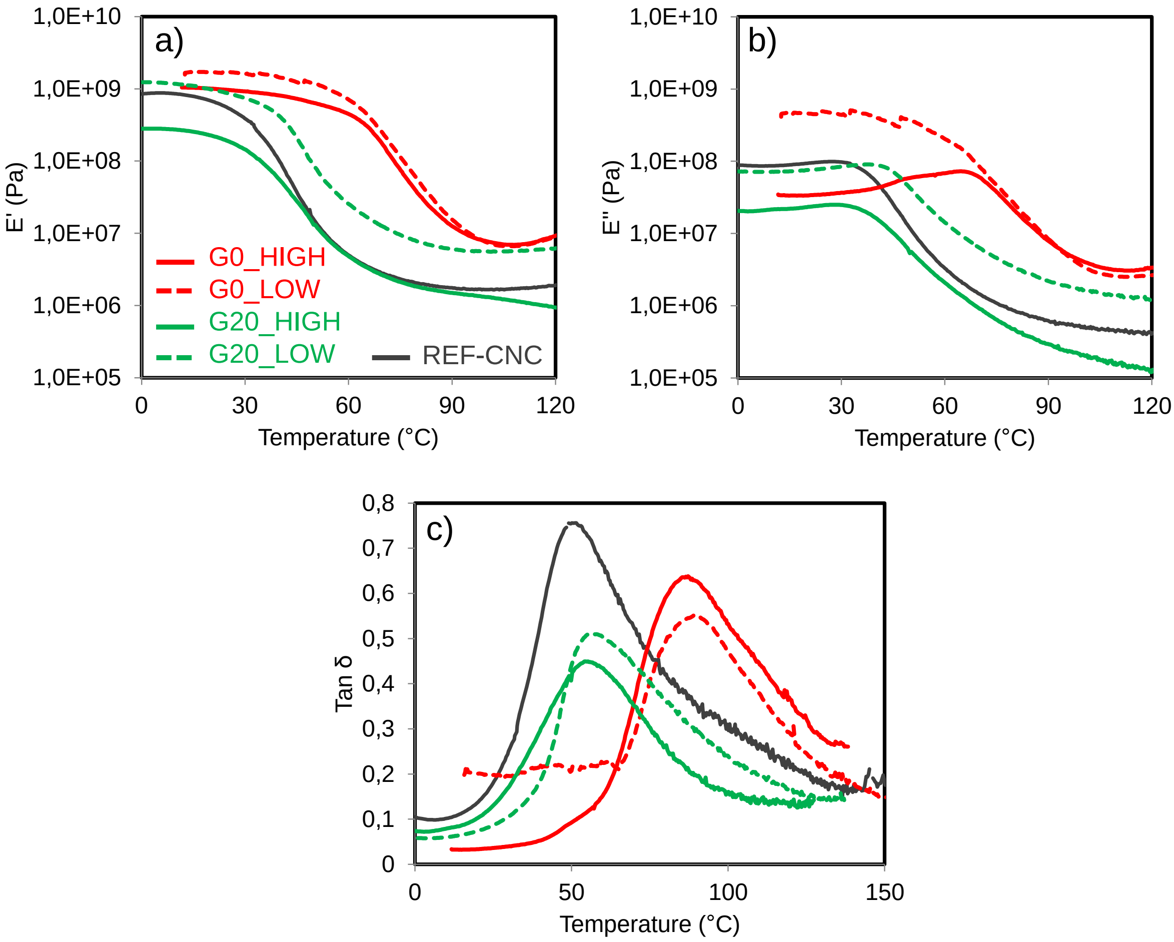

Figure IV-14: a) *Storage modulus (E'),* **b)** *loss modulus (E'') and* **c)** *damping factor (Tan δ) of starch-based matrices.*

In the glassy region (up to ~30-40°C for glycerol-plasticized samples and ~70°C for non-plasticized samples) storage modulus ranges between $4 \cdot 10^8$ and $2 \cdot 10^9$ Pa, while loss modulus varied between $4 \cdot 10^7$ and $6 \cdot 10^8$ Pa, due to reduced starch chain mobility (**Figure IV-14a** and **b**). A decrease of two orders of magnitude of E' and E" is observed between 40 and 90°C for glycerol-plasticized samples (G20) and between 70 and 110°C for non-plasticized samples (G0), corresponding to the α-relaxation associated to the Tg.

Then, at higher temperatures, all materials behave as rubber, with a storage modulus ranging between $1 \cdot 10^6$ and $1 \cdot 10^7$ Pa, and a loss modulus between $1 \cdot 10^5$ and $6 \cdot 10^6$ Pa, depending on the formulation and the presence of granular starch. While no major effect on the value of E' and E" has been observed between G0 samples (except for E" of G0_LOW in the glassy state, which could be due the shape of this sample, see *Dynamic Mechanical Thermal Analysis* set up above), G20 and REF-CNC samples show significant differences both in the glassy and the rubbery domain. The higher value of E' and E" observed for G20_LOW can be attributed to the presence of native granules (25%, see **Table III-1**) in the sample, which act as fillers, reinforcing the starchy network. G0_LOW has native granules as well (16%, see **Table III-1**), but it does not behave differently from G0_HIGH because of the already rigid structure in absence of glycerol, which imparts G0 samples of higher stiffness compared to G20 samples.

Differences in relaxation temperature between G0 and G20 samples are highlighted by Tan δ results (**Figure IV-14c**). The addition of glycerol in G20 and REF-CNC samples induces a shift of the Tα of G20 samples, from ~90°C to ~56°C, because starch chains are more mobile in presence of glycerol, in good agreement with the results obtained by DSC.

REF-CNC shows the highest damping factor (Tanδ = 0.76, **Figure IV-14c**). As damping is the ratio of loss (E") to storage (E'), the high maximum Tanδ value of REF-CNC could indicate a more viscous behavior of this sample compared to the others. The almost non-degradation of REF-CNC starch chains (see AF4 results, III-2) and the absence of native granules (which could reinforce the structure, as observed for G20_LOW matrix) could be responsible for this behavior. Indeed, the high starch chains depolymerization in the strongly destructurized matrix G20_HIGH could hinder a viscous behavior by DMTA, because starch chains are shorter.

To check if the differences observed by DMTA had important consequences on the properties at the dry state, glycerol-plasticized matrices were tested using the protocol reported below for uniaxial deformation. Starch-based matrices extruded without glycerol could not be tested by large tensile deformation because of their high brittleness, which made it difficult to cut specimens from the bands and fix them on the tensile machine used for testing.

Uniaxial deformation

A tensile test machine, Synergie 100 (MTS, Eden Prairie, MN, US) equipped with a 100 N load cell was used for uniaxial traction measurements. The samples were cut from the extruded bands in dog bone shape (utile length = 15 mm) and stabilized at constant humidity (0.59 a_w *with NaBr solution) for two weeks before to be subjected to large deformations at a temperature of 20°C. Force/elongation curves were recorded for a cross head velocity of 5 mm* min^{-1}*, and resulting nominal stress/nominal strain curves were obtained knowing the initial section and the utile length. The Young's modulus (E, MPa) is determined by the slope at the curve's origin. Standard deviations are high because of the significant thickness and the less repeatable structure of the materials analyzed in this work.*

For this reason, a minimum of 4 experimental curves was used to get reliable results with reduced standard deviations.

The results obtained by mechanical testing at high deformation of starch-based matrices at 20°C are reported in **Figure IV-15**, and numerical values are listed in **Table IV-5**. However, the interpretation of these results is a very sensitive issue as they have been measured at 20°C: a temperature close to the Tg of glycerol-plasticized samples. Because of this temperature condition and the different strain applied during DMTA and uniaxial deformation measurements, the mechanical properties measured with the two techniques could sometimes slightly differ. Besides, at this temperature (20°C), glycerol-plasticized materials are still glassy.

Under uniaxial deformation, samples show a rapid increase in stress until a maximum value, between 5 and 10% elongation, and then remain relatively constant until sample break, except for REF-CNC (**Figure IV-15**). Although the standard deviations are high, the Young's modulus (E) from the initial slope of the stress-strain curve seems much more reduced for the matrix extruded at high SME (G20_HIGH, 110 ± 40 MPa) than for the one extruded at low SME (G20_LOW, 210 ± 30 MPa, **Table IV-5**). In addition, G20_HIGH starts breaking around 65 ± 5% in strain, while G20_LOW starts breaking at lower strain, around 40 ± 10%, and it shows higher maximum stress (**Table IV-5**). This result may be explained by the presence of native granules (25%, see **Table III-1**) in G20_LOW, which increase the stiffness of the matrix, as pointed out above by DMTA results, and reduce its deformability.

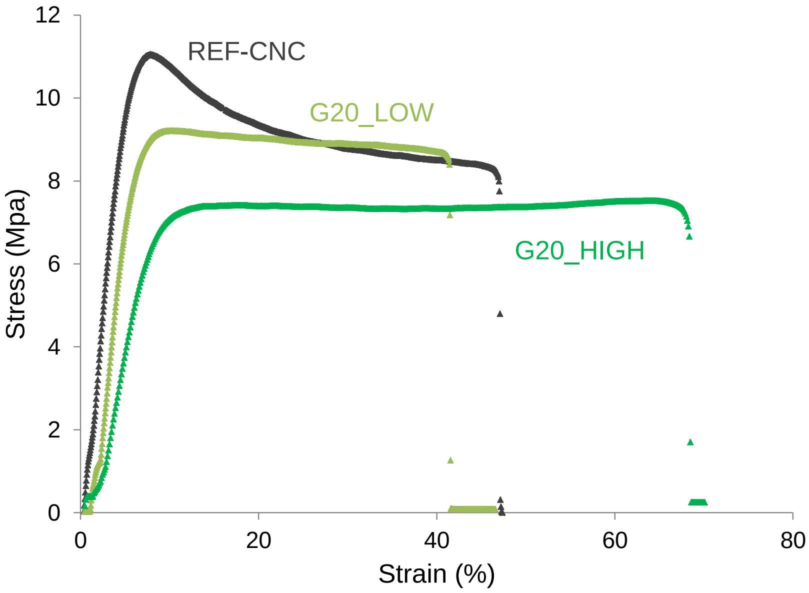

Figure IV-15: *Nominal stress/nominal strain curves at elongation rate of 5 mm min*$^{-1}$ *for glycerol-plasticized starch-based matrices.*

REF-CNC shows Young's modulus, elongation at break and maximum stress close to G20_LOW (see **Table IV-5**). However, the shape of the curve obtained by uniaxial deformation of this sample is different from the other matrices (see **Figure IV-15**).

The important elongation at break observed by uniaxial deformation highlights the high deformability of all glycerol-plasticized matrices already at room temperature (20°C), in accordance with their low Tg value (35°C). Thereby, these materials are more deformable than G0 ones.

Table IV-5: *Numerical values of Young's modulus, maximum stress and elongation at break obtained from stress/strain curves for glycerol-plasticized starch-based matrices.*

Sample	E (Mpa)	Maximum stress (Mpa)	Elongation at break (%)
G20_LOW	210 ± 30	9.5 ± 0.5	40 ± 10
G20_HIGH	110 ± 40	7.5 ± 1	65 ± 5
REF-CNC	233 ± 35	10.5 ± 0.5	45 ± 5

3.2 Thermomechanical properties and uniaxial deformation in nanocomposites

3.2.1 Cellulose nanocrystals-starch nanocomposites

The thermomechanical properties of the matrices now widely characterized, the study can focus on the effect on nanofillers on these properties, independently from the other parameters (extrusion parameters, glycerol).

Figure IV-16 reports the thermomechanical properties of CNCs-starch nanocomposites.

In the glassy region (up to 30-40°C) storage modulus ranges between $5{\cdot}10^8$ and $1{\cdot}10^9$ Pa, while loss modulus ranges between $5{\cdot}10^7$ and $1{\cdot}10^8$ Pa, as typical of glassy glycerol-plasticized thermoplastic starch (see **Figure IV-14a** and **b**). The decrease of the storage (between $2{\cdot}10^6$ and $9{\cdot}10^6$ Pa) and loss (between $4{\cdot}10^5$ and $2{\cdot}10^6$ Pa) moduli, observed between 40 and 90°C, corresponds to the α-relaxation.

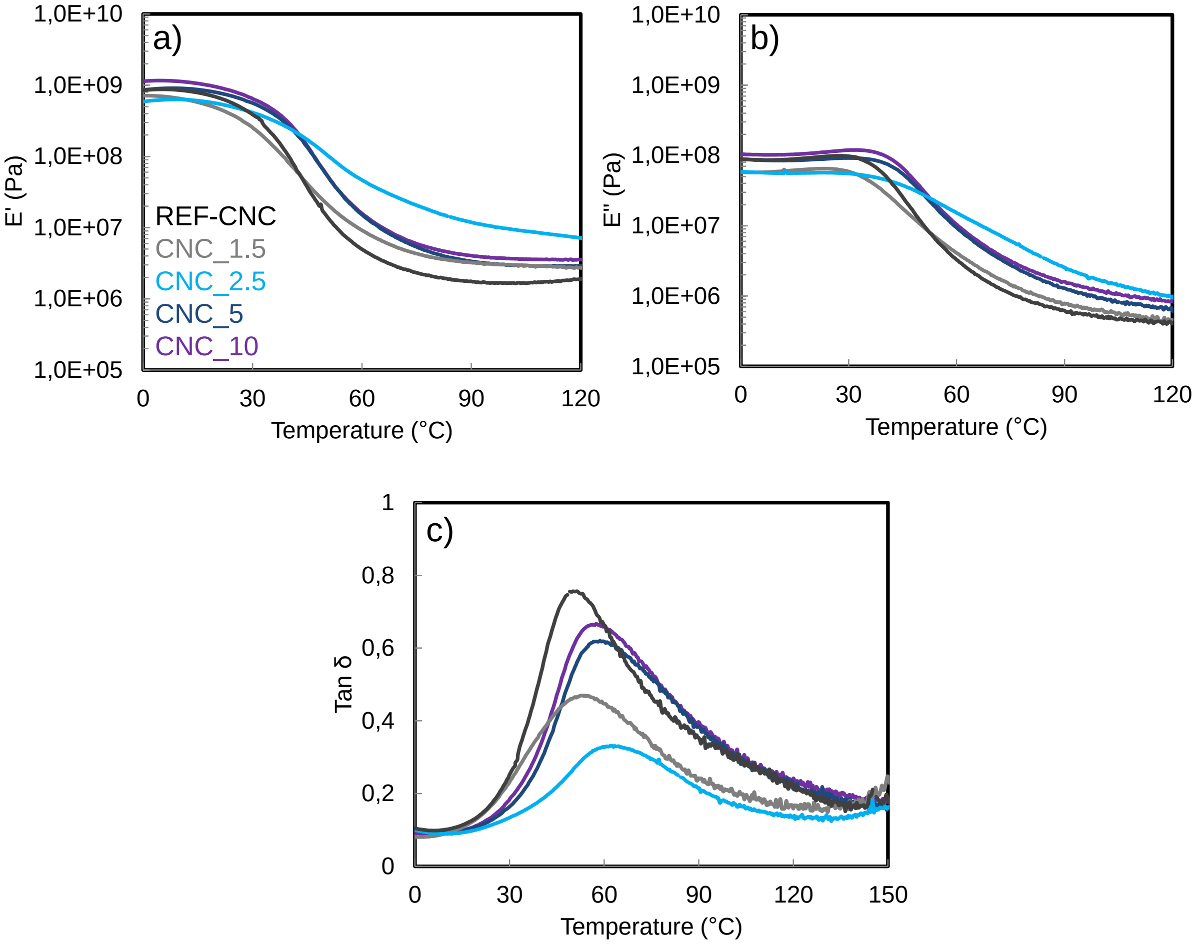

Figure IV-16: **a)** *Storage modulus (E'),* **b)** *loss modulus (E'') and* **c)** *damping factor (Tan δ) of starch-CNCs nanocomposites. REF-CNC is reported for comparison.*

No significant differences on the value of E' and E" are detected between the samples in the glassy domain. Conversely, in the rubbery domain all nanocomposites show higher values of E' and E" than REF-CNC (**Figure IV-16a** and **b**).

This result is particularly striking for the nanocomposite CNC_2.5, suggesting that a maximum reinforcement occurs in this sample. Indeed, CNC_2.5 shows a relaxation spread on a large temperature domain compared to the other nanocomposites (**Figure IV-16a** and **b**). This may signify that CNCs at this amount (2.5wt%) in the sample restrict starch chains mobility, due to the strong interaction between starch and fillers (Lu et al. 2005). This reinforcing may be optimal in the nanocomposite CNC_2.5 but lost at higher CNCs concentrations (≥ 5wt%). Hence, at 2.5wt% CNCs the sample would be composed of an important rigid amorphous phase compared to the other nanocomposites.

This hypothesis of reinforcement could explain the gradual decrease in damping, observed as CNCs are introduced in the matrix. Maximum Tanδ value drops from 0.76 in REF-CNC to 0.41 in CNC_1.5 and 0.33 in CNC_2.5 (because the cellulose/starch interaction restrict starch chains mobility), but it increases once again in CNC_5 and CNC_10 (Tan δ = 0.61 and 0.63 respectively, **Figure IV-16c**).

The addition of CNCs seems to induce an evolution of Tα as well (**Figure IV-16c**). The damping factor of CNC_1.5 nanocomposite shows a peak around 53°C, as for the starch-based matrix of reference REF-CNC. The peak position is shifted to higher temperatures (~ 60°C) in CNC_2.5, and remains stable in CNC_5 and CNC_10, suggesting that a mechanical coupling may occur between starch and nanofillers from 2.5wt% CNCs content in the sample. Indeed, many authors report that Tα of nanocomposites increases in response to the numerous hydrogen bonds which form between starch and cellulose nanocrystals (Avérous et al. 2001). CNCs may act like a junction and promote the intermolecular interaction of starch chains and reduce their relaxation (Chang, Jian, Zheng, et al. 2010).

The mechanical coupling which occurs as CNCs are introduced in the system is reflected by the rigid behavior observed for the nanocomposites by uniaxial deformation.

As visible in **Figure IV-17**, the elongation at break slightly decreases from REF-CNC (45 ± 5%) to the lowest concentrated nanocomposite (CNC_1.5, 40 ± 5%) to then significantly decrease at higher CNC concentration (~7-15 ± 1%, **Table IV-6**). Thereby, the nanocomposites are less deformable than their matrix of reference (REF-CNC), and their rigidity increases with CNC concentration in the sample. This result is imputable to the CNCs only, as no residual granules remained in any of the samples. The introduction of CNCs may disrupt the continuous network of starch, reducing its deformability.

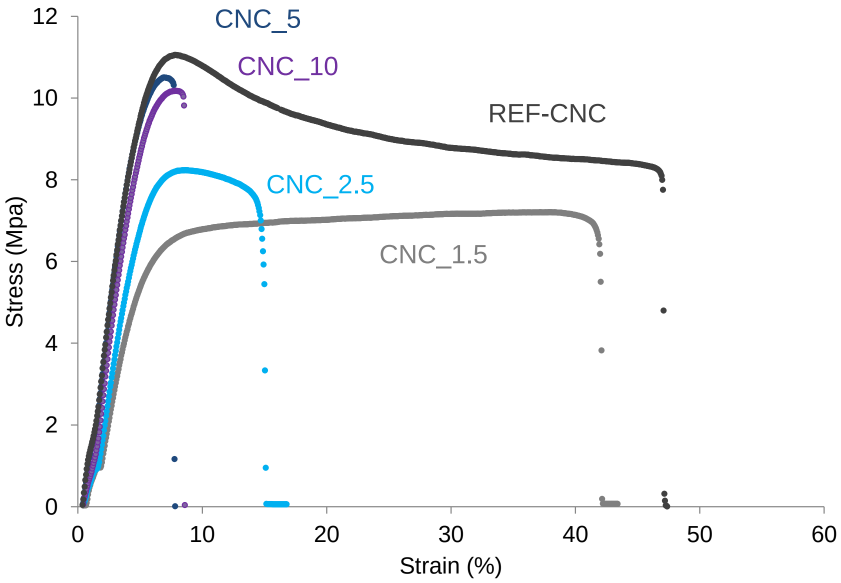

Figure IV-17: *Nominal tress/nominal strain curves at elongation rate of 5 mm min^{-1} for starch-CNCs nanocomposites. REF-CNC curve is reported for comparison.*

The effect of CNCs on Young's modulus (E) and maximum stress is less clear: standard deviations are too high to identify significant differences between the behaviour of the matrix and the nanocomposites.

Table IV-6: *Numerical values of Young's modulus, maximum stress and elongation at break obtained from stress/strain curves for starch-CNCs nanocomposites. REF-CNC values are reported for comparison.*

Sample	E (Mpa)	Maximum stress (Mpa)	Elongation at break (%)
REF-CNC	233 ± 35	10.5 ± 0.5	45 ± 5
CNC_1.5	145 ± 20	7 ± 0.5	40 ± 5
CNC_2.5	196 ± 20	7.5 ± 0.5	15 ± 1
CNC_5	201 ± 35	10.5 ± 2	8 ± 1
CNC_10	195 ± 20	10.5 ± 1	7 ± 1

3.2.2 Chitin nanocrystals-starch nanocomposites

ChNCs-starch nanocomposites show the same storage ($1\cdot10^9$ Pa) and loss ($5\text{-}9\cdot10^7$ Pa) modulus in the glassy domain, up to ~40°C (**Figure IV-18a**).

At higher temperatures (40-90°C) α-relaxation occurs and, in the rubbery region (90-110°C), the storage and loss moduli decrease to values of $1\cdot10^7$ Pa and $2\cdot10^6$ Pa respectively (for G20_LOW and ChNC_2) and to $2\cdot10^6$ Pa and $8\cdot10^5$ Pa respectively (for ChNC_4 and ChNC_8). These values are comparable to the ones observed before for glycerol-plasticized starch-based matrices and starch-CNCs nanocomposites.

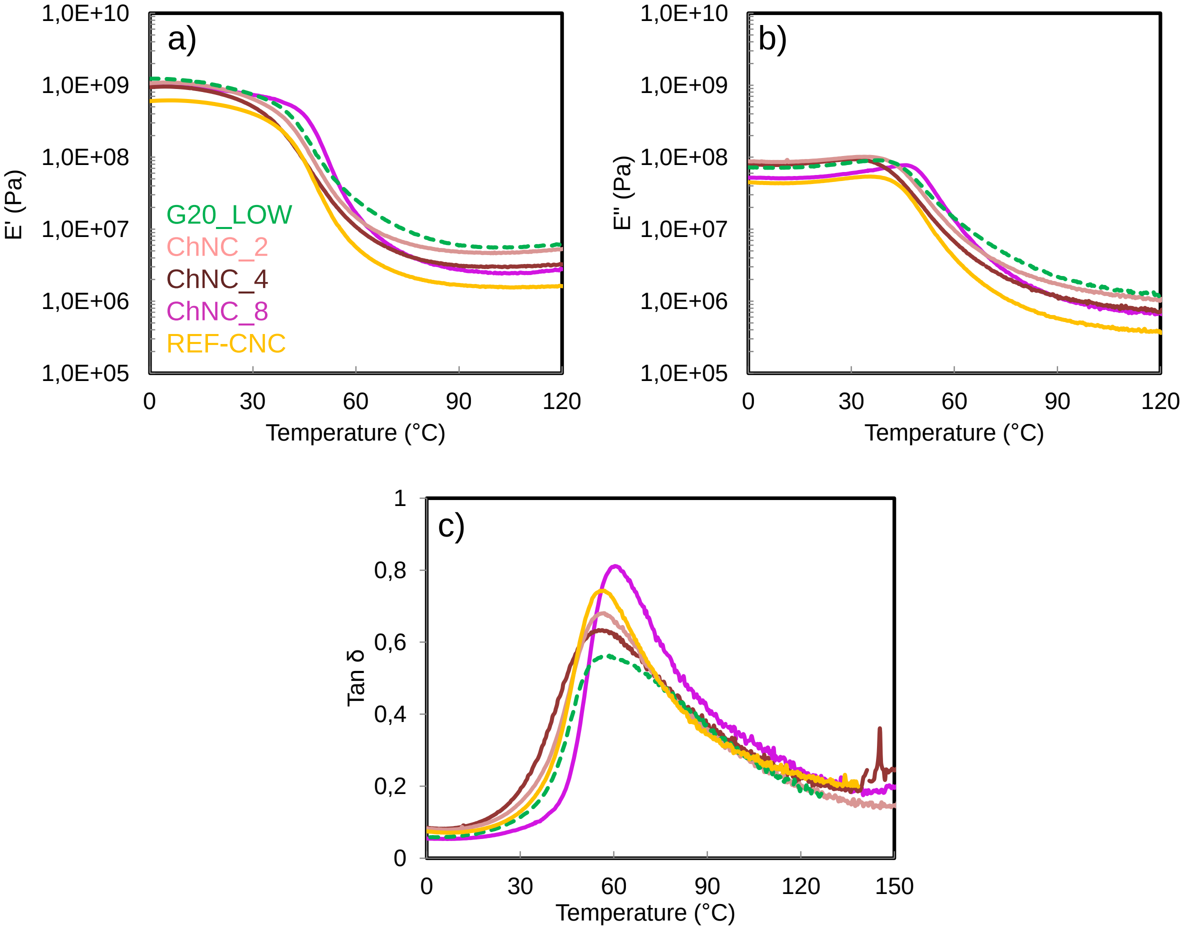

Figure IV-18: a) *Storage modulus (E'),* **b)** *loss modulus (E'') and* **c)** *damping factor (Tan δ) of starch-ChNCs nanocomposites and CNC_4. G20_LOW is reported for comparison.*

Residual granules in G20_LOW matrix (~25%, see **Table III-1**) and ChNC_2 nanocomposite (~18%, see **Table III-3**) are responsible for their close thermomechanical behavior: native granules rigidify the amorphous starch matrix and induce an increase in E' and E'' values in the rubbery domain, compared to samples without any granule (ChNC_4 and ChNC_8).

The addition of ChNCs seems to induce an evolution of Tα at the highest ChNCs concentration only (**Figure IV-18c**): damping factors of ChNC_2 and ChNC_4 show a peak around 56°C, similarly to G20_LOW matrix, while peak position is shifted to slightly higher temperatures (~60°C) only for ChNC_8.

Besides, maximum Tanδ value increases gradually as ChNCs are introduced in the formulation, from 0.65-0.61 (for ChNC_2 and ChNC_4) to 0.81 (for ChNC_8), the lowest value being for the reference matrix (G20_LOW, maximum Tan δ = 0.5, **Figure IV-18c**). The increase in damping might point out the absence of any kind of chitin/starch interaction in the nanocomposites already at the lowest ChNC concentration (2wt%).

The thermomechanical behavior of ChNC_4 is close to CNC_4 one: in the rubbery domain CNC_4 shows low storage ($1\cdot10^6$ Pa) and loss ($4\cdot10^5$ Pa) moduli (**Figure IV-18a** and **b**) and high maximum Tanδ (0.75), meaning that no mechanical coupling occurs between CNCs and starch in this sample. Independently from the type of filler, ChNCs and CNCs at this rate in the sample (4wt%) seem not to reinforce the starch matrix.

Some slight differences among the starch-ChNCs nanocomposites can be observed by uniaxial deformation: the Young's modulus seems to increase as higher concentrations of nanocrystals are introduced in the sample, from 166 ± 40 to 299 ± 15 MPa (**Table IV-7**).

Besides, elongation at break is significantly reduced (of about 30%) already at low ChNC content in the sample (from 40 ± 10% for G20_LOW to 6 ± 1% for ChNC_2) and remains stable at low values also at higher ChNCs concentrations (see **Figure IV-19**).

Conversely, no difference in maximum stress can be measured among the starch-ChNCs nanocomposites and the matrix (11-12 ± 1 and 9.5 ± 0.5 MPa respectively, **Table IV-7**).

Table IV-7: *Numerical values of Young's modulus, maximum stress and elongation at break obtained from stress/strain curves for starch-ChNCs nanocomposites. G20_LOW values are reported for comparison.*

Sample	E (Mpa)	Maximum stress (Mpa)	Elongation at break (%)
G20_LOW	210 ± 30	9.5 ± 0.5	40 ± 10
ChNC_2	166 ± 40	11 ± 2	6 ± 1
ChNC_4	243 ± 30	11 ± 1	12 ± 6
ChNC_8	299 ± 15	12 ± 1	5 ± 1
CNC_4	196 ± 15	8.5 ± 2	6 ± 1

As observed by DMTA, CNC_4 mechanical behaviour is comparable to ChNC_4 one, with a very low elongation at break. No significant differences on the mechanical behaviour of the nanocomposite at large deformation have been observed to be dependent on the nature of the filler (CNCs and ChNCs).

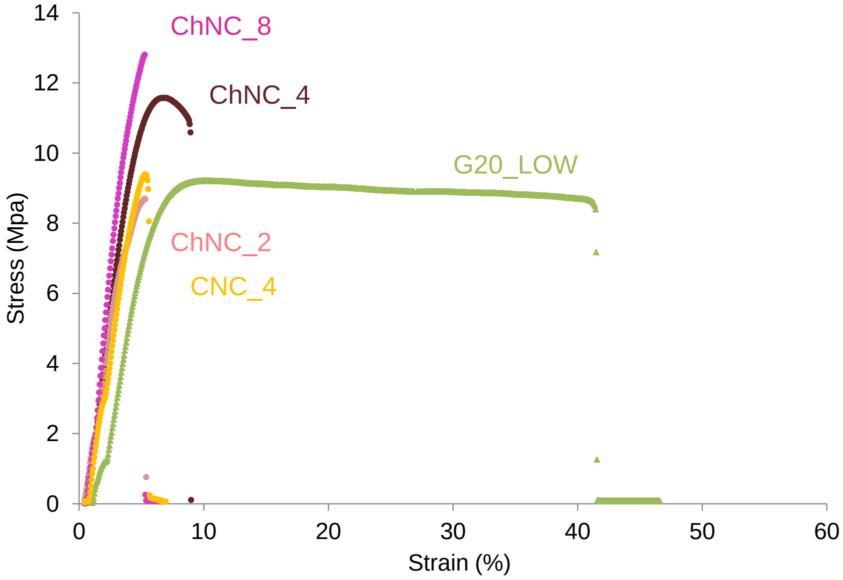

Figure IV-19: *Nominal stress/nominal strain curves at elongation rate of 5 mm min^{-1} for starch-ChNCs nanocomposites and CNC_4. G20_LOW curve is reported for comparison.*

4. General discussion about structure of starch-based matrices and nanocomposites, and relationship with the extrusion process

4.1 Starch-based matrices

Starch-based materials with different structures were produced by playing on both processing and formulation. More in detail, the macromolecular characterization of the extruded starches pointed out the presence of different structures and local orders, depending on plasticizer content and extrusion parameters applied for their production (temperature, SME). This first characterization, without any nanofiller, was necessary to understand the structure generated in processed starch by extrusion and its outcomes on the properties at the dry state.

The use of low extrusion energies (SME = 100 J g^{-1}, **Table II-3**), short screw profile (15.5 L/D), low temperature and glycerol addition (G20 samples) favored the preservation of native starch granules. Indeed, starches processed with the softest parameters still present remnants of native granules in their structure, as visible in SEM micrographs (**Figure III-1**). Granules are preserved in higher proportion in the glycerol-plasticized sample G20_LOW, as pointed out by DSC results (see III-1). The glycerol present in G20 samples acts like a lubricant, giving more mobility to amylose and amylopectin chains (Shogren 1993) and it helps in preserving starch structure during extrusion. At the same time, glycerol promotes the formation of intermolecular double helical structures of amylose and amylopectin during storage after extrusion and induces an increase in B-type crystallinity (Lehmann & Robin 2007; Bizot et al. 1997; Trommsdorff & Tomka 1995), as confirmed by solid-state NMR and WAXS results (see IV-1). This result is particularly striking for samples extruded at high SME: though no granule remnants are detected in the sample, G20_HIGH presents 7% of B-type crystallinity because of post-process recrystallization. Similarly, NMR results show that the glycerol-plasticized sample extruded at high SME (G20_HIGH) possesses a higher number of double-helical and/or paracrystalline structures (B and C peaks) than the amorphous sample G0_LOW, despite the significant difference in SME.

Lower crystallinity rates are observed for both plasticized and non-plasticized samples when those are extruded at higher SME, because of the destruction of starch native structure. At a smaller scale, high extrusion energies (1900 J g^{-1}) are responsible for amylopectin chains degradation (Liu et al. 2010), which contributes to reducing crystallinity as well, as amylopectin is the support of crystallinity in starch granules (Buléon et al. 2007; Jenkins & Donald 1995).

Starch chains degradation at high SME is pointed out by AF4 results (see III-2): though both G20_HIGH and G0_HIGH show drastically reduced molecular size and mass, degradation is more important for the amorphous sample G0_HIGH.

These structural results indicate that the combined use of low SME and temperature, together with the use of short screw profiles and glycerol addition to starch before extrusion, lead to highly crystalline 3D matrices, the crystallinity being generated from both granules preservation during extrusion and starch chains reorganization during storage.

Conversely, the extrusion of starch at high SME and temperature, with long destructurizing screw profiles and without any non-aqueous plasticizer, produces amorphous samples with no residual granules and crystallinity.

For a better comprehension, the obtained structures are represented schematically in **Figure IV-20**.

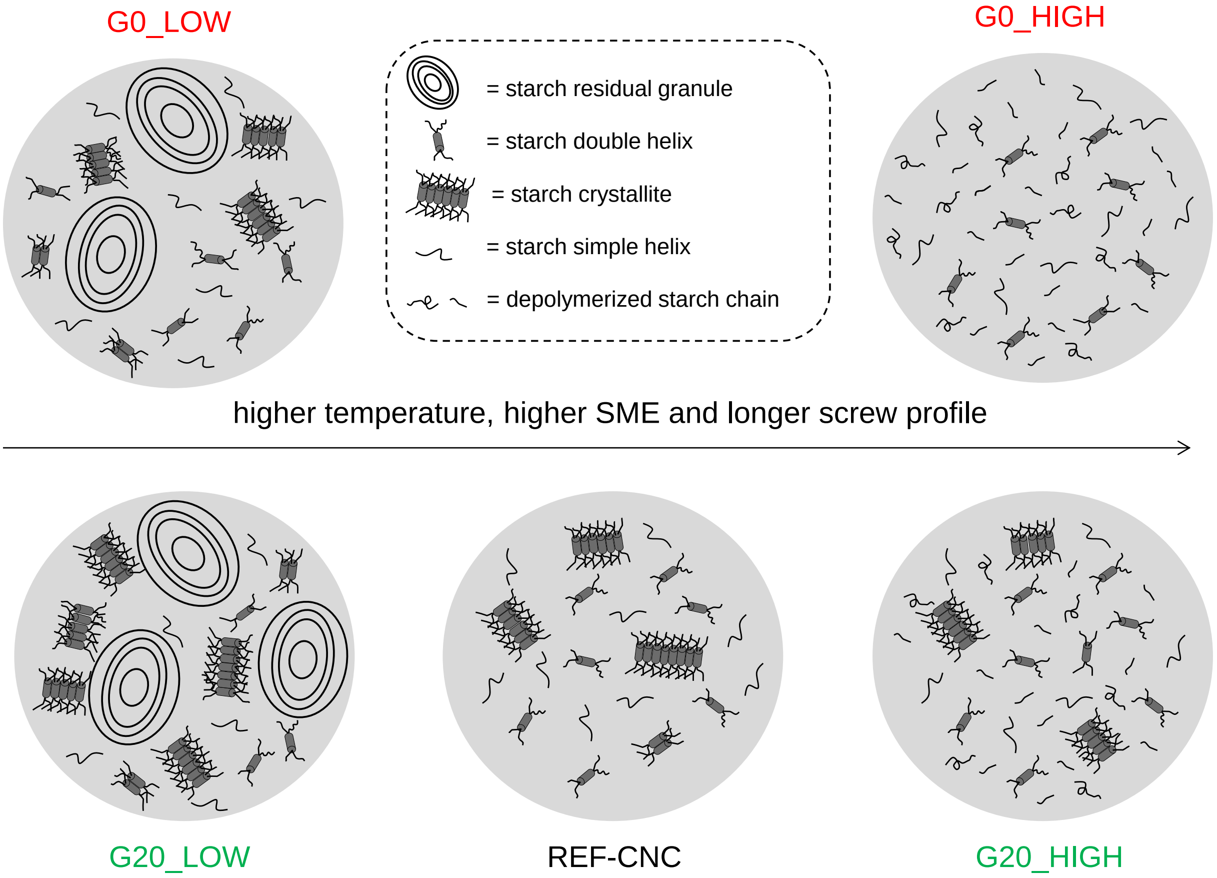

Figure IV-20: *Schematic representation of starch-based matrices structure after extrusion.*

However, it is not always easy to control the extrusion parameters to obtain well-defined structural features. Indeed the bordure between the preservation and the loss of native starch structure in presence of glycerol is very thin: the REF-CNC matrix constitutes a clear example of this. The slight increase in temperature and residence time of starch in the barrel during extrusion induce the complete melting of native starch granules (see DSC gelatinization test and SEM results, III-1) and an important loss in crystalline and local orders (WAXS and NMR results, IV-1), even when light shear stress is applied (see **Table II-3** and **Figure IV-20**). As for G20_HIGH, glycerol favors starch chains reorganization after extrusion in semi-crystalline structures.

The higher chain mobility induced by the plasticization with the polyol in G20 and REF-CNC matrices is confirmed by uniaxial deformation, DMTA and DSC results: indeed “at the dry state” and at room temperature (20°C), glycerol-plasticized samples show high deformability because they are close to their Tg (35°C). The stiffness of the extruded material increases gradually when the native granules are partially preserved in the sample (see **Figure IV-15**). The starch granules preserved in the extruded matrix may act as fillers, reducing the mobility of starch chains in the amorphous fraction of the sample and contributing to stiffen the sample (J.J.G. van Soest, Hulleman, et al. 1996).
Conversely, TPS without glycerol (G0) is completely glassy at 20°C, and this is responsible for the rigid and brittle behavior of G0 samples.

In order to make the structures of the starch-based matrices clearer, they have been positioned on the scheme of Barron (Barron et al. 2001) (**Figure IV-21**). This representation is purely qualitative and it is limited to the hydration/plasticization conditions used in this study (37wt% water content and 22.5wt% glycerol on starch dry mass).

Figure IV-21 reports the transformations (labelled with letters) induced by the isolated or combined effect of SME and temperature. **a**, **b** and **c** structures have been already described in detail by Barron and colleagues (see Chapter I, Section 1, 2.2.2).
d and **e** have been added to describe intermediate structures, obtained by modulating heating and mechanical energy. **d** describes a heterogeneous and inconsistent material obtained by partial destructurization of starch granules and incomplete melting, while **e** represents a more cohesive material, constituted by granule ghosts in a melted matrix.

Actually, the structure of G20_LOW and G0_LOW matrices can be positioned between case **d** and **e**, while the structures of G20_HIGH and G0_HIGH are near to case **c**. REF-CNC is closer to case **e**, because the higher temperatures used for its extrusion induced the complete melting of the native structure, compared to G20_LOW sample.

In **Figure IV-21**, G20_HIGH and G20_LOW positioning is shifted to the left compared to their respective non-plasticized counterparts, to illustrate that, in presence of glycerol, starch is less destructurized than expected. This is mainly due to the higher melting temperature of glycerol-plasticized formulations (see II-2.1) than non-plasticized ones.

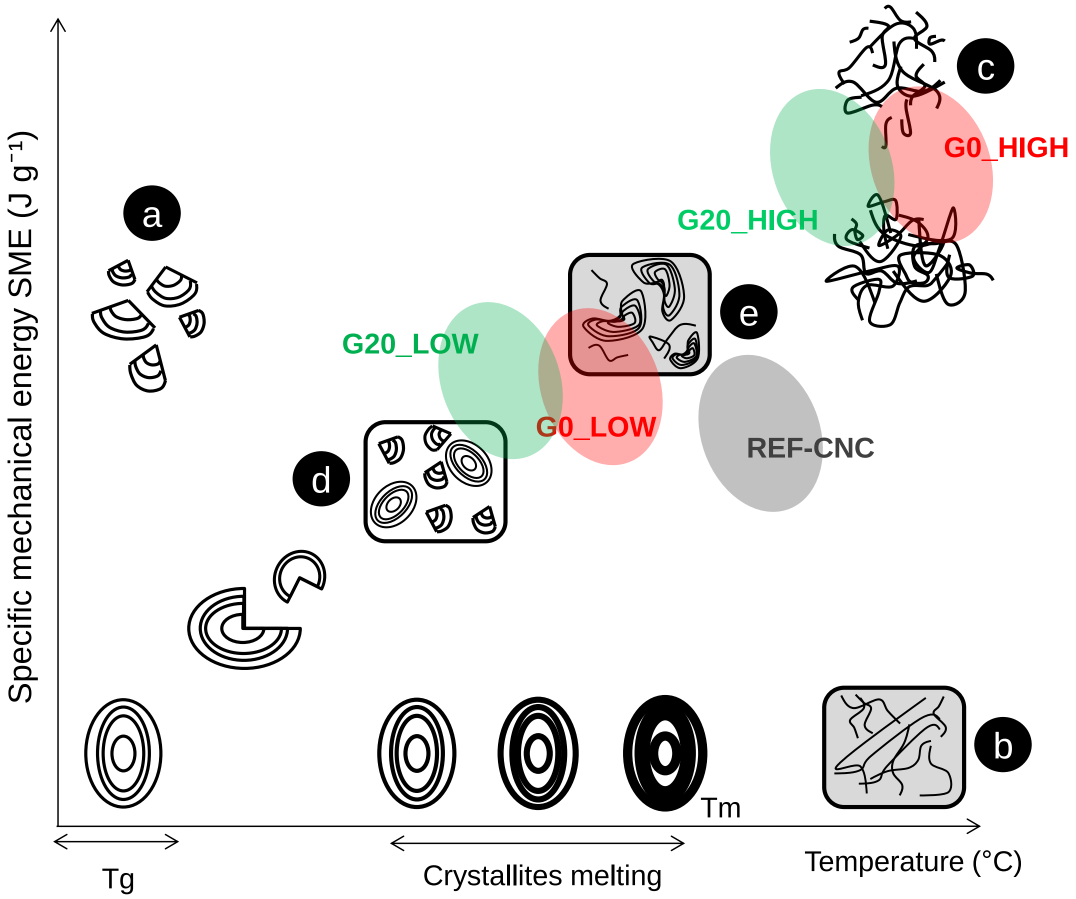

Figure IV-21: *Schematic representation of the mechanism of starch melting under shear, adapted from (Barron et al. 2001). Colored halos are used to illustrate the positioning of starch-based matrices structure after extrusion.*

4.2 Nanocomposites

Two types of starch-based nanocomposites, one with cellulose nanocrystals (CNCs), another with chitin nanocrystals (ChNCs), were successfully processed by extrusion. Good interfacial adhesion was expected in using starch as a matrix and cellulose and chitin as fillers, given their similar chemical structure (Dufresne & Castaño 2017).

4.2.1 Starch-CNCs nanocomposites

From the study of structure (CP-MAS NMR, WAXS, SEM) of the starch-CNCs nanocomposites, they appear to be divided into two groups: one with lower concentrations of CNCs (CNC_1.5 and CNC_2.5), and one with larger concentrations (CNC_5, CNC_10).

All starch-CNCs nanocomposites share some common characteristics: their starch chains have a lower average molar mass compared to the ones in the reference, as measured by AF4. This can be attributed either to the slight differences in SME between REF-CNC and starch-CNCs nanocomposites during extrusion, or to an increased shear induced by CNCs on starch chains. They also do not present any measurable amount of remaining starch granules, as evidenced by the DSC gelatinization test.

But beside that, structure clearly separates CNC-starch nanocomposites into two groups.

Whichever the scale, no significant differences are found between lower-filler-concentration nanocomposites and their matrix of reference. CNCs in CNC_1.5 and CNC_2.5 have no effect on starch crystallinity or short-range organization, and samples are microscopically homogeneous.

The second group of higher-filler-concentration nanocomposites (CNC_5 and CNC_10) includes samples which are structurally different from their reference: they appear less ordered, showing more amorphous conformations and less paracrystalline and double helical conformations in the CP-MAS spectra analyzes.

It is possible that nanocrystals act as a physical obstacle to starch chains during the structural rearrangement of starch in paracrystalline and double-helical structures. CNCs could insert themselves between the chains in melted starch during extrusion and hinder their reorganization during storage. Previous works suggested that nanofillers might disrupt the inter- and intra-molecular hydrogen bonds in starch double-helices and thus reduce the amount of these structures (Liu et al. 2016; Liu et al. 2017). Other studies suggest that nanofillers reduce the mobility of starch chains at room temperature which would result in a considerable slowdown of starch recrystallization during storage in humid atmosphere (Angellier et al. 2006; Zeng et al. 2012).

The reduction in the amount of double-helical structures could as well induce a decrease in crystallinity, as double-helices constitute part of the crystal structure of starch (J. J. G. van Soest et al. 1996). This reduction would be significant for higher CNC (CNC_5 and CNC_10) concentrations (Liu et al. 2016). However, due to the partial overlay of starch and CNCs crystalline profiles (WAXS results, IV-2), we were not able to determine if an effective reduction in starch crystallinity occurs at higher CNC concentrations.

Because of this overlay, CNC_10 shows a particularly high crystallinity rate.

At a large scale, as seen via SEM, high-CNCs-concentration nanocomposites show a heterogeneous fracture surface, with voids and discontinuities.

Low-concentrated nanocomposites (CNC_1.5 and CNC_2.5) present reduced intensity of α-relaxation as measured by DMTA, compared to the starch-based matrix without CNC, even if, whichever the scale, no significant differences were found between the structure of CNC_1.5, CNC_2.5 and REF-CNC. The modified property is an indication of the strong interactions between starch (matrix) and cellulose (fillers).

Cellulose nanocrystals are supposed to form numerous hydrogen bonds with starch when they are well-dispersed in the matrix, and they may act as a junction to promote the intermolecular interaction of starch chains. This interaction would also reduce their relaxation (Chang, Jian, Zheng, et al. 2010) and increase the rigidity of the material (see stress/strain curves in **Figure IV-17**). It also decreases the mobility of starch chains (Avérous et al. 2001) and the transition from the glassy to the rubbery state is weaker, as confirmed here by the DMTA results. The results obtained for this portion of the samples are all coherent with well-dispersed nanocrystals, modifying relevant properties already at 1.5wt%.

At higher CNCs concentrations (≥ 5wt%), the intensity of α-relaxation as measured by DMTA comes back to the values of the matrix without CNCs. In addition, mechanical properties at large deformation do not vary significantly from the ones observed at lower CNCs concentration. The only difference (the lower elongation at break, see **Table IV-6**) comes from the higher concentration in CNCs, which break the continuous starch network rather than interact with starch.

This change in properties and structure compared to the group of samples with a lesser amount of fillers is coherent with an aggregation of the nanocrystals, occurring above 2.5wt% but below 5wt%. Indeed, homogeneous dispersion of nanofillers in the matrix and strong interactions between the two components are key factors to obtain functional nanocomposites (Dufresne & Castaño 2017). Higher CNCs concentrations apparently induce the formation of aggregates of unknown size, and possibly a heterogeneous dispersion, as represented in **Figure IV-22**. Thus the matrix/filler interaction is greatly reduced (smaller interface) and the “nanocomposite”, now simply “composite” since the “nano-effect” is lost, comes closer to the behavior of the matrix alone.

The hypothesis of nanofillers aggregation occurring above 2.5wt% is supported by percolation values and theoretical inter-particle distance computed for this type of nanocrystal. Assuming a length comprised between 50 and 250 nm, a width between 5 and 20 nm (STEM measurements, **Table II-1**) and a density of 1.6 g cm^{-3}, the CNCs studied here have a percolation ratio of 9.8 ± 1.2% on the weight basis (Capadona et al. 2008). Achieving the percolation threshold would involve a significant change in the material structure and properties, which is not the case for the nanocomposites analyzed in this study, because of CNCs aggregation.

Besides, inter-particle distance calculations pointed out the potential aggregation of CNCs between 5 and 10wt% in the sample in case of packed nanocrystals (**Figure III-13a**), which is the most realistic given the low water content of starch-based formulations.

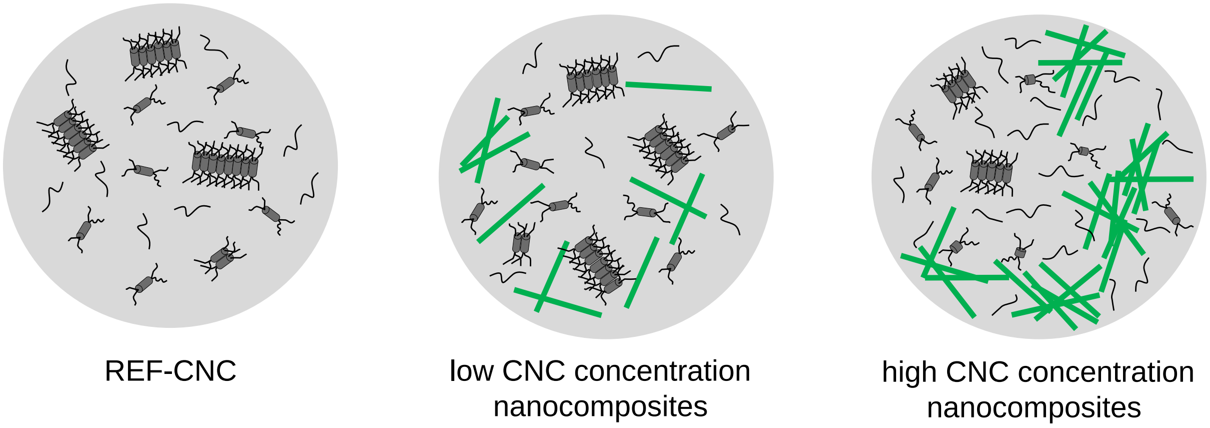

Figure IV-22: *Illustration of starch-based matrix REF-CNC, low and high CNC concentration nanocomposites potential structural organization. Starch simple (black line) or double (grey cylinder) helices, crystallites (packing of grey cylinders) and CNCs (green color) are represented in the system.*

To make the comprehension of the structure of the starch fraction in the nanocomposite clearer, we decided to represent it (**Figure IV-23**) on the scheme of Barron (Barron et al. 2001), as previously done for matrices.

Once again, this representation is purely qualitative and it is limited to the hydration/plasticization conditions used in this study (37wt% water content and 22.5wt% glycerol on starch dry mass).

As visible in **Figure IV-23**, starch structure in CNC_1.5 and CNC_2.5 partially overlay to the one of REF-CNC, while CNC_5 and CNC_10 starch structure positioning is shifted to higher depolymerization.

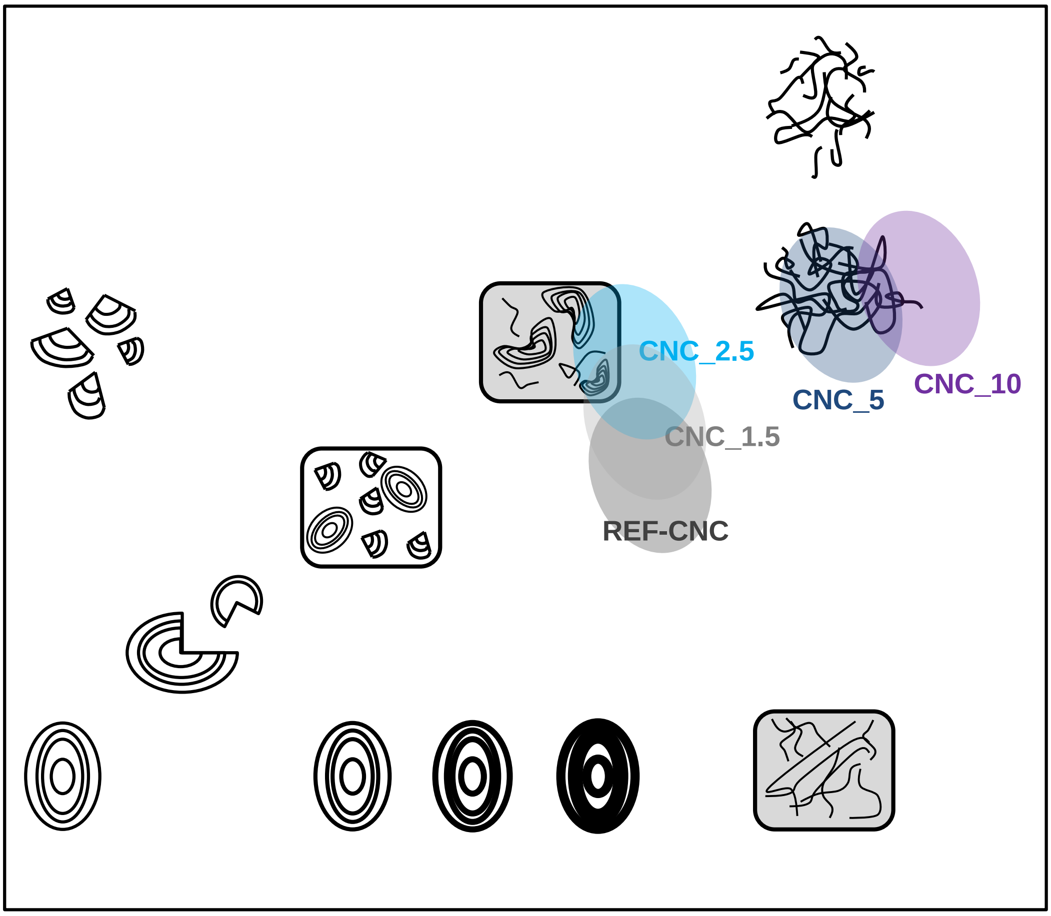

Figure IV-23: *Schematic representation of the mechanism of starch melting under shear, adapted from (Barron et al. 2001). Colored halos are used to illustrate the positioning of starch matrix structure in starch-CNCs nanocomposites after extrusion.*

4.2.2 Starch-ChNCs nanocomposites

Unlike starch-CNCs nanocomposites, starch-ChNCs nanocomposites show a gradual evolution of their structure with increasing ChNC loading in the sample.

At a larger scale, the 2wt% chitin-starch sample ChNC_2 still presents native granules in its structure, similarly to its matrix of reference G20_LOW, due to the shorter screw profile used for its extrusion. Temperature was increased for the subsequent extrusions of ChNC_4 and ChNC_8, and this induced the complete loss of the granular structure.

The presence of residual granules (in ChNC_2) and increasing nanofiller concentrations (in ChNC_4 and ChNC_8) give a visually uneven surface when cryo-fractured nanocomposites are observed by SEM (see III-3). Both constituents (residual granules in ChNC_2 and nanofillers in ChNC_4 and ChNC_8) play a stiffening effect on the starch matrix as well, as pointed out by uniaxial deformation results (see Young's modulus values, **Table IV-7**).

At a smaller scale, starch-ChNCs nanocomposites show different local organizations (crystallinity, local orders) than their reference (G20_LOW). For all starch-ChNCs nanocomposites, the amount of amorphous conformations (as measured through NMR) increases proportionally with ChNC concentration in the sample.
Likewise, the crystalline peaks typical of B-type crystallinity decrease progressively from 2 to 4wt% ChNCs in the sample, and then partially superimpose to the ones of crystalline chitin in ChNC_8.

From a thermomechanical point on view, no reduced intensity of α-relaxation was measured for any chitin-based nanocomposite by DMTA. This confirms that no strong interactions form between starch and nanochitins. The absence of interactions with visible effect on the thermomechanical properties could be explained by the aggregation of ChNCs in the sample already at low loadings (< 2wt%), as represented in **Figure IV-24**.

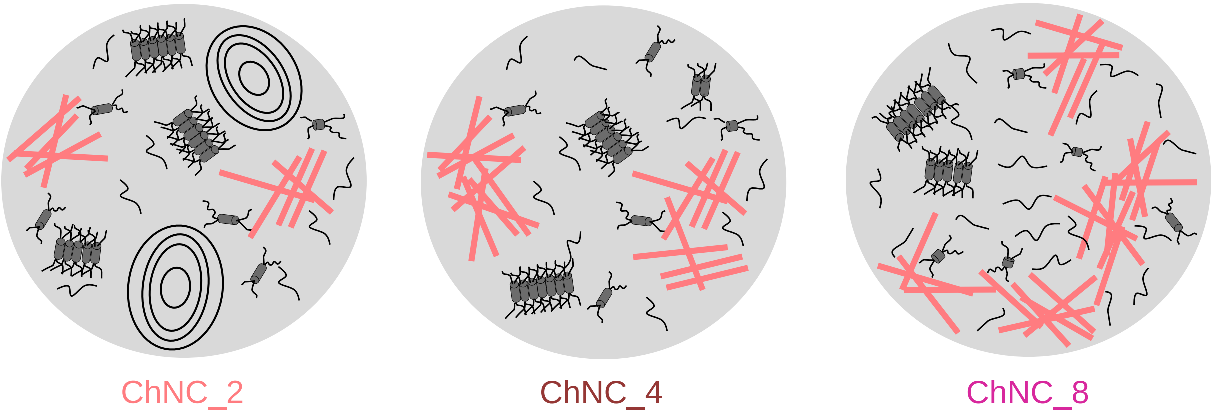

Figure IV-24: *Illustration of starch-ChNCs nanocomposites potential structural organization. Starch simple (black line) or double (grey cylinder) helices, crystallites (packing of grey cylinders), granules (concentric black lines) and ChNCs (pink color) are represented in the system.*

From our inter-particle distance calculations, aggregation between ChNCs could occur between 4 and 8wt% ChNCs in the sample in the case of packed nanocrystals (**Figure III-13b**), which does not agree with the physical properties observed for these samples. It is more probable that aggregation occurs even before extrusion, because of the multiple drying steps necessary in preparing starch-ChNCs formulations (see **Figure II-3**), and any drying step is an opportunity for nanofillers to aggregate.

This hypothesis is confirmed by the lack of percolation in starch-ChNCs nanocomposites: a percolating network should form in the highest concentrated nanocomposite ChNC_8 (ChNCs percolating threshold = 7.5 ± 2.5wt%), but it does not occur here, meaning that the chitin nanocrystals are aggregated.

CNC_4 sample was used to decorrelate the effect of nanofiller type (CNC or ChNC) from the effect of the extrusion parameters on the structure of the nanocomposite. As explained in **Table II-3**, this sample was added with 4wt% of CNCs but it was produced using the same screw profile and extrusion parameters as for ChNC_4.

ChNC_4 and CNC_4 do not present any residual granular structure and their crystalline profiles are very similar, pointing out no differences coming from nanofiller type. Besides, the thermomechanical properties (DMTA) and the behavior at large deformation are the same for the two composites.

The only difference between the two formulations comes from the local organization measured by CP-MAS NMR: ChNCs affect local orders to a lesser extent than CNCs (CNC_4 shows about 10% more simple-helices and 6% less double-helical and paracrystalline structures compared to ChNC_4), meaning that nanofiller type (CNC or ChNC) is an important factor to consider while evaluating local orders.

The schematic representation of starch matrix structure in chitin nanocomposites and CNC_4 is reported in **Figure IV-25**.

As visible from **Figure IV-25**, the positioning of starch structure in the lowest-concentrated nanocomposite (ChNC_2) is quite far from the ones of the other more concentrated nanocomposites, because of the exclusive residual granular organization in this nanocomposite.

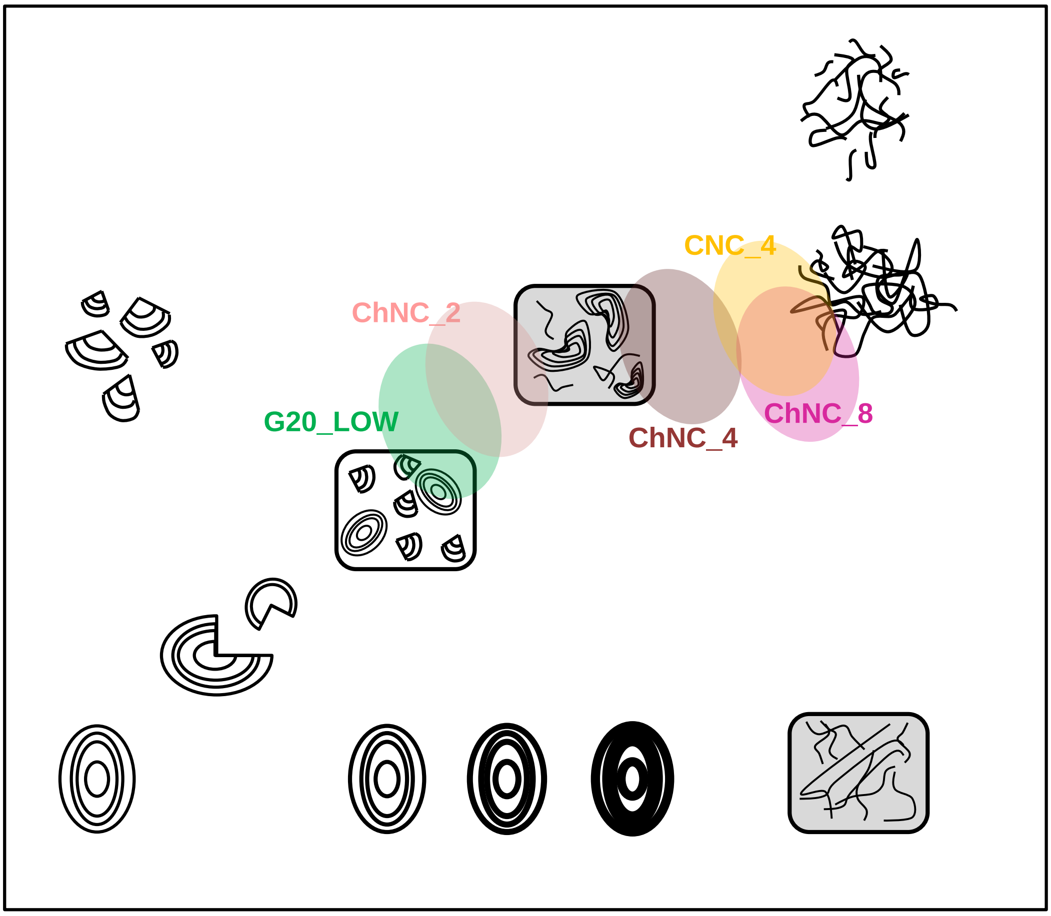

Figure IV-25: *Schematic representation of the mechanism of starch melting under shear, adapted from (Barron et al. 2001). Colored halos are used to illustrate the positioning of starch matrix structure in starch-ChNCs nanocomposites and CNC_4 after extrusion.*

Chapter V

BEHAVIOR IN PHYSIOLOGICAL CONDITIONS

Table of contents

The structure now well-understood and characterized, this study can move onto samples' behavior in physiological conditions (immersion in phosphate buffer at 37-40°C). Hydrophilic materials such as starch sorb water and go through degradation when in contact with water and enzyme. However, the kinetics will depend on the structure and the composition of the sample. At the same time, the material releases glycerol in water (obviously, only for glycerol-plasticized formulations). Those three phenomena occurring together (water ingress in the sample, enzymatic degradation and glycerol release) are deeply intertwined, and are important properties to consider when producing biomaterials: the following chapter will describe them in-depth separately before discussing how they are woven to each other.

1. Glycerol release

^{1}H NMR in D_2O

As done for the determination of the glycerol content in the samples (II-4), one starch-based matrix, one CNCs-starch and one ChNCs-starch nanocomposites were studied for their kinetic of glycerol release in phosphate buffer saline (PBS) over time.

To do this 500 mg of G20_LOW, CNC_5 and ChNC_4 were immersed in 84mL each of PBS (20mM pH 7.0) in which water was substituted with deuterium oxide (D_2O, Eurisotop, FR) and kept in an agitated bath at 37°C for all the duration of the kinetic (see Annexes for the detailed composition of PBS). All samples were cut in square shape from their respective band-shaped extrudate, and thickness was homogeneous among the samples (1.2mm).

At the time of the sampling (0, 5, 10, 15, 30, 60, 90, 240 and 1440min) 1mL of aqueous suspension in contact with the sample was withdrew and put in NMR tubes for glycerol content measurement. The high quantity of PBS-D_2O used for each sample (84mL) was necessary in order not to perturb the concentration of glycerol in the aqueous suspension after each sampling. The glycerol content was analyzed using a Bruker AvanceIII-400 MHz spectrometer for ^{1}H detection operating at a frequency of 400.16 MHz.

Calibration solutions at 0.1, 0.54, 1.08, 3.26, 10.8 and 21.7mM of glycerol and 3-(trimethylsilyl) proprionic-2,2,3,3-d_4 acid sodium salt (Tps, Sigma Aldrich, DE) in PBS-D_2O were prepared as well. Tps was added as standard to confirm the quantitative potential of the technique (**Figure V-1**)*. In addition, PBS-D_2O and calibration solutions were developed in a glove box to avoid solvent (D_2O) denaturation.*

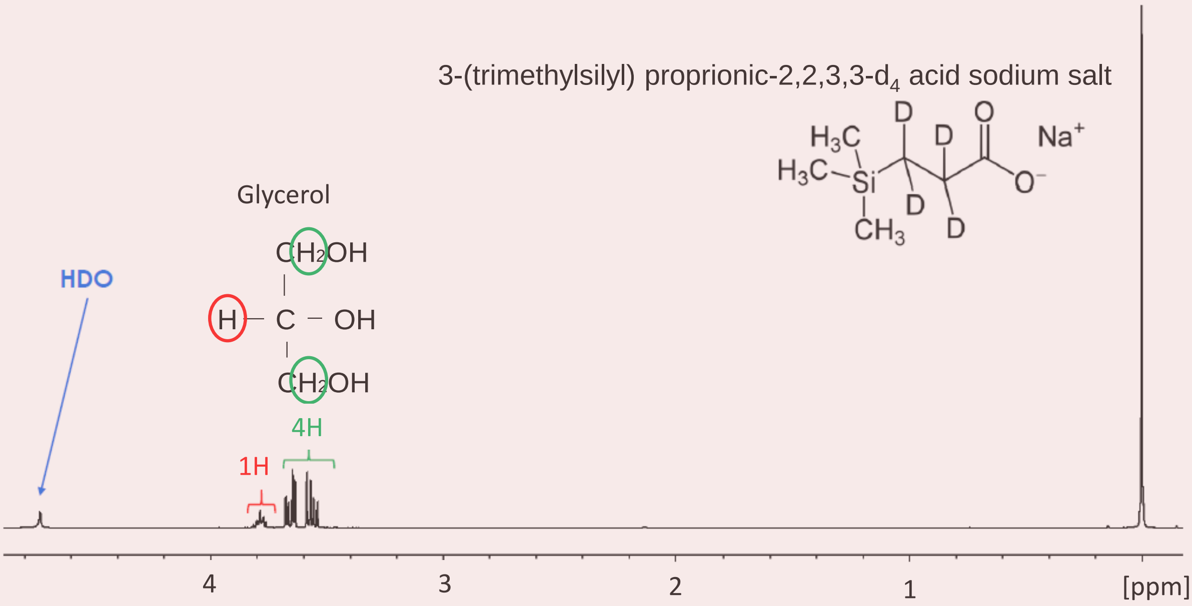

Figure V-1: Typical spectrum of glycerol and Tps solubilized in PBS-D_2O.

Three samples were chosen for their representative composition (one starch-based matrix, one starch-CNCs and one starch-ChNCs nanocomposite), and the kinetic of glycerol release in each was studied using NMR (see the experimental set up above for details, *^1H NMR in D_2O*).

The percentage of glycerol released over time by the samples, reported in **Table V-1**, is computed from the ratio of the concentration (mM) of glycerol at each sampling time and the final concentration of glycerol at equilibrium (t_{1440}) (corresponding to total glycerol content in the sample). See **Equation V-1**:

$$glycerol\,released\ (\%) = \frac{[glycerol_s]}{[glycerol_{tot\,1440}]} \cdot 100 \quad \textbf{[V-1]}$$

As visible from **Figure V-2** the glycerol release is very fast and after 1h of immersion in a phosphate buffer made with deuterium oxide (PBS-D_2O), almost all of the glycerol in the samples has been released.

After 1h, the samples continue to release glycerol, although slower, and after 4h the percentage of glycerol released is near zero and a steady state (**Figure V-2**) is reached for almost all the samples, except for CNC_5 which releases about 2% of glycerol between 4 and 24h. This sample shows the fastest glycerol release at the beginning of the measurement (3.3% at t_0 and 28% at t_5, **Table V-1**) but it rapidly slows down compared to the matrix and the chitin/starch nanocomposite. Half an hour after immersion in PBS-D2O, CNC_5 has only released ~55% of its glycerol content while the other samples have released ~70-75%.

Except for this variation, no significant differences depending on the formulation of the thermoplastic starch-based samples were detected in the kinetics of glycerol release in physiological condition and almost all glycerol was released in the very first hour and a half of immersion in PBS-D_2O, in agreement with the works of Velasquez and colleagues (Velasquez et al. 2015) on glycerol-plasticized starch-based samples.

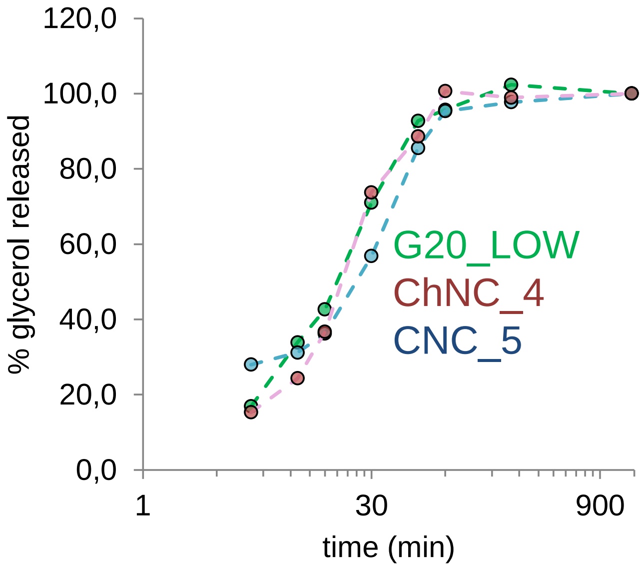

Figure V-2: *Kinetic of glycerol release in physiological conditions of starch-based samples.*

Table V-1: *Numerical values of glycerol release (%) over time from the samples.*

Time (h)	**Glycerol released (%)**		
	G20_LOW	**CNC_5**	**ChNC_4**
0	0.0	3.3	0.8
5	16.9	28.0	15.3
10	33.9	31.2	24.3
15	42.6	36.2	36.7
30	71.0	56.8	73.7
60	92.8	85.6	88.6
90	95.7	95.3	100.7
240	102.3	97.7	98.9
1440	100.0	100.0	100.0

2. Swelling and enzymatic degradation of starch-based matrices

2.1 Swelling

Swelling

Swelling was determined on rounded sections with 1.2 mm thickness and 5 mm diameter cut from the extruded samples. The sections were immersed in 3mL of phosphate buffer saline (PBS, 20mM pH 7.0) and kept in a heater set at 40°C and available in the lab for all the experiment duration.

The experiments were carried out by monitoring the surface increase as a function of the immersion time in PBS. The observations were developed with a binocular (MZ 12.5 Leica) equipped with a camera (SVS-EXO250MGE) for image recording (**Figure V-3**). *Images were registered at predetermined time intervals until equilibrium was reached. The grey level of the images was treated with Matlab® and ImageJ® software to measure the surface expansion of the section as a function of time.*

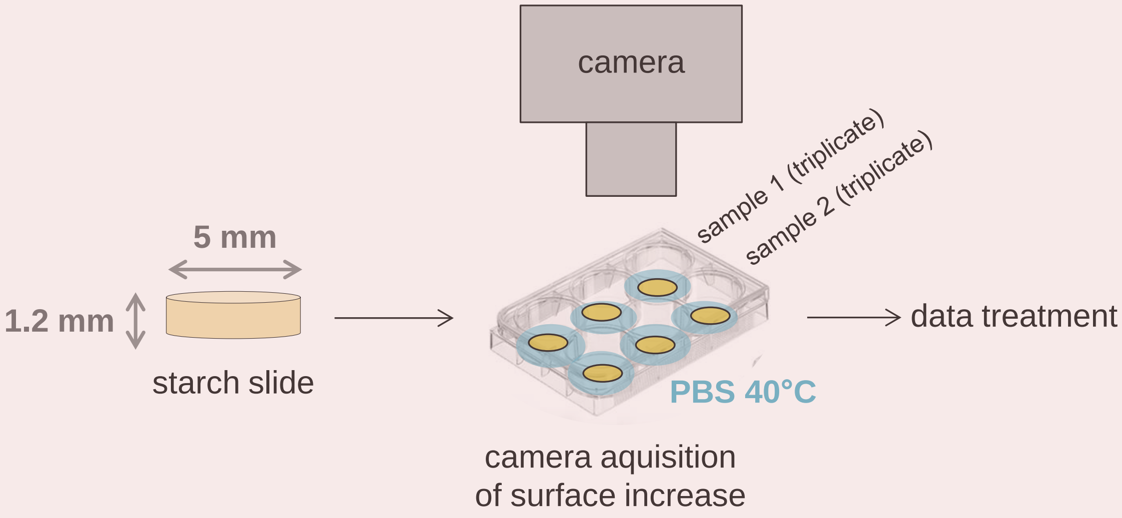

Figure V-3: Swelling experimental setup.

Considering the swelling of the samples as isotropic, the volume of the samples over time is computed by estimating their thickness from their diameter variation, and by multiplying it for the recorded surface. Then the swelling ratio is computed as follows:

$$\textit{Swelling ratio} = \frac{V_t}{V_i} = \frac{l_e \cdot \pi \cdot \left(\frac{d_t}{2}\right)^2}{l_i \cdot \pi \cdot \left(\frac{d_i}{2}\right)^2} \qquad \textbf{[V-2]}$$

where V_i, d_i *and* l_i *are respectively the volume, diameter and thickness at initial time* $t=0$. V_t *and* d_t *are respectively the volume and the diameter at time* t, *while* l_e *is the estimated thickness of the sample at time* t *computed on diameter variation over time. Swelling ratio values are thus comprised between 1 and infinite. Each sample was analyzed in triplicate.*

Starch-based matrices were immersed in a phosphate buffer saline (PBS) solution at 40°C and their swelling was monitored over time with a camera (for details see the experimental set up above, *Swelling*).

As visible in **Figure V-4**, G20 matrices keep a compact and sound shape all over swelling and, at stabilization (t = 24h of immersion in PBS at 40°C), no disintegration occurs for these samples when they are manipulated.

By contrast, during swelling G0 matrices form a gel at their periphery (not visible in the figure) and at the end of the experience they disintegrate if manipulated.

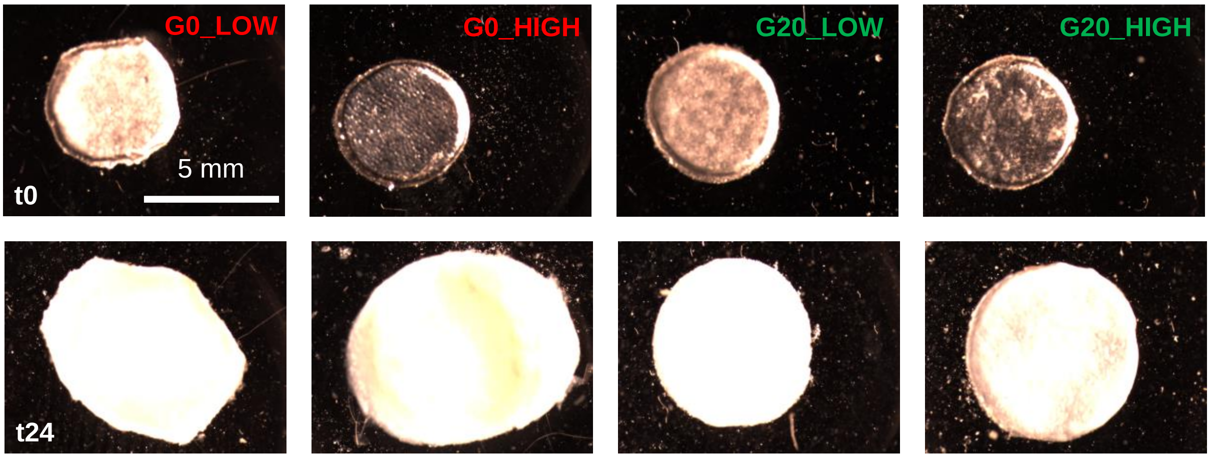

Figure V-4: *Images of sample swelling in PBS at 40°C at the beginning (t=0h) and at the end (t=24h) of the kinetic.*

Swelling ratio evolution over time of the extruded starch-based matrices is reported in **Figure V-5**. As detailed in the experimental set up above, swelling is expressed as a ratio varying between 1 (corresponding to the starting volume of the sample = 0% swelling) and infinite. Before analyzing the swelling ratio kinetics, we can notice that in all the extruded samples swelling is much quicker at the beginning of the suspension in water and then it decreases until the steady state is reached starting from 6h of immersion in PBS, in agreement with previous works (Shi et al. 2006; Velasquez et al. 2015). Stabilization is even faster for G20 samples and REF-CNC, especially for G20_LOW (**Figure V-5**), which is already stable from 90 minutes onward.

The rapid stabilization during immersion that the plasticized samples show is a typical behavior of those materials obtained by extrusion (Nessi et al. 2018; Chevigny et al. 2018). Glycerol, which is very mobile and highly soluble in water, quickly leaves the material when immersed and water takes its place. As a result, the fast exchange of glycerol with water during immersion (see V-1, *Glycerol release*) accelerates stabilization, as proven in previous works (Nessi et al. 2018; Velasquez et al. 2015).

In addition, the crystalline structure which forms in presence of glycerol during stabilization opposes resistance to water and contributes to the limited total swelling of the samples. Indeed G20_HIGH, REF-CNC and G20_LOW stabilize at the low swelling ratios of 2.7 (170 ± 25% swelling of the starting volume), 2.5 (150 ± 25% of the starting volume) and 1.8 (80 ± 10% of the starting volume) respectively (**Figure V-5**). Swelling is the lowest for G20_LOW (**Table V-2**) because of the presence, in this sample, of 25% residual granules, which are almost insoluble in PBS at this temperature (40°C).

Swelling is the highest for G0_HIGH and it stabilizes at a swelling ratio of ~ 4 (which corresponds to 300 ± 25% of the starting volume) from 24h (**Figure V-5**) of immersion in PBS; this is due to the total absence of a semi-crystalline network, glycerol and residual granules in this highly-destructurized amorphous matrix. G0_LOW stabilizes as well from 24h at a lower swelling value of 3.5 (250 ± 35% of the starting volume) because of the partial preservation of native granules (16%) in the sample (**Table V-2**).

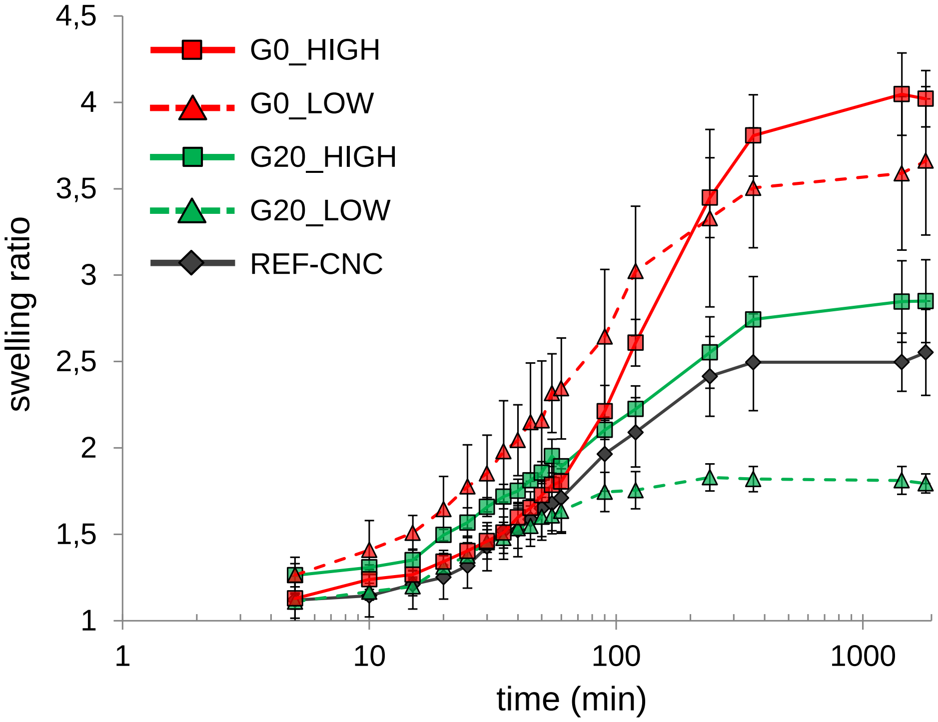

Figure V-5: *Swelling ratio of extruded starch-based samples as a function of immersion time in PBS at 40°C.*

Peppas and Sinclair (Peppas & Sinclair 1983) developed a semi-empirical model to analyze the water transport process in glassy polymer samples. Even if the samples analyzed in this work are glassy at room temperature, the use of this model is quite delicate, because of the differences in Tg among the samples. This model is useful to determine if the transport diffusion mechanism follows a Fickian, a Case II or anomalous transport behaviour. This model suggests that normalized water uptake $\left(\frac{M_t}{M_\infty}\right)$ at any time can be characterized as reported in **Equation V-3**:

$$\frac{M_t}{M_\infty} = a\, t^b \quad \text{[V-3]}$$

Where M_t and M_∞ are the mass of water (mg) absorbed at time *t* (s) and at equilibrium respectively. a is a constant incorporating characteristics of the macromolecule network system and the penetrant, and *b* is a diffusional exponent, which is indicative of the transport diffusion mechanism. This equation is valid only in the first 60% of the total water uptake $\frac{M_t}{M_\infty}$. Fickian diffusion is defined by *b* equal to 0.5 while Case II diffusion is obtained for *b* equal to 1. Anomalous transport behaviour is obtained for *b* values intermediate between 0.5 and 1 (Peppas & Brannon-Peppas 1994).

The starch-based matrices developed in this work show a behaviour which is intermediate between the Fickian and the Case II transport behavior (*b* coefficient comprised between 0.5 and 1, **Table V-2**). However the Fickian model can fit the experimental data well enough to approximate a diffusion coefficient. The Fickian model for thin polymer samples (**Equation V-4**) was used to estimate the magnitude of water diffusion in the extruded samples:

$$\frac{M_t}{M_\infty} = 1 - \sum_{n=0}^{\infty} \frac{8}{(2n+1)^2\pi^2}\, exp\left(\frac{-D(2n+1)^2\pi^2}{l^2}\, t\right) \quad \text{[V-4]}$$

Where *l* (m) is the thickness of the thin polymer sample and *t* (s) is the time at which M_t is measured. The choice of the "thin polymer samples" model was driven by the geometry of the samples used for the swelling test (large surface and reduced thickness).

The results obtained using this model are reported in **Table V-2**.

From the study of diffusion coefficients in **Table V-2**, matrices extruded with glycerol G20_LOW and REF-CNC show the highest diffusion coefficients, especially G20_LOW (D = 3.9E-11 m s^{-1}, **Table V-2**). Water enters rapidly in these samples because of the fast exit of glycerol (which induces free volume in the material) and, when native granules are preserved as in G20_LOW, diffusion is even faster. The semi-crystalline granules preserved may form a heterogeneous structure which sustains the ingress of water, while contributing to maintain the initial structure of the sample during immersion, because of the bonding (cross-linking or hydrogen bonding) of the residual granules with neighbouring molecules (Nessi et al. 2018).

Table V-2: *Diffusion coefficients and diffusional exponent (b) for starch-based matrices.*

Sample	D ($m^2 s^{-1}$)	b coefficient	Swelling max (%)	Residual granules (%)
G0_LOW	1.9E-11	0.52	250 ± 35	16
G0_HIGH	6.2E-12	0.78	300 ± 25	0
G20_LOW	3.9E-11	0.80	80 ± 10	25
G20_HIGH	1.9E-11	0.56	170 ± 25	0
REF-CNC	2.3E-11	0.82	150 ± 25	0

Water diffusion decreases to lower values when the native structure is completely destroyed (the sample is more homogeneous), the structure is more amorphous and starch chains are partially depolymerized as in G20_HIGH (D = 1.9E-11 m s^{-1}, **Table V-2**). The same low water diffusion coefficient is observed for G0_LOW (D = 1.9E-11 m s^{-1}, **Table V-2**), even if this matrix possesses a microstructure with residual granules; the slow entry of water is due to the lack of a fast water-glycerol exchange in this sample during immersion. Besides, the reduced chain mobility (see Tg values, IV-3.1) in the glassy materials extruded without glycerol is responsible for the slower relaxation of the polymer network, which accounts for the slow entry of water.

Water diffuses even slower in the glassy highly-destructurized matrix G0_HIGH (D = 6.2E-12 m s^{-1}, **Table V-2**), because of its more amorphous and homogeneous structure.

2.2 Enzymatic degradation

The rate at which water enters in the sample determines the rapidity at which enzymes attain starch and start the hydrolysis process. To assess the correlation between swelling and enzymatic degradation, starch-based samples have been hydrolyzed by using α-amylase as reported below.

Enzymatic hydrolysis

Enzymatic hydrolysis is performed using porcine pancreatic α-amylase (PPA, Sigma-Aldrich, EU). Rather than mix multiple enzymes, the use of amylase is a more rapid and well accepted method to estimate starch-based materials enzymatic degradation (Vikman et al. 1995).

For every hydrolysis test, an enzymatic solution of 1 g of PPA in 20 mL of phosphate buffer (PBS, 20mM pH 7.0) is prepared.

The enzyme is suspended in PBS by mild stirring and then centrifuged at 9000g at 4°C for 10 min to free the suspension from the most insoluble fraction.

To free the enzyme from lactose (which would interfere with total sugar content determination), the enzymatic solution is dialyzed against a Spectra/Por Dialysis Membrane (MWCO: 6-8.000) for 24h at 4°C before each test.

Enzyme concentration and activity are checked before every hydrolysis to adjust the quantity of enzymatic solution to add in every vial and have the same ratio enzyme/substrate for each hydrolysis. Enzyme activity was computed as:

$$Enzyme\ activity\ (IU\ mL^{-1}) = \frac{\Delta DO}{P} * \frac{1}{t} * \frac{v}{Ve} * F \quad \textbf{[V-5]}$$

Where ΔD0 *is the difference in absorbance at 405 nm between the sample and the calibration,* P *is the slope of p-nitrophenol calibration curve at 405 nm (mL µmol^{-1}),* t *is time at which the absorbance at 405 nm is measured (min),* v *is the final volume of the test (0.15 mL),* Ve *is the volume of extract used for the test (0.025 mL) and* F *is the enzyme dilution factor.*

200 mg of starch-based sample are incubated with 200 mL of PBS supplemented with 0.25mM of $CaCl_2$ and containing 1200 IU of PPA. Enzyme excess conditions were used to obtain a complete hydrolysis kinetic of the samples in three days. Samples were analyzed in duplicate.

Enzymatic hydrolysis was carried out on 52 h in water agitated bath at 37°C. Substrate blank test (only sample in PBS) and enzyme blank test (only enzyme in PBS) were carried out as controls. Aliquots were collected at predetermined time intervals and put into an ice bath, in order to stop the hydrolysis process. Aliquots were centrifuged twice at 4630g for 5 min at 4°C, kept in boiling water bath at 90°C for 5 min and centrifuged again in order to remove enzyme and impurities. Supernatants were analyzed for their total sugar content by the orcinol sulfuric method (Planchot et al. 1997) (see III-2, Determination of total sugar concentration by the orcinol-sulfuric method).

The following equation **[V-6]** *was used to calculate the fraction of total sugar release at a given time:*

$$\%\ total\ sugar\ release = \frac{C \cdot 0.9 \cdot V \cdot 100}{m \cdot \%DM} \quad \textbf{[V-6]}$$

Where C *is the glucose concentration (mg L^{-1}),* 0.9 *is the conversion factor of glucose in polymer,* V *is the reactive initial volume (L) and* 100 *is a factor to express results in percentage.*

m *is the weighted substrate mass (mg) and* %DM *is the dried starch percentage of the sample. The use of* %DM *allows normalizing the total sugar release at a given time on the weight fraction of starch in the sample (without water or glycerol or nanofillers).*

The total sugar release is an indirect index of the susceptibility of starch to the enzymatic digestion and gives information about the sample degradation degree. The time-series of sugar release were fitted using a Weibull function, as proposed by Kansou and colleagues (Kansou et al. 2015) for hydrolysis of starch. The Weibull function is a general empirical model used for modelling first-order reaction kinetics in heterogeneous conditions (Kansou et al. 2015):

$$f(t) = a(1 - exp(-bt^{1-c})) \quad \textbf{[V-7]}$$

Where f(t) is the total sugar content at the time of the sampling.

The three parameters provide information about the kinetic of the hydrolysis process.
***a** refers to the total sugar release at infinity.*
***b** is the reaction coefficient; formally it is an estimation of the slope during the first hour relatively to **a** (higher is **b** value and faster is the degradation kinetic during the first stage).*
***c** is a curve shape parameter with a value usually comprised between 0 and 1; for **c**=0 the function is exponential while for **c**=1 a constant function is obtained. **c** expresses the linear decrease of the reaction coefficient over time (whose maximum is **b**).*
*The more **c** is close to 1, the more the total sugar release kinetic rate decreases during time (Kopelman 1988). If the fitting assigns a negative value for **c**, this produces a sigmoid curve and indicates an acceleration of the hydrolysis kinetics during the very first instant of the reaction.*

Figure V-6 reports the total sugar release kinetics of starch-based matrices by α-amylase during immersion in phosphate buffer (PBS) while **Table V-3** accounts for Weibull function parameters values for hydrolysis kinetics.

In analogy with the work of Englyst (Englyst et al. 1996) on the digestion of starch *in vitro*, starch could be classified in three major fractions (rapidly digestible, slowly digestible and resistant starch) depending on the rate and the extent of its enzymatic hydrolysis. The experimental times and procedure used by Englyst are not the same used in this work but it is of interest to mention the classification developed by this author.

On the whole, the amount of free sugar increases rapidly following a linear dependence with time in the first hours of hydrolysis, as visible in **Figure V-6**. This behavior is classical of hydrolysis of starch in heterogeneous condition (Tawil et al. 2011).

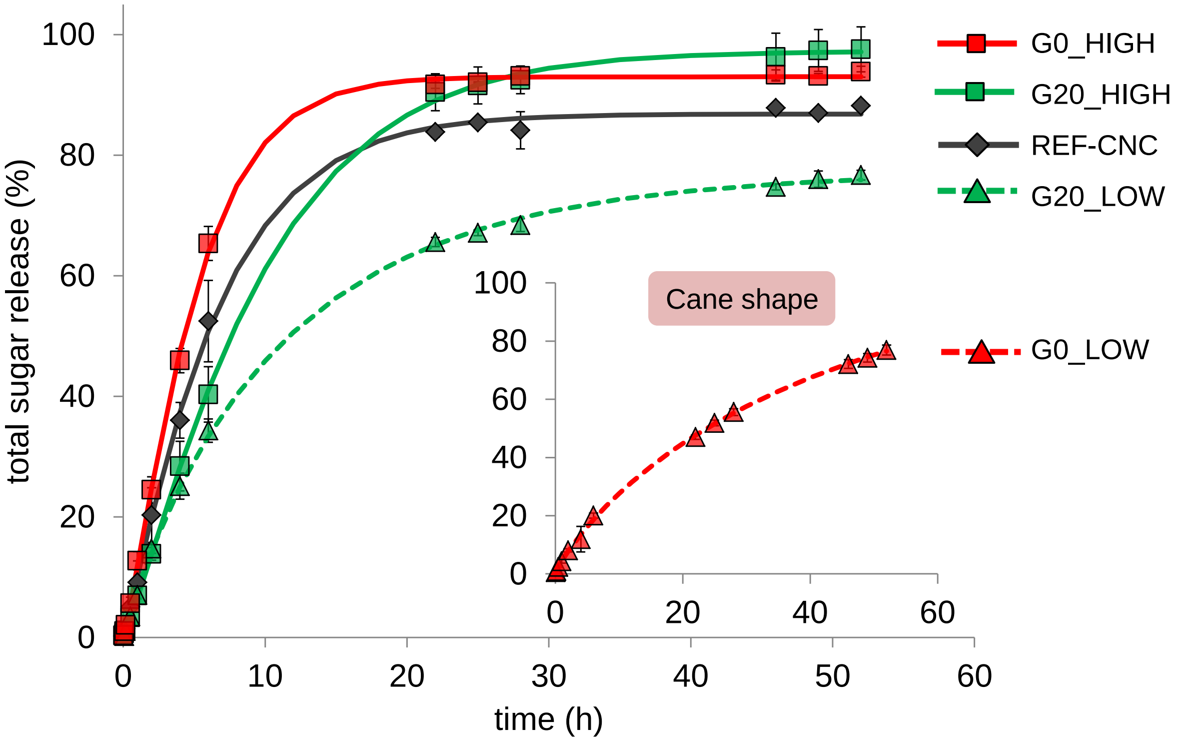

Figure V-6: *Total sugar release from starch-based matrices over time. Curve fitting is provided by the Weibull model.*

The rapid sugar release corresponds to the degradation of rapidly digestible starch (RDS) fractions generated during the extrusion process.

From 8-10 h the slope of the curve changes, the kinetic slows down leading to a stabilization of the hydrolysis from 22 h, except for G0_LOW. Here slowly digestible starch (SDS) fractions are degraded by the enzyme. Then, stabilization is reached when only resistant starch (RS) is leftover in the sample, likely comprising retrograded starch and residual native granules (Englyst et al. 1992) in the sample.

RS is computed as the difference between the maximum possible total sugar release (100%) at infinity and the effective total sugar released by the sample, given by the sum of RDS and SDS fractions (**Equation V-8**):

$$\mathrm{RS} = 100 - (RDS + SDS) \qquad \textbf{[V-8]}$$

As expected from its microstructure, G20_LOW shows the lowest total sugar release at infinity (*a* = 77 ± 5%, **Table V-3**). As the semi-crystalline structures in the samples decrease, the hydrolysis reaches higher total sugar release values, as in REF-CNC (*a* = 87 ± 5%, **Table V-3**) and G20_HIGH (*a* = 97 ± 5%, **Table V-3**) respectively.

G0_HIGH reaches similar total sugar release at infinity (*a* = 93 ± 5%, **Table V-3**) compared to G20_HIGH, in accordance with its completely amorphous structure (see IV-1).

G0_LOW behaves differently from all the other samples; this sample was extruded in cane-shape because its high viscosity made it impossible to use the plate die to produce a band-shaped sample (see II-3.1). The cylindrical shape of the sample is responsible for the lower surface exposed to the enzyme and the restricted access to its core; this slows down the kinetic, giving a quasi-linear shape to the curve and leading to a maximum estimated hydrolysis value of about 100% at infinite time (*a* value, **Table V-3**).

b and *c* parameters (**Table V-3**) were then used to support the description of total sugar release kinetics reported in **Figure V-6**.

Table V-3: *Values of Weibull function parameters for total sugar release kinetics of starch based matrices; a=maximum value (%), b=average slope during the first hour, c=curvature strength.*

Sample	coefficient			R²
	a¹	b²	c²	
G0_LOW	100*	0.04	0.15	0.99
G20_LOW	77	0.11	0.09	0.99
G0_HIGH	93	0.14	-0.19	0.99
G20_HIGH	97	0.07	-0.16	0.99
REF-CNC	87	0.12	-0.11	0.99

computed standard deviations
1 = 5%
2 = 0.01
** fixed at bound*

In G20_LOW and REF-CNC the enzyme enters rapidly with water (see diffusion values, **Table V-2**) and this leads to the high reaction coefficient (*b* = 0.11 and *b* = 0.12 respectively, **Table V-3**) observed for these samples. The reaction coefficient is even higher in G0_HIGH (*b* = 0.14, **Table V-3**), pointing out the high speed of sugar release in the first hour: this is due to the solubilizing of an important part of the sample in water (not shown), in addition to enzymatic hydrolysis.

The reaction is slower for G20_HIGH and G0_LOW (b = 0.07 and b = 0.04 respectively, **Table V-3**). In G20_HIGH water diffuses slower (see diffusion values, **Table V-2**) and, with it, the enzyme inside the sample. In G0_LOW the cylindrical shape of the sample must have slowed down the access of water and enzyme to the core of the sample and, thus, its hydrolysis.

For the curve shape parameter c, more destructurized samples (G0_HIGH, G20_HIGH and, to a lesser extent, REF-CNC) show a negative value of c, which means that the kinetic is accelerated at the very beginning of the hydrolysis process. This is probably linked to the reduced length of their starch chains, which are thus more digestible for the enzyme (Butterworth et al. 2011). Indeed acceleration is more accentuated for G0_HIGH and G20_HIGH (c = – 0.19 and c = – 0.16 respectively, **Table V-3**) than for REF-CNC (c = – 0.11, **Table V-3**) which shows longer starch chains (see III-2).

3. Swelling and enzymatic degradation in nanocomposites

3.1 Cellulose nanocrystal-starch nanocomposites

3.1.1 Swelling

Swelling kinetics of starch-CNCs nanocomposites are reported in **Figure V-7**. All the samples maintain a compact and sound structure until the end of the experiment, as seen for the other glycerol-plasticized samples (G20) in **Figure V-4**. No disintegration is observed during immersion in water.

Although all samples present a classical swelling behavior with a fast water sorption and the reaching of a plateau after few hours (**Figure V-7**), some differences persist among the samples. The swelling ratio of nanocomposites at lower CNC concentrations (CNC_1.5 and CNC_2.5) stabilizes at around 2.3 (which corresponds to 130 ± 10% swelling of the starting volume) from 4h (**Figure V-7**) of immersion in phosphate buffer. On the contrary, nanocomposites at higher CNC concentrations stabilize after a longer immersion time (6h) and at swelling ratios higher than reference REF-CNC (swelling ratio = 2.5, 150 ± 25% of the starting volume): 2.7 (170 ± 7% of the starting volume) for CNC_5 and 3.3 (230 ± 15% of the starting volume) for CNC_10.

Differences in swelling among the nanocomposites are due to the presence of CNCs in the sample. Starch and cellulose are highly hydrophilic materials because of their numerous hydroxyl groups. However CNCs cannot be responsible for the high swelling ratio of the sample because they are less hygroscopic than starch due to their high degree of crystallinity (Rico et al. 2016). Previous works have shown that the introduction of well-dispersed CNCs in a hydrophilic matrix induces the formation of inter-molecular hydrogen bonds between the two components (Popescu 2017). As a result, the water sorption of the nanocomposite decreases with increasing nanofiller concentration due to the formation of a physical bonding with the matrix. Indeed the bonding of starch with cellulose decreases the number of sites available for water to bind, reducing the sensitivity of starch to water.

CNC_1.5 and CNC_2.5 show a lower swelling compared to the matrix which supports this hypothesis. This effect is however lost at higher concentrations (5 and 10wt%), which agrees with the hypothesis of aggregation. CNCs no more do interact with starch and rather form unconnected aggregates with a drastically lower specific surface: the nano-effect is thus lost.

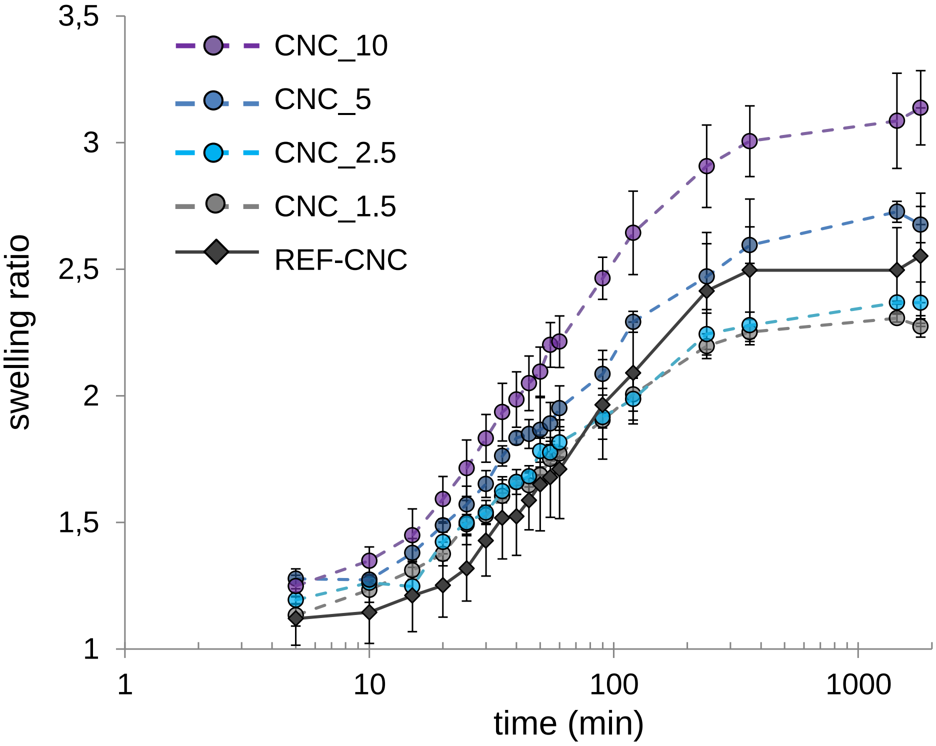

Figure V-7: *Swelling ratio of CNCs-starch nanocomposites as a function of immersion time in PBS at 40°C. REF-CNC curve is reported for comparison.*

As done for starch-based matrices, a Fickian model for thin polymer samples (see **Equation V-4**) was applied to model the composites swelling kinetics to obtain an approximation of their diffusion coefficients (**Table V-4**). All the samples present an anomalous behavior as pointed out by *b* coefficient in **Table V-4**, but their experimental data fit well enough this Fickian model to approximate diffusion coefficients.

Diffusion coefficients of all starch-CNCs nanocomposites are very similar to the one approximated for REF-CNC (**Table V-4**), meaning that CNCs do not influence the water diffusion in the composites.

Table V-4: *Diffusion coefficients and diffusional exponent (b) for starch-CNCs nanocomposites and their matrix of reference REF-CNC.*

Sample	D ($m^2\ s^{-1}$)	b coefficient	Swelling max (%)	Residual granules (%)	Potential NPs aggregation
REF-CNC	2.3E-11	0.82	150 ± 25	0	-
CNC_1.5	2.7E-11	0.72	130 ± 10	0	no
CNC_2.5	2.6E-11	0.64	130 ± 10	0	no
CNC_5	2.5E-11	0.58	170 ± 7	0	yes
CNC_10	2.4E-11	0.68	230 ± 15	0	yes

3.1.2 Enzymatic hydrolysis

When enzymes are added to the physiological system, they cleave down starch molecules and sugars are released from the sample. Total sugar release kinetics of starch-CNCs nanocomposites are reported in **Figure V-8.**

Nanocomposites do not show any clear correlation between CNC content and total sugar release at infinity or curvature strength (*a* and *c* parameter respectively, **Table V-5**).

Table V-5: *Values of Weibull function parameters for total sugar release kinetics of starch-CNCs nanocomposites. Values of REF-CNC are reported for comparison; a=maximum value (%), b=average slope during the first hour, c=curvature strength.*

Sample	coefficient			R^2
	a^1	b^2	c^2	
REF-CNC	87	0.12	-0.11	0.99
CNC_1.5	92	0.08	-0.11	0.99
CNC_2.5	87	0.06	-0.16	0.99
CNC_5	84	0.12	-0.07	0.99
CNC_10	92	0.14	0.13	0.99

computed standard deviations
1 = 5%
2= 0.01

All samples are hydrolyzed between 85 and 90% (±5%) and present a negative curvature strength parameter, as observed for destructurized starch-based matrices (**Table V-3**). Only

CNC_10 presents a value of *c* near to zero but positive, but we are not able to explain this difference. In any case, the values are closer to 0 than to 1, pointing out the high speed of the kinetic already at the very beginning of the enzymatic degradation process.

It is interesting to notice that nanocomposites of lower CNC concentrations (CNC_1.5 and CNC_2.5) are degraded differently from nanocomposites of higher CNC concentrations and their matrix of reference (REF-CNC). CNC_1.5 and CNC_2.5 swell less compared to the other nanocomposites and this possibly slows down the entrance of the enzyme, with water, in the sample. Up to 6 h of hydrolysis CNC_1.5 and CNC_2.5 are hydrolyzed up to 39 and 31% respectively, while REF-CNC and nanocomposites at high CNC concentrations are hydrolyzed up to ~50%.
Indeed CNC_5 and CNC_10 show a reaction coefficient (*b* = 0.12 and *b* = 0.14 respectively, **Table V-5**) similar to the one of REF-CNC and much higher compared to CNC_1.5 and CNC_2.5 (*b* = 0.08 and *b* = 0.06 respectively, **Table V-5**).

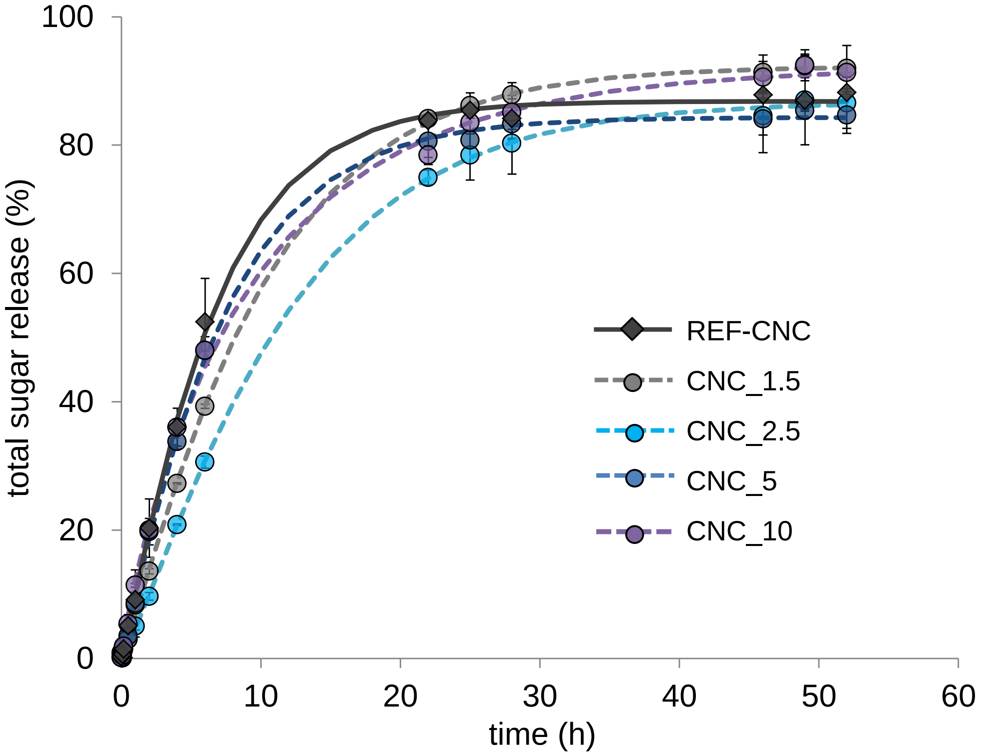

Figure V-8: *Total sugar release from starch-CNCs nanocomposites over time. REF-CNC curve is reported for comparison. Curve fitting is provided by the Weibull model.*

As previously suggested for swelling, the slowed down enzymatic hydrolysis observed for CNC_1.5 and CNC_2.5 is compatible with the formation of an inter-molecular hydrogen bonding between starch and CNCs; this would hinder the easy and rapid access of the enzyme to starch chains, slowing down the hydrolysis.

3.2 Chitin nanocrystal-starch nanocomposites

3.2.1 Swelling

Figure V-9 accounts for swelling kinetics of starch-ChNCs nanocomposites. Their matrix of reference (G20_LOW) is reported for comparison.

Like the other glycerol-plasticized samples (see **Figure V-4**), starch-ChNCs show no disintegration during immersion in water.

Because of the structural differences identified in the previous chapter (complete loss of native granules, the more amorphous local structure as measured by NMR and the less crystalline structure as measured by WAXS) the starch/chitin nanocomposites with higher ChNC concentrations (ChNC_4 and ChNC_8) behave differently in physiological conditions from the composite at the lowest ChNC concentration (ChNC_2).

The swelling ratio of ChNC_2 stabilizes at the low value of about 2.3 (which corresponds to 130 ± 10% swelling of the starting volume) (**Figure V-9**). Already at this low amount of ChNCs in the sample, the swelling ratio is higher than in the reference G20_LOW and it stabilizes later, from 6h compared to the 1h and half of the reference (**Figure V-9**). The presence of a lower amount of residual native granules in the nanocomposite (18% for ChNC_2 against 25% for G20_LOW) and the potential nanofiller aggregation could be responsible for the higher swelling ratio observed for this sample.

ChNC_2 shows a diffusion coefficient (D = 3.2E-11 m s^{-1}) very similar to the one of its reference (G20_LOW, D = 3.9E-11 m s^{-1}, **Table V-6**) which indicates unambiguously the fast diffusion of water in this nanocomposite.

The swelling rises with the ChNCs concentration to 2.7 (170 ± 7% of the starting volume) and 2.9 (190 ± 5% of the starting volume) for ChNC_8 and ChNC_4, respectively (**Figure V-9**), because of the structural changes described above and because of the increasing nanofiller aggregation.

As previously mentioned for starch/cellulose composites, aggregates expose lower specific surface to the starch matrix, preventing the formation of numerous inter-molecular hydrogen bonds with it. Besides, ChNCs aggregates may perturb thermoplastic starch continuous network and increase the sensitivity of starch to water.

Water diffusion speed decreases as ChNCs are added at increasing concentration in thermoplastic starch (**Table V-6**). This could be generated, in addition to the more amorphous structure and the loss of the granular structure in the nanocomposites with ChNCs, by the creation of a tortuous path by the nanocrystals in the sample.

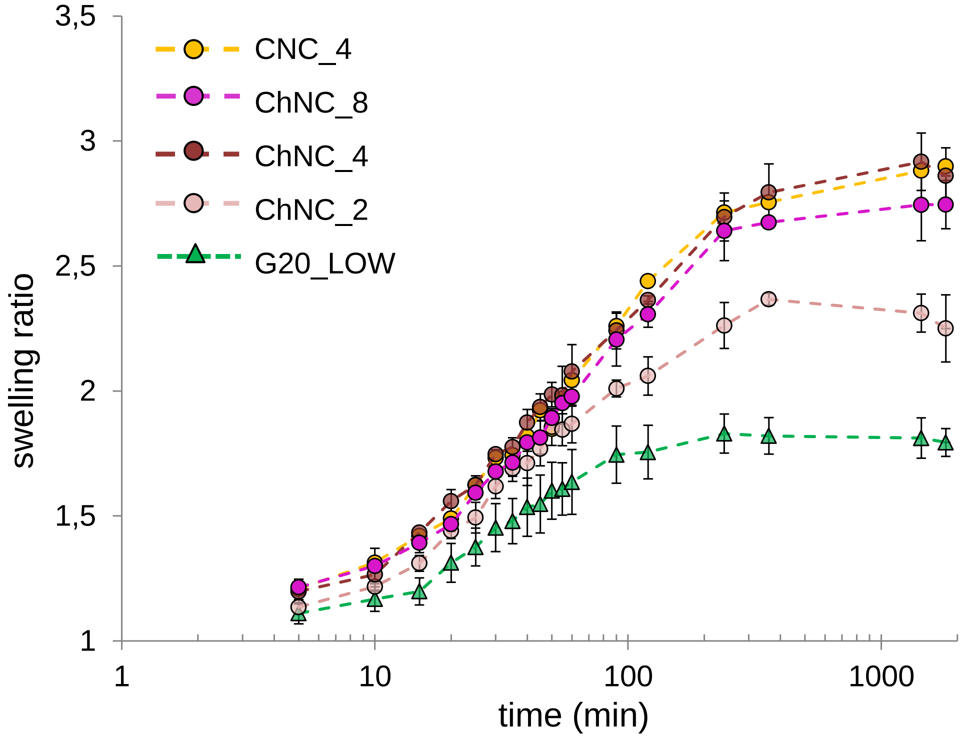

Figure V-9: *Swelling ratio of ChNCs-starch nanocomposites as a function of immersion time in PBS at 40°C. G20_LOW curve is reported for comparison.*

The sample CNC_4 shows exactly the same behavior as ChNC_4 and it reaches the same maximum swelling ratio of 2.9 (190 ± 7% of the starting volume), meaning that nanofiller type does not affect swelling properties.

Table V-6: *Diffusion coefficients and diffusional exponent (b) for starch-ChNCs nanocomposites and their matrix of reference G20_LOW.*

Sample	**D ($m^2 s^{-1}$)**	**b coefficient**	**Swelling max (%)**	**Residual granules (%)**	**Potential NPs aggregation**
G20_LOW	3.9E-11	0.80	80 ± 10	25	-
ChNC_2	3.2E-11	0.84	130 ± 10	18	yes
ChNC_4	2.4E-11	0.72	190 ± 5	0	yes
ChNC_8	1.3E-11	0.64	170 ± 7	0	yes
CNC_4	2.1E-11	0.66	190 ± 7	0	yes

3.2.2 Enzymatic hydrolysis

Figure V-10 reports the total sugar release of starch-ChNCs nanocomposites during immersion in PBS at 37°C in the presence of enzymes (α-amylase). Numerical values for Weibull fitting are reported in **Table V-7**.

As previously observed for swelling, a clear tendency between ChNCs content and total sugar release at infinity, reaction coefficient and curvature strength (*a*, *b* and *c* parameters respectively, **Table V-7**) can be established between lower (2wt%) and higher (4 and 8wt%) nanofiller content in the starch matrix.

ChNC_2 shows a lower total sugar release at infinity (*a* = 78 ± 5%) and a higher reaction coefficient (*b* = 0.21, **Table V-7**) compared to ChNC_4 and ChNC_8 which, conversely, are hydrolyzed between 87 and 92% (± 5%) at infinity and show a slightly slower kinetic during the first hour (*b* = 0.15-0.16, **Table V-7**, see **Figure V-10 focus**). After one hour, the more concentrated nanocomposites are hydrolyzed much faster compared to ChNC_2, as visible from the kinetics of sugar release in **Figure V-10**.

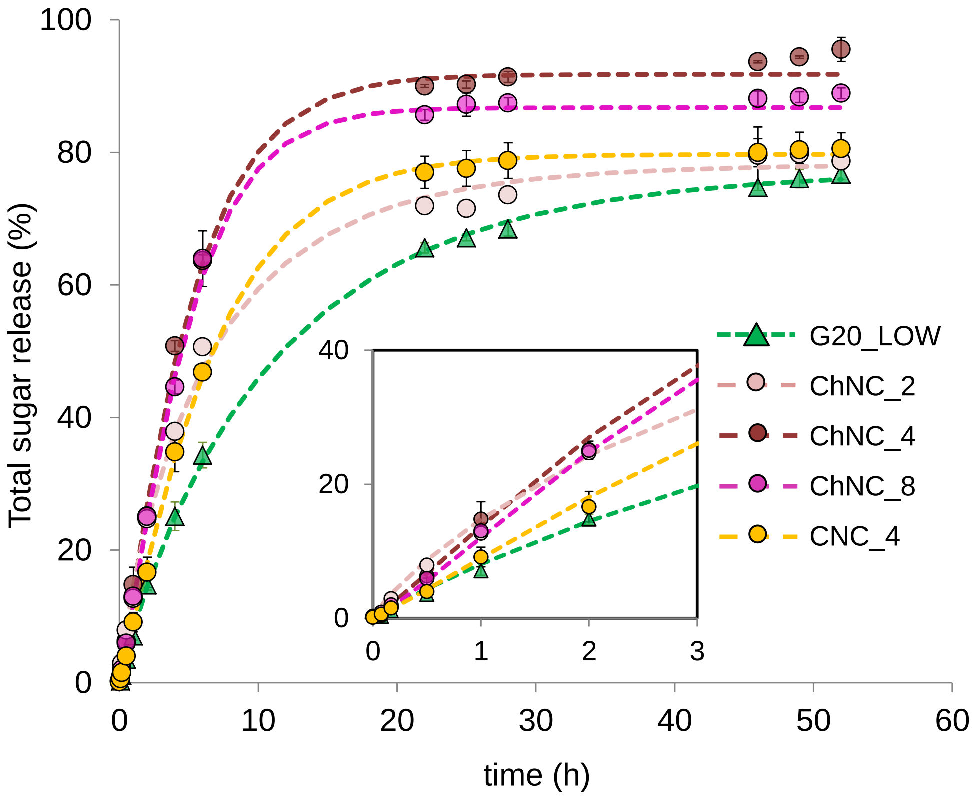

Figure V-10: *Enzymatic hydrolysis of starch-ChNCs nanocomposites over time. G20_LOW curve is reported for comparison. Curve fitting is provided by the Weibull model.*

As expected, ChNC_2 sugar release at 52h is close to the one of its matrix of reference (G20_LOW, **Figure V-10**) because it presents an important resistant starch (RS) fraction (18% residual granules, see **Table V-6**). However, compared to the matrix, the nanocomposite shows a significantly faster kinetic, probably because of the higher swelling of the sample (**Figure V-9**) which favors the fast diffusion of the enzyme inside the sample. For example, after 6h of hydrolysis, ChNC_2 is hydrolyzed up to 50% while G20_LOW up to 33% only.

Due to its exponential sugar release kinetic, ChNC_2 shows a positive curvature strength parameter (c = 0.17, **Table V-7**) while ChNC_4 and ChNC_8 show negatives values for this parameter (c = -0.11 and -0.18 respectively, **Table V-7**). The negative curve strength parameter observed for the more concentrated nanocomposites is coherent with the ones observed for starch-CNCs nanocomposites and matrices without any residual granule: the loss of highly-organized structures as is the native starch granules and the reduced length of their starch chains in these samples (compared to G0_LOW and G20_LOW) may facilitate the access of enzymes to larger and more digestible starch fractions.

Table V-7: *Values of Weibull function parameters for hydrolysis kinetics of starch-ChNCs nanocomposites; a=maximum value (%), b=average slope during the first hour, c=curvature strength.*

Sample	coefficient			R^2
	a^1	b^2	c^2	
G20_LOW	76	0.10	0.05	0.99
ChNC_2	78	0.21	0.17	0.99
ChNC_4	92	0.16	-0.11	0.99
ChNC_8	87	0.15	-0.18	0.99
CNC_4	80	0.12	-0.11	0.99

computed standard deviations
1 = 5%
2= 0.01

The CNC_4 reaction coefficient (b = 0.12) and curvature strength parameter (c = -0.11, **Table V-7**) are close to ChNC_4 ones. However, CNC_4 has a much lower total sugar release at infinity than ChNC_4 (a = 80 and 92 ± 5% respectively), pointing out the presence of more RS in the cellulose-based nanocomposite compared to the chitin-based one. The extrusion of CNC_4 starch/cellulose blend with a shorter screw profile might be the reason for this higher RS fraction even if, structurally, this sample is not different from ChNC_4 (same rate of B-type crystallinity, no residual granules).

4. Degradation of starch-based samples in blood plasma conditions

The starch-based matrix REF-CNC was also hydrolyzed at a lower enzyme activity, to have an idea of the average lifespan of the extruded materials during implantation, far from sites with high α-amylase concentration. This was done at the average enzyme activity of blood plasma, 68 IU L^{-1}, measured by (Nagler et al. 2002).

The protocol reported in V-2.2 for enzymatic hydrolysis was modified by reducing the enzyme activity from 1200 to 13.6 IU in 200 mL (68 IU L^{-1}) of PBS.

Figure V-11 reports the amount of sugar release over time obtained from the hydrolysis of REF-CNC, and numerical values for the Weibull fitting are reported in **Table V-8**. The Figure and the Table also present the results obtained at 1200 IU in 200 mL of PBS for comparison (same as **Figure V-6** and **8** and **Table V-3** and **5**).

As visible in **Figure V-11**, the hydrolysis curve of REF-CNC obtained at lower enzyme activity is almost linear and it does not seem to stabilize even after 52h of reaction. Indeed, the reaction coefficient is really low in the first hour (*b* = 0.01, **Table V-8**) and the sugar release increases slowly over time. Mathematically, the lower its concentration, the more time the enzyme needs to hydrolyze the same amount of starch.

It is interesting to notice that the maximum hydrolysis value at infinity estimated with the Weibull model differs significantly for the two enzyme activities (*a* = 87 ± 5% for 1200 IU and *a* = 100% for 13.6 IU, **Table V-8**). Maybe more experimental points are needed at low enzyme activity, in order to fit more accurately the entire kinetic.

Table V-8: *Values of Weibull function parameters for hydrolysis kinetics of REF-CNC at different enzyme activity; a=maximum value (%), b=average slope during the first hour, c=curvature strength.*

Enzyme activity	**coefficient**			**R^2**
	a[1]	**b**[2]	**c**[2]	
1200	87	0.12	-0.11	0.99
13.6	100*	0.01	-0.14	0.99

computed standard deviations
1 = 5%
2= 0.01
** fixed at bound*

The **Equation 7** has been applied to compute the theoretical time to completely degrade the starch-based matrix at this lower enzyme activity. To do this, the Weibull function values reported in **Table V-8** have been employed.

This simple calculation gave an estimated time of about 142 h, which corresponds to ~6 days of hydrolysis for complete degradation of the sample (instead of ~25h as in enzyme excess conditions).

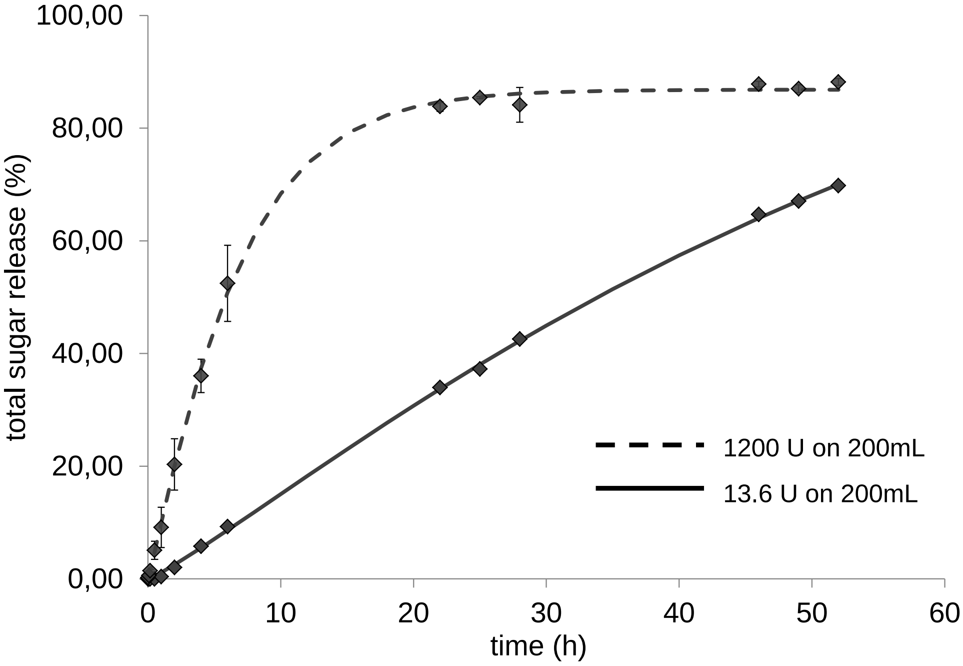

Figure V-11: *Comparison of REF-CNC hydrolysis curve at high (dotted line) and low (continuous line) enzyme activity. Curve fitting is provided by the Weibull model.*

5. Discussion about the influence of structure on the properties in physiological conditions of starch-based samples

5.1 Starch-based matrices

Three main structural factors are responsible for the behavior of starch-based materials in physiological conditions:

1) the plasticization with glycerol;
2) the semi-crystalline structure of the sample and the presence of residual granules;
3) the degree of depolymerization of starch chains.

Glycerol is a highly soluble polyol and it leaches out rapidly from the sample when immersed in water, as proven in V-1. The exit of glycerol from the sample is readily counterbalanced by the fast entry of water, as pointed out by the high approximated diffusion coefficient computed for glycerol-plasticized samples (see **Table V-2**); due to this rapid exchange, the water concentration gradient is very weak and this limits the perturbation of the initial structure of the sample (Chevigny et al. 2018). Indeed, during swelling glycerol-plasticized materials retain their shape (see **Figure V-4**) while increasing their volume radially, as typical of starch-based matrices (Russo et al. 2007; Chevigny et al. 2018).
Swelling is also limited in these samples because of the formation of a semi-crystalline network during stabilization, which creates resistance to the binding of starch with water molecules. Swelling is even more reduced and stabilizes faster when residual granules are preserved in the structure of the sample (as in G20_LOW), because of their almost insoluble nature coming from their multi-scale hierarchical organization.

In amorphous samples, extruded without glycerol, water diffuses slowly from the interface to the inside of the sample (see **Table V-2**), especially when starch is strongly destructurized (as in G0_HIGH). In the meantime, starch chains, probably mostly amylose (Chevigny et al. 2018), slowly diffuse outside the sample, forming a gel. The slow ingress of water induces the formation of a gradient of water in amorphous starch, which is responsible for the perturbation of the initial structure.

The residual granules and the semi-crystalline structure forming in the presence of glycerol contribute too to the resistant starch (RS) fraction, which cannot be degraded by α-amylase during enzymatic hydrolysis. The loss of these two elements, together with the high depolymerization of starch chains in very destructurized samples, leads to a complete and fast degradation of the starch matrix (as observed for G0_HIGH and, to a lesser extent, for G20_HIGH), because of the higher digestibility of amorphous starch (Butterworth et al. 2011).

5.2 Nanocomposites

In chapter IV, starch-CNCs nanocomposites were separated into two groups on the basis of their structural differences. Lower-concentrated nanocomposites (1.5 and 2.5wt%) showed local orders and structure similar to their matrix of reference, while nanocomposites at higher concentrations of CNCs appeared less ordered, showing more amorphous conformations.

A similar separation can be established from the observation of the properties in physiological conditions of the samples.

Despite their similar structure (same crystallinity rate by WAXS, same local structure by NMR, no residual granules), lower-concentrated nanocomposites (≤ 2.5wt%) swell less than the matrix, and the enzymatic degradation is slowed down. The modified properties are an indication of the strong interactions between starch (matrix) and cellulose (fillers), as already suggested by DMTA results and extensively discussed in terms of structure (see IV-4.2.1). These interactions would reduce the number of available sites for water to bind and enzyme to cut, explaining the reduced swelling and slowed down total sugar release observed at this low CNCs concentration in the samples. Alternatively, the enzymatic degradation could be slowed down because of the reduced amount of water which enters in these samples (see swelling results, **Figure V-7**), which in turn would slow down the diffusion of the enzyme inside the sample.

The results obtained for this portion of the samples confirm the hypothesis of well-dispersed nanocrystals, modifying relevant properties already at 1.5wt%.

At higher CNC concentrations (≥ 5wt%), nanocomposites swell more than the starch-based matrix, and are degraded at similar rates by enzymes.

The more disorganized and amorphous structure of these higher-concentration nanocomposites, together with the formation of disconnected nanofiller aggregates (see DMTA results, IV-3.2.1) surely contributed to the increased swelling. The discontinuities which form at higher nanofiller concentrations (see SEM micrographs) ease the diffusion of enzymes with water through the sample, while nanofiller aggregation is responsible for the loss of the starch/cellulose interaction and the enzymatic degradation of the composite comes closer to the one of the matrix without any nanofiller.

Starch-ChNCs nanocomposites behave like more-concentrated starch-CNCs nanocomposites, the only difference coming from the partial preservation of native granules in the lowest-concentrated sample (ChNCs = 2wt%).

The presence of residual granules in this sample helps in keeping swelling and total sugar release values more similar to the ones of a highly-crystalline glycerol-plasticized matrix with residual native granules (G20_LOW) rather than to the other starch-ChNCs nanocomposites. However, already at 2wt%, ChNCs induce the formation of less organized structures which are responsible for the higher sensitivity of the nanocomposite to water and enzyme compared to the starch matrix alone. As observed on the other, cellulose-based composite system, the percentage of amorphous structures increases at higher ChNC concentration (> 4wt%) and induces an increase in swelling and enzymatic degradation.

This worsening effect is an indication that no interactions occur between starch and ChNCs, as suggested, structurally, by the increase in α-relaxation observed for these samples with increasing nanofiller content (see IV-3.2.2). This networking does not seem to form even at the lowest nanofiller concentration.

Chapter VI

BIOLOGICAL PROPERTIES

Table of contents

1. Introduction

The development of degradable implants for the biomedical field constitutes one of the potential high-value applications of the starch-based materials (matrices and nanocomposites) produced in this work.
However, before developing any implant, the cytotoxicity (the toxicity towards cells) of the materials must be investigated attentively, by following the available standards.
In his work, Velasquez (Velasquez 2014) assessed the cytotoxicity of his starch-based materials by following the international standard ISO-10993-5: tests for in vitro cytotoxicity (ISO/EN10993-5 2009). This directive reports several means for the biological evaluation of biomedical devices. The choice of the type of evaluation is left open and depends on the nature of the samples, the type of cultured cells and the way the cells are exposed to the testing material or its extracts.

The numerous methods which can be used for cytotoxicity determination can be separated into four categories: assessment of cell damage by morphological means, measurement of cell damage, measurement of cell growth, and measurements of changes in cellular metabolism. Besides, the test can be performed on an extract of the test sample and/or on the test sample itself.

To determine the cytotoxicity of our starch-based materials, we chose to evaluate the effect of their extraction fluids (aqueous suspensions obtained by immersing the material in culture medium) on cellular viability, following ISO-10993-5 directive: this test is relatively easy and it can be performed on fluids varying in concentration. Flow cytometry has been employed to measure quantitatively the cellular viability from the cells in contact with the extracts, because it can precisely analyze a high number of cells in a very short time. With this method, the cytotoxicity limit of the material can be determined: a material which reduces the cell viability from 30% or more is defined as cytotoxic (ISO/EN10993-5 2009).

A second test, rather focused on the direct cell-material interaction, was performed as well: the cellular adhesion on the surface of the materials was evaluated by confocal microscopy. This test aims at estimating the potential of starch-based materials for colonization by cells.

Glycerol-plasticized matrices and nanocomposites were characterized separately in order to be able to decorrelate the effect of nanofillers from other effects (mainly process parameters).

2. Starch-based materials and cells for biological evaluation

2.1 Cell lines

Two different cell lines were selected to develop these tests: human colorectal carcinoma epithelial cells (HT-29) and mouse fibroblastic cells (L-929).

HT-29 cell line is composed of resistant and relatively big epithelial cells. These cells are round (see **Figure VI-1a**) and form flat monolayers (see **Figure VI-1b**) on materials surfaces.

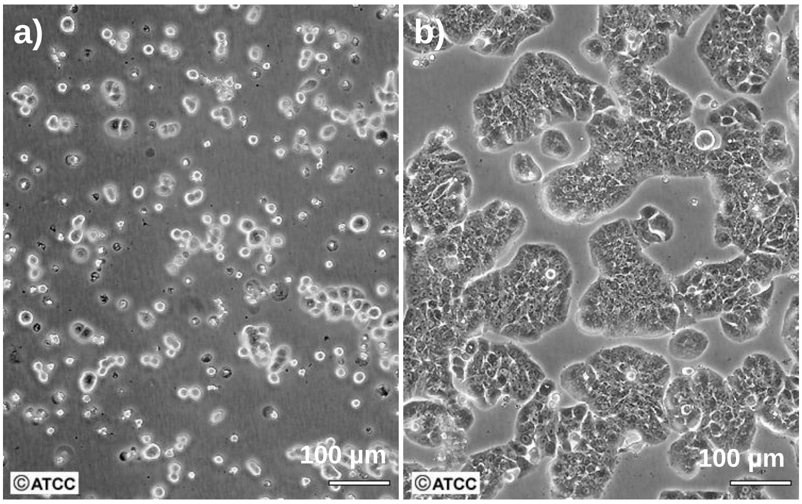

Figure VI-1: *Morphology of human colorectal carcinoma epithelial cells (HT-29) at* ***a)*** *low and* ***b)*** *high density from ©ATCC.*

A second cell line was used afterwards: L-929 fibroblastic cells. Fibroblastic cells are the most common in connective tissues and are responsible for the extracellular matrix and collagen synthesis. Moreover, this type of cells is one of the most employed in the literature for cytotoxic assessment of biomaterials.

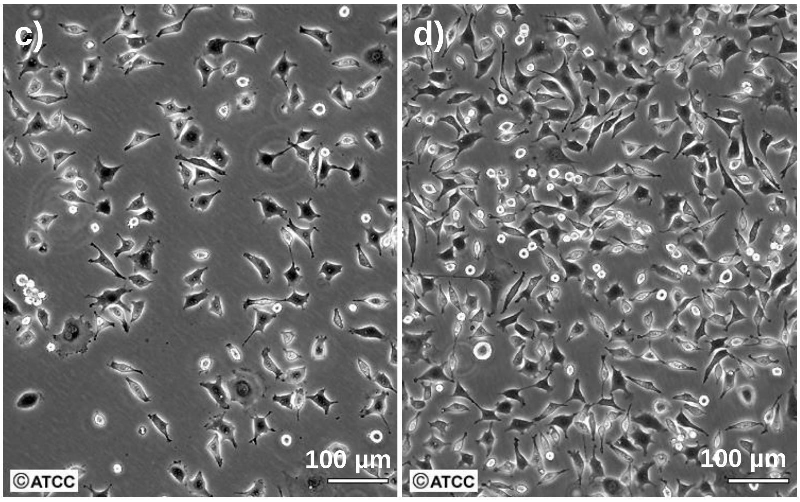

Figure VI-2: *Morphology of mouse fibroblastic cells (L-929) at* ***a)*** *low and* ***b)*** *high density from ©ATCC.*

These cells are very different from the epithelial ones (see **Figure VI-2a**), because of their branched cytoplasm surrounding an elliptical nucleus. Besides, they do not form flat cellular monolayers at high density (see **Figure VI-2b**).

The use of such different cell lines for biological testing makes it possible to evaluate the cytotoxicity of starch-based materials widely.

2.2 Sample forming and sterilization

Glycerol-plasticized matrices and nanocomposites were treated to make them suitable to the contact with cell cultures. To do this, the materials were thermo-molded and then sterilized using the protocols reported below.

Thermo-molding was used to obtain materials with a standardized size: same surface/volume ratio and same surface roughness, while sterilization was necessary to avoid contaminating the cell culture with microorganisms, mold and fungi which potentially remain in the materials.

a) Thermo-molding

Extruded band-shape samples were thermo-molded using a hydraulic press for molding (VS 35, PINETTE P.E.I, FR, EU) and by applying soft parameters to not excessively transform the materials structure. Samples underwent compression at 60°C during 3 min at a pressure lower than 10 MPa. The resulting materials presented very smooth surface, with a thickness comprised between 0.85 and 1 mm.

After molding, samples were cut in small squares about 10 mm in size and stored in individual pouches for sterilization.

b) Sterilization

The pouches containing the thermo-molded materials were sterilized by γ-ray ionization at a minimal standardized dose of 25 kGy. Sterilization was developed by IONISOS enterprise (Sablé-sur- Sarthe, FR, EU) according to ISO-11137. Samples were kept in their sterilization pouch until testing with cellular cultures.

The influence of thermo-molding and sterilization on the structure of the materials was assessed by DMTA and WAXS measurements, following the same protocols used for the non-sterilized materials (see the experimental sets up in Chapter 4).

The results obtained from these analyses do not reveal any difference between the crystalline structure and the thermomechanical properties of sterilized and unsterilized materials. This means also that, additionally to ionization, the thermo-molding treatment applied was weak enough to not significantly modify the sample structure.

The obtained results are in accordance with a previous study which showed that γ-ray ionization at a low dose as 25kGy does not modify the crystallinity rate of the sample (Beilvert, Chaubet, et al. 2014).

2.3 Cellular culture

HT-29 cell culture

*Human colorectal carcinoma epithelial cells (**HT-29**, ATCC®, strain: HTB-38™) were grown in Dulbeccos's Modified Eagle Medium (DMEM, Gibco, Thermo Fisher Scientific, FR), supplemented with 10% foetal calf serum (Eurobio, FR, EU) to support cell growth and 1% penicillin/streptomycin (Gibco, Thermo Fisher Scientific, FR) for avoiding bacterial contamination.*

Cells were cultured in 75 cm^3 culture flasks (BD Falcon, FR) incubated under standard culture conditions (37°C, >95% relative humidity, 5% CO$_2$). Every 3 to 4 days, when a complete monolayer of cells formed in the flask (confluence), cells were detached from the flask using Tryple ™ (Thermo Fisher Scientific, FR) and diluted in new flasks, until the next passage.

HT-29 cells were used for testing until passage 17.

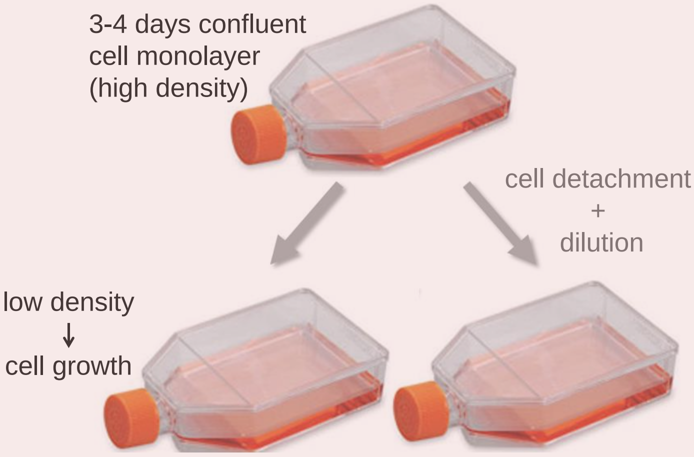

Figure VI-3: Schematic representation of cellular culture in 75 cm³ flasks and passage (cell detachment and dilution in other flasks) of confluent cell monolayers each 3-4 days.

L-929 cell culture

*Mouse fibroblastic cells (***L-929***, ATCC®, strain: C3H/An, designation: NCTC clone 929) were cultured as done for epithelial cells (see above, HT-29 cell culture). The only difference with HT-29 cell culture is that L-929 cells do not form monolayers at high cellular density (confluence), so they were detached and diluted in other flasks each 3-4 days, when a semi-confluent layer of cells was formed (as in* **Figure VI-2b***).*

L-929 cell line was used for testing until passage 17.

3. Cellular viability

As mentioned in the introduction, the materials cytotoxicity was evaluated by measuring the cellular viability after contact with their extraction fluids, following the directive ISO-10993-5. In this work, extraction fluids are obtained by immersing the material in culture media for 24h in standard culture conditions (see the following experimental set up for details).

The main steps of the materials cytotoxicity assessment are then: 1) fluid extraction from the materials, 2) contact cells/fluid and 3) quantitative measurement of cellular viability by flow cytometry.

Production of materials extraction fluids and deposition on cellular culture

5 mL of 2×10^5 *epithelial cells (HT-29)* mL^{-1} *were seeded in 6-well plates and cultured for 48h, until 70% of a complete monolayer of cells (confluence) was reached* (**Figure VI-4**).

Likewise, 1×10^5 *fibroblastic cells (L-929)* mL^{-1} *were seeded in 6-well plates and cultured for 24h, until 70% confluence was reached* (**Figure VI-4**).

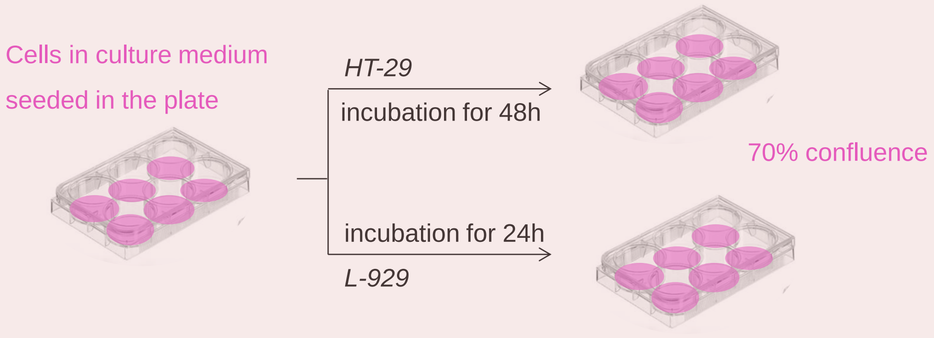

Figure VI-4: Cells seeding and culturing for the cytotoxicity test.

In the meantime, fluids were extracted from the extruded materials for 24h in the complete culture medium (the same used for cell culture) in standard incubating conditions (37°C, >95% relative humidity, 5% CO_2) (**Figure VI-5**).

At the beginning of the tests, the culture medium in each well was replaced by 1.2 mL of non-diluted extraction fluid, as reported in **Figure VI-5**.

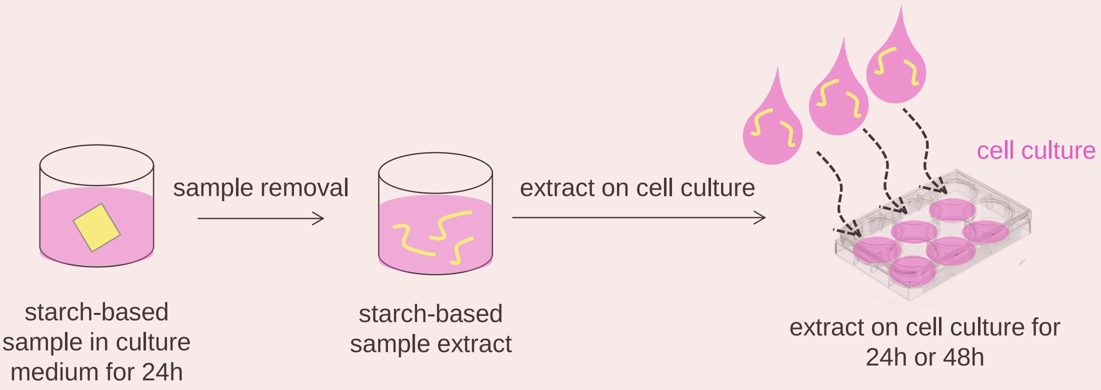

Figure VI-5: Simplified representation of material extraction fluid deposition for cytotoxic evaluation.

Cells remained in contact with the extraction fluid for 24 and 48h in incubator at standard conditions. Each sample was analyzed in triplicate. After 24 and 48h of contact with the extraction fluid, the supernatants were discarded and cells were prepared for flow cytometry.

Two controls were developed to decorrelate the cytotoxic effect of the extraction fluid from the one coming from other parameters (i.e. cellular culture conditions, etc.). The negative control is defined as a material which does not produce a cytotoxic response, while the positive control is used to generate the opposite reaction (strong cytotoxicity). 1.2 mL of culture medium and 1.2 mL of dimethyl sulfoxide (DMSO, Sigma-Aldrich, FR) were used as negative and positive control respectively.

Cellular staining for flow cytometry

Flow cytometry is a classically used technique to differentiate populations of cells on the basis of their optical properties. In a flow cytometer cells are flowed one at a time through a laser beam and the scattered light gives information about cell characteristics (**Figure VI-6**).

To precisely separate cell populations, cells are usually labelled with fluorescent dyes. In this case of study, the dye employed enters permeable plasma cell membranes of necrotic cells and covalently binds to cellular amines, increasing their fluorescence (**Figure VI-6**).

Cellular viability is then determined by comparing the number of necrotic cells (with higher fluorescence) obtained for the two controls and the materials.

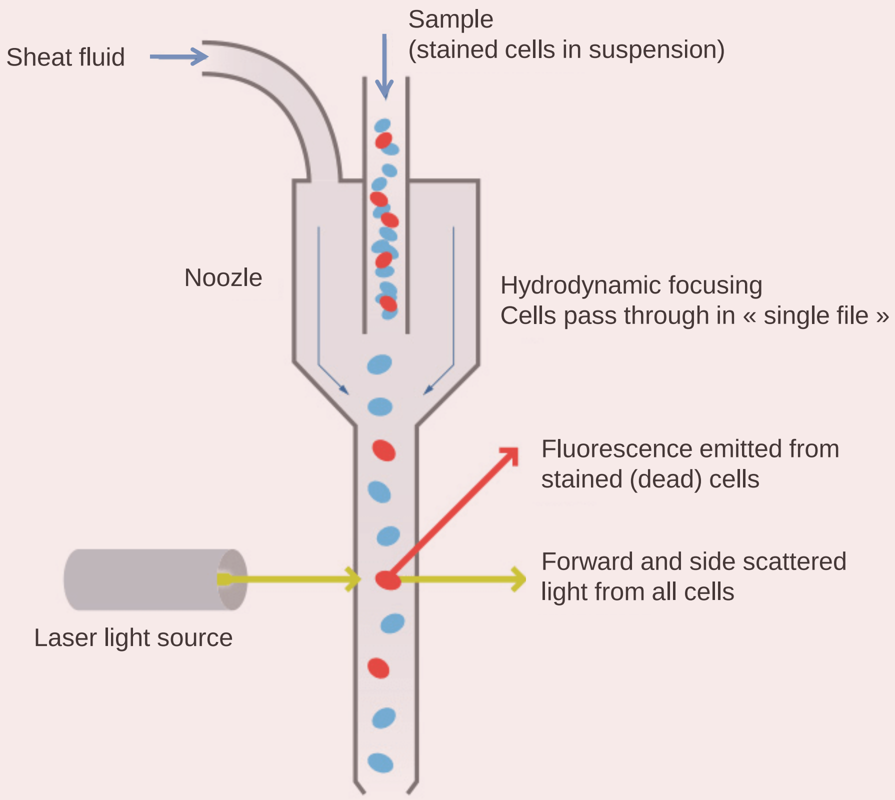

Figure VI-6: Working principle of flow cytometry, from Abcam©.

To differentiate necrotic cells from living ones, staining was performed with the intracellular dye Fixable Viability 570 (FVS570, 1µL mL^{-1}, BD Bioscience, US). Then cells were fixed in 2% paraformaldehyde (PFA, Electron Microscopy Science, US) to preserve them until analysis. Staining and fixation lasted 20 min each, protected from light at 4°C.

Finally cells were rinsed and dispersed in FACS buffer (phosphate buffer added with 5% foetal calf serum and 0.01M ethylenediaminetetraacetic acid - EDTA) for cytometric analysis.

A Canto II flow cytometer (BD Biosciences) was used for flow cytometry. Data were acquired using Diva 8.0 software and analyzed with FlowJo® X (TreeStar, Williamson Way, Ashland, USA). 2 × 10^4 cells per sample were analyzed at the cytometer.

Figure VI-7 and **Figure VI-8** report the viability of epithelial (HT-29) and fibroblastic (L-929) cells, respectively, after exposition to non-diluted fluids leached from the materials, along with negative (culture medium, no cytotoxicity) and positive (DMSO, strong cytotoxicity) controls.

For tests on epithelial HT-29 cell line, the positive control was constituted by pure DMSO (100%) and this induced the almost full destruction of the cellular structure (only cellular fragments were detected, **Figure VI-7**). Hence, a diluted solution (10% DMSO) was used during testing on fibroblastic L-929 cells, in order to study the evolution of cellular death over time (**Figure VI-8**).

All cells show the same viability of about 100% whether at 24 or 48 h, independently from the material used in the test. According to the norm, this means that all the materials extraction fluids are non-cytotoxic on epithelial (HT-29) and fibroblastic (L-929) cell lines at these contact times, as their viability is higher than 70% (ISO/EN10993-5 2009).

For matrices, no direct dependence between structure and cellular viability can be determined. No visible effects are detected on cellular viability from the nanofillers presence either.

The only visible difference between epithelial (HT-29) and fibroblastic (L-929) cell lines is the higher standard deviation observed for L-929 viability (**Figure VI-8**). Standard deviations are higher for fibroblastic cells in contact with extraction fluids coming from starch-based matrices (between 2 and 5.5%) and starch-CNCs nanocomposites (between 4 and 6.5%), while starch-ChNCs nanocomposites show no variability in cellular viability.

Glycerol was expected to have an effect on cellular viability, as previously shown by (Velasquez et al. 2015) on BALB/c3T3 cell line. However, in this work, glycerol does not appear to influence either the cells viability. The lower viability observed by Velasquez could be linked to the use of a different technique for the assessment of cellular viability, or to the use of different cell lines.

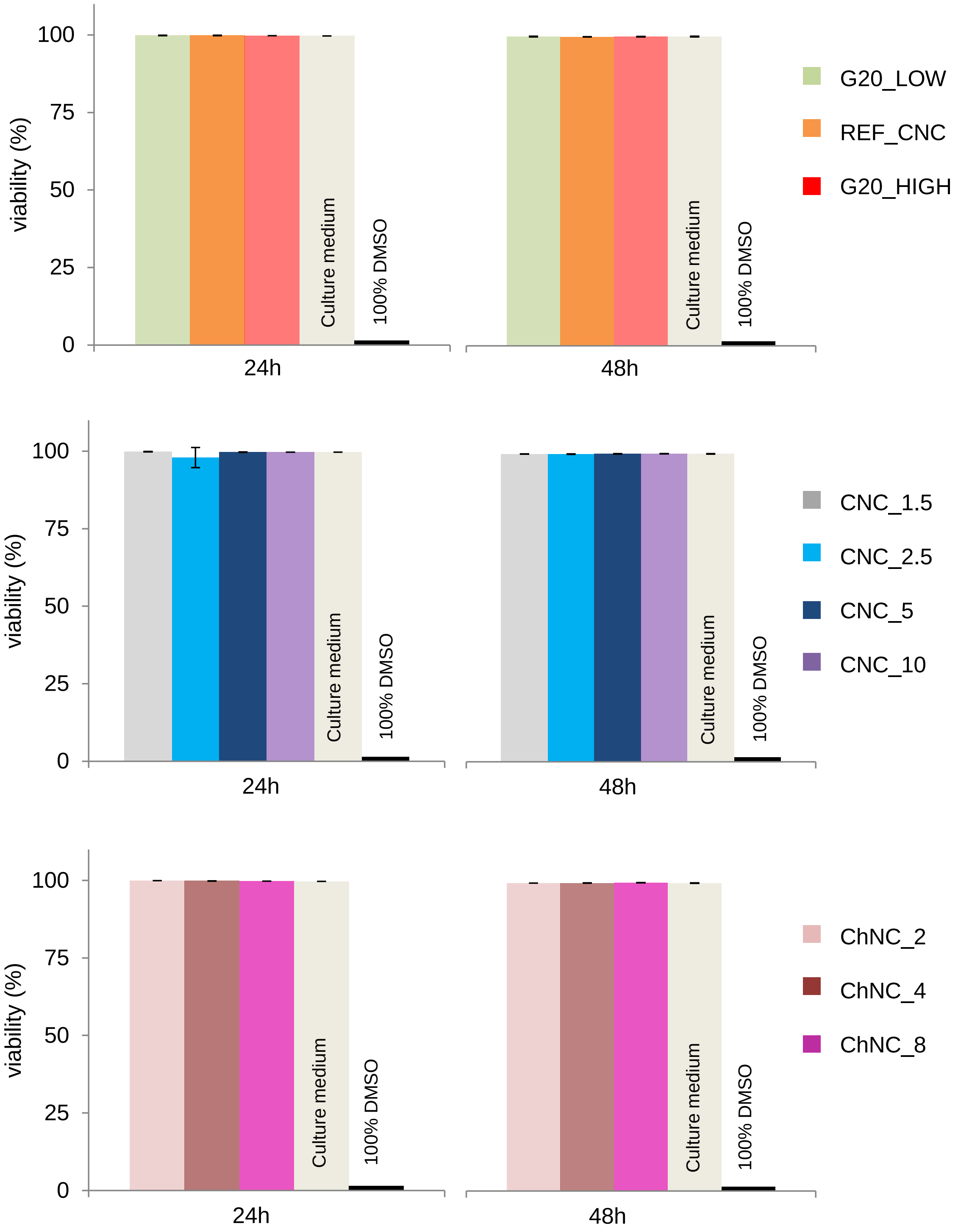

Figure VI-7: *HT-29 cellular viability after exposition to extraction fluids of glycerol-plasticized starch-based matrices and nanocomposites at 24 and 48h.*

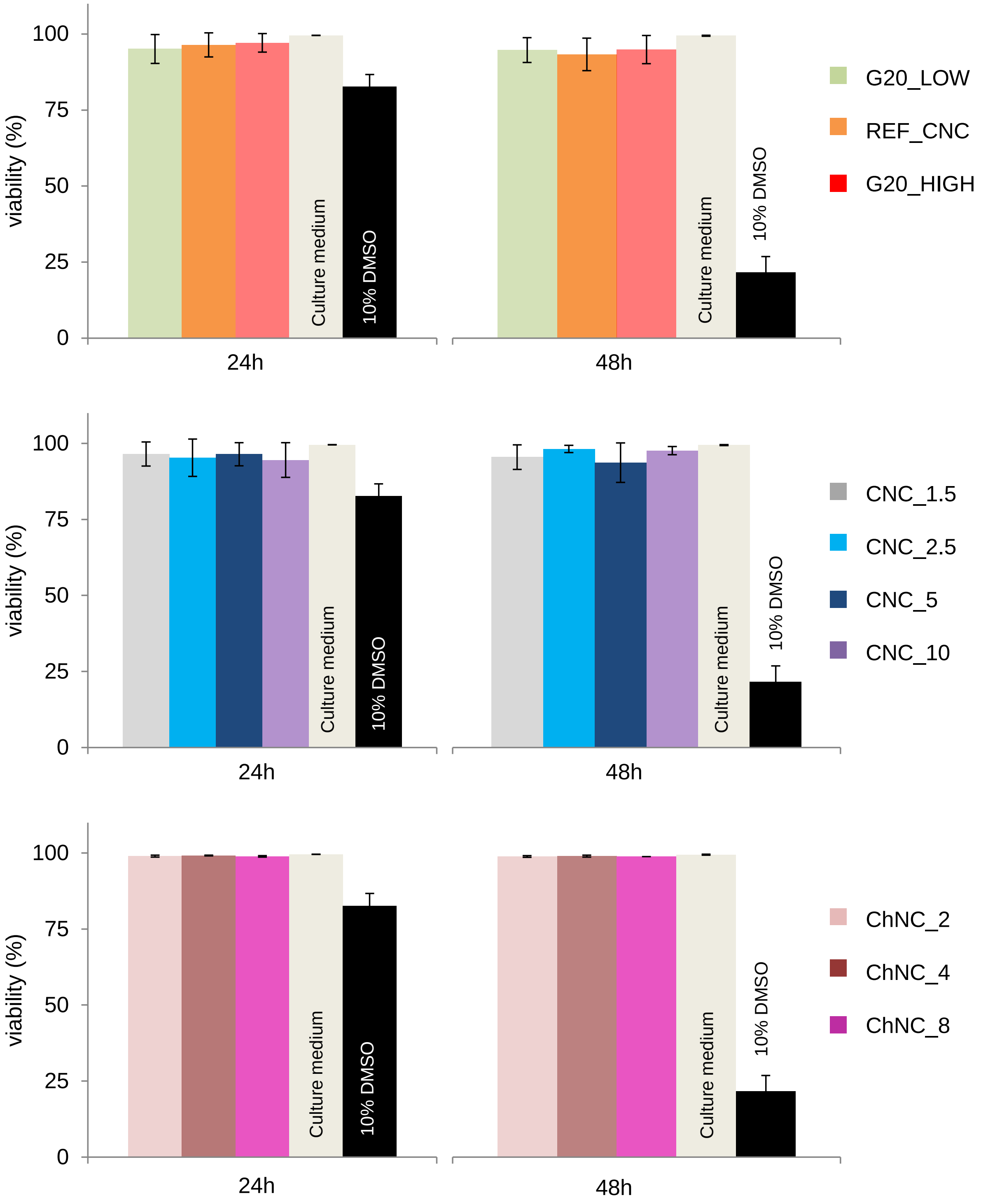

Figure VI-8: *L-929 cellular viability after exposition to extraction fluids of glycerol-plasticized starch-based matrices and nanocomposites at 24 and 48h.*

3.1 Effect of nanofillers on cellular viability

Production of nanofiller suspensions and deposition on cellular culture

The cytotoxicity of pure nanofillers was evaluated as well using a protocol similar to the one reported above (see Production of materials extraction fluids and deposition on cellular culture).

After culture medium removal, instead of adding extraction fluids coming from materials suspension, epithelial (HT-29) cells were added with 1.2mL of cellulose nanocrystals (CNCs) or chitin nanocrystals (ChNCs) suspensions at different concentration (from 10 to 1 000 g mL^{-1} in culture medium), as reported in **Figure VI-9**.

However, all CNC and ChNCs suspensions appeared heterogeneous visually, because nanofillers aggregated and precipitated when dispersed in the culture medium. This is explained by the difference in pH between the culture medium and the nanofiller suspension. Hence nanofillers surface exposed to the cells was significantly reduced.

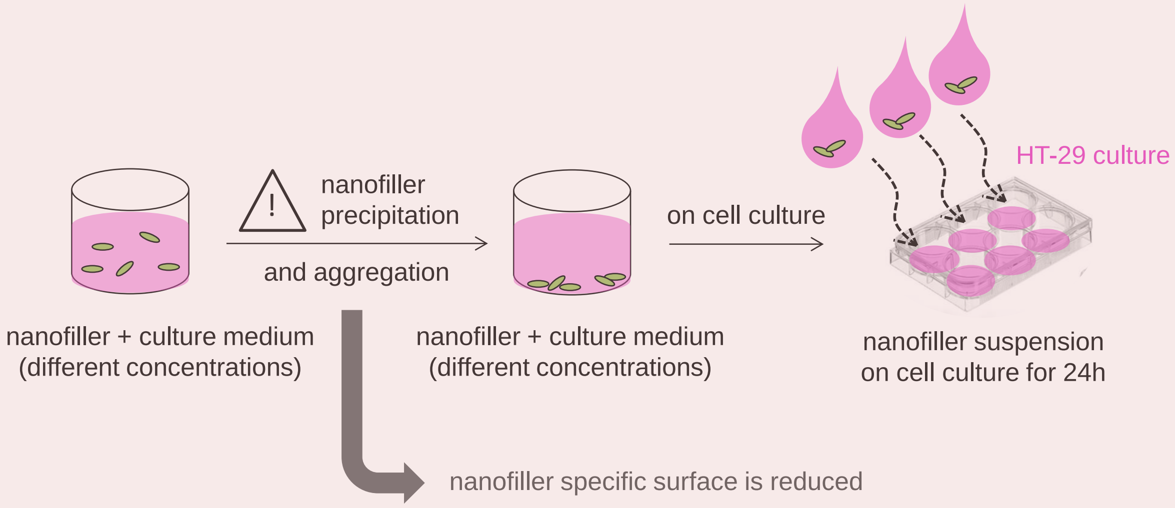

Figure VI-9: Simplified representation of nanofiller suspension deposition for cytotoxic evaluation.

After 24 h of contact between cells and nanofillers, cells were treated and analyzed as reported above for extruded materials cytotoxicity. The reaction of cells to nanofiller suspensions was analyzed by flow cytometry.

The cytotoxicity of CNCs and ChNCs suspensions at different concentration were tested on the epithelial HT-29 cell line, along with a negative control (culture medium, no cytotoxicity) and a positive control (strong cytotoxicity), constituted by pure DMSO (100%), similarly to the protocol used above on starch-based materials.

As pointed out by **Figure VI-10**, cellular viability is near to 100% after 24h of direct contact with all the nanofiller concentrations tested (from 10 to 1 000 g L^{-1}), whether for CNCs (96.3±1%) or ChNCs (96.5±0.6%).

The findings obtained by using this methodology seem to confirm the low cytotoxic potential of CNCs and ChNCs when in contact with epithelial cells for short times (24h in this case).

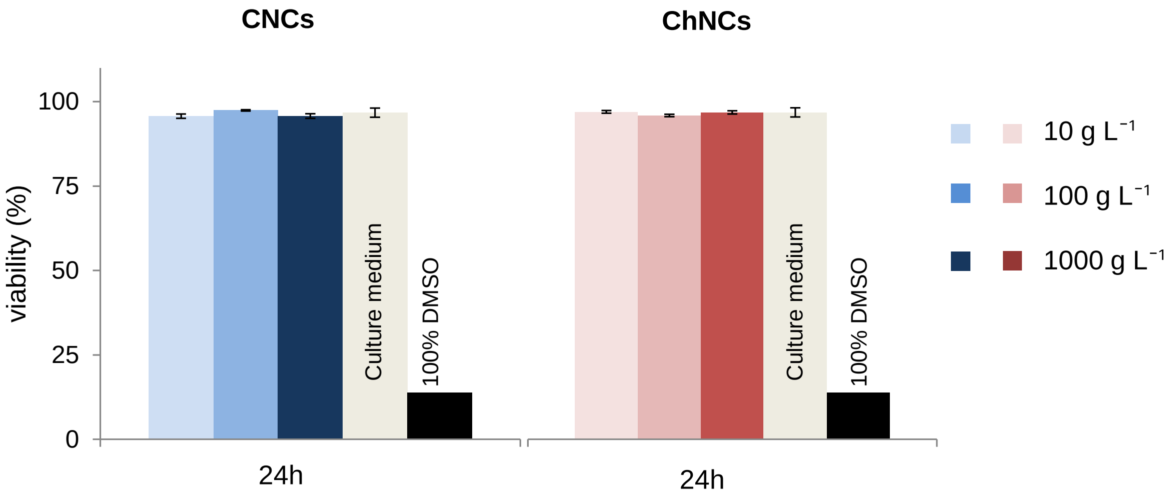

Figure VI-10: *HT-29 cells viability after exposition to cellulose nanocrystals (CNCs) and chitin nanocrystals (ChNCs) at different concentration at 24h.*

However, one could question the validity of this test because of the nanofillers aggregation which occurs in the culture medium. One option to solve this would be to investigate if nanofillers aggregate when in contact with human interstitial fluids too, which the nanofiller-containing implant would be in contact with. If they do, it is expected that they aggregate as well during implantation, exposing less surface to contact with the cells and therefore probably having little to no effect on their viability.

4. Material colonization

The material-cell interaction is not exclusively influenced by extraction fluids: in real implantation conditions, cells come in contact with the material and they may directly interact with it, leading to the material colonization (if the requirements for cell growth are satisfied). For this reason, the study of direct contact between materials and cells is a fundamental step in achieving the assessment of biological properties. To do this, here too we proceeded according to ISO-10993-5 guidelines.

Cellular adhesion *in vitro* on material surface

To assess their potential colonization by epithelial (HT-29) and fibroblastic (L-929) cells, the extruded materials were put in direct contact with the cells for 24h and then their surface was observed by confocal microscopy to determine the cellular density on the material.

Before experiments, sterilized squares of samples were put in 12-well plates. Then 4 mL of 5 × 10^4 cells mL^{-1} were seeded on the materials. Cells remained in contact with the material for 24h in incubator at standard conditions (37°C, 5% CO_2 atmosphere, **Figure VI-11***).*

After 24h testing, culture supernatants were discarded and the materials were gently washed two times using phosphate buffer (PBS, pH 7.4, Gibco Thermo Fisher Scientific, FR). Prior to observation by confocal microscopy, the cells had to be stained (labelled with a fluorescent dye) to allow their identification on the materials surface (**Figure VI-11**).

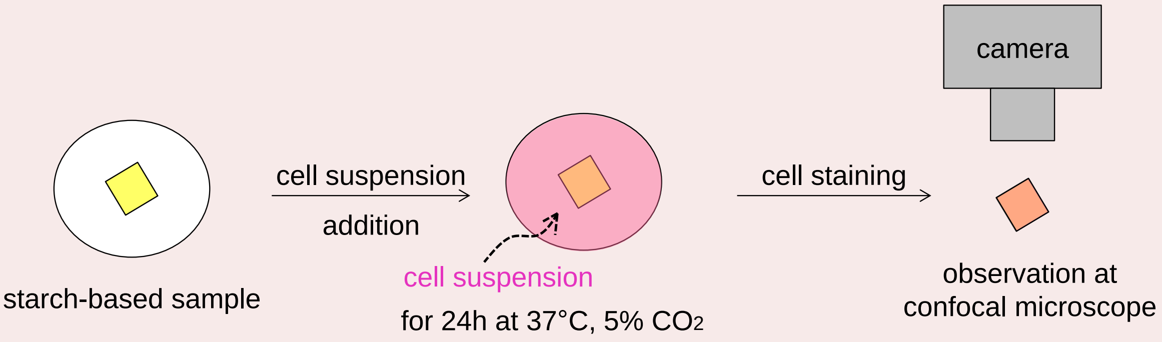

Figure VI-11: Simplified representation of cellular staining and confocal microscope analysis for cellular colonization of material surface.

Confocal images were obtained with a Laser Scanning Confocal Microscope (CLSM, Nikon A1) with an attached Nikon Imaging Software (NIS) system (Nikon, DE).

Each formulation was analyzed in triplicate and a minimum of 10 images were registered for each specimen.

Cellular staining for confocal microscopy observation

Three different fluorescent dyes were employed to stain cells and enable their visualization by confocal microscopy.

- ***DAPI*** *(4',6-Diamidino-2-Phenylindole, Dilactate, 1µL mL*$^{-1}$*, Merck, DE, EU): is a fluorescent stain used for labelling DNA in nuclei of all cells (both viable and non-viable). This dye is excited at a wavelength of 358 nm and it emits at 461 nm (****blue color****).*
- ***FVS 570*** *(Fixable Viability Stain 570, 1µL mL*$^{-1}$*, BD Bioscience, US): is a fluorescent dye used for discriminating viable from non-viable/suffering mammalian cells (used above for cellular viability determination by flow cytometry). FVS 570 covalently binds to cellular amines in cellular membranes of non-viable/suffering cells exclusively. This dye is excited at 547 nm and it emits at 573 nm (labelled in* **red color** *in this work to enhance its visualization).*
- ***AlexaFluor 488*** *(mouse monoclonal anti-alpha-tubulin antibody, Clone: DM1A, 1µg mL*$^{-1}$ *in PBS, eBioscience™, FR): is a fluorescent dye which covalently binds to tubulin (structural protein in cell cytoplasm) of all cells (both viable and non-viable). This dye is excited at 488 nm and it emits at 519 nm (****green color****).*

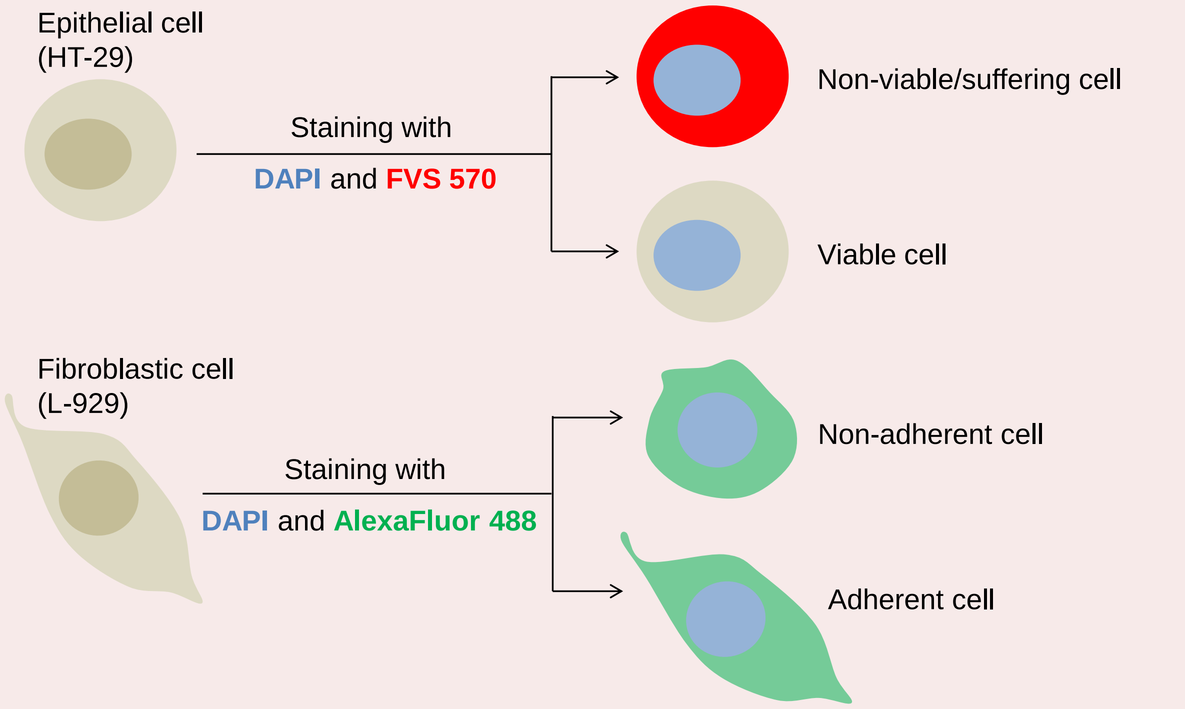

Figure VI-12: Staining of epithelial (HT-29) and fibroblastic (L-929) cells.

Epithelial (HT-29) cells were stained with DAPI and FVS 570 for nuclei and non-viable/suffering cells discrimination respectively, as reported in **Figure VI-12**.

Fibroblastic (L-929) cells were stained with DAPI and AlexaFluor 488. The use of AlexaFluor 488 instead of FVS 570 was needed to better visualize the morphology of the fibroblastic cells which adhered on the materials surface.

All staining steps were developed protected from light. Samples were stored at 4°C until confocal microscope observation.

Observing cellular adhesion on the materials surface is not easy because of their important thickness, already at the dry state and even more when immersed in culture medium. The highly swollen and irregular surface which forms hinders the simultaneous observation of all the adherent cells on the material surface. Multiple z-plans should be observed to have an idea of the total number of cells colonizing the material (**Figure VI-13**). Since it was not possible to exactly count the cells that adhered at the surface of the materials, the results obtained from this experience are simply qualitative.

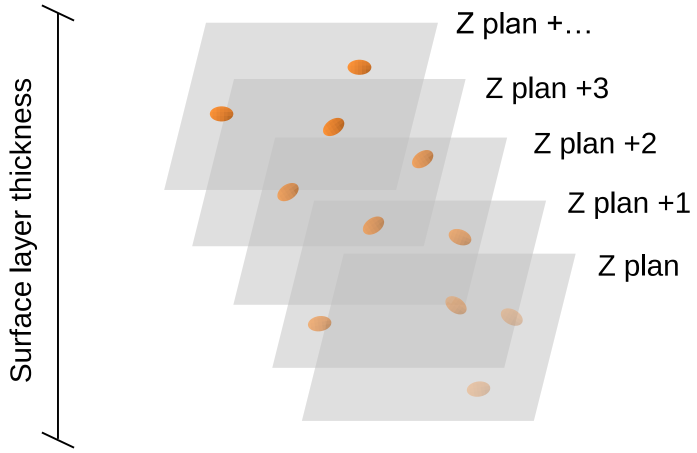

Figure VI-13: *Cells (orange oval-shaped elements) distributed in the z-plans which constitute the surface of the sample. Plans cannot be focused simultaneously by confocal microscopy.*

To get representative results, each composition was analyzed in triplicate (three different sterilized squares samples in three different wells added with the cellular culture) and numerous images (10 minimum) were taken for each sample at different z-plans to have an idea of the degree of colonization of the material by HT-29 and L-929 cell lines.

4.1 Epithelial (HT-29) cells adhesion on material surface

Very few cells are visible on the surface of glycerol-plasticized starch-based matrices and starch-CNCs nanocomposites (**Figure VI-14a** and **c**), in regard to the high cellular density of the surface of the wells in which the samples were placed (figure not shown).
In the case of starch-based matrices, the low cellular density is particularly striking for G20_HIGH, on which the few adherent cells have been encircled with a dotted white line to make them more visible (**Figure VI-14a**). However, for all matrices, the observed cellular density is too low to establish a clear link between cellular colonization and thermoplastic starch structure.

In starch-CNCs nanocomposites, only a few cells adhere on nanocomposites surface; however, the group of high-CNC-concentration samples (CNC_5 and CNC_10) present an intense staining on almost all the material surface (**Figure VI-14c**). This could come from the very heterogeneous morphology of these nanocomposites (see **Figure III-8**, SEM results), which would retain the dyes used for cellular staining. These discontinuities could also “trap” extra cells, as visible in CNC_5 image (**Figure VI-14c**).

Most of the cells in starch-based matrices and starch-CNCs nanocomposites are stained by both DAPI (blue color) and Fixable Viability 570 (FVS 570, red color), giving a violet signal. This means that epithelial (HT-29) cells are non-viable or suffering when they are in contact with these materials (see VI-4, *Cellular staining for confocal microscopy observation*). This signifies that epithelial cells are not able to colonize starch-based matrices and starch-cellulose nanocomposites, at least during this short contact time (24h).

A slightly higher number of cells seems to adhere on the surface of the starch/chitin composites. Some of these cells are also not stained by FVS 570, as visible in **Figure VI-14b**, meaning that they are still viable, and thus that these nanocomposites induce lower cellular stress. This result is particularly true for the ChNC_8 sample, on which cells are almost exclusively stained with DAPI (**Figure VI-14b**, blue color).

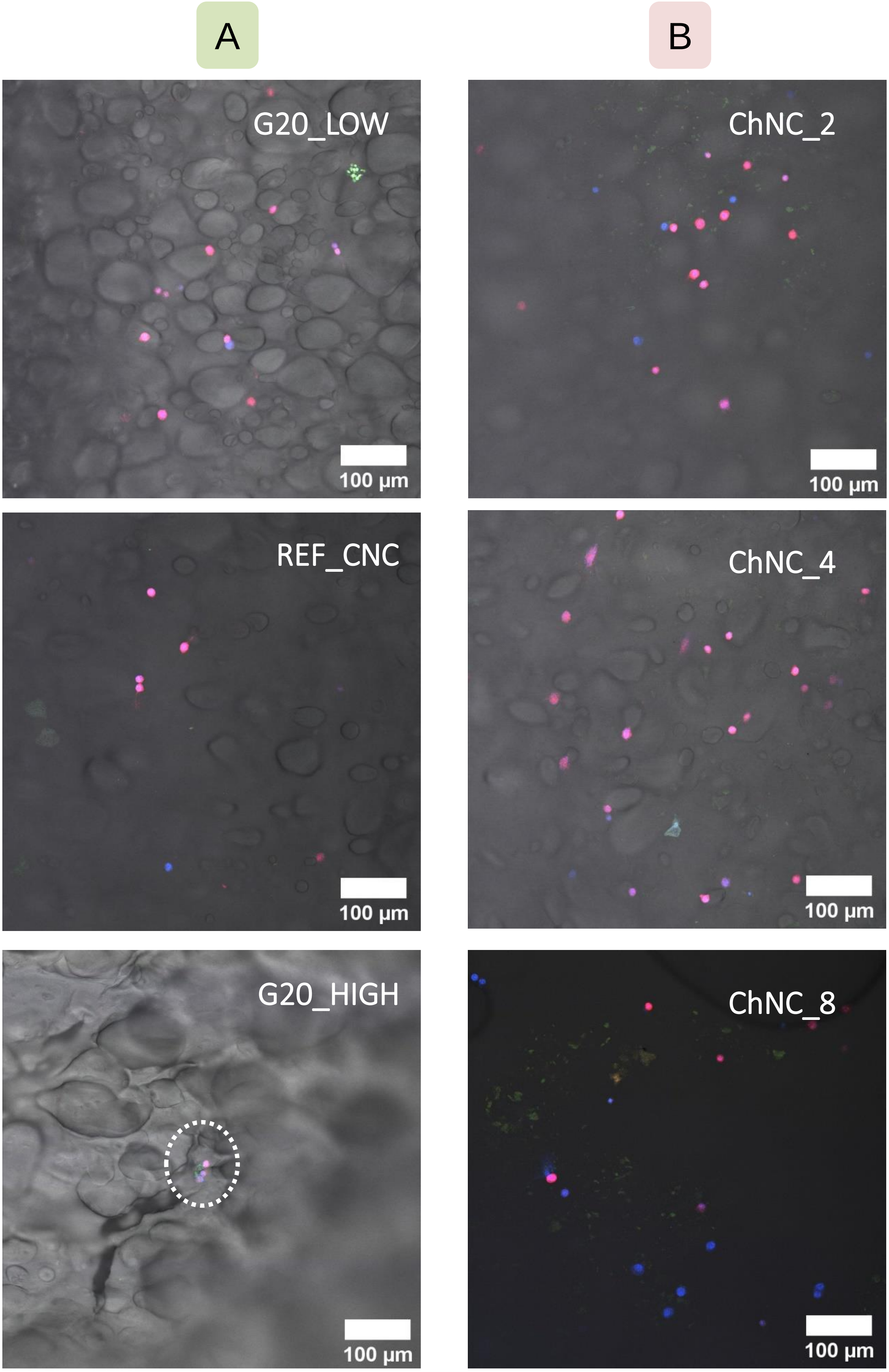
A
B
G20_LOW
100 µm
ChNC_2
100 µm
REF_CNC
100 µm
ChNC_4
100 µm
G20_HIGH
100 µm
ChNC_8
100 µm

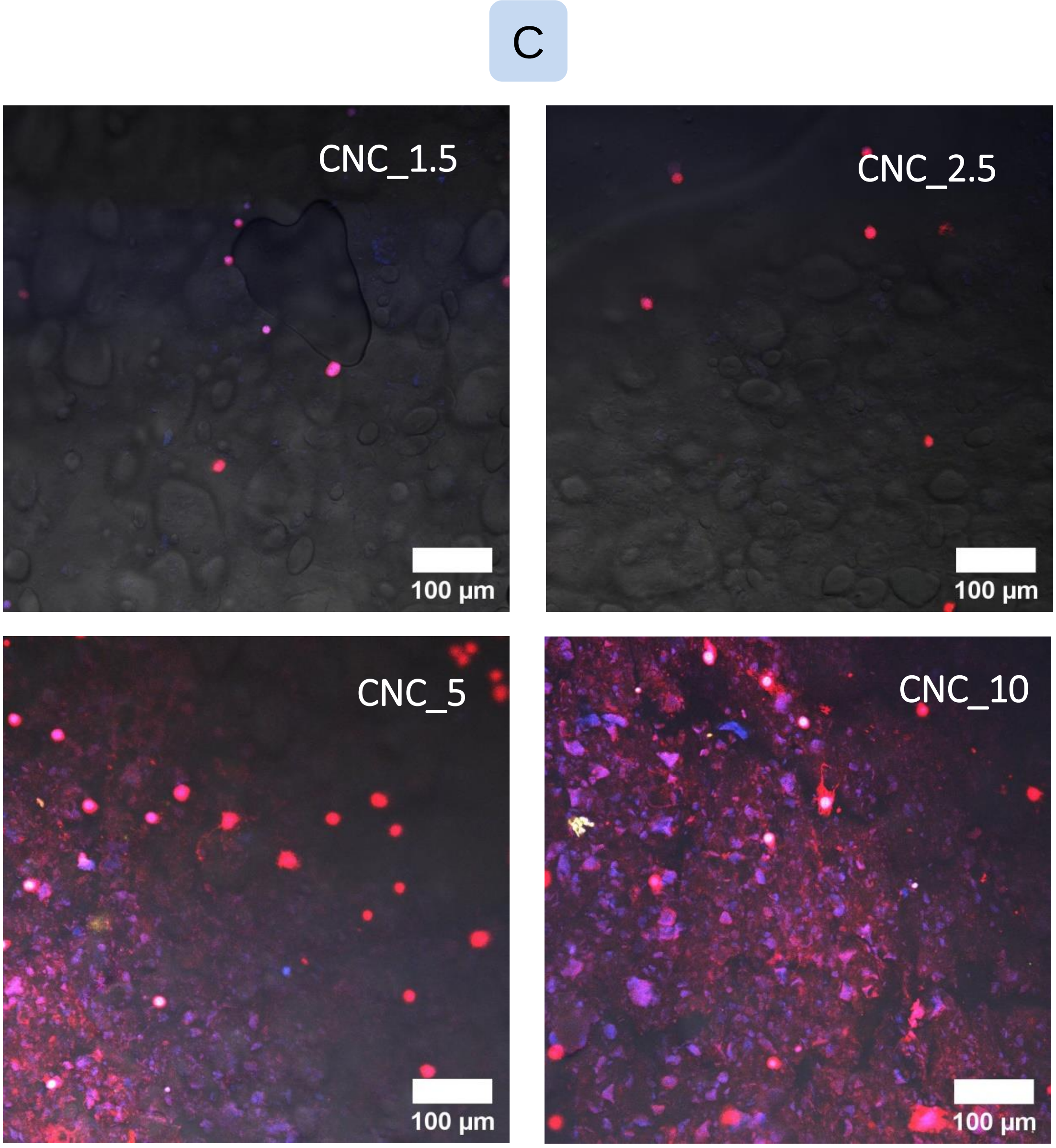

Figure VI-14: *Adhesion of epithelial cells (HT-29) on* **a)** *glycerol-plasticized starch-based matrices* **b)** *starch-ChNCs and* **c)** *starch-CNCs nanocomposites surface. Fixable Viability 570 stains the cytoplasm of suffering cells (red color) while nuclei are marked with DAPI (blue color). The superposition of FVS570 and DAPI gives a violet signal.*

4.2 Fibroblastic (L-929) cells adhesion on material surface

L-929 fibroblastic cells were stained with Alexa Fluor 488 rather than FVS 570: it seemed like a more adapted marker to determine the shape of the cells adhering on materials surface (see above, *Cellular staining for confocal microscopy observation*). Fibroblastic cells present a typically elongated shape when they adhere on a surface (see **Figure V-15**) otherwise they are spherical.

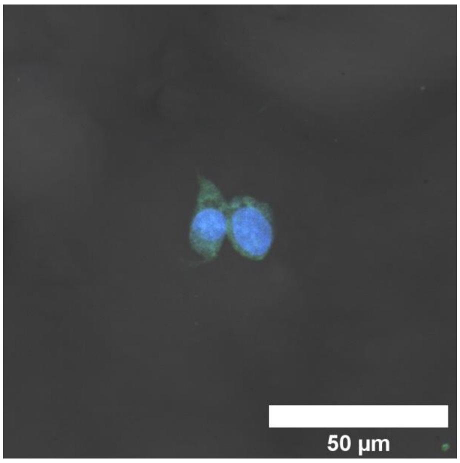

Figure VI-15: *L-929 elongated morphology when adhering on a surface. Alexa Fluor 488 stains the tubulin in the cytoplasm (green color) while nuclei are marked with DAPI (blue color).*

Figure VI-16 reports L-929 fibroblastic cells adhesion on the surface of glycerol-plasticized starch-based matrices and nanocomposites. Almost all cells in **Figure VI-16** present a spherical shape, meaning that fibroblastic cells cannot easily adhere on the surface of starch-based materials.

Small cellular aggregates are visible on all samples surface but, as previously observed for the epithelial cell line HT-29, no clear link between sample composition/structure and cellular colonization can be established for the fibroblastic cell line either. It seems likely that the weak cellular colonization of the samples is caused by their extremely hydrophilic surfaces, which have been accounted to slow down cellular adhesion and proliferation in other works (Koyano et al. 1998).

A strong green fluorescence, surrounding a few blue-stained cells, is visible in all starch-ChNCs nanocomposites (**Figure VI-16b**). The green fluorescence is probably generated by the organic residues (such as chitin amorphous regions) present in the ChNCs aqueous suspensions used for the production of the starch/chitin nanocomposites.

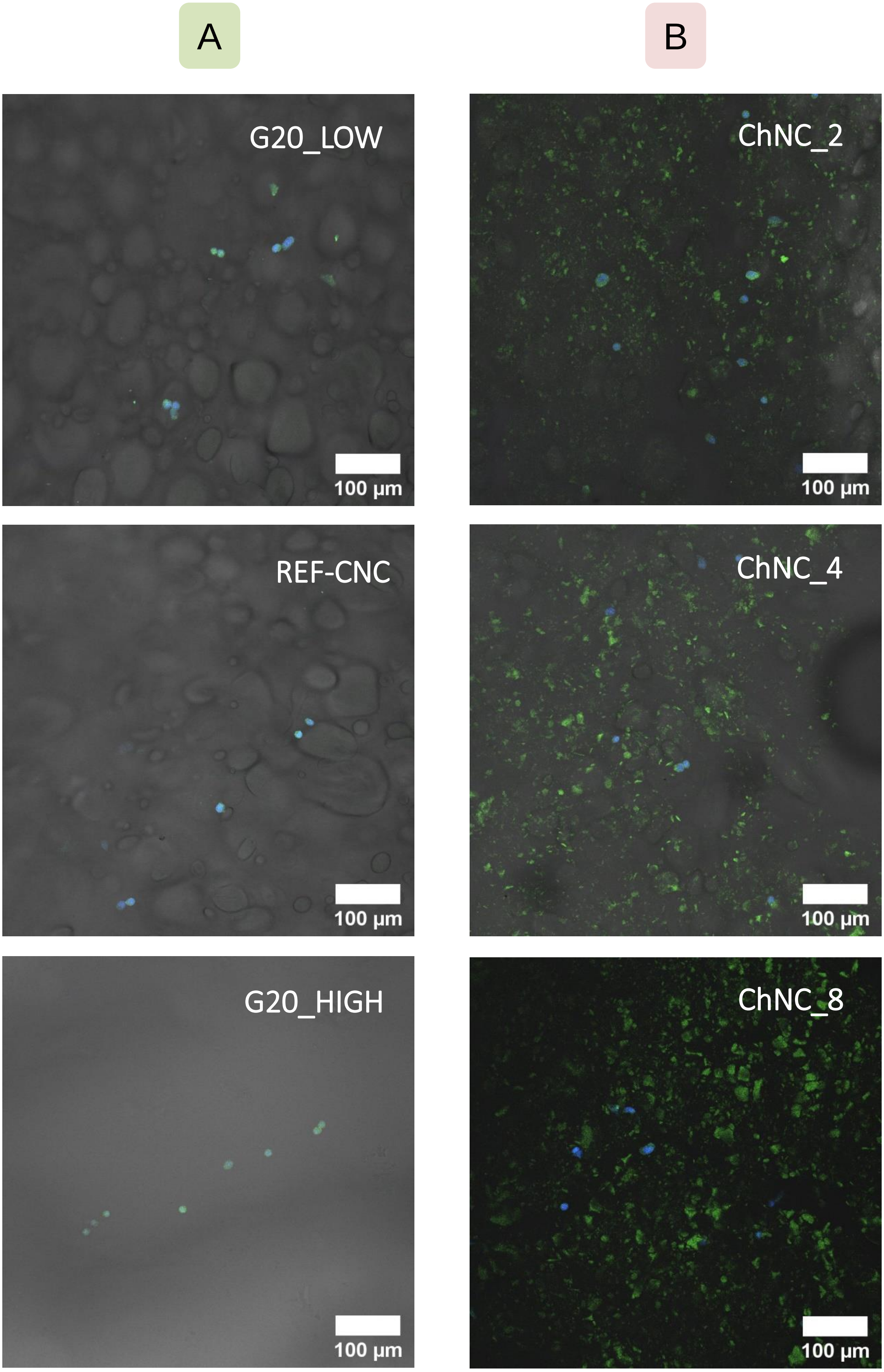
A
B
G20_LOW
ChNC_2
100 µm
100 µm
REF-CNC
ChNC_4
100 µm
100 µm
G20_HIGH
ChNC_8
100 µm
100 µm

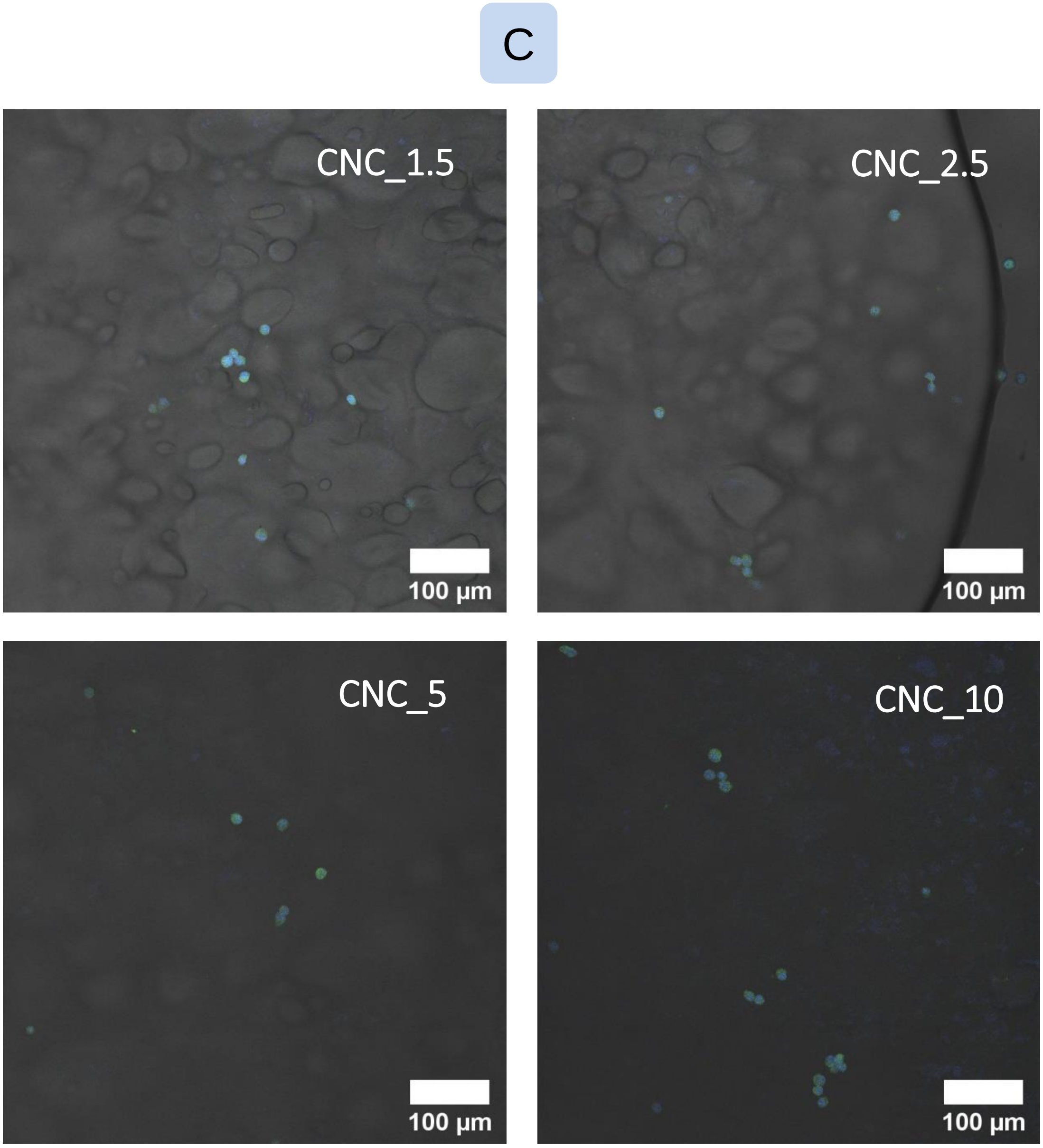

Figure VI-16: *L-929 cellular adhesion on* **a)** *glycerol-plasticized starch-based matrices* **b)** *starch-ChNCs and* **c)** *starch-CNCs nanocomposites surface. Alexa Fluor 488 stains the tubulin in the cytoplasm of all cells (green color) while nuclei are marked with DAPI (blue color).*

5. Discussion about starch-based materials potentiality of application as biomaterials

The ISO-10993-5 norm defines a material as non-cytotoxic when *the cellular viability induced by the contact with the material itself or its extraction fluids is reduced by no more than 30%* (see **Table VI-1**). Along this narrow definition, all materials (matrices and nanocomposites) produced in this work are non-cytotoxic, since the viability of epithelial (HT-29) and fibroblastic (L-929) cells subjected to contact with extraction fluids is near to 100% for all the materials tested.

To widen this result, the cytotoxicity of the materials extraction fluids should be tested during longer times, similar to those of implant lifespan in the human body (about 30 days in absence of α-amylase, (Velasquez et al. 2015)).

Table VI-1: *Summary of ISO-10993-5 requirements for testing the materials cytotoxicity.*

ISO/EN10993-5-2009: tests for in vitro cytotoxicity
• methodology: direct contact
- on material itself
- on material extraction fluids
- diluted
- non-diluted
• results
- viability < 70% → cytotoxic
- viability > 70% → non-cytotoxic

Strictly following ISO-10993-5 guidelines, in contact with samples of all nanofillers types and concentrations, the cellular viability is high. However, other tests should be performed to check the safety regarding the nano size of the fillers: for example, it would be useful to assess if cells internalize nanoparticles and, if this is the case, the effects of nanoparticles internalization by the cells should be studied in detail.

Although the high viability of cells in contact with the materials extraction fluids was proven, the cellular adhesion on their surfaces is weak and only a few spherical-shaped cells are observed, indicating no adhesion is taking place. Indeed, cell adhesion and proliferation is strictly dependent on the physicochemical characteristics of polymeric materials surfaces, such as hydrophilicity, surface charge and morphology. Hydrophilicity in particular is a key parameter for cellular adhesion, as it allows cells to deposit their own adhesion proteins on the surface of the material (Marques et al. 2002). However, it is possible that the extreme hydrophilicity of the starch-based substrates analyzed in this study hinders the adhesion and proliferation of cells on the materials, explaining the weak cellular density observed by confocal microscopy. Indeed, in previous works (Koyano et al. 1998; Lee et al. 1998), it was suggested that moderate hydrophilicity favors the adsorption of serum proteins (like fibronectin and vitronectin) which are known to favor better cell adhesion. Conversely, the serum protein adsorption is disfavored on materials with excessively hydrophilic (as in the case of the materials analyzed in this work) or hydrophobic surface.

It is less likely, but the poor cellular adhesion could be caused by the disintegration of the material or by the cytotoxic effect of glycerol as previously proposed by (Velasquez 2014). However, no disintegration or cytotoxic effect of glycerol were observed here.

One way of solving this problem would be to promote cell adhesion by adding coating reagents, which would favor cellular protein absorption on the material surface, as proposed by Torres (Torres et al. 2011) for starch-based films produced by casting.

General conclusion and perspectives

This work aimed to understand the interdependence between structure and properties in physiological conditions of starch-based composite materials. These materials have been obtained by adding low quantities of nano-sized fillers (cellulose nanocrystals and chitin nanocrystals) to starch and by submitting this formulation to extrusion. The goal was to obtain a good compatibility between the starch matrix and the fillers, to significantly decrease the sensitivity to water and enzymatic degradation of thermoplastic starch.

To decorrelate the effect of processing from the one played by nanofillers, the study first focused on the characterization of the structure and the properties of pure starch-based matrices: more in detail, we focused on the effect of glycerol addition and “severe” or “soft” extrusion.

This first step enabled the identification of the most suited formulation and extrusion parameters to obtain starch-based materials more resistant to water and enzyme (α-amylase): “soft” extrusion with glycerol. The preservation of part of starch granules and the formation of a semi-crystalline structure during stabilization in humid environment after extrusion are responsible for the lower swelling and reduced enzymatic degradation of the starch matrix, compared to a more homogeneous thermoplastic starch without any residual granule.

A key role is played by glycerol, which both acts as a lubricant during extrusion, helping in preserving starch native structure, and increases starch chains mobility with important outcomes on the structure and the behavior of the material: indeed glycerol-plasticized starch-based materials are rubbery at a temperature close to room temperature and this, together with the highly-organized structure of starch granules, induces the fast entry of water and stabilization at lower values compared to amorphous starch.

Conversely, the application of strong extrusion parameters without any glycerol leads to a totally amorphous and more depolymerized starch structure which is highly hydrophilic and sensitive to enzymatic degradation.

From this first characterization, it was possible to identify the main structural elements which determine the behavior of starch matrices alone in physiological conditions. These are:

1. residual starch granules;
2. the semi-crystalline structure;
3. starch chains depolymerization.

Cellulose or chitin nanocrystals were added to glycerol-plasticized thermoplastic starch in form of aqueous suspensions and then these formulations were extruded using "soft" extrusion parameters, so as not to degrade the nanofillers.

When cellulose nanocrystals are added to starch, both the swelling and the rate of enzymatic degradation decrease significantly for concentrations up to 2.5wt%, compared to a matrix extruded with the same parameters. Nevertheless, structurally, the matrix and the nanocomposite were very similar: same crystallinity rate, same local organization by NMR, no residual granules. The improvement of these properties has been attributed to a good nanocrystals dispersion and good compatibility between starch and cellulose.

At higher concentrations however (5 and 10wt%), these improved properties disappear: nanocrystals aggregate and possibly disperse heterogeneously. Thus the "nanocomposite" becomes a simple "composite" and its behavior approaches that of the matrix alone.

Besides, at these concentrations cellulose nanocrystals seem to favor starch amorphous conformations, and this in turn worsens the behavior in physiological conditions: for example, swelling is more important at 5 and 10wt% cellulose nanocrystals in the matrix than in the glycerol-plasticized starch matrix alone.

Likewise, when chitin nanocrystals are used as nanofillers, swelling and enzymatic degradation increase, and those increases are more important the more concentrated the sample is. As for nanocelluloses, this comes from a more amorphous matrix and nanocrystals aggregation. Although unlike cellulose nanocrystals, chitin nanocrystals aggregate already at the lowest tested concentration (2wt%).

Hence, new experimental pathways need to be studied in order to better disperse the nanofillers in the starch matrix and obtain an optimal adhesion between the two components. For example, the use of "water-assisted" extrusion, mentioned in Chapter 1, could reveal an effective mean to homogeneously disperse nanofillers in the starch matrix, thanks to the high vapor pressure which forms in the heated barrel.

In all the nanocomposite systems studied, nanocrystals induced a stiffening of the starch matrix "at the dry state". An interesting perspective would be to check if this stiffening persists in physiological conditions; in this case nanomaterials with controlled mechanical properties could be produced by adding few of these nanometric materials. For this reason, an in-depth investigation of the mechanical properties of the nanocomposites in physiological conditions deserves to be implemented.

Despite the differences in structure and behavior in physiological conditions, all samples tested are non-cytotoxic towards epithelial and fibroblastic cells, which confirms their potentiality as biomaterials. Glycerol does not seem to reduce cellular viability (as, on the contrary, was suggested in a previous study) and neither do the nanocrystals. However other tests, more adapted to nanofillers, should be performed to confirm the safety of these nano-objects. For example, an insight about the internalization mechanisms associated to the cellulose and chitin nanocrystals analyzed in this study would be worthwhile. Besides, to enlarge the domain of application of these materials it would be interesting to test their cytotoxicity for longer times and on other types of cells.

The strategy that was chosen at the beginning of this work: reducing the sensitivity of thermoplastic starch to water and enzymatic degradation by adding nano-sized fillers, revealed partially effective but needs to be improved. For example the use of more complex screw profiles for extrusion or the use of lyophilized nanofillers (rather than in aqueous suspension) could favor their homogeneous dispersion and non-aggregation during extrusion.

The experimental pathway that was developed in this thesis and the advances that it provided on the comprehension of the physical-chemical interaction in nanocomposites opens many perspectives for future investigations. For example other types of nanofillers should be tested, of a different morphology like nanofibers and/or a different nature (starch nanocrystals, bacterial cellulose). The effect of nanofillers surface treatment on their dispersion/aggregation is an approach that deserves to be studied as well.

To conclude, this thesis work is one of the first studies focusing on the behavior in physiological conditions of 3D starch-based nanocomposites, entirely produced from natural resources and by an industrial process as the extrusion, for creating industrially credible alternatives to non-renewable materials. In particular, this is the first study, up to now, describing the enzymatic degradation of this type of nanocomposites.

This work potentially contributes to pave the way for the potential use of starch-based composites alone, and not in blend with other synthetic polymers, in the biomedical domain: for example, scaffolding systems could be developed starting from the materials analyzed in this thesis.

ANNEXES

Table of contents

1. Chitin nanocrystals production by hydrochloric acid hydrolysis

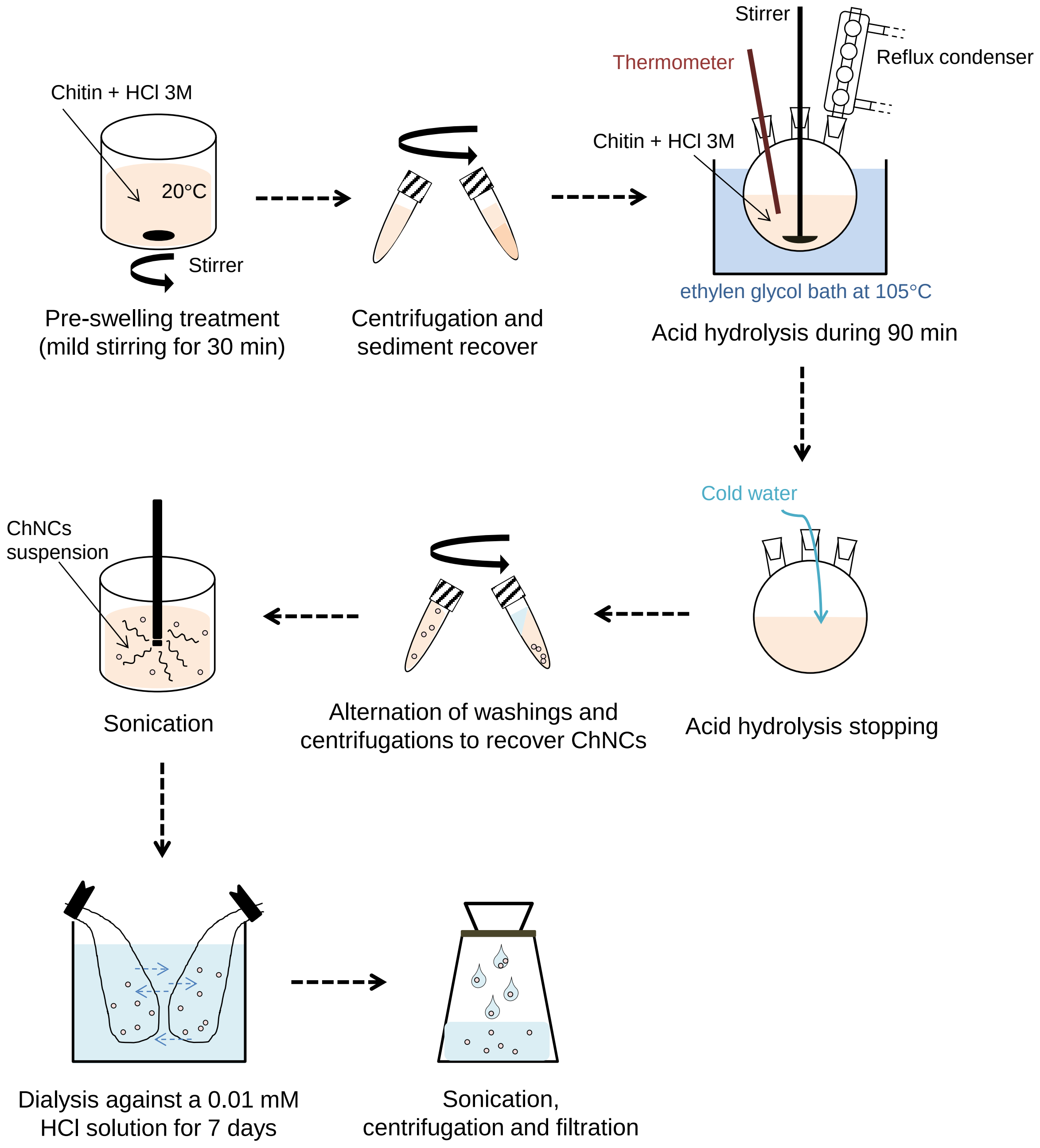

Figure A-1: *Protocol steps for the production of ChNCs by hydrochloric acid hydrolysis.*

Chitin nanocrystals (ChNCs) were produced by hydrochloric acid hydrolysis of chitin powder from shrimp shells (Sigma Aldrich, practical grade) following the protocol proposed by Perrin et al. (Perrin et al. 2014) on the example of Revol et al. (Revol et al. 1993).

In order to clean the powder, a swelling pre-treatment with 3 M HCl followed by centrifugation for 10 min at 15000g was carried out.

Twenty grams of chitin were hydrolyzed in 200 mL of a 3 M HCl boiling solution for 90 min. The hydrolysis was stopped with 500 mL of Milli-Q water at 4°C and the resulting suspension was washed with Milli-Q water by three centrifugations for 20 min at 10000g.
Then, Milli-Q water was added and the suspensions were let disperse at 4°C for two days. The slurry was then sonicated (QSonica Sonicator, 700 w) with intermittent cycles for an effective sonication time of 5 min and dialyzed against a 0.01 mM HCl solution for 7 days, then sonicated a second time. After two centrifugations at 12000g for 15 min to remove the residual detritus and a third sonication to disperse the potential aggregates, the suspension was filtrated using cellulose nitrate membranes with a 5-µm and then 1.2-µm pore size.

A schematic representation of this protocol is reported in **Figure A-1**.

2. Characterization of cellulose and chitin nanocrystals

2.1 Determination of nanofiller aqueous suspension concentration

Concentrations of nanofiller aqueous suspensions were determined via Thermo-Gravimetric Analysis (TGA 2050, T.A. Instruments, US). Aliquots of nanofiller aqueous suspensions were dried at 100°C until stable weight was reached. The concentration of each suspension was expressed in percentage on their starting mass as follows:

$$C\ (\%) = \frac{W_f - W_s}{W_s} \cdot 100 \quad \textbf{[A-1]}$$

Where W_f is the final weight of the dried suspension and W_s is the starting weight of the aqueous suspension.

2.2 Conductometric titration and pH

Conductometric titration and pH determination were developed with a Metrohm 905 Titrando associated to TIAMO software (Metrohm, Switzerland), as reported in (Perrin et al. 2014).
The titration consists in quantifying the surface charge density at the nanofiller surface using a 0.01N solution of NaOH. The total amount of sulfate (for CNCs) and amino (for ChNCs) groups at the surface of the nanocrystals is computed as follows:

$$C\ (mol\ g^{-1}) = \frac{V_{eq} \cdot C_{NaOH}}{m} \qquad \textbf{[A-2]}$$

where V_{eq} is the volume (L) of NaOH at the equivalent point, C_{NaOH} is the concentration (mol L^{-1}), and m is the weight of titrated cellulose and chitin (g).

The degree of substitution of sulfate and amino groups at the surface of CNCs and ChNCs is then computed by multiplying the surface charge density by the average molar mass of the nanocrystal. This value is used to convert surface charge density from $mol\ g^{-1}$ to $e\ nm^{-2}$.

3. Correction of temperature deviation in DMTA experiences

There is a deviation between the temperature measured by the thermocouple in the DMTA oven and the real temperature inside the sample. To adjust the data, the protocol consists in drilling one sample's side to insert a temperature probe and measure the deviation between the temperature measured by the thermocouple outside the sample and the real one assessed by the probe.

As visible in **Figure A-2**, the differences between the two temperatures is significant, and it increases linearly with heating.

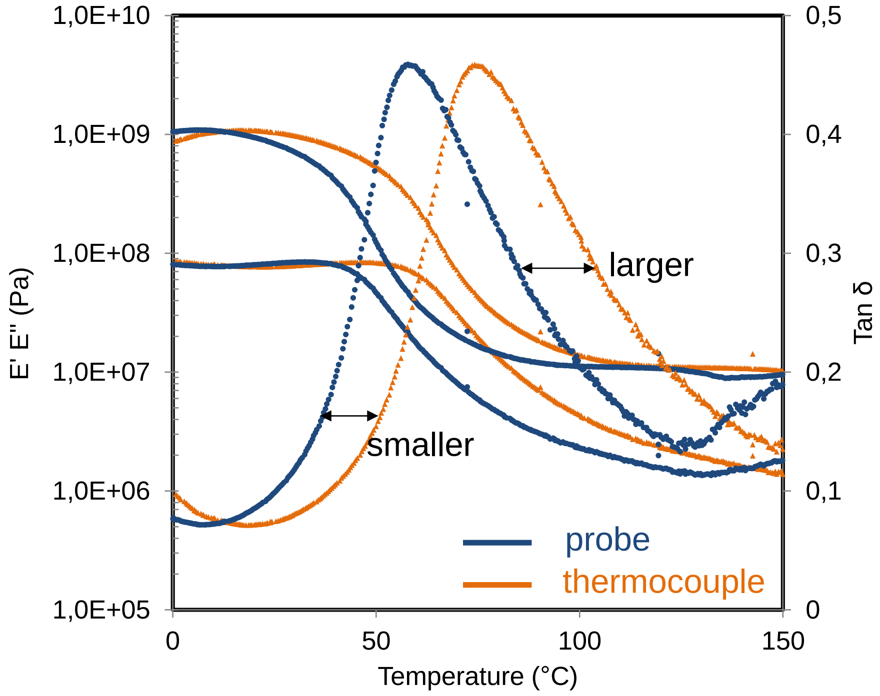

Figure A-2: *Differences in the temperature measured by DMTA thermocouple outside the sample (orange) and by the probe positioned inside the sample (blue). The difference between the two temperatures increases with the heating, as pointed out by black arrows.*

To apply the correction to DMTA data of all the samples, **Equation A-3** has been developed from the differences between the two measured temperatures, as showed in **Figure A-3**; the real temperature in the sample is computed from the temperature measured by the thermocouple as follows:

$$T_{real} = 0.9012 \cdot T_{thermocouple} - 9.0628 \qquad \textbf{[A-3]}$$

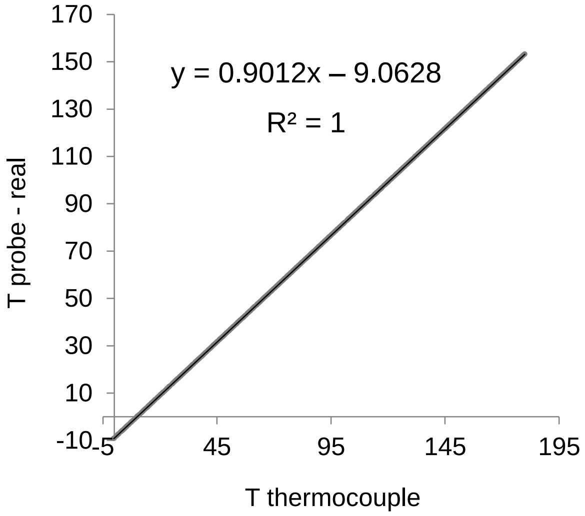

Figure A-3: *Linear correlation between the temperature measured by the thermocouple outside the sample and the temperature measured by the probe inside the sample (real one).*

4. Glass transition temperature in the extruded samples

Differential Scanning Calorimetry (DSC) was used to determine the glass transition temperature (Tg) of the extruded matrices and nanocomposites, following the protocol reported below.

Differential Scanning Calorimetry for Tg determination

Glass transition temperature (Tg) was determined using a Q100 DSC (T.A. Instruments, New Castle, DE, US). Samples of 10-15 mg mass were stabilized at $a_w = 0.59$ *for two weeks and then sealed in aluminum hermetic pans. The samples were heated with a first ramp from - 80°C to 90°C at 10°C* min^{-1}*, in order to erase the sample history. Then, the samples were cooled to -80°C and heated again to 150°C at 10°C* min^{-1}*. The Tg was determined from the thermogram obtained with the second heating ramp, as the midpoint of the transition between the glassy and the rubbery state.*

An example of thermogram obtained for a glycerol-plasticized sample (REF-CNC) is reported in **Figure A-4**.

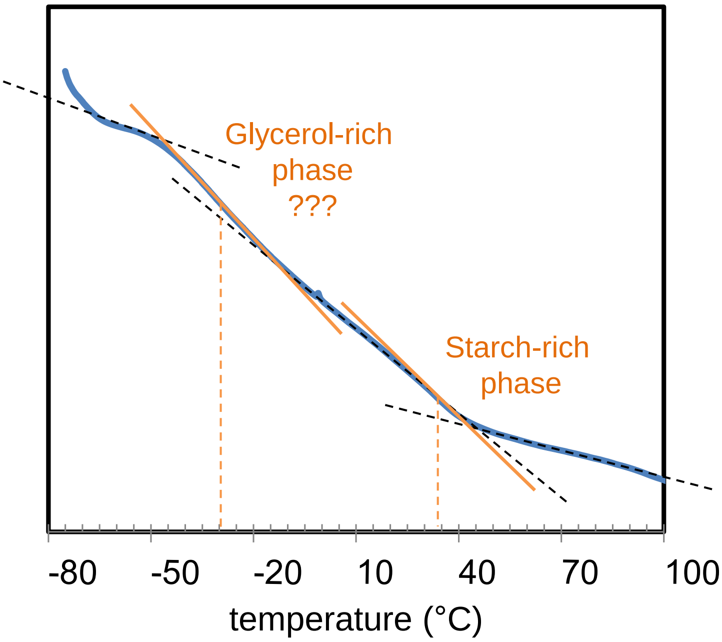

Figure A-4: *DSC heating curve (second scan) with indication of the glass transition temperature for the glycerol-plasticized matrix REF-CNC.*

The glass transition temperature was the same for all the glycerol-plasticized materials (~35°C), without any difference coming from structure or, for nanocomposites, nanofiller concentration. In addition, it seems that a second glass transition, associated to the glycerol-rich phase of the sample, is present at about – 30°C (see **Figure A-4**). However, the signal is too weak to be certain of this assignment.

For non-plasticized samples, Tg was at ~ 70°C.

5. Composition of phosphate buffer saline (PBS) 20mM pH 7

Exactly 6.9g of sodium phosphate monobasic monohydrate (NaH_2PO_4) are solubilized in 250mL of ultrapure water. Meanwhile 14.19g of disodium hydrogen phosphate (Na_2HPO_4) are solubilized in 500mL of ultrapure water.

Then 195mL of the first solution are mixed with 305mL of the second one and 1g of sodium azide (NaN_3, Sigma-Aldrich) is added to it. Ultrapure water is added until a 1L total volume and the pH is measured (pH = 7). This solution (**PBS 0.1M**) can be conserved up to six months at room temperature (20°C).

A solution of calcium chloride ($CaCl_2$) 1M is prepared by solubilizing 14.7g of powder in 100mL of ultrapure water.

Similarly, a solution of sodium chloride (NaCl) 1M is prepared by mixing 5.84g of NaCl in 100mL of ultrapure water. These two solutions can be stored up to one year at 4°C.

To prepare the final PBS (**PBS 20mM pH 7**), 200mL of PBS 0.1M are added of 2mL of NaCl 1M and of 0.25mL of $CaCl_2$ 1M. Ultrapure water is added until a final volume of 1L. This solution can be stored at 4°C up to 1 month. For PBS-D_2O, smaller quantities are prepared replacing water with D_2O (Eurisotop, ref D214K, lot N3371).

6. Preliminary study about the water sorption of starch-based composite films

Starch-CNCs nanocomposite films were prepared by casting (as shown in **Figure A-5**) to test their behavior in humid environment and compare it to the one of starch-based nanocomposites produced by extrusion. In addition to nanocomposite films, two references (pure starch film and pure CNCs film) were developed as well.

Solvent casting for film production

*The formulations for the films were prepared by mixing starch, glycerol and water as reported in **Figure A-5**. In order to break the organized semi-crystalline state of native starch, starch suspension is first heated to 130°C and stirred (under pressure in an autoclave) for 20 min, before cooling to 70°C (below that temperature starch would begin recrystallization).*
*The amorphous starch solution is then added with cellulose nanocrystals (CNCs) aqueous suspensions at different concentration and mixed for 5 minutes (**Figure A-5**) before to be casted.*
To do this, the starch-CNCs suspensions are spread on a Teflon-coated surface and dried in a ventilated oven at 70°C, to form thin films.
Once dried, they are then left in controlled humidity (0.59 a_w with NaBr solution) at 20°C for 2 weeks in order to get the same moisture content.

One pure glycerol-plasticized starch and one pure CNCs films have been developed to be used as references.
The starch-CNCs nanocomposites produced by casting (at 2.5, 5, 10 and 25wt% CNCs concentrations) are very close, for composition, to the ones produced by extrusion (except for the film at 25wt% CNCs, which is more concentrated).

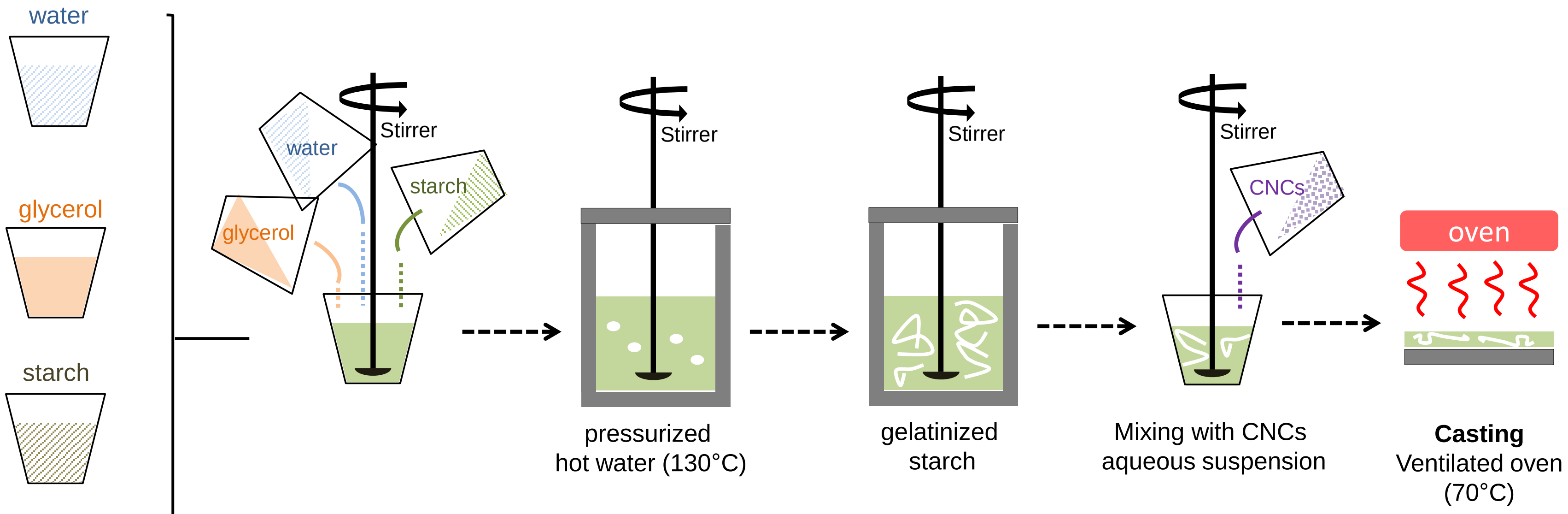

Figure A-5: *Preparation of starch-based nanocomposites by solvent-casting.*

The final composition of the films, before and after drying, is reported in **Table A-1**.

Table A-1: *Samples' nomenclature and composition.*

Sample	**Theoretical ratio (%wt) starch:water:glycerol:CNCs** **before drying**	 **at stabilization**
G20_cast	2.4:97.1:0.5:0	71:13:16:0
CNC_2.5_cast	2.3:97.1:0.5:0.1	68.9:13:15.6:2.5
CNC_5_cast	2.3:97:0.5:0.2	66.9:13:15.1:5
CNC_10_cast	2.2:96.9:0.5:0.4	62.8:13:14.2:10
CNC_25_cast	2:96.5:0.5:1.0	50.6:13:11.4:25
CNCs_cast	0:88:0:12.0	0:5:0:95

To get a good estimation of their water sorption, these nanocomposite films have been analyzed by using the Dynamic Vapor Sorption (DVS) technique (see the experimental set up below for details)

Dynamic Vapor Sorption of casted films

Dynamic Vapor Sorption (DVS) is a gravimetric sorption technique used to determine the kinetic and the quantity of solvent absorbed or desorbed by the sample over time.

The principle consists in varying the vapor concentration surrounding the sample and measuring the change in mass due to the solvent gradual sorption or desorption. Water vapor is commonly used (as in this specific case of study), but a wide range of organic solvents can be employed as well.

The carrier gas is set at a specified relative humidity (or partial pressure) over a sample suspended in a pan connected to an ultra-sensitive recording microbalance. The sample mass must stabilize at each step change in humidity before moving to the next humidity step. Then, the sorption or desorption isotherm is generated by plotting the set of equilibrium mass values at each relative humidity level. The time necessary to complete de isotherm can vary a lot and it is dependent upon the sample weight (usually between 1 mg and 4 g) and nature.

In this work DVS experiences were developed on very small sample sizes (10 mg on average), to minimize the equilibration time required. Even at this low mass value, one week per sample was necessary to obtain a complete sorption isotherm.

Because of the high precision of this technique, only one sample per formulation was analyzed.

The sorption curves of the casted nanocomposites and their references are reported in **Figure A-6a**, while the values normalized exclusively on the mass of starch in the films are reported in **Figure A-6b**.

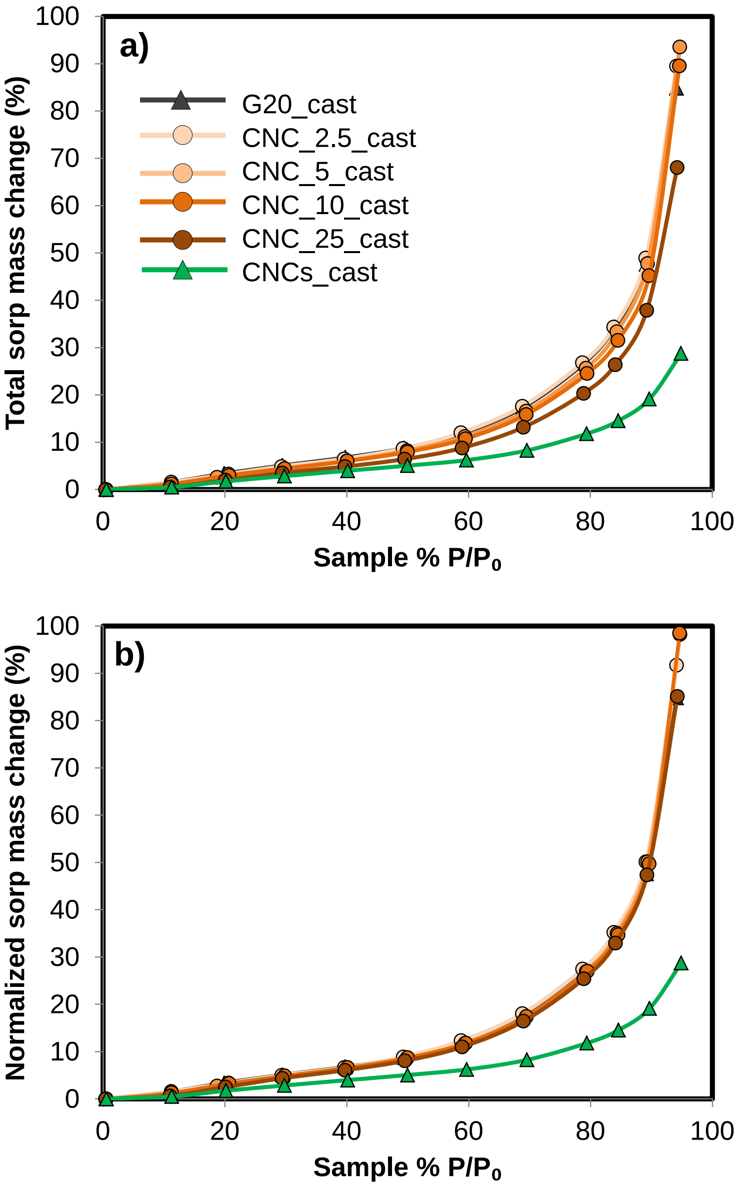

Figure A-6: Sorption curves of starch-CNCs nanocomposite films compared to the sorption kinetic of a film without any nanofiller (G20_cast) and a film of CNCs (CNCs_cast).

By comparing **Figure A-6a** and **b**, it is clear that the sorption behavior of the film is determined by the ratio starch/CNC: higher this ratio, higher the water sorption of the film. Indeed, because of their highly crystalline structure, CNCs do absorb less water than starch (see CNCs sorption curve, **Figure A-6**), which explains the global lower quantity of water absorbed at increasing nanofiller concentrations.

As pointed out by the results reported in **Figure A-6b**, CNCs do not seem to interact with starch and reduce its sensitivity to water, as it has been observed for the low-concentrated CNCs nanocomposites (CNC_1.5 and CNC_2.5) produced by extrusion.

In addition to water sorption, CNCs are reported to slow down the velocity at which water enters in the sample, because they create a tortuous path, more difficult for water to follow. To verify if CNCs played this effect in our nanocomposite films, the sample mass (%) has been plotted as a function of time. The sorption curves obtained with this treatment are reported in **Figure A-7**. To ease the interpretation of the figure, all samples masses have been normalized by the mass they reach at the end of the sorption isotherm (fixed to 100%).

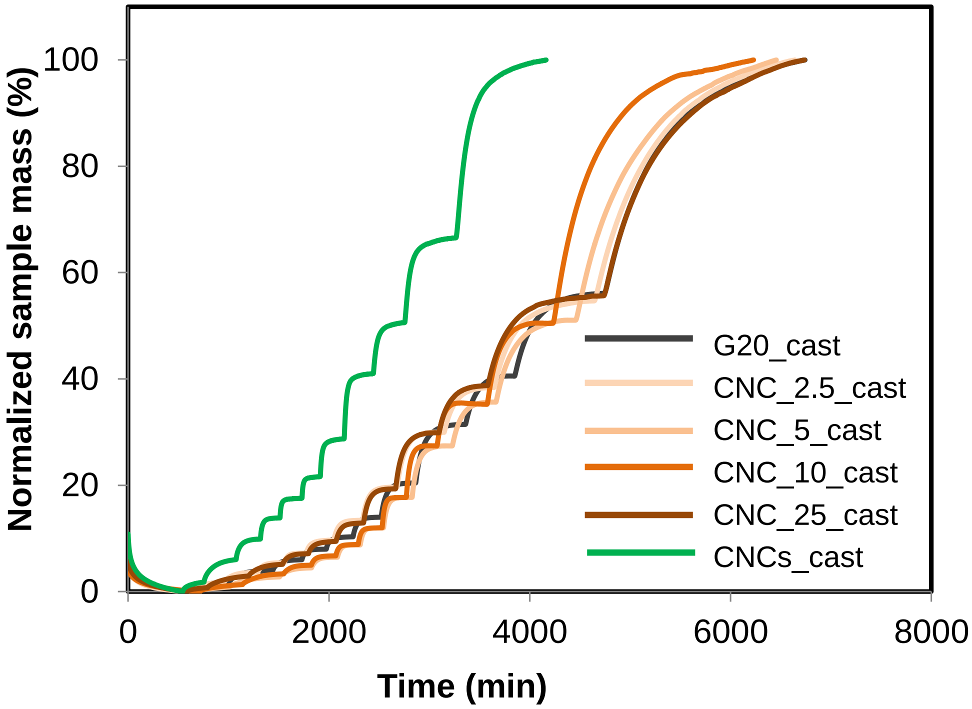

Figure A-7: *Nanocomposite films mass evolution over time. The mass of each sample is normalized by its final mass reached at the end of the sorption isotherm.*

By the study of **Figure A-7** we can notice that no significant differences occur in the sorption kinetics of nanocomposite films.

The lack of any influence of CNCs on starch water sorption might be explained by the non-homogeneous dispersion of the nanofillers in the matrix either to their aggregation. Hence, no modification of starch sorption properties is obtained in these specific casted systems.

Résumé de la thèse en langue française

Table des matières

1. Contexte et objectif de l'étude

Au cours des dernières décennies l'intérêt pour des matériaux durables, dégradables et bio-sourcés est croissant. Ces matériaux peuvent entre autres être créés en valorisant des coproduits provenant de la filière bois et agro-alimentaire. Parmi les polymères naturels les plus utilisés on retrouve l'amidon, la cellulose, la chitine et les alginates, qui, en plus d'être biodégradables, ont aussi l'avantage d'être biocompatibles avec le corps humain, ce qui étend leur domaine d'application.

L'un des avantages de l'amidon par rapport aux autres bio-polymères est sa capacité de mise en forme par des techniques thermiques (casting) ou thermomécaniques (extrusion, thermo-moulage, etc.) simples, sans solvants chimiques organiques. Ces techniques permettent d'obtenir des matériaux 3D, faciles à manipuler et dont la production peut être facilement étendue à l'échelle industrielle. Grâce à ces propriétés l'amidon est utilisé pour les applications les plus diverses, des emballages aux échafaudages tissulaires.

Une application potentielle pour l'amidon thermoplastique est le développement d'implants dégradables sur des temps relativement courts de quelques jours, comme montré précédemment lors de travaux menés dans l'équipe (Velasquez et al. 2015; Beilvert, Chaubet, et al. 2014; Beilvert, Faure, et al. 2014). L'utilisation de ces matériaux pour le traitement de pathologies des canaux salivaires a démontré que la durée de vie de ce type de matériaux est trop courte pour envisager des applications à plus longue durée (quelques semaines), à cause de la dégradation rapide de l'amidon thermoplastique en présence d'eau et, implanté, par les amylases.

Toutefois cette dégradation rapide peut être ralentie : soit en jouant sur les paramètres du procédé de mise en forme de l'amidon, soit en ajoutant d'autres composants au matériau, comme par exemple des nanoparticules.

En effet les nanocristaux présentent une surface spécifique élevée qui leur permet de former des interactions (hydrogène) fortes avec l'amidon. La taille nanométrique des charges constitue un élément clé : pour le même volume de particules, si la dispersion est homogène, l'effet sur les propriétés macroscopiques sera plus important pour des particules plus petites (nano), à cause de la plus grande interface d'interaction entre le polymère et les charges (Cho et al. 2006). C'est dans ce contexte que se positionne cette thèse.

L'objectif est de comprendre l'effet de l'ajout de nanoparticules sur la structure et les propriétés des matériaux (nanocomposites à base d'amidon), afin de contrôler le taux de dégradation des matériaux et améliorer leur fonctionnalité.

2. Préparation et composition des matériaux

Les nanocomposites ont été produits par extrusion bi-vis (**Figure R-1**); l'enjeu est de développer des matériaux complétement bio-sourcés produits par extrusion, en utilisant de l'amidon de pomme de terre plastifié avec du glycérol comme matrice et des nanocristaux de cellulose (CNC) ou de chitine (ChNC) comme charges.

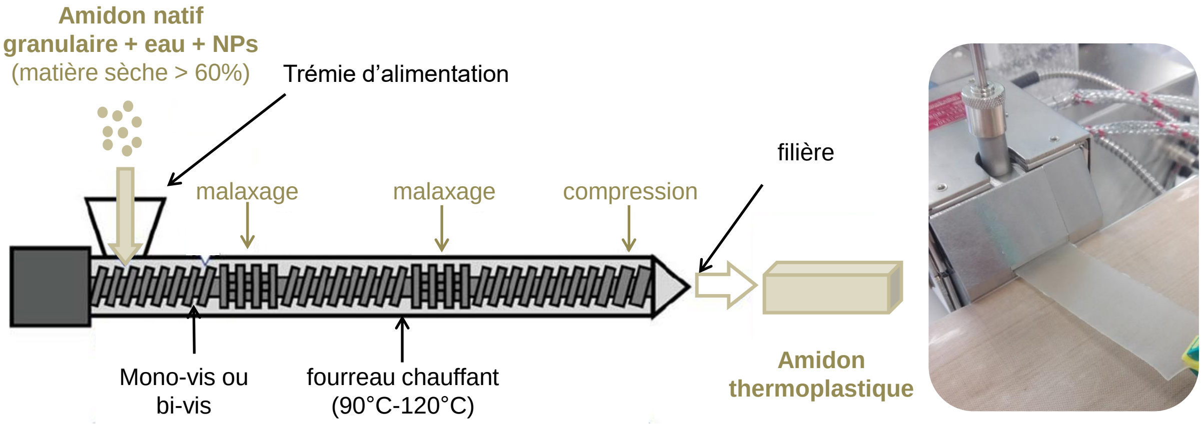

Figure R-1 : *Préparation de nanocomposites par extrusion bi-vis.*

Pour séparer l'effet des paramètres d'extrusion des effets de la présence des nanoparticules, plusieurs matrices-test à base d'amidon mais sans nanocharges, extrudées en absence (G0) et en présence (G20) de glycérol (22.5% sur la masse d'amidon sec) ont été produites lors d'une étude préliminaire.

Plus en détail, des basses températures (max = 90°C) et une faible énergie mécanique spécifique (EMS) ont été appliquées (100 J g^{-1}) pour produire des matrices faiblement déstructurées (G0_LOW en absence et G20_LOW en présence de glycérol) en utilisant un profil de vis court (15.5 L/D) et simple ; réciproquement des températures d'extrusion élevées (max = 115°C) ont été couplées à un stress mécanique important (EMS = 1900 J g^{-1}) et un profil de vis long (40 L/D) additionné de malaxeurs pour produire des matrices hautement déstructurées (G0_HIGH en absence et G20_HIGH en présence de glycérol).

Ensuite, les nanocomposites ont été produits en ajoutant le mélange glycérol/suspensions aqueuses de CNC ou ChNC à l'amidon granulaire avant extrusion. Les deux types de nanocomposites ont été extrudés en utilisant des paramètres légèrement différents, afin de produire des structures de l'amidon différentes et étudier l'effet des nanocharges sur ces structures.

Après stabilisation en milieu humide (0.59 a_w avec une solution de NaBr) pendant deux semaines, la teneur en eau et en glycérol de tous les matériaux extrudés ont étés mesurés par gravimétrie et par Résonance Magnétique Nucléaire du proton (^{1}H RMN) respectivement : les matrices contiennent entre 12 et 15% d'eau et, quand il est présent, 16% de glycérol sur le poids total de l'échantillon. Rapportées au poids total, les nanocomposites présentent des teneurs en eau et glycérol plus variables: l'eau varie entre 11 et 12.5% et le glycérol entre 14.5 et 16% (**Tableau R-1**).

Tableau R-1 : *Composition et nomenclature des échantillons.*

Nomenclature	Ratio théorique (en masse) amidon:eau:glycérol:NPs après stabilisation
G0	85:15:00:0
G20	72:12:16:0
CNC_1.5	70.5:12:16:1.5
CNC_2.5	70:12:15.5:2.5
CNC_5	68:11.5:15.5:5
CNC_10	63.5:12:14.5:10
CNC_4	69:11.5:15.5:4
ChNC_2	70:12.5:15.5:2
ChNC_4	68:12.5:15.5:4
ChNC_8	66:11:15:8

Le poids restant du matériau est constitué par l'amidon et des nanoparticules (dans le cas des nanocomposites). Pour les nanocomposites à base de cellulose, la concentration théorique en CNC varie entre 1.5% et 10%, alors que pour les ChNC les concentrations théoriques varient entre 2% et 8% (**Tableau R-1**).

Un échantillon supplémentaire, contenant 4% de CNC (**Tableau R-1**) mais produit avec les paramètres d'extrusion des nanocomposites à base de chitine, permet de découpler l'effet du type de charge utilisée de l'effet des paramètres d'extrusion.

Selon les formulations, les paramètres d'extrusion ont dû être parfois ajustés afin d'obtenir, pour chaque formulation, un matériau visuellement homogène (sans fractions non fondues) à la sortie de la filière. Par exemple, les températures d'extrusion ont été légèrement augmentées dans le cas des nanocomposites les plus chargés (CNC et ChNC ≥ 4%).

3. Organisations à large échelle : microscopie, structure granulaire et longueur de chaînes

La caractérisation des matrices (sans nanocharges) débute par l'observation de l'état de leurs surfaces de fracture par Microscopie Electronique à Balayage (MEB). Cet examen a été couplé à une mesure d'enthalpie de gélatinisation par Analyse Enthalpique Différentielle (AED ou DSC en anglais pour Differential Scanning Calorimetry) afin de déterminer la présence éventuelle de grains d'amidon ayant résisté au procédé d'extrusion.

Ces premiers résultats ont montré que l'extrusion « agressive » (hautes température et EMS (1900 J g^{-1})) induit la complète disparition de la structure granulaire native de l'amidon et l'obtention de matériaux à la surface homogène et lisse, indépendamment de la présence de glycérol.

En revanche, l'extrusion « douce » (basse température et faible EMS (100 J g^{-1})) favorise la préservation d'une partie importante des structures granulaires natives de l'amidon, ce qui génère des surfaces de fracture irrégulières.

La quantité de grains préservés dans l'échantillon est plus élevée lorsque le glycérol est ajouté à la formulation (25% avec glycérol et 16% sans glycérol) grâce à son action lubrifiante, qui aide à préserver la structure granulaire de l'amidon pendant extrusion (Nessi et al. 2018).

Les nanocomposites amidon/cellulose ayant été extrudés avec des conditions légèrement plus agressives que la référence d'extrusion « douce » (profil de vis de longueur intermédiaire et températures légèrement plus élevées (max = 105°C)), une nouvelle matrice de référence, REF-CNC, a été produite.

L'observation de cette référence montre que ce léger changement des conditions induit, malgré l'EMS restée faible (80 J g^{-1}), la perte complète de la structure granulaire native et une surface de fracture homogène, semblable à celles des matrices produites par extrusion « agressive ».

À une échelle plus petite, les masses moléculaires de l'amidon sont caractérisées par fractionnement par couplage flux-force hydrodynamique couplé à un détecteur de diffusion de la lumière et un détecteur réfractométrique (AF4-MALLS-DRI). Les EMS élevées (1900 J g^{-1}) sont responsables de la dégradation importante des chaînes d'amidon : la masse molaire

(M_w) et le rayon de giration (R_{Gz}) moyens des molécules d'amidon (amylose et amylopectine) passent de 13.5×10^7 g mol^{-1} et 198 nm pour l'amidon natif à 0.8×10^7 g mol^{-1} et 60 nm pour G0_HIGH. L'effet lubrifiant et protecteur du glycérol observé auparavant est confirmé ici par la plus faible dégradation des chaînes d'amidon observée pour G20_HIGH ($M_w = 1.6 \times 10^7$ g mol^{-1} et $R_{Gz} = 76$ nm).

Pour ces deux matrices la dégradation des molécules d'amylopectine est si importante que les deux populations de macromolécules (amylose et amylopectine) constituant l'amidon ne sont plus distinguables (**Figure R-2**).

Au contraire, une EMS faible (100 J g^{-1}) ne dégrade que peu les chaînes d'amidon, dont la masse molaire et la taille restent alors très proches de celles de l'amidon natif (**Figure R-2**) : pour G0_LOW la masse molaire et le rayon de giration sont de 13.3×10^7 g mol^{-1} et 202 nm et, pour G20_LOW, de 11.3×10^7 g mol^{-1} et 188 nm.

Un profil de vis légèrement plus long que celui utilisé pour G20_LOW entraine une dégradation des chaînes d'amidon plus importante : REF-CNC a une M_w de 9.2×10^7 g mol^{-1} et un rayon de 179 nm.

Pour G0_LOW, G20_LOW et REF-CNC la distribution bimodale des deux populations d'amylose (masse plus petite) et d'amylopectine (masse plus grande) reste séparée et bien identifiable (**Figure R-2**).

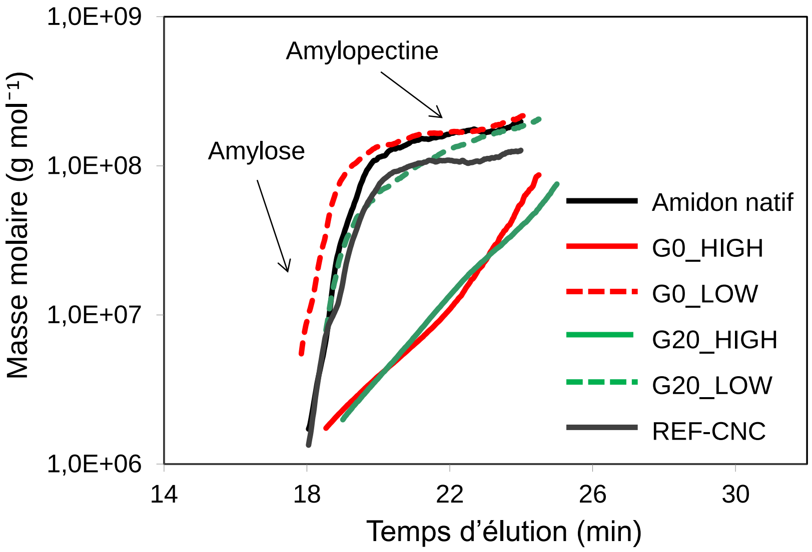

Figure R-2 : *Evolution de la masse molaire en fonction du temps d'élution pour les matrices à base d'amidon et l'amidon natif.*

En ce qui concerne les nanocomposites, les observations de microscopie et les mesures d'enthalpie de gélatinisation montrent que, de même que leur matrice de référence REF-CNC,

les nanocomposites amidon-CNC ne possèdent pas de grains résiduels dans leur structure.
Contrairement à ces derniers, des grains d'amidon résiduels sont détectés dans le nanocomposite à 2% de ChNC (mais pas aux concentrations supérieures en nanocristaux de chitine) : la proportion de grains préservés (18%) est cependant plus faible que celle de la matrice de référence (G20_LOW, 25%). Le fait que ces grains résiduels disparaissent aux concentrations supérieures peut être dû à un effet « dégradant » des nanocristaux de chitine sur les grains d'amidon ou aux températures plus élevées lors de l'extrusion des nanocomposites les plus chargés (ChNC_4 et ChNC_8).

Indifféremment du type de nanocristaux (cellulose ou chitine), l'ajout de nanocristaux accroit clairement l'irrégularité des surfaces de fracture, et ce de façon proportionnelle avec leur concentration dans l'échantillon (**Figure R-3**).

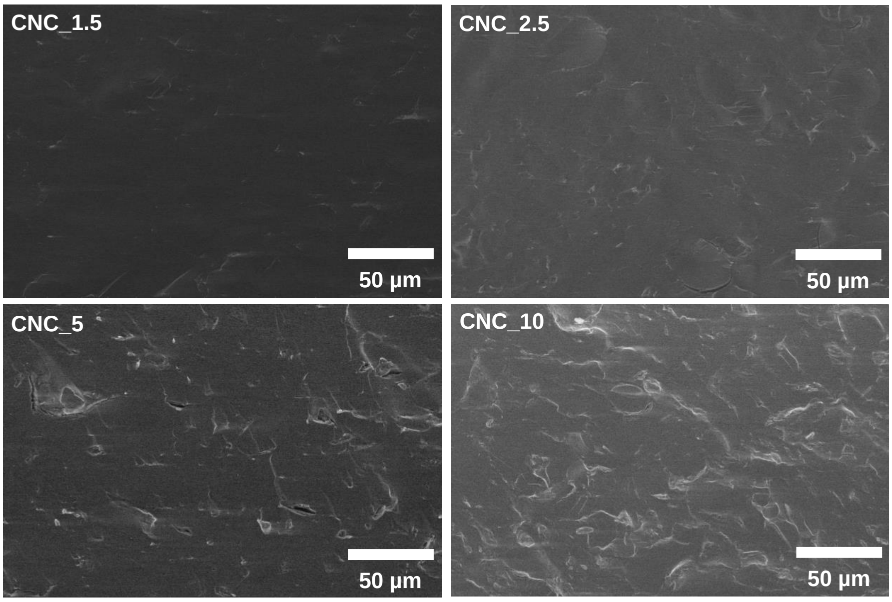

Figure R-3 : *Etat de la surface de rupture de nanocomposites amidon-CNC observé par MEB.*

L'ajout de CNC dans les nanocomposites induit une légère dégradation supplémentaire des chaînes d'amidon, dont la masse molaire et le rayon varient entre 7.3 - 9.3 × 10^7 g mol^{-1} et 142 - 189 nm. L'incidence des nanocristaux de chitine (ChNC) sur ces mêmes caractéristiques n'a pas pu être déterminée, à cause de l'incapacité de séparer la partie amylacée de l'échantillon des nanocharges de chitine.

4. Structure locale et propriétés à l'état sec : diffraction, RMN et propriétés thermomécaniques

4.1 Structure locale et cristalline

La structure cristalline et les ordres locaux des échantillons ont ensuite été caractérisés par Diffractions aux Rayons X (DRX) et Résonance Magnétique Nucléaire à l'état solide (RMN).
En ce qui concerne les matrices, le traitement d'extrusion est responsable de la perte de la structure cristalline native initiale (30% de cristallinité de type B): perte totale de cristallinité pour G0_HIGH (0%) et taux réduit pour G0_LOW (8% de cristallinité B), conformément aux résultats obtenus par les mesures d'enthalpie de gélatinisation.
L'ajout de glycérol permet, d'une part, de préserver la structure cristalline native pendant l'extrusion (seulement pour le traitement d'extrusion « douce ») et d'autre part de réorganiser les chaînes d'amidon dans l'échantillon (recristallisation) : ces deux effets sont prouvés par le très haut taux de cristallinité observé pour G20_LOW (17% de cristallinité B). La perte totale de cristallinité native due à la plus haute intensité du traitement d'extrusion justifie les taux de cristallinité plus faibles observés pour REF-CNC (7% de cristallinité B) et G20_HIGH (7% de cristallinité B), dont la cristallinité provient exclusivement de la recristallisation.

Les résultats obtenus par DRX concordent avec ceux obtenus au niveau de la structure locale par RMN du solide (**Figure R-4**). L'analyse de la région du C1 du spectre montre que dans les échantillons sans glycérol les chaînes d'amidon sont majoritairement en conformations amorphes (pic A).
Au contraire, les matrices plastifiées montrent une plus grande proportion de conformations paracristallines et cristallines (pics B et C, **Figure R-4**), probablement car le glycérol augmente la mobilité des chaînes d'amidon, ce qui leur permet de se réorganiser en double hélices après l'extrusion. De plus, la présence de plastifiant diminue visiblement la proportion de structures énergiquement non favorables (pic D et E, **Figure R-4**) générées par le procédé d'extrusion.

Indépendamment de la formulation (avec ou sans glycérol), les structures amorphes sont majoritaires lorsque l'EMS appliquée est élevée.

En DRX, il était impossible de découpler le signal des nanoparticules de celui de l'amidon à cause de la superposition de leurs pics cristallins. Toutefois, au niveau des ordres locaux mesurés par RMN, il apparaît que les nanocharges sont responsables de la transformation des structures cristallines et paracristallines de l'amidon en structure plus amorphes. Il est possible que les nanocristaux favorisent les structures amorphes en agissant comme obstacles physiques pendant la réorganisation des chaînes d'amidon en structures semi-cristallines après extrusion (Liu et al. 2016; Liu et al. 2017). Cet effet apparait à partir de 4% de CNC et 2% de ChNC, et il est plus important avec la cellulose qu'avec la chitine.

A concentration inférieure en CNC (1.5% et 2.5%), les CNC n'influencent pas la structure locale de l'amidon.

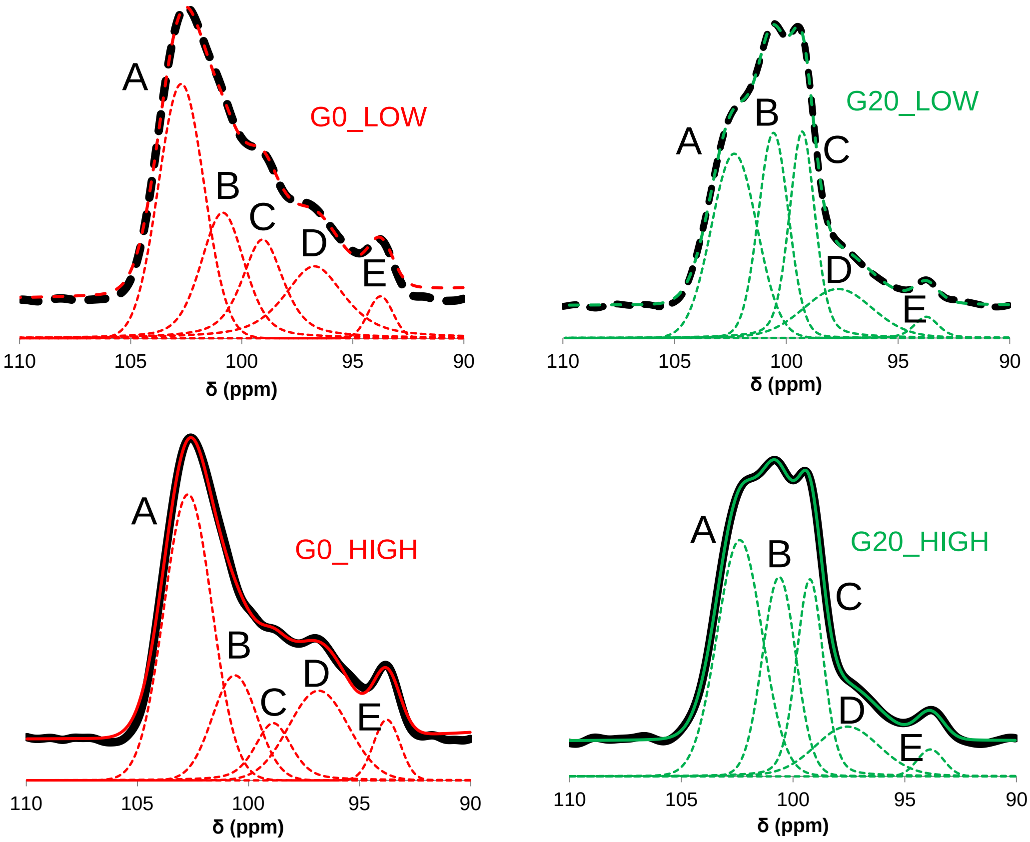

Figure R-4 : *Focus sur la région du C1 des spectres RMN des matrices. Chaque spectre reporte les valeurs mesurées (ligne noir), les valeurs calculées (ligne colorée) et la déconvolution des pics constituant les spectres (ligne colorée pointillée).*

4.2 Propriétés à l'état sec et organisation amidon-charges

Afin de compléter notre connaissance de la structure des matériaux produits et faire le lien avec leurs propriétés, nous avons étudié les transitions de phase et les mobilités moléculaires associées à la mobilité des chaînes d'amidon par Analyse Enthalpique Différentielle (AED) et Analyse Thermique Mécanique Dynamique (ATMD ou DMTA en anglais pour Dynamic Mechanical Thermal Analysis), couplée avec une caractérisation des propriétés mécaniques des matériaux aux grandes déformations en traction. Ces analyses, réalisées sur les matériaux

« secs » (stabilisés pendant deux semaines à a_w = 0.59), confirment une mobilité moléculaire plus importante en présence de glycérol, avec un matériau caoutchoutique à température proche de la température ambiante (35°C) et facilement déformable. La déformabilité du matériau diminue quand des grains résiduels sont préservés dans la matrice d'amidon (par exemple pour la matrice G20_LOW).

Une diminution similaire de déformabilité est obtenue lorsque des nanoparticules sont ajoutées à la matrice thermoplastique : les composites amidon-ChNC sont moins déformables et leur module d'Young augmente avec la concentration en nanocristaux dans l'échantillon (de 166 ± 40 MPa pour ChNC_2 jusqu'à 299 ± 15 MPa pour ChNC_8). Les nanocomposites amidon-CNC sont également moins déformables à mesure de l'augmentation de la concentration de nanocharges dans la matrice alors que le module d'Young reste constant (145 ± 20 MPa pour CNC_1.5 jusqu'à 195 ± 20 MPa pour CNC_10).

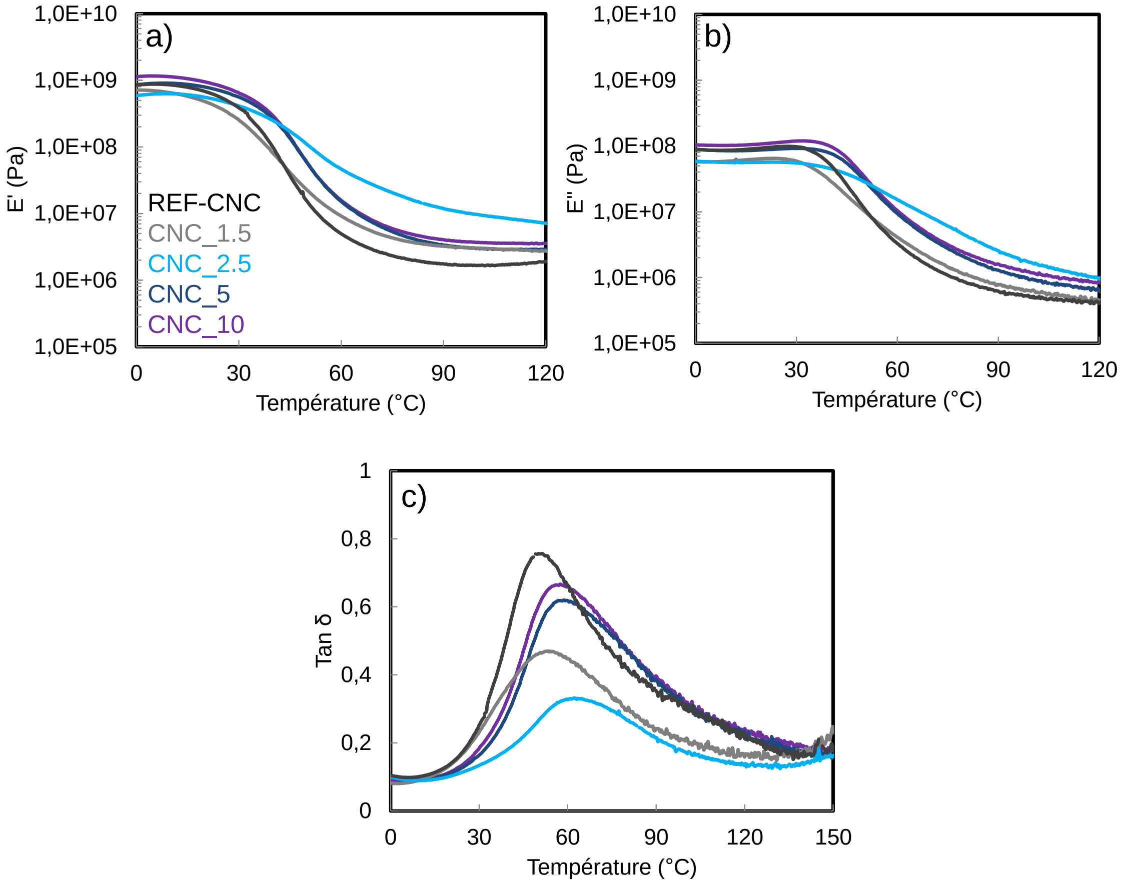

Figure R-5 : a) *Module de conservation (E'),* **b)** *modules de perte (E'') et* **c)** *facteur d'amortissement (Tan δ) de nanocomposites amidon-CNC et leur matrice de référence REF-CNC.*

Le rôle de renfort mécanique joué par les CNC jusqu'à 2.5% est également observé par

DMTA : les modules de conservation (E') et de perte (E") augmentent entre 1.5% et 2.5%, pour après diminuer à 5 et 10% de CNC. De même, la mobilité des chaînes (Tan δ) diminue quand la concentration en CNC augmente, atteint un minimum pour 2.5%, et augmente à nouveau à 5 et 10% en CNC (**Figure R-5**).

Pour les nanocomposites amidon-ChNC, quelle que soit la teneur en cristaux de chitine, le matériau montre un comportement moins rigide (E' et E" plus faibles, Tan δ augmenté) que celui de la matrice de référence G20_LOW.

Le changement de structure et des propriétés à sec observé pour les composites amidon/cellulose est en accord une agrégation des nanocristaux se produisant à une concentration comprise entre 2.5% et 5%. Au-delà de 5%, nos observations pointent vers un regroupement des nanocristaux en agrégats de taille inconnue et, potentiellement, une dispersion irrégulière dans la matrice d'amidon (**Figure R-6a**). À cause de cette agrégation, la surface d'interaction entre cellulose et amidon est alors réduite de façon significative et le « nanocomposite », désormais simple « composite », a un comportement qui se rapproche d'une simple matrice d'amidon.

Aux plus faibles concentrations (1.5 et 2.5% de CNC) la structure des composites amidon/cellulose est très similaire à celle de la matrice : même taux de cristallinité (~10%), structure locale proche (RMN), pas de grain résiduels. Toutefois les propriétés thermomécaniques (DMTA) varient significativement : ceci pourrait être expliqué par la formation de liaisons hydrogène entre les nanocharges et l'amidon. Les observations réalisées à ces faibles concentrations de CNC sont cohérentes avec des nanocristaux globalement non-agrégés et bien dispersés dans la matrice d'amidon, ce qui maximise les interactions amidon/cellulose.

Pour les nanocomposites amidon-ChNC il est probable que les nanocristaux soient agrégés quelle que soit leur concentration : les propriétés changent peu, indiquant des interactions amidon (matrice)/chitine (nanocharge) peu importantes (**Figure R-6b**).

Cette hypothèse est supportée par des calculs théoriques simplifiés de percolation des cristaux dans les composites. Dans le cas de nanocristaux parfaitement dispersés, un réseau percolant devrait se former autour d'une concentration en CNC de 9.8 ± 1.2% et en ChNC de 7.5 ± 2.5% ; ce réseau devrait induire un changement significatif de la structure et des propriétés mécaniques, hors ce n'est pas le cas pour les matériaux analysés ici. L'explication la plus commune à cette observation est l'agrégation des charges.

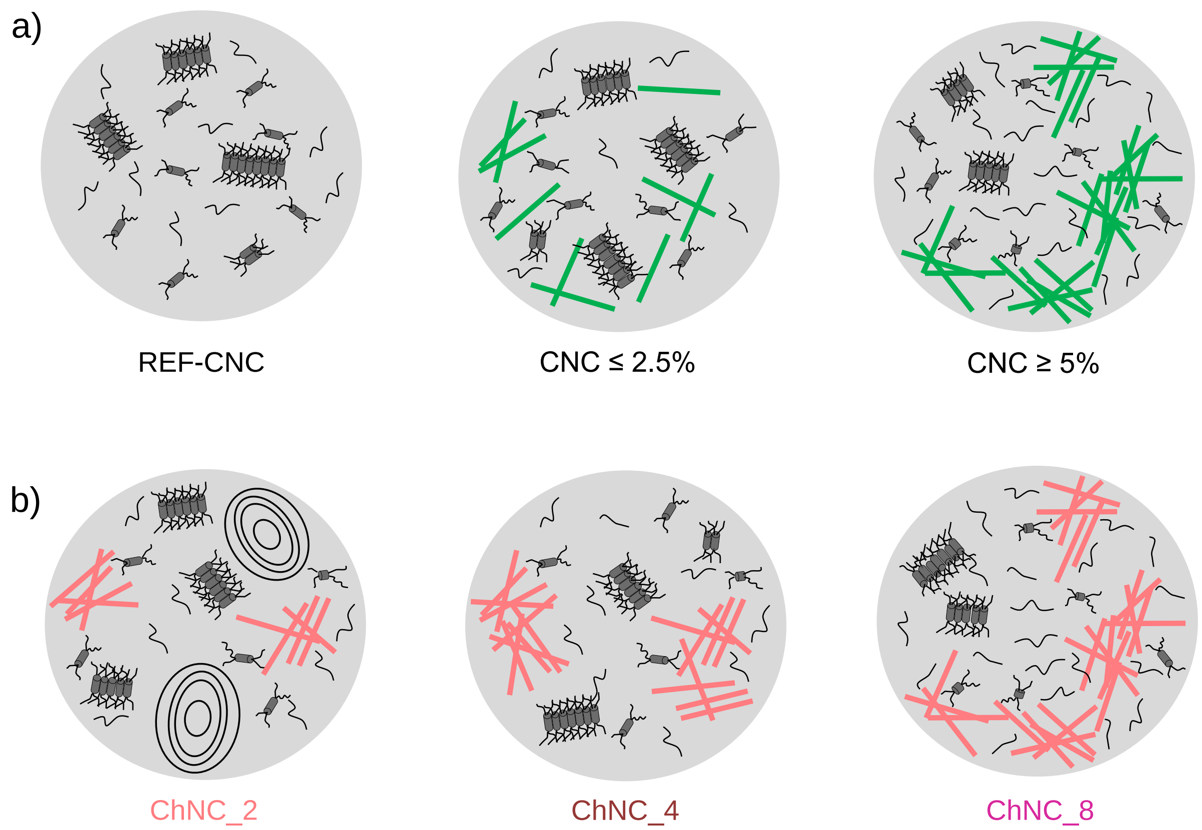

Figure R-6 : *Représentation de la structure des* **a)** *nanocomposites amidon-CNC à basse (1.5, 2.5%) et haute (5, 10%) concentration en nanocristaux en comparaison avec leur matrice de référence REF-CNC et* **b)** *des nanocomposites amidon-ChNC. Les simples (ligne noir) ou double (cylindre gris) hélices d'amidon, les cristaux (regroupement de plusieurs cylindres gris) et les grains (lignes noir concentriques) d'amidon, les CNC (bâtonnés verts) et les ChNC (bâtonnés roses) sont représentés dans le système.*

5. Comportement en conditions physiologiques

Suite à ces caractérisations, certaines propriétés d'intérêt pour l'application des composites dans le domaine biomédical ont été retenues : la dégradation enzymatique (par l'α-amylase) et le gonflement des matériaux dans des conditions physiologiques ont été caractérisés à des températures proches de celles du corps humain (37-40°C), afin d'avoir une première approximation de leur valeur pour un usage comme implants biomédicaux.

L'absence de structure native (comme dans la matrice G0_HIGH) rend le matériau très sensible au gonflement et à la dégradation enzymatique : cette matrice gonfle jusqu'à 300 ± 25% le volume de départ de l'échantillon et est rapidement hydrolysée par l'enzyme qui pénètre avec l'eau dans l'échantillon. Lorsque le glycérol est introduit dans la formulation (matrice G20_HIGH), cette sensibilité est réduite : une partie des molécules d'amylose et d’amylopectine est dans ce cas réorganisée en structures semi-cristallines, plus résistantes aux conditions physiologiques (Singh et al. 2010). Dans ce cas le gonflement est réduit à 170 ± 25% le volume initial de l’échantillon, et l’hydrolyse est beaucoup plus lente.

Lorsque la structure native granulaire est partiellement préservée (comme dans G0_LOW et G20_LOW), la sensibilité à l’eau et à l’enzyme est encore moins marquée : les structures granulaires résiduelles (semi-cristallines et très organisées, sous forme de feuillets) sont plus résistantes à la pénétration de l’eau et à l’action de dégradation de l’α-amylase. G0_LOW gonfle jusqu’à 250 ± 35% son volume initial (contre 300% sans grains résiduels) mais est tout de même complètement hydrolysé, alors que G20_LOW gonfle peu, 80 ± 10% du volume initial, et présente de plus une importante fraction d’amidon (~25%) résistante à l’action de l’enzyme.

L’ajout de faibles concentrations de CNC (jusqu’à 2.5%) a pour effet de réduire le gonflement des nanocomposites (130 ± 10% du volume initial) et de ralentir la dégradation enzymatique (40% de moins à 6h d’hydrolyse) par rapport à référence (REF-CNC, gonflement 150 ± 25% du volume initial) (**Figure R-7a** et **b**). La modification des propriétés macroscopiques observées pourrait être un indice supplémentaire de l’importance des interactions entre matrice (amidon) et charges (nanocelluloses). Ces interactions vont réduire le nombre de sites disponibles à l’eau et à l’enzyme, diminuant donc le gonflement et la vitesse de dégradation enzymatique.

À concentrations plus élevées en CNC (5 et 10%), le gonflement augmente (respectivement 170 ± 7% et 230 ± 15% du volume initial pour CNC_5 et CNC_10) et la dégradation enzymatique redevient similaire à la référence (**Figure R-7a** et **b**). Cet effet est à relier à la quantité plus importante de structures amorphes (mesurées par RMN) dans les composites les plus chargés (5 et 10% CNC).

Dans le cas des nanocomposites amidon-ChNC, l’ajout de nanocristaux induit, quelle que soit la concentration, un gonflement et une dégradation enzymatique plus importante de celle de la référence (G20_LOW, **Figure R-7c** et **d**) : le taux de gonflement passe de 130 ± 10% du volume initial pour ChNC_2 à 170 ± 7% et 190 ± 5% respectivement pour ChNC_8 et ChNC_4 (**Figure R-7 c**), et le taux final d’amidon hydrolysé augmente, de 79 ± 5% (ChNC_2) à ~90 ± 5% (ChNC_4 et ChNC_8, **Figure R-7d**). La concentration croissante en nanocharges semble donc induire une augmentation de la sensibilité de l’amidon à l’action combinée de l’eau et de l’enzyme à cause des changements structuraux décrits plus haut : structure amorphe et pas de grains résiduels.

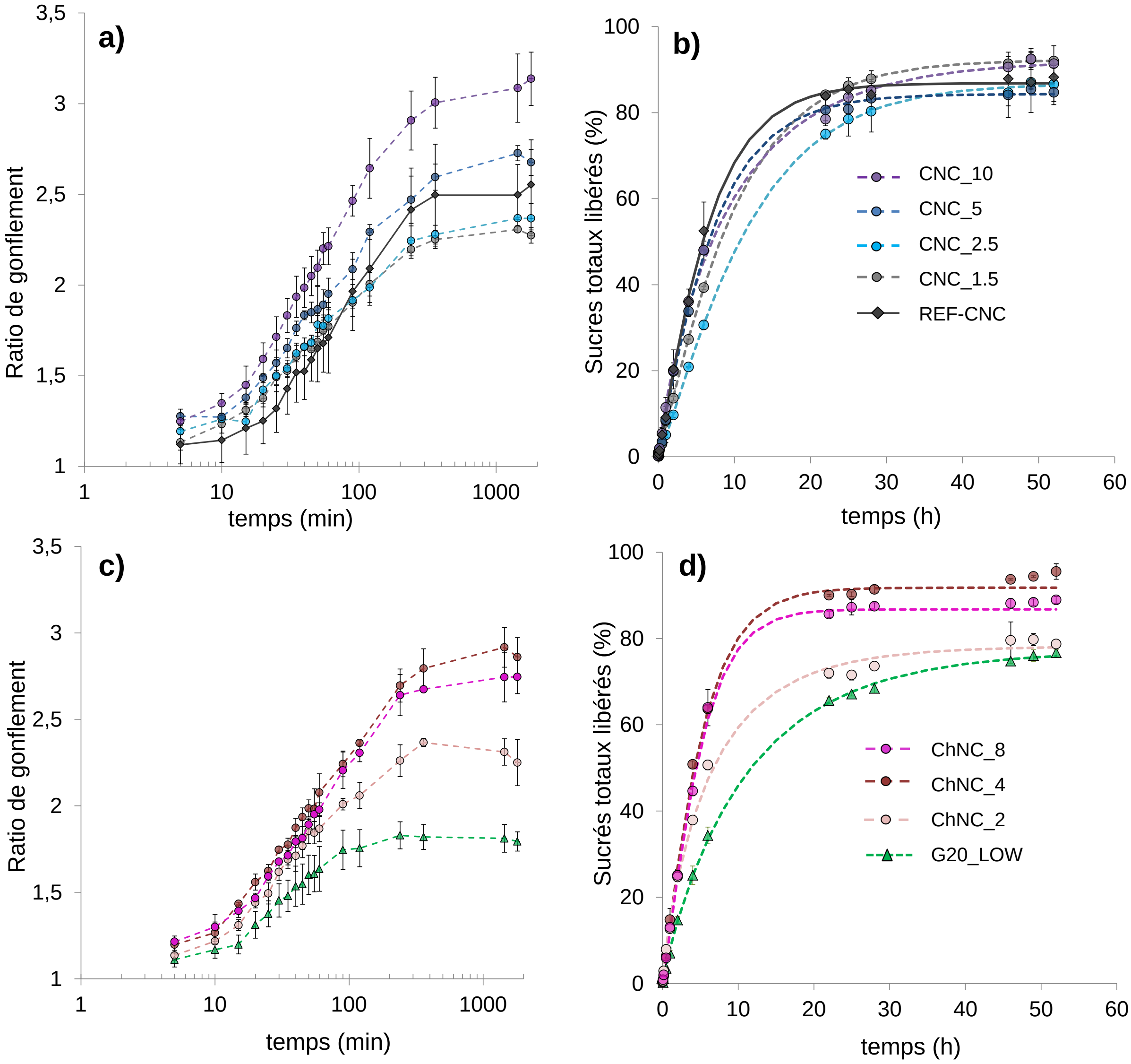

Figure R-7 : a) *Gonflement et* **b)** *hydrolyse enzymatiques des nanocomposites amidon-CNC et de leur matrice de référence REF-CNC.* **c)** *Gonflement et* **d)** *hydrolyse enzymatiques des nanocomposites amidon-ChNC et de leur matrice de référence G20_LOW.*

6. Propriétés biologiques

Afin de tester leurs possibilités d'application dans le domaine biomédical, certaines propriétés biologiques (cytotoxicité et adhérence cellulaire) des matériaux ont été étudiées *in vitro* conformément aux directives de la norme ISO-10993-5. Pour ces essais, deux types cellulaires, cellules épithéliales et fibroblastes, ont été testés pendant 24 et 48 heures.

Nos études de cytotoxicité sur les fluides d'extraction provenant des matériaux plastifiés avec du glycérol (matrices et nanocomposites) ont montrés que ni le plastifiant ni la concentration en nanoparticules ne semblent avoir un effet sur la viabilité cellulaire, qui reste proche de 100% (voir **Figure R-8a**). Selon la norme (ISO/EN10993-5 2009) un matériau est défini noncytotoxique quand la viabilité cellulaire suite au contact avec le matériau ou ses extraits n'est pas réduite de plus de 30% ; par conséquence tous les matériaux testés dans cet étude ne sont pas cytotoxiques.

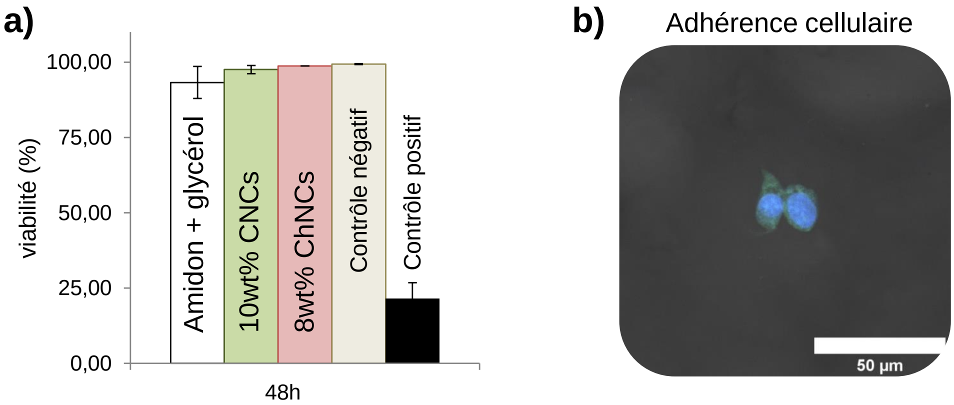

Figure R-8 : a) *Viabilité cellulaire de fibroblastes en contact avec une matrice d'amidon plastifié avec du glycérol, un nanocomposite à base de CNC et de ChNC, comparée à la viabilité d'un contrôle négatif (milieu de culture) et positif (10% diméthylsulfoxyde) ;* **b)** *adhérence cellulaire de fibroblastes sur la surface d'une matrice d'amidon plastifiée avec du glycérol : la membrane cellulaire est marquée en vert et le noyau en bleu.*

Toutefois des mesures d'adhérence cellulaire ont démontré que les surfaces de ces matériaux sont peu colonisées par les cellules (**Figure R-8b**). L'adhésion et la prolifération de différents types cellulaires sur la surface des matériaux polymériques dépend des caractéristiques de surface, comme les propriétés physicochimiques ainsi que la charge de surface et la morphologie (Marques et al. 2002). Parmi les propriétés physicochimiques, l'hydrophilie est déterminante pour l'adhérence des cellules. Il est possible que l'extrême hydrophilie des matériaux à base d'amidon produits dans cette étude ne favorise pas l'adhérence cellulaire et la prolifération sur leurs surfaces (Koyano et al. 1998).

7. Conclusions et perspectives

Pour conclure, l'étude préliminaire sur les matrices nous a permis de choisir les conditions d'extrusion (faible EMS, basse température) et la formulation (ajout de glycérol) les plus adaptées pour le développement de nanocomposites en vue d'applications biomédicales. Ce travail montre que l'incorporation de nanoparticules bio-sourcées aux matrices d'amidon est une méthode efficace pour modifier la structure et les propriétés de l'amidon thermoplastique. Ceci est possible seulement quand la surface d'interaction matrice-nanoparticule est maximisée. Pour ce faire les nanoparticules doivent être distribuées de façon homogène dans la matrice. Le respect de ces conditions permet d'obtenir des matériaux composites qui peuvent être appliqués dans le domaine biomédical, étant donné leur très faible cytotoxicité.

Les perspectives de ce travail incluent l’étude de nouvelles stratégies afin de mieux maitriser la dispersion des nanoparticules dans la matrice et accroître la résistance de l’amidon aux conditions physiologiques.

Pour corroborer l’application biomédicale, il serait également intéressant d’investiguer plus finement l’interaction des nanoparticules avec les cellules du corps humain, afin d’assurer la complète compréhension des enjeux biologiques générés par ces matériaux.

List of Experimental Sets-Up

Glossary

Samples nomenclature

G0_LOW	Potato starch-based matrix extruded at 100 J g^{-1}, screw length = 15.5 L/D, temperature max = 90°C, without glycerol
G0_HIGH	Potato starch-based matrix extruded at 1900 J g^{-1}, screw length = 40 L/D, temperature max = 115°C, without glycerol
G20_LOW	Potato starch-based matrix extruded at 100 J g^{-1}, screw length = 15.5 L/D, temperature max = 90°C, with glycerol
G20_HIGH	Potato starch-based matrix extruded at 1900 J g^{-1}, screw length = 40 L/D, temperature max = 115°C, with glycerol
REF_CNC	Potato starch-based matrix extruded at 80 J g^{-1}, screw length = 26.5 L/D, temperature max = 105°C, with glycerol
CNC_1.5	Potato starch-based nanocomposite extruded at 130 J g^{-1}, screw length = 26.5 L/D, temperature max = 105°C, with glycerol and 1.5wt% CNCs
CNC_2.5	Potato starch-based nanocomposite extruded at 110 J g^{-1}, screw length = 26.5 L/D, temperature max = 105°C, with glycerol and 2.5wt% CNCs
CNC_5	Potato starch-based nanocomposite extruded at 90 J g^{-1}, screw length = 26.5 L/D, temperature max = 105°C, with glycerol and 5wt% CNCs
CNC_10	Potato starch-based nanocomposite extruded at 90 J g^{-1}, screw length = 26.5 L/D, temperature max = 110°C, with glycerol and 10wt% CNCs
ChNC_2	Potato starch-based nanocomposite extruded at 115 J g^{-1}, screw length = 15.5 L/D, temperature max = 90°C, with glycerol and 2wt% ChNCs
ChNC_4	Potato starch-based nanocomposite extruded at 60 J g^{-1}, screw length = 15.5 L/D, temperature max = 105°C, with glycerol and 4wt% ChNCs
ChNC_8	Potato starch-based nanocomposite extruded at 80 J g^{-1}, screw length = 15.5 L/D, temperature max = 105°C, with glycerol and 8wt% ChNCs
CNC_4	Potato starch-based nanocomposite extruded at 90 J g^{-1}, screw length = 15.5 L/D, temperature max = 105°C, with glycerol and 4wt% CNCs

Abbreviations

AC	Cellulose Acetate
AF4	Asymmetrical Flow Field Flow Fractionation
AlexaFluor 488	Mouse monoclonal anti-alpha-tubulin antibody (fluorescent dye for tubulin)
BALB/c 3T3	Mouse cell line (fibroblastic cells)
BC	Bacterial Cellulose
CI	Cellulose I allomorph
CII	Cellulose II allomorph
ChNCs	Chitin nanocrystals
ChNFs	Chitin nanofibers
CNCs	Cellulose nanocrystals
CNFs	Cellulose nanofibers
CP-MAS	Carbon Probe-Magic Angle Spinning
DAPI	4’,6-Diamidino-2-Phenylindole (fluorescent dye for DNA)
DMEM	Dulbeccos’s Modified Eagle Medium
DMSO-d6	Deuterated Dimethyl Sulfoxide
DMTA	Dynamic Mechanical Thermal Analysis
DP	Degree of polymerization
DRI	Differential Refractive Index
DSC	Differential Scanning Calorimetry
DVS	Dynamic Vapor Sorption
D_2O	Deuterium oxide
EVOH	Ethylene-vinyl alcohol
FVS 570	Fixable Viability Stain 570 (intracellular fluorescent dye)
HT-29	Human colorectal adenocarcinoma cell line (epithelial cells)
L/d	Ratio of the nanofiller length to its thickness
L/D	Ratio of the flighted length of the screw to its outside diameter
L/S	Ratio long/short starch chains
L-929	Mouse cell line (fibroblastic cells)
MALLS	Multi-Angle Laser Light Scattering
MMT-Na	Sodium montmorillonite clay nanoparticles

NMR	Nuclear Magnetic Resonance
NPs	Nanoparticles
PAA	Polyacrylic acid
PBS	Phosphate Buffer Saline
PBSA	Polybutylene succinate adipate
PCL	Polycaprolactone
PE	Polyethylene
PET	Polyethylene terephthalate
PFA	Paraformaldehyde
PHAs	Polyhydroxyalkanoates
PHEMA	Polyhydroxyethylmethacrylate
PLA	Polylactic acid
PMMA	Polymethyl methacrylate
PP	Polypropylene
PTFE	Polytetrafluoroethylene
PUU	Polyurethane-urea
PVA	Poly(vinyl alcohol)
PVC	Polyvinyl chloride
RDS	Rapidly Digestible Starch
RS	Resistant Starch
SANS	Small Angle Neutron Scattering
SAXS	Small Angle X-ray Scattering
SDS	Slowly Digestible Starch
SEM	Scanning Electron Microscopy
SHG	Second Harmonic Generation imaging
SME	Specific Mechanical Energy
STEM	Scanning Transmission Electron Microscopy
TEM	Transmission Electron Microscopy
TGA	Thermogravimetric Analysis
TPS	Thermoplastic starch
Tps	3-(trimethylsilyl) proprionic-2,2,3,3-d_4 acid sodium salt
WAXS	Wide Angle X-ray Scattering
XRD	X-Ray Diffraction

Main symbols

A	Nanofiller shape factor
a_w	Water activity
D	Water diffusion coefficient
E	Young’s modulus
E'	Storage modulus
E''	Loss modulus
M_n	Number molar mass
M_w	Weight molar mass
M_w/ M_n	Polydispersity
R_{Gz}	z-average radius of gyration
Tanδ	Damping factor
Tα	α relaxation temperature
T_c	Conclusion temperature of the melting endotherm
Tg	Glass transition temperature
Tm	Melting temperature
T_o	Onset temperature of the melting endotherm
T_p	Peak temperature of the melting endotherm
wt%	Mass fraction expressed in percentage (weight basis)
%wc	Water content percentage on the weight basis
ΔH	Enthalpy
2θ	X-rays diffraction angle

REFERENCES

Ahamed, M. et al., 2008. DNA damage response to different surface chemistry of silver nanoparticles in mammalian cells. *Toxicology and Applied Pharmacology*, 233(3), pp.404–410.

Albanese, A., Tang, P.S. & Chan, W.C.W., 2012. The Effect of Nanoparticle Size, Shape, and Surface Chemistry on Biological Systems. *Annual Review of Biomedical Engineering*, 14(1), pp.1–16.

Alexandrescu, L. et al., 2013. Cytotoxicity tests of cellulose nanofibril-based structures. *Cellulose*, 20(4), pp.1765–1775.

Angellier, H. et al., 2006. Thermoplastic starch - Waxy maize starch nanocrystals nanocomposites. *Biomacromolecules*, 7(2), pp.531–539.

Anguita, M. et al., 2006. Study of the effect of technological processes on starch hydrolysis, non-starch polysaccharides solubilization and physicochemical properties of different ingredients using a two-step in vitro system. *Animal Feed Science and Technology*, 129(1–2), pp.99–115.

Anitha, A. et al., 2014. Chitin and chitosan in selected biomedical applications. *Progress in Polymer Science*, 39(9), pp.1644–1667.

AshaRani, P. V. et al., 2009. Cytotoxicity and Genotoxicity of Silver Nanoparticles in Human Cells. *ACS Nano*, 3(2), pp.279–290.

Avérous, L., 2004. Biodegradable Multiphase Systems Based on Plasticized Starch: A Review. *Journal of Macromolecular Science, Part C: Polymer Reviews*, 44(3), pp.231–274.

Avérous, L., Fringant, C. & Moro, L., 2001. Plasticized starch-cellulose interactions in polysaccharide composites. *Polymer*, 42(15), pp.6565–6572.

Azevedo, H.S., Gama, F.M. & Reis, R.L., 2003. In Vitro Assessment of the Enzymatic Degradation of Several Starch Based Biomaterials. *Biomacromolecules*, 4(6), pp.1703–1712.

Babaee, M. et al., 2015. Biodegradability and mechanical properties of reinforced starch nanocomposites using cellulose nanofibers. *Carbohydrate Polymers*, 132, pp.1–8.

Barron, C. et al., 2001. Microscopical Study of the Destructuring of Waxy Maize and Smooth Pea Starches by Shear and Heat at Low Hydration. *Journal of Cereal Science*, 33(3), pp.289–300.

Bastioli, C. et al., 1995. Physical state and biodegradation behavior of starch-polycaprolactone systems. *Journal of Environmental Polymer Degradation*, 3(2), pp.81–95.

Bastioli, C., 1998. Properties and applications of Mater-Bi starch-based materials. *Polymer Degradation and Stability*, 59(1–3), pp.263–272.

Beilvert, A., Faure, F., et al., 2014. A resorbable shape-memory starch-based stent for the treatment of salivary ducts under sialendoscopic surgery. *Laryngoscope*, 124(4), pp.875–881.

Beilvert, A., Chaubet, F., et al., 2014. Shape-memory starch for resorbable biomedical devices. *Carbohydrate Polymers*, 99, pp.242–248.

Bennett, D., 2016. *Chem 309 general, organic, & biochemistry*, LibreTexts Project.

Van Den Berg, C. et al., 2007. Water binding by potato starch. *International Journal of Food Science & Technology*, 10(6), pp.589–602.

Bialleck, S. & Rein, H., 2012. Drug release mechanisms of hot-melt extruded starch-based pellets. *Starch/Staerke*, 64(5), pp.408–419.

Bizot, H. et al., 1997. Calorimetric evaluation of the glass transition in hydrated, linear and branched polyanhydroglucose compounds. *Carbohydrate Polymers*, 32(1), pp.33–50.

Buléon, A. et al., 1987. Comparison of X-ray diffraction patterns and sorption properties of the hydrolyzed starches of potato, wrinkled and smooth pea, broad bean and wheat. *Carbohydrate Polymers*, 7(6), pp.461–482.

Buléon, A. et al., 1998. Starch granules: Structure and biosynthesis. *International Journal of Biological Macromolecules*, 23(2), pp.85–112.

Buléon, A., Véronèse, G. & Putaux, J.L., 2007. Self-association and crystallization of amylose. *Australian Journal of Chemistry*, 60(10), pp.706–718.

Burdick, J.A. & Prestwich, G.D., 2011. Hyaluronic acid hydrogels for biomedical applications. *Advanced Materials*, 23(12), pp.41–56.

Butterworth, P.J., Warren, F.J. & Ellis, P.R., 2011. Human α-amylase and starch digestion: An interesting marriage. *Starch/Staerke*, 63(7), pp.395–405.

Cao, X., Chen, Y., Chang, P.R., Stumborg, M., et al., 2008. Green composites reinforced with hemp nanocrystals in plasticized starch. *Journal of Applied Polymer Science*, 109(6), pp.3804–3810.

Cao, X., Chen, Y., Chang, P.R., Muir, A.D., et al., 2008. Starch-based nanocomposites reinforced with flax cellulose nanocrystals. *Express Polymer Letters*, 2(7), pp.502–510.

Capadona, J.R. et al., 2008. Stimuli-Responsive Polymer Nanocomposites Inspired by the Sea Cucumber Dermis. *Science*, 319(5868), pp.1370–1374.

Chang, P.R., Jian, R., Zheng, P., et al., 2010. Preparation and properties of glycerol plasticized-starch (GPS)/cellulose nanoparticle (CN) composites. *Carbohydrate Polymers*, 79(2), pp.301–305.

Chang, P.R., Jian, R., Yu, J., et al., 2010. Starch-based composites reinforced with novel chitin nanoparticles. *Carbohydrate Polymers*, 80(2), pp.421–426.

Chanvrier, H. et al., 2007. Influence of storage conditions on the structure, thermal behaviour and formation of enyzme resistant starch in extruded starches. *Journal of Agricultural and Food Chemistry*, 55, pp.9883–9890.

Chen, Y. et al., 2009. Bionanocomposites based on pea starch and cellulose nanowhiskers hydrolyzed from pea hull fibre: Effect of hydrolysis time. *Carbohydrate Polymers*, 76(4), pp.607–615.

Chevigny, C. et al., 2018. In-Situ Quantitative and Multiscale Structural Study of Starch-Based Biomaterials Immersed in Water. *Biomacromolecules*, 19(3), pp.838–848.

Chevigny, C. et al., 2016. Shape-memory effect in amorphous potato starch: The influence of local orders and paracrystallinity. *Carbohydrate Polymers*, 146, pp.411–419.

Cho, J., Joshi, M.S. & Sun, C.T., 2006. Effect of inclusion size on mechanical properties of polymeric composites with micro and nano particles. *Composites Science and Technology*, 66, pp.1941–1952.

Coativy, G., 2013. *Optimisation des propriétés de mémoire de forme de l'amidon : rôle des procédés thermomécaniques et apport de l'introduction de nanocharges*. Université de Nantes.

Colonna, P., Leloup, V. & Buléon, A., 1992. Limiting factors of starch hydrolysis. *European Journal of Clinical Nutrition*, 46, pp.S17–S32.

Copeland, L. et al., 2009. Form and functionality of starch. *Food Hydrocolloids*, 23(6), pp.1527–1534.

Dev, A. et al., 2010. Novel carboxymethyl chitin nanoparticles for cancer drug delivery applications. *Carbohydrate Polymers*, 79(4), pp.1073–1079.

Dong, S. et al., 2012. Cytotoxicity and cellular uptake of cellulose nanocrystals. *Nano LIFE*, 2(3), p.1241006.

Donovan, J.W., 1979. Phase transitions of the starch–water system. *Biopolymers*, 18(2), pp.263–275.

Dufresne, A. & Castaño, J., 2017. Polysaccharide nanomaterial reinforced starch nanocomposites: A review. *Starch/Staerke*, 69(1–2), pp.1–19.

Dufresne, A. & Vignon, M.R., 1998. Improvement of Starch Film Performances Using Cellulose Microfibrils. *Macromolecules*, 31(97), pp.2693–2696.

Englyst, H.N., Kingman, S.M. & Cummings, J.H., 1992. Classification and measurement of nutritionally important starch fractions. *European journal of clinical nutrition*, 46 Suppl 2, pp.S33-50.

Englyst, H.N., Veenstra, J. & Hudson, G.J., 1996. Measurement of rapidly available glucose (RAG) in plant foods: a potential in vitro predictor of the glycaemic response. *British Journal of Nutrition*, 75(3), pp.327–337.

Favier, V. et al., 1995. Polymers for Advanced Technologies Nanocomposite Materials from Latex and Cellulose Whiskers. *Polymers for Advanced Technologies*, 6, pp.351–355.

Favier, V. et al., 1997. Simulation and modeling of three-dimensional percolating structures: Case of a latex matrix reinforced by a network of cellulose fibers. *Acta Materialia*, 45(4), pp.1557–1565.

Favier, V., Chanzy, H. & Cavaille, J.Y., 1995. Polymer Nanocomposites Reinforced by Cellulose Whiskers. *Macromolecules*, 28(18), pp.6365–6367.

Ferreira, A.M. & Carvalho, A.J.F., 2014. TPS Nanocomposite reinforced with MFC by melting process. *Materials Research*, 17(4), pp.807–810.

Furó, I. et al., 1987. C.P.-D.D.-M.A.S. 13C-N.M.R. Investigations of anhydrous and hydrated cyclomalto-oligosaccharides: The role of water of hydration. *Carbohydrate Research*, 166, pp.27–33.

G'Sell, C. et al., 1994. *Introduction à la mécanique des polymères*, Institut national polytechnique de Lorraine.

Gagner, J.E., Kim, W. & Chaikof, E.L., 2014. Designing protein-based biomaterials for medical applications. *Acta Biomaterialia*, 10(4), pp.1542–1557.

De Gennes, P.G., 1979. *Scaling Concepts in Polymer Physics*, Cornell University Press.

Gidley, M.J. & Bociek, S.M., 1988. Carbon-13 CP/MAS NMR studies of amylose inclusion complexes, cyclodextrins, and the amorphous phase of starch granules: relationships between glycosidic linkage conformation and solid-state carbon-13 chemical shifts. *Journal of the American Chemical Society*, 110, pp.3820–3829.

Giri, P., Tambe, C. & Narayan, R., 2018. Using reactive extrusion to manufacture greener products: From laboratory fundamentals to commercial scale. *ACS Symposium Series*, 1304(August), pp.1–23.

Gomes, M.E. et al., 2001. Cytocompatibility and response of osteoblastic-like cells to starch-based polymers: Effect of several additives and processing conditions. *Biomaterials*, 22(13), pp.1911–1917.

Goodrich, J.D. & Winter, W.T., 2007. α-Chitin Nanocrystals Prepared from Shrimp Shells and Their Specific Surface Area Measurement. *Biomacromolecules*, 8(1), pp.252–257.

Gopalan Nair, K. & Dufresne, A., 2003. Crab shell chitin whisker reinforced natural rubber nanocomposites. 2. Mechanical behavior. *Biomacromolecules*, 4(3), pp.666–674.

Gratton, S.E.A. et al., 2008. The effect of particle design on cellular internalization pathways. *Proceedings of the National Academy of Sciences*, 105(33), pp.11613–11618.

Gunaratne, A. & Hoover, R., 2002. Effect of heat-moisture treatment on the structure and physicochemical properties of tuber and root starches. *Carbohydrate Polymers*, 49(4), pp.425–437.

Habibi, Y., Lucia, L.A. & Rojas, O.J., 2010. Cellulose Nanocrystals: Chemistry, Self-Assembly, and Applications. *Chemical Reviews*, 110(6), pp.3479–3500.

Hanif, Z. et al., 2014. Size- and dose-dependent toxicity of cellulose nanocrystals (CNC) on human fibroblasts and colon adenocarcinoma. *Colloids and Surfaces B: Biointerfaces*, 119, pp.162–165.

Hietala, M., Mathew, A.P. & Oksman, K., 2013. Bionanocomposites of thermoplastic starch and cellulose nanofibers manufactured using twin-screw extrusion. *European Polymer Journal*, 49(4), pp.950–956.

Hua, K. et al., 2014. Translational study between structure and biological response of nanocellulose from wood and green algae. *RSC Adv.*, 4(6), pp.2892–2903.

ISO/EN10993-5, 2009. B. *International Standard ISO 10993-5 Biological evaluation of medical devices - Part 5: Tests for cytotoxicity: in vitro methods*, 3 Ed, p.42.

Isogai, A., 2013. Wood nanocelluloses: Fundamentals and applications as new bio-based nanomaterials. *Journal of Wood Science*, 59(6), pp.449–459.

Jayakumar, R. et al., 2010. Novel chitin and chitosan nanofibers in biomedical applications. *Biotechnology Advances*, 28(1), pp.142–150.

Jenkins, P.J. & Donald, A.M., 1998. Gelatinisation of starch : a combined SAXS / WAXS / DSC and SANS study. *Carbohydrate Research*, 308, pp.133–147.

Jenkins, P.J. & Donald, A.M., 1995. The influence of amylose on starch granule structure. *International Journal of Biological Macromolecules*, 17(6), pp.315–321.

Jiménez Saelices, C. & Capron, I., 2018. Design of Pickering Micro- and Nanoemulsions Based on the Structural Characteristics of Nanocelluloses. *Biomacromolecules*, 19(2), pp.460–469.

Jorfi, M. & Foster, E.J., 2015. Recent advances in nanocellulose for biomedical applications. *Journal of Applied Polymer Science*, 132(14), pp.1–19.

Kansou, K. et al., 2015. Amylolysis of maize mutant starches described with a fractal-like kinetics model. *Carbohydrate Polymers*, 123(August 2016), pp.266–274.

Karger-Kocsis, J. et al., 2015. Water-assisted production of thermoplastic nanocomposites: A review. *Materials*, 8(1), pp.72–95.

Khalil, H.P.S.A., Bhat, A.H. & Yusra, A.F.I., 2012. Green composites from sustainable cellulose nanofibrils : A review. *Carbohydrate Polymers*, 87(2), pp.963–979.

Khan, F. & Ahmad, S.R., 2013. Polysaccharides and Their Derivatives for Versatile Tissue Engineering Application. *Macromolecular Bioscience*, 13(4), pp.395–421.

Kipps, A.E. & Whitehead, P.H., 1975. The significance of amylase in forensic investigations of body fluids. *Forensic Science*, 6(3), pp.137–144.

Kogan, G. et al., 2007. Hyaluronic acid: A natural biopolymer with a broad range of biomedical and industrial applications. *Biotechnology Letters*, 29(1), pp.17–25.

Kono, H. & Numata, Y., 2004. Two-dimensional spin-exchange solid-state NMR study of the crystal structure of cellulose II. *Polymer*, 45(13), pp.4541–4547.

Kopelman, R., 1988. Fractal Reaction Kinetics. *Science*, 241, pp.1620–1626.

Koyano, T. et al., 1998. Attachment and growth of cultures fibroblast cells on PVA/chitosan-blended hydrogels. *Journal of Biomedical Materials Research*, 39(3), pp.486–490.

Kunal, P., Banthia, A.K. & Majumdar, D.K., 2006. Starch Based Hydrogel with Potential Biomedical Application as Artificial Skin. *African Journal of Biomedical Research*, 9, pp.23–29.

Lee, J.H. et al., 1998. Interaction of different types of cells on polymer surfaces with wettability gradient. *Journal of Colloid and Interface Science*, 205(2), pp.323–330.

Lehmann, U. & Robin, F., 2007. Slowly digestible starch - its structure and health implications: a review. *Trends in Food Science and Technology*, 18(7), pp.346–355.

Li, M. et al., 2014. Shear degradation of molecular, crystalline, and granular structures of starch during extrusion. *Starch - Stärke*, 66(7–8), pp.595–605.

Li, Y., Kröger, M. & Liu, W.K., 2015. Shape effect in cellular uptake of PEGylated nanoparticles: comparison between sphere, rod, cube and disk. *Nanoscale*, 7(40), pp.16631–16646.

Lin, N. & Dufresne, A., 2014. Nanocellulose in biomedicine: Current status and future prospect. *European Polymer Journal*, 59, pp.302–325.

Ling, D., Hackett, M.J. & Hyeon, T., 2014. Surface ligands in synthesis, modification, assembly and biomedical applications of nanoparticles. *Nano Today*, 9(4), pp.457–477.

Liu, P. et al., 2011. Phase transitions of maize starches with different amylose contents in glycerol – water systems. *Carbohydrate Polymers*, 85(1), pp.180–187.

Liu, S. et al., 2016. Effect of film multi-scale structure on the water vapor permeability in hydroxypropyl starch (HPS)/Na-MMT nanocomposites. *Carbohydrate Polymers*, 154, pp.186–193.

Liu, S. et al., 2017. Understanding physicochemical properties changes from multi-scale structures of starch/CNT nanocomposite films. *International Journal of Biological Macromolecules*, 104, pp.1330–1337.

Liu, W.C., Halley, P.J. & Gilbert, R.G., 2010. Mechanism of degradation of starch, a highly branched polymer, during extrusion. *Macromolecules*, 43(6), pp.2855–2864.

Logié, N. et al., 2018. How does temperature govern mechanisms of starch changes during extrusion? *Carbohydrate Polymers*, 184(October 2017), pp.57–65.

Lourdin, D. et al., 2016. Concentration driven cocrystallisation and percolation in all-cellulose nanocomposites. *Cellulose*, 23(1), pp.529–543.

Lourdin, D. et al., 1997. Influence of equilibrium relative humidity and plasticizer concentration on the water content and glass transition of starch materials. *Polymer*, 38(21), pp.5401–5406.

Lourdin, D., Bizot, H. & Colonna, P., 1997. "‘ Antiplasticization ’" in Starch – Glycerol Films ? *Journal of Applied Polymer Science*, 63(8), pp.1047–1053.

Lu, Y., Weng, L. & Cao, X., 2005. Biocomposites of Plasticized Starch Reinforced with Cellulose Crystallites from Cottonseed Linter. *Macromolecular Bioscience*, 5(11), pp.1101–1107.

Lu, Y., Weng, L. & Cao, X., 2006. Morphological, thermal and mechanical properties of ramie crystallites—reinforced plasticized starch biocomposites. *Carbohydrate Polymers*, 63(2), pp.198–204.

Lu, Y., Weng, L. & Zhang, L., 2004. Morphology and properties of soy protein isolate thermoplastics reinforced with chitin whiskers. *Biomacromolecules*, 5(3), pp.1046–1051.

Luo, Z.P. & Koo, J.H., 2008. Quantification of the layer dispersion degree in polymer layered silicate nanocomposites by transmission electron microscopy. *Polymer*, 49(7), pp.1841–1852.

Malcom Brown Jr, R., Saxena, I. & Kudlicka, K., 1996. Cellulose biosynthesis in higher plants. *Trends in Plant Science*, 1(5), pp.149–156.

Marques, A.P., Reis, R.L. & Hunt, J.A., 2002. The biocompatibility of novel starch-based polymers and composites: In vitro studies. *Biomaterials*, 23(6), pp.1471–1478.

Marques, L. et al., 2013. Subcutaneous tissue reaction and cytotoxicity of polyvinylidene fluoride and polyvinylidene fluoride-trifluoroethylene blends associated with natural polymers. *Journal of Biomedical Materials Research - Part B Applied Biomaterials*, 101(7), pp.1284–1293.

Mendes, S.C. et al., 2001. Biocompatibility testing of novel starch-based materials with potential application in orthopaedic surgery: a preliminary study. *Biomaterials*, 22(14), pp.2057–2064.

Mikus, P.Y. et al., 2014. Deformation mechanisms of plasticized starch materials. *Carbohydrate Polymers*, 114, pp.450–457.

Mincea, M., Negrulescu, A. & Ostafe, V., 2012. Preparation, modification, and applications of chitin nanowhiskers: A review. *Reviews on Advanced Materials Science*, 30(3), pp.225–242.

Missoum, K., Belgacem, M.N. & Bras, J., 2013. Nanofibrillated cellulose surface modification: A review. *Materials*, 6(5), pp.1745–1766.

Miyamoto, T. et al., 1989. Tissue biocompatibility of cellulose and its derivatives. *Journal of Biomedical Materials Research*, 23(1), pp.125–133.

Moberg, T. et al., 2017. Rheological properties of nanocellulose suspensions : effects of fibril / particle dimensions and surface characteristics. *Cellulose*, 24(6), pp.2499–2510.

Montero, B. et al., 2017. Effect of nanocellulose as a filler on biodegradable thermoplastic starch films from tuber , cereal and legume. *Carbohydrate Polymers*, 157, pp.1094–1104.

Morin, A. & Dufresne, A., 2002. Nanocomposites of chitin whiskers from Riftia tubes and poly(caprolactone). *Macromolecules*, 35(6), pp.2190–2199.

Mushi, N.E. et al., 2019. Strong and Tough Chitin Film from α-Chitin Nanofibers Prepared by High Pressure Homogenization and Chitosan Addition. *ACS Sustainable Chemistry and Engineering*, 7(1), pp.1692–1697.

Nagler, R.M. et al., 2002. Saliva Analysis in the Clinical Setting : Revisiting an Underused Diagnostic Tool. *Journal of Investigative Medicine*, 50(3), pp.214–226.

Nashed, G., Rutgers, R.P.G. & Sopade, P.A., 2003. The Plasticisation Effect of Glycerol and Water on the Gelatinisation of Wheat Starch. *Starch - Stärke*, 55(34), pp.131–137.

Nel, A., 2007. Toxic Potential of Materials. *Science*, 311(5726), pp.622–627.

Nessi, V. et al., 2018. Multi-scale characterization of thermoplastic starch structure using Second Harmonic Generation imaging and NMR. *Carbohydrate Polymers*, 194(April), pp.80–88.

Nilsson, L., 2013. Separation and characterization of food macromolecules using field-flow fractionation: A review. *Food Hydrocolloids*, 30(1), pp.1–11.

Oliveira, J.T. et al., 2007. A cartilage tissue engineering approach combining starch-polycaprolactone fibre mesh scaffolds with bovine articular chondrocytes. *Journal of Materials Science: Materials in Medicine*, 18(2), pp.295–302.

Paillet, M. & Dufresne, A., 2001. Chitin Whisker Reinforced Thermoplastic Nanocomposites. *Macromolecules*, 34(19), pp.6527–6530.

Paris, M. et al., 1999. Crystallinity and structuring role of water in native and recrystallized starches by 13C CP-MAS NMR spectroscopy. 1: Spectral decomposition. *Carbohydrate Polymers*, 39(4), pp.327–339.

Paris, M., 2000. *Etude de l'ordre local dans les biopolymères par RMN du solide: applications aux traitements physico-chimiques de l'amidon*. L'Université du Maine.

Paris, M. et al., 2001. NMR local range investigations in amorphous starchy substrates I. Structural heterogeneity probed by 13C CP-MAS NMR. *International Journal of Biological Macromolecules*, 29(2), pp.127–136.

Park, J., 2012. *Biomaterials Science and Engineering*, Springer Science & Business Media.

Park, J. & Lakes, R.S., 2007. *Biomaterials: An Introduction* 3rd ed., Springer Science & Business Media.

Peppas, N.A. & Brannon-Peppas, L., 1994. Water diffusion and sorption in amorphous macromolecular systems and foods. *Journal of Food Engineering*, 22(1–4), pp.189–210.

Peppas, N.A. & Sinclair, J.L., 1983. Anomalous transport of penetrants in glassy polymers. *Colloid & Polymer Science*, 261(5), pp.404–408.

Percot, A., Viton, C. & Domard, A., 2003. Optimization of chitin extraction from shrimp shells. *Biomacromolecules*, 4(1), pp.12–18.

Pereira, M.M. et al., 2013. Cytotoxicity and expression of genes involved in the cellular stress response and apoptosis in mammalian fibroblast exposed to cotton cellulose nanofibers. *Nanotechnology*, 24(7), p.75103.

Pérez, S. & Bertoft, E., 2010. The molecular structures of starch components and their contribution to the architecture of starch granules: A comprehensive review. *Starch/Staerke*, 62(8), pp.389–420.

Perrin, E. et al., 2014. Chitin nanocrystals for pickering high internal phase emulsions. *Biomacromolecules*, 15(10), pp.3766–3771.

Planchot, V., Colonna, P. & Saulnier, L., 1997. Séparation et dosage des glucides et des amylases. *Sciences et Techniques Agro-alimentaire (INRA-Lavoisier).*

Popescu, M.C., 2017. Structure and sorption properties of CNC reinforced PVA films. *International Journal of Biological Macromolecules*, 101, pp.783–790.

Porter, D., Metcalfe, E. & Thomas, M.J.K., 2000. Nanocomposite fire retardants - a review. *Fire and Materials*, 24(1), pp.45–52.

Raabe, D. et al., 2007. Preferred crystallographic texture of α-chitin as a microscopic and macroscopic design principle of the exoskeleton of the lobster Homarus americanus. *Acta Biomaterialia*, 3(6), pp.882–895.

Ratner, B.D. et al., 2004. *Biomaterials Science: An Introduction to Materials in Medicine*, Elsevier.

von Recum, A.F., 1998. *Handbook Of Biomaterials Evaluation: Scientific, Technical And Clinical Testing Of Implant Materials* 2nd ed., CRC Press.

Reis, R.L. et al., 2008. *Natural-Based Polymers for Biomedical Applications*, Elsevier.

Revol, J.-F. et al., 1993. Chiral nematic suspensions of cellulose crystallites; phase separation and magnetic field orientation. *Liquid Crystals*, pp.127–134.

Rico, M. et al., 2016. Processing and characterization of polyols plasticized-starch reinforced with microcrystalline cellulose. *Carbohydrate Polymers*, 149, pp.83–93.

Rinaudo, M., 2006. Chitin and chitosan: Properties and applications. *Progress in Polymer Science (Oxford)*, 31(7), pp.603–632.

Rodrigues, A.P.H. et al., 2017. Control of properties of nanocomposites bio-based collagen and cellulose nanocrystals. *Cellulose*, pp.1731–1744.

Rolland-Sabaté, A. et al., 2007. Branching features of amylopectins and glycogen determined by asymmetrical flow field flow fractionation coupled with multiangle laser light scattering. *Biomacromolecules*, 8(8), pp.2520–2532.

Rolland-Sabaté, A. et al., 2011. Molecular size and mass distributions of native starches using complementary separation methods: Asymmetrical Flow Field Flow Fractionation (A4F) and Hydrodynamic and Size Exclusion Chromatography (HDC-SEC). *Analytical and Bioanalytical Chemistry*, 399(4), pp.1493–1505.

Roman, M. & Winter, W.T., 2004. Effect of sulfate groups from sulfuric acid hydrolysis on the thermal degradation behavior of bacterial cellulose. *Biomacromolecules*, 5(5), pp.1671–1677.

Rouse, J.G. & Van Dyke, M.E., 2010. A review of keratin-based biomaterials for biomedical applications. *Materials*, 3(2), pp.999–1014.

Russo, M.A.L. et al., 2007. A study of water diffusion into a high-amylose starch blend: The effect of moisture content and temperature. *Biomacromolecules*, 8(1), pp.296–301.

Salaberria, A.M. et al., 2015. Role of chitin nanocrystals and nanofibers on physical, mechanical and functional properties in thermoplastic starch films. *Food Hydrocolloids*, 46, pp.93–102.

Salaberria, A.M., Labidi, J. & Fernandes, S.C.M., 2014. Chitin nanocrystals and nanofibers as nano-sized fillers into thermoplastic starch-based biocomposites processed by melt-mixing. *Chemical Engineering Journal*, 256, pp.356–364.

Salgado, A.J. et al., 2002. Preliminary study on the adhesion and proliferation of human osteoblasts on starch-based scaffolds. *Materials Science and Engineering: C*, 20(1–2), pp.27–33.

Dos Santos, T. et al., 2011. Quantitative assessment of the comparative nanoparticle-uptake efficiency of a range of cell lines. *Small*, 7(23), pp.3341–3349.

Sarko, A. & Wu, H. -C H., 1978. The Crystal Structures of A-, B- and C-Polymorphs of Amylose and Starch. *Starch - Stärke*, 30(3), pp.73–78.

Schmitt, D.F. et al., 1991. Toxicologic Evaluation of Cellulon$^{\text{TM}}$ Fiber; Genotoxicity, Pyrogenicity, Acute and Subchronic Toxicity. *Journal of the American College of Toxicology*, 10(5), pp.541–554.

Shi, R. et al., 2006. In vitro degradation and swelling behaviour of rubbery thermoplastic starch in simulated body and simulated saliva fluid and effects of the degradation products on cells. *Polymer Degradation and Stability*, 91(12), pp.3289–3300.

Shogren, R.L., 1993. *Biodegradable Polymers and Packaging*, Technomic Publishing.

Singh, J., Dartois, A. & Kaur, L., 2010. Starch digestibility in food matrix: a review. *Trends in Food Science and Technology*, 21(4), pp.168–180.

Siró, I. & Plackett, D., 2010. Microfibrillated cellulose and new nanocomposite materials: A review. *Cellulose*, 17(3), pp.459–494.

Slade, L., Levine, H. & Reid, D.S., 1991. Beyond water activity: Recent advances based on an alternative approach to the assessment of food quality and safety. *Critical Reviews in*

Food Science and Nutrition, 30(2–3), pp.115–360.

Slavutsky, A.M. & Bertuzzi, M.A., 2014. Water barrier properties of starch films reinforced with cellulose nanocrystals obtained from sugarcane bagasse. *Carbohydrate Polymers*, 110, pp.53–61.

Smits, A.L.M. et al., 2003. Interaction between dry starch and plasticisers glycerol or ethylene glycol, measured by differential scanning calorimetry and solid state NMR spectroscopy. *Carbohydrate Polymers*, 53(4), pp.409–416.

van Soest, J.J.G., Hulleman, S.H.D., et al., 1996. Changes in the mechanical properties of thermoplastic potato starch in relation with changes in B-type crystallinity. *Carbohydrate Polymers*, 29(3), pp.225–232.

van Soest, J.J.G., Bezemer, R.C., et al., 1996. Influence of glycerol on the melting of potato starch. *Industrial Crops and Products*, 5(1), pp.1–9.

van Soest, J.J.G., 1996. *Starch plastics: structure-property relationships*, P&L Press.

van Soest, J.J.G., Benes, K., et al., 1996. The influence of starch molecular mass on the properties of extruded thermoplastic starch. *Polymer*, 37(16), pp.3543–3552.

van Soest, J.J.G., de Wit, D. & Vliegenthart, J.F.G., 1996. Mechanical properties of thermoplastic waxy maize starch. *Journal of Applied Polymer Science*, 61(11), pp.1927–1937.

Sriupayo, J. et al., 2005a. Preparation and characterization of α-chitin whisker-reinforced chitosan nanocomposite films with or without heat treatment. *Carbohydrate Polymers*, 62(2), pp.130–136.

Sriupayo, J. et al., 2005b. Preparation and characterization of α-chitin whisker-reinforced poly(vinyl alcohol) nanocomposite films with or without heat treatment. *Polymer*, 46(15), pp.5637–5644.

Svensson, A. et al., 2005. Bacterial cellulose as a potential scaffold for tissue engineering of cartilage. *Biomaterials*, 26(4), pp.419–431.

Szekalska, M. et al., 2016. Alginate: Current Use and Future Perspectives in Pharmaceutical and Biomedical Applications. *International Journal of Polymer Science*, 2016.

Taghizadeh, M.T., Abbasi, Z. & Nasrollahzade, Z., 2012. Study of enzymatic degradation and water absorption of nanocomposites starch/polyvinyl alcohol and sodium montmorillonite clay. *Journal of the Taiwan Institute of Chemical Engineers*, 43(1), pp.120–124.

Tang, H.-R., Godward, J. & Hills, B., 2000. The distribution of water in native starch granules—a multinuclear NMR study. *Carbohydrate Polymers*, 43(4), pp.375–387.

Tawil, G. et al., 2011. In depth study of a new highly efficient raw starch hydrolyzing α-amylase from rhizomucor sp. *Biomacromolecules*, 12(1), pp.34–42.

Tester, R.F., Karkalas, J. & Qi, X., 2004. Starch - Composition, fine structure and architecture. *Journal of Cereal Science*, 39(2), pp.151–165.

Torres, F.G. et al., 2011. Biocompatibilty of starch-based films from starch of Andean crops for biomedical applications. *Materials Science and Engineering C*, 31(8), pp.1737–1740.

Trommsdorff, U. & Tomka, I., 1995. Structure of Amorphous Starch. 2. Molecular Interactions with Water. *Macromolecules*, 28(18), pp.6138–6150.

Velasquez, D. et al., 2015. Effect of crystallinity and plasticizer on mechanical properties and tissue integration of starch-based materials from two botanical origins. *Carbohydrate Polymers*, 124, pp.180–187.

Velasquez, D., 2014. *Matériaux à base d'amidon pour un usage biomédical*. Université de Nantes.

Vergnes, B. & Chapet, M., 2001. Procédés d'extrusion bivis. *Techniques de l'ingénieur*, p.33.

Vikman, M., Itävaara, M. & Poutanen, K., 1995. Measurement of the biodegradation of starch-based materials by enzymatic methods and composting. *Journal of Environmental Polymer Degradation*, 3(1), pp.23–29.

Waigh, T.A. et al., 2000. The phase transformations in starch during gelatinisation: A liquid crystalline approach. *Carbohydrate Research*, 328(2), pp.165–176.

Wakelin, J.H., Virgin, H.S. & Crystal, E., 1959. Development and Comparison of Two X-Ray Methods for determining the Crystallinity of Cotton Cellulose. *Journal of Applied Physics*, 30(11).

Williams, D.F., 2008. On the mechanisms of biocompatibility. *Biomaterials*, 29(20), pp.2941–2953.

Williams, D.F., 2009. On the nature of biomaterials. *Biomaterials*, 30(30), pp.5897–5909.

Wu, X. et al., 2007. Influence of the Processing Conditions on the Mechanical Properties of Chitin Whisker Reinforced Poly(caprolactone) Nanocomposites. *Journal of Biobased Materials and Bioenergy*, 1(3), pp.341–350.

Xie, F. et al., 2013. Starch-based nano-biocomposites. *Progress in Polymer Science*, 38(10–11), pp.1590–1628.

Xie, F., Halley, P.J. & Avérous, L., 2012. Rheology to understand and optimize processibility, structures and properties of starch polymeric materials. *Progress in Polymer Science (Oxford)*, 37(4), pp.595–623.

Yan, D. et al., 2018. Microstructure Analysis of Bismuth Absorbers for Transition-Edge Sensor X-ray Microcalorimeters. *Journal of Low Temperature Physics*, 193(3–4), pp.225–230.

Yu, H. et al., 2013. Structure and physicochemical properties of starches in lotus (Nelumbo nucifera Gaertn.) rhizome. *Food Science & Nutrition*, 1(4), pp.273–283.

Yue, Z.G. et al., 2011. Surface charge affects cellular uptake and intracellular trafficking of chitosan-based nanoparticles. *Biomacromolecules*, 12(7), pp.2440–2446.

Zeng, J.B. et al., 2012. Chitin whiskers: An overview. *Biomacromolecules*, 13(1), pp.1–11.

Zhang, B. et al., 2017. Shape dependent cytotoxicity of PLGA-PEG nanoparticles on human cells. *Scientific Reports*, 7(1), pp.1–8.

Zhang, X. et al., 2010. Structure and properties of polysaccharide nanocrystal-doped supramolecular hydrogels based on Cyclodextrin inclusion. *Polymer*, 51(19), pp.4398–4407.

Zhao, X., Andersson, M. & Andersson, R., 2018. Resistant starch and other dietary fiber components in tubers from a high-amylose potato. *Food Chemistry*, 251(March), pp.58–63.

UNIVERSITE / ECOLOGIE
BRETAGNE \ GEOSCIENCES
LOIRE / AGRONOMIE ALIMENTATION

Oniris
École Nationale Vétérinaire, Agroalimentaire et de l'Alimentation Nantes Atlantique
Santé et alimentation au cœur de la vie

Titre : Elaboration de nanocomposites à base d'amidon et potentiel d'application dans le domaine des biomatériaux

Mots clés : amidon, nanocomposite, extrusion, structure, hydrolyse enzymatique, cytotoxicité

Résumé : L'objectif principal de cette étude est de caractériser les relations structure-propriétés en condition physiologique de matériaux composites produits par extrusion à partir d'amidon de pomme de terre plastifié avec du glycérol et renforcés par des nanocristaux de cellulose (CNC) ou de chitine (ChNC). Afin de prédire leur comportement dans des applications biomédicales telles que les implants dégradables, la structure à différentes échelles (masse moléculaire, structure cristalline et locale, structure granulaire de l'amidon) est reliée aux propriétés mécaniques à sec des matériaux et à leur comportement en conditions physiologiques (gonflement, dégradation enzymatique, libération du plastifiant). Une étude préliminaire sur des matrices d'amidon pur a permis de dissocier l'effet des paramètres d'extrusion et du plastifiant de ceux des nanoparticules.

Les composites contenant jusqu'à 2.5% de CNC présentent un gonflement réduit et une hydrolyse enzymatique ralentie comparé à une matrice d'amidon pur, ce qui est attribué aux interactions amidon/cellulose. En revanche, un effet opposé est observé pour des concentrations supérieures en CNC (5-10%) ou lorsqu'on utilise de la chitine. Ce résultat est vraisemblablement dû à l'agrégation et/ou à la dispersion hétérogène des cristaux dans la matrice d'amidon. Afin d'étudier la réponse *in vitro* des matériaux, des tests de cytotoxicité et d'adhérence cellulaire ont été réalisés pendant 24 et 48h sur des cellules épithéliales et fibroblastiques. Les matériaux ne sont pas cytotoxiques selon les tests réalisés mais des tests plus précis, spécifiquement pensés pour les nanoparticules, devraient être réalisés pour évaluer leur innocuité.

Title : Development of starch-based nanocomposites and potentiality of application as biomaterials

Keywords : starch, nanocomposite, extrusion, structure, enzymatic hydrolysis, cytotoxicity

Abstract: The main purpose of this study is to characterize the structure-properties relationships in physiological conditions of composite materials developed by extrusion from potato starch plasticized with glycerol and reinforced with cellulose (CNCs) or chitin (ChNCs) nanocrystals. To predict their behavior in biomedical applications such as degradable implants, the multi-scale characterization of the structure (molecular mass, crystalline and local structure, starch granular structure) is linked to the mechanical properties of the materials at the dry state and their behavior in physiological conditions (swelling, enzymatic degradation, release of the plasticizer). A preliminary study on purely starch-based matrices has enabled to separate the effects of extrusion parameters and plasticizer from the ones of the nanofillers.

The samples, up to 2.5wt% CNCs, present a milder swelling and slowed-down enzymatic hydrolysis when compared to a pure starch-based matrix, due to strong starch/nanofiller interactions. However, the opposite effect (stronger swelling, faster hydrolysis) is observed when increasing the CNCs concentration (up to 10wt%) or by replacing cellulose with chitin: this comes from the nanocrystals aggregating and/or dispersing more heterogeneously in the matrix. In order to study the *in vitro* response to these materials, cytotoxicity and cellular adhesion assays have been developed for 24 and 48h by using epithelial and fibroblastic cells. All matrices and composite materials are non-cytotoxic within the limits of these tests but more precise tests, specific to nanofillers, should be performed to evaluate their safety more accurately.